EPFL

Quench behavior of high-temperature superconductor tapes for power applications: a strategy toward resilience

Nicolò RIVA

École
polytechnique
fédérale
de Lausanne

2021

Quench behavior of High-Temperature Superconductor tapes for power applications:

A strategy toward resilience

by

Nicolò Riva

To obtain the Doctor of Philosophy in Electrical Engineering and Applied Superconductivity at the École Polytechnique Fédérale de Lausanne.

Sciper Number:	281918	
Project duration:	2017 – 2020	
Advisors:	Dr. Bertrand Dutoit	Thesis Director, EPFL
	Apl. Prof. Dr. Francesco Grilli	Advisor, KIT
	Prof. Frédéric Sirois	Advisor, PM
Jury:	Prof. Mario Paolone	President, EPFL
	Prof. Yifeng Yang	Member, University of Southampton
	Dr. Bernard Auchmann	Member, PSI
	Dr. Brandon Sorbom	Member, CFS/PSFC-MIT

KIT Karlsruher Institut für Technologie **EPFL** **POLYTECHNIQUE MONTRÉAL**

Abstract

High-Temperature Superconductors (HTS) can be superconducting in liquid nitrogen (77 K), holding immense promises for our future. They can enable disruptive technologies such as nuclear fusion, lossless power transmission, cancer treatment devices, and technologies for future transportation. In the past years, the numerical models to describe the electrical resistivity of REBCO commercial tapes for devices working near and above the critical current, have been shown to be not accurate or very empirical. The resistivity in this regime in fact, is not very well known. The lack of this knowledge is a significant issue in developing quality simulation tools. The major challenge in retrieving such properties lies in the fact that for $I > I_c$, heating effects and thermal instabilities can quickly destroy the conductor if nothing is done to protect it. Moreover, due to the current sharing between the layers, it is difficult to know the amount of current carried by the superconducting layer, and hence, its resistivity. The present work aims to understand better the overcritical current regime combining ultra-fast pulsed current measurements performed on HTS REBCO based coated conductors with Finite Element Modeling. The experimental activities were carried out mostly at EPFL and in part at PM and KIT. The modeling activities were carried out between EPFL and KIT. The major result is a resistivity relationship describing the overcritical current regime to be used in numerical simulations of REBCO tapes. The first part of the thesis illustrates a post-processing method based on the so-called Uniform Current (UC) model to estimate the REBCO material's resistivity in the overcritical from experimental measurements. Pulsed current measurements as short as 15 μs and with current magnitude up to $I = 5 I_c$ were performed in liquid nitrogen bath (77 K) on samples from various manufacturer, without damaging the tapes. The second part of the thesis discusses a post-processing method based on *regularization of data* to treat the experimental measurements extracted in the overcritical current regime. The output of this technique is a look-up table that can be shared with interested partners and used in numerical modeling afterwards. The third part of the thesis presents the overcritical current model ($\rho_{\eta\beta}$): a mathematical relationship of the overcritical current regime based on measurements performed between 77 K and 90 K and in self-field conditions. We first compare the overcritical current model with the power-law model, and then we provide a short discussion of the fitting parameters of the overcritical current model. The last part of the thesis presents and experimental validation of the overcritical current model. The model is then used to show that for the case of a superconducting fault current limiter when the power-law model is used to model its electro-thermal response, the device quenches faster than with the overcritical model. In conclusion, this work can help optimize the use of superconducting material as well as the the amount of stabilizer. More interestingly, it opens the study of the overcritical current regime, a new exciting aspect of REBCO commercial tapes.

Keywords: Resistivity, Modeling, Overcritical current regime, HTS, REBCO, Finite Element Modeling, Pulsed Current Measurements.

Résumé

Les supraconducteurs à haute température critique (HTS) peuvent être supraconducteurs dans l'azote liquide (77 K), ce qui est porteur d'immenses promesses pour notre avenir. Ils peuvent permettre la mise en œuvre de technologies de rupture telles que la fusion nucléaire, la transmission d'énergie sans perte, les dispositifs pour le traitement du cancer et les technologies pour les transports futur. Ces dernières années, les modèles numériques permettant de décrire la résistivité électrique des rubans commerciaux de REBCO pour les appareils fonctionnant à proximité et au-dessus du courant critique, se sont révélés peu précis ou très empiriques. En fait, la résistivité dans ce régime n'est pas très bien connue. Cette méconnaissance est un problème important pour le développement d'outils de simulation de qualité. La principale difficulté pour mesurer de telles propriétés réside dans le fait que lorsque $I > I_c$, les effets de chauffage peuvent rapidement détruire le conducteur si rien n'est fait pour le protéger. De plus, en raison du partage du courant entre les différentes couches constitutives, il est difficile de connaître la quantité de courant transporté par la seule couche supraconductrice et donc sa résistivité. Le présent travail vise à obtenir une meilleure connaissance du régime de courant surcritique en combinant des mesures de courant pulsé ultra-rapide effectuées sur des conducteurs en rubans à couche mince à base de HTS REBCO avec de la modélisation par éléments finis. Les activités expérimentales ont été menées principalement à l'EPFL et en partie au PM et au KIT. Les activités de modélisation ont été réalisées entre l'EPFL et le KIT. Le résultat principal est une relation pour la résistivité décrivant le régime de courant surcritique à utiliser dans les simulations numériques des rubans REBCO. La première partie de la thèse illustre une méthode de post-traitement basée sur le modèle dit de courant uniforme (UC) pour estimer avec précision la résistivité du matériau REBCO dans le surcritique à partir de mesures expérimentales. Des mesures de courant pulsé aussi brèves que 15 µs et avec une magnitude de courant allant jusqu'à $I = 5\,I_c$ ont été effectuées dans un bain d'azote liquide (77 K) sur des échantillons de différents fabricants, sans endommager les rubans. La deuxième partie de la thèse traite d'une méthode de post-traitement basée sur la régularisation des données pour traiter les mesures expérimentales faites dans le régime de courant surcritique. De cette technique résulte une table de référence qui peut être partagée avec tout partenaire intéressé pour leur utilisation dans la modélisation numérique impliquant des rubans supraconducteurs. La troisième partie de la thèse présente le modèle de courant surcritique: une description mathématique du régime de courant surcritique basée sur des mesures effectuées entre 77 K et 90 K et en champ magnétique propre. Nous comparons ces modèles avec le modèle de loi de puissance, et nous présentons une brève discussion des paramètres d'ajustement et de leurs valeurs typiques. La dernière partie de la thèse traite du modèle de courant surcritique, toujours sur la base des mesures expérimentales. Le modèle a été validé expérimentalement et utilisé pour montrer que dans le cas d'un limiteur de courant de défaut supraconducteur, les simulations montrent que lorsque le modèle de loi de puissance est utilisé le limiteur surchauffe plus rapidement qu'avec le modèle surcritique. En conclusion, ces travaux peuvent contribuer à étendre l'utilisation des supraconducteurs par l'optimisation de leur stabilisation. Plus intéressant encore, il ouvre l'étude du régime de courant surcritique, un nouvel aspect passionnant des rubans commerciaux de REBCO.

Riassunto

I superconduttori ad alta temperatura critica (HTS) possono essere superconduttori in azoto liquido (77 K), portando con sé un potenziale immenso per il nostro futuro. Gli HTS potrebbero permettere lo sviluppo di *tecnologie distruttive* quali la fusione nucleare, la trasmissione di energia senza perdite, dispositivi per il trattamento del cancro ed anche tecnologie per i mezzi di trasporto del futuro. Negli ultimi anni, i modelli numerici per descrivere la resistività elettrica dei nastri commerciali di HTS, per dispositivi superconduttori che lavorano vicino e al di sopra della corrente critica, si sono rivelati poco accurati o molto empirici. La resistività in questo regime infatti, è poco conosciuta.

La mancanza di questa conoscenza è un problema significativo nello sviluppo di strumenti di simulazione di qualità. La sfida principale nello studio di questo regime, risiede nel fatto che nel regime sovracritico ($I > I_c$) gli effetti di riscaldamento per effetto Joule e le instabilità termiche, possono distruggere rapidamente il conduttore se non si fa nulla per proteggerlo. Inoltre, a causa della ripartizione di corrente tra gli strati del cavo, è difficile conoscere la quantità di corrente trasportata dallo strato superconduttore e la sua resistività.

Il presente lavoro mira ad ottenere una migliore conoscenza del regime di corrente sovracritico, combinando misure di corrente pulsata ultraveloci eseguite su cavi HTS con la modellazione ad elementi finiti. Le attività sperimentali sono state svolte perlopiù presso l'EPFL ed in parte presso il PM ed il KIT. Le attività di modellazione sono state effettuate principalmente tra EPFL e KIT. Il risultato principale è una relazione di resistività che descrive il regime di corrente sovracritico da utilizzare nelle simulazioni numeriche dei nastri REBCO.

La prima parte della tesi illustra un metodo di post-elaborazione basato sul cosiddetto modello di corrente uniforme (Uniform Current - UC) per stimare con precisione la resistività del materiale REBCO nella sovracritica da misure sperimentali. Senza danneggiare i nastri, abbiamo eseguito misurazioni di corrente pulsata su campioni di vari produttori a 15 µs e con un ampiezza di corrente fino a $I = 5\,I_c$ in un bagno di azoto liquido (77 K).

La seconda parte della tesi tratta un metodo di post-elaborazione basato sulla *regolarizzazione dei dati* per trattare le misure sperimentali estratte nel regime corrente sovracritico. Il risultato dell'utilizzo di questa tecnica è una tabella numerica che può essere condivisa ed utilizzata in seguito nella modellazione numerica dai partner interessati.

La terza parte della tesi presenta il modello di corrente sovracritico ($\rho_{\eta\beta}$): una relazione matematica del regime di corrente sovracritico basata su misure effettuate tra 77 K e 90 K ed in condizioni di *auto-campo*. Confrontiamo i modelli sovracritici con il modello della legge di potenza, e forniamo una breve discussione dei parametri di modellizzazione e dei loro valori tipici. Infine, l'ultima parte della tesi valida sperimentalmente il modello sovracritico. Viene poi utilizzato per dimostrare che, nel caso di un Superconducting Fault Current Limiter, quando il modello di potenza viene utilizzato per modellare la sua risposta elettrotermica, il dispositivo transisce più velocemente allo stato normale (*quench*) rispetto al modello sovracritico. In conclusione, questo lavoro può essere utile per l'ottimizzazione dei cavi superconduttori HTS e, di conseguenza, dei suoi materiali. Questo studio inoltre, apre lo strada alla caratterizzazione e conoscenza del regime sovracritico, un nuovo entusiasmante aspetto dei nastri commerciali REBCO.

Structure of the thesis

This work of thesis's main goal is to achieve a better knowledge of the overcritical current regime of REBCO based HTS coated conductors. The thesis is structured as it follows:

Chapter 1 provides introductory elements of superconductivity, of REBCO coated conductors, and of their characterization using DC transport and pulsed current measurements.

Chapter 2 describes the experimental setup used during this work at EPFL and KIT.

Chapter 3 describes the procedure followed to obtain the overcritical current data. The procedure combines experimental measurements with numerical methods to perform the data analysis. The post-processed overcritical data are presented in this chapter. Lastly, this post-processing method's limits and validity (e.g. uncertainties and material inhomogeneities) are briefly discussed.

Chapter 4 reports the application of an advanced interpolating technique, based on data regularization. The raw overcritical current data were processed using data regularization in order to reconstruct suitable surfaces for FEA. The regularized data can be deployed with interested partners, in the forms of a look-up table to be used in numerical simulations.

Chapter 5 provides a mathematical expression (an heuristic model) of the overcritical current regime for fitting the experimental data. A comparison between this model and the power-law model is made. The presented data show a similar trend: for all the samples characterized it was observed a remarkable decrease of the slope in the overcritical current resistivity regime with respect to the power-law model (this softening has a marked impact in terms of simulations).

Chapter 6 presents the experimental validation of the overcritical current mode, then the impact of the overcritical current model on numerical simulations is assessed. The scenarios of homogeneous DC and AC faults for SFCL are studied, demonstrating how crucial is a good knowledge of REBCO tapes' resistivity in the overcritical current regime. Specifically, it is showed that, for the simple case of a Superconducting Fault Current Limiter, when the power-law model is used, the device quenches much faster than with the overcritical resistivity model.

Chapter 7 summarizes the conclusions and the future work. It is emphasized that the knowledge achieved for the overcritical current regime is very important. It can be used in numerical simulations for case scenarios where the current sharing plays an important role, such as during a hotspot in superconducting devices, in a non-insulated coil, during pulsed field magnetization, or in Superconducting Fault Current Limiters.

La Passione è un dono, introduttivo alla Bellezza.

Passion is a gift, that introduces you to Beauty.

A wise and very dear person I know

Acknowledgements

I was taught that *Passion* is a gift, an introductory *path* to something priceless: *Beauty*. Robert Musil, in *Der Mann ohne Eigenschaften* (The Man without Qualities), reminds us that it is complex to express the tension that exists on the *path* connecting mathematical exactitude and approximation of human events. Well, for me, it is "slightly easier" to interpret a certain physical phenomenon using the former; however, it is a colossal task to pay homage to all the people who - by means of a wide and tangled stream of situations - have constituted the *Beauty* of this *path* through human events. Therefore, I hope to pen down the *Beauty* that has made me *Passionate* about the people who accompanied me during this journey. I will do this without using that overused and somewhat trite word for gratitude; I would rather leverage some concepts that, in recent years, I have encountered and made my own.

Before you embark on a *path*, you must question yourself about its goals and challenges. You speculate about questions like "What is your destination? How long is the journey? Are you prepared for the journey you wish to undertake? Will you emerge successful?". Well, I'm still trying to answer most of these questions. Of course, leaving these answers open leads to the intriguing consequence of finding more questions. Isn't it too ambitious to look for questions rather than answers? No. Goethe himself, who did not appreciate the ferments of Romanticism, nurtured the ambitious idea of a "book about the universe[1] [2]".
Ylenia: you (but not only you) flank me in my quest for these answers (you're looking for them too!). Your beauty is that you have shown me how in the art (and in my case in science) a great desire of purposes and ambitions is not reproachable, as it is in other fields.

For any *path*, you need the right shoes. Sometimes they are tight, and you have to get used to them, but you have them on every difficult part of the *path*, and without them, you don't even start. *Dad*, *Mom*, *Anna*, *Ale* and *Bianca*...all cousins, especially *Andrea*: you have reminded me that I am from Baceno, in Ossola. This certainty has given me (and not only me) a solid imprint, left by safe boots that make you take important steps. It's nice to always look back and check that the mountains I grew up on are on the horizon.

A *path* must necessarily be marked to avoid getting lost. As in Kafka's Der Kübelreiter (The Bucket Rider), I set off with my light, empty bucket on my quest for coal. *Bertand*, *Francesco*, *Frédéric*: you were the signs and whispers to the coalman: you were the "wind of lightness blown over the bucket". The trust you all placed in me, the endless calls and the time you invested to allow me to start my *path* to be a researcher... all of this allowed me to conquer the most difficult stage: believing in my work and in myself. Your beauty is your exceptional humility and empathy, not always reconcilable with those who possess your culture.

It's nice to know that a *path* continues without interruption. If, however, it involves an intricate tangle of *Helvetic-Canadian-Germanic* stages, unforeseen events (especially bureaucratic) are just around the corner. The hospitality of *Prof. Noe*, the incredible opportunity to spend a year at ITEP at *Kalsruhe Institute for Technology* (KIT), to explore German tradition and culture, and funds granted by the Swiss Federal Office of Energy (SFOE) allowed me to continue the entire *path* undisturbed.

---

[1] Six Memos for the Next Millenium (American Lectures) - Italo Calvino
[2] Die Lesbarkeit der Welt (The Readability of the World) - Hans Blumenberg

It happens that you lose your way along the *path*. You are left dazed and without much time to orient yourself. Luckily, with an invisible hand, firm and aware, some shake the true foundation of your beliefs to redirect you to the right *path*. *Mauro*, *Antonio* and *Chiara*, *Lorenzo* and *Chiara*, *Tianshu*, *Jaime*, *Auri* and *Stefano*. Getting to know you has helped me connect and order the mental circuits that populate my vision. Your beauty is that you have shown me how essential it is to "make yourself crazy by behaving normally[3]". How to take the risk of being different, but carefully and *cum grano salis* (using the head) to follow what has been given.

Following a *path* alone is deleterious (though it's priceless in small doses). I had the honor of sharing the *path* with colleagues who were paramount in my education. My Super(conducting) colleagues: *Arooj*, *Enrico*, *Simon*, *Ruslan*, *Shahab*, *Roland*, *Tara* and *Christian*... My Hyper(loop) colleagues from EPFLoop: *Simone*, *Jerome*, *Martin*, *Zsofi*, *Fedele*, *Outmann*, *Denis* and many others...then irreplaceable and ever-present characters such as *Mario* and *Sven*. Like Zarathustra for the young boy in the story "Of the Tree on the Mount[4]", you have witnessed my long transformation: you have seen how "my today was the refutation of my yesterday". Your beauty is that, unlike the young man in the story, you never left me alone,

As a good marathon runner, I know that you can't last long if you're tired and have an empty stomach. Friends and roommates in Lausanne were able to provide for that. *Eugi* - my inestimable brother - *Cinzia* and *Sissy* - unique quarantine companions. Then *Leo*, *Tommy*, *Enrica*, *Mathieu* and *The Architects*. The conformity of shared fates distilled a bizarre friendship of fondue, gnocchi, pizza, beers and Primitivo di Manduria. Your beauty is that, like Leopardi in the Zibaldone or in the Infinito, you have challenged me to taste the beauty of the indeterminate and of the "dolce naufragar" (gentle shipwreck) along the way, to be able to run across the *path* with a renewed energy.

A *path* must finally be pursued in a *Constant* manner, but without fixing the eyes on the road. Peering beyond the confines of the *path* frees us from the toils and specters we create in our heads - just like the slave in Plato's cave. Of course, you have to be lucky as I have been. Beyond the boundaries of the *path* I have found those who support me, those who inspire me, those who smile at me, and those who carry me on a physical and/or mental journey. *Fermata Piola*, *Piola*'s family, *Anna* and *Maria Cristina*, *Max* and *Ale*, *Maurizio* and *Paolo*. Then *Edo* and *Stella*, *Fabi*, *Nicholas*, *Alessandro*, *Merlo*, *Pashu* and many others. Having met you - for minutes or months - make me indecently lucky. The lessons, laughter, toasts, and friendship you have given me have punctuated the journey with milestones otherwise unattainable to me.

In short, you may have guessed that I'm *passionate* about a *path* if I can throw myself headlong into it, with the right people and with the right time learn as much as possible: *Festina Lente...* (make haste slowly...)! I am even more passionate if it's a very long *path*, at the limit of my strength and, maybe, done by running: *...sed Mere Alis Tuis* (...but earn your wings!).

Well...did you expect a finish line and an end in this story? I didn't reach any finish line, just another stage. The *path* gets more interesting now, and I want you with me, now more than ever! Will you be there? Yes, I am certain you will.

---

[3]Veronika decides morrer (Veronika decides to die) - Paulo Coelho
[4]Also sprach Zarathustra (Thus Spoke Zarathustra) - Friedrich Nietzsche

Contents

1

Introduction: Theory and characterization aspects of REBCO tapes

This chapter provides introductory elements of superconductivity, High-Temperature Superconducting (HTS) REBCO tapes, and the Ph.D. research motivations.

1.1. Short introduction to superconductors

The story of Feynman's strive with superconductivity is a little-known chapter in both Feynman's career and superconductivity history. As evidenced by the interview, even the 1965 Nobel Prize in Physics struggled in understanding the underlying complex quantum behavior of superconductivity, discovered over 100 years ago.

1.1.1. Origins and introductory elements of superconductivity

Superconductivity is a remarkable combination of electric and magnetic properties. It was observed for the first time in 1911 by Kamerlingh Onnes [2], who measured a sharp transition of the electrical resistivity of solid Mercury wire to zero at the temperature of 4.2 K, the critical temperature. A material with no resistance means that there is no voltage drop along the material when a current is passed through it, hence no power is generated by the passage of the current[1], holding immense potential for applications where high currents are needed. Later, in 1933, Meissner and Ochsenfeld investigated the effects of a magnetic field on a superconductor, observing that the specimens spontaneously became perfectly diamagnetic, canceling all at the transition temperature magnetic flux inside the material. This property took the name of Meissner–Ochsenfeld effect [4]. These electrical and magnetic properties appear only if the material is in the superconducting state. More precisely, the superconducting state is lost (and the material becomes normal resistive) if the carried current density, temperature, and magnetic field at which he is subjected, individuate together a coordinate below the Figure 1.1a, named critical surface. Surprisingly, superconductivity is not rare and can be observed among several elements of the periodic table. Over the years, superconducting properties were also found in many compounds with increasing critical temperatures.

The superconductivity's microscopic origin is due to an attractive interaction between elec-

---

[1]In reality, the absence of generated power is strictly valid only for direct current (DC) of constant value. If the current changes (AC) an electric field develops on the material and some power is dissipated [3].
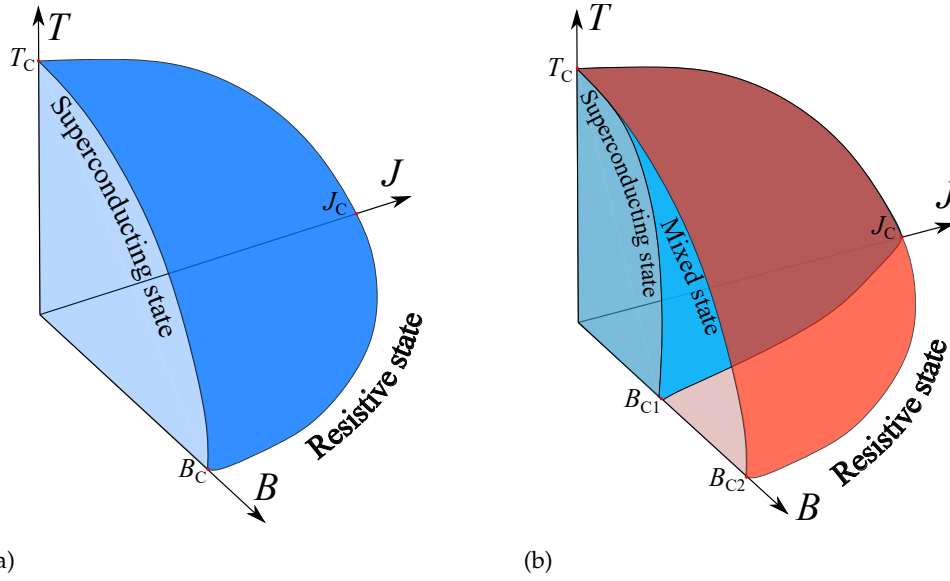
Figure 1.1: (a) The critical surface of Type I superconductors delimits the superconducting and normal states. (b) The critical surface of Type II superconductors delimits the superconducting, mixed and normal states.

trons that generate the Cooper pairs, and it is mediated by the ion lattice's vibrations [5]. Together, the Cooper pairs form a macroscopic coherent quantum state, a condensate, extended through the entire superconducting material. Because of the condensate nature, the Cooper pairs behave coherently, and it takes a significant amount of energy to scatter an electron from the condensate. Thanks to this unique mechanism, the paired electrons can flow without being scattered and, therefore, without any electrical resistance. An external input of energy given by sufficiently high temperature, external magnetic field, or carried current density will break down the Cooper pairs, destroying the superconducting properties.

Today, over 100 years after the first superconductor was discovered, some of these materials are used in practical superconducting wires, cables, and tapes for several applications such as magnetic imaging machines, magnets for particle accelerators, superconducting fault current limiters, permanent magnets, motors, nuclear fusion and devices for cancer treatment.

1.1.2. Classification: type-I and type-II superconductors

Superconductors can be classified according to their magnetic behavior in response to an external magnetic field, distinguishing them in type-I and type-II. Most of the elements which are superconductors exhibit type-I superconductivity, whereas alloys generally exhibit type-II superconductivity. In type-I superconductors the Meissner state is lost when the applied magnetic field on the specimen is $\boldsymbol{B}_{app} > \boldsymbol{B}_c$, the critical field (Figure 1.1a). However, if the specimen's shape is such that considerable demagnetizing effects appear[2], even relatively small $\boldsymbol{B}_{app}$ will exceed $\boldsymbol{B}_c$ on the edges of the sample [3]. In such regions, the field penetrates the superconductor and normal conducting regions (with a penetrating field of $\boldsymbol{B}_c$), and superconducting regions (in the Meissner state) will coexist in the sample. This state is called the intermediate state.

The type-II superconductors exhibit a complete Meissner effect only at low magnetic fields $\boldsymbol{B} = \boldsymbol{B}_{c1}$ (lower critical field), which is typically smaller than the critical field of type I su-

---

[2]The demagnetizing field is the magnetic field generated by the magnetization in a magnet, outside the sample is also named stray-field. The total magnetic field in a region containing magnets is the sum of the demagnetizing fields of the magnets and the magnetic field due to any free currents or displacement currents [6].

Type	Material	T_c (K)	B_c or B_{irr} (T)	Characteristic
I	Al	1.2	0.01 @ 0 K	Metallic/ductile
	Pb	7.2	0.08 @ 0 K	Metallic/ductile
II-LTS	NbTi	9	10 @ 4.2 K	Metallic/ductile
	Nb_3Sn	18	20 @ 4.2 K	Metallic/brittle
II-HTS	MgB_2	39	5.5 @ 20 K	Anisotropic, Ceramic/brittle
	$Bi_2Sr_2Ca_2Cu_3O_{10}$	110	5 @ 26 K	Anisotropic, Ceramic/brittle
	$Bi_2Sr_2Ca_2Cu_2O_8$	85	5 @ 16 K	Anisotropic, Ceramic/brittle
	$YBa_2Cu_3O_7$	90 − 92	9 @ 86 K	Anisotropic, Ceramic/brittle

Table 1.1: Classification of superconductors [9]. Iron-based superconductors are not included [10].

perconductors B_c. When the applied field increases above the lower critical field ($B > B_{c1}$), the material enters in the mixed state (Shubnikov phase[3]). In the mixed state the material is still superconducting, but resistive regions in form of tubes named vortex nucleate in the superconductor, each carrying a quantized magnetic flux Φ_0):

$$\Phi_0 = \frac{h}{2e} \simeq 2.07 \cdot 10^{-15} \, \text{Wb}, \tag{1.1}$$

where h is the Planck constant and e the fundamental electron charge. The illustration in Figure 1.2a, shows the penetration of the vortices (cylinders). For $B > B_{c2}$ (upper critical field), the vortices cover the material entirely, meaning that it is transparent to the external magnetic field and that the superconducting state is lost (Figure 1.1b). Type-II superconductors are those used for practical applications, since B_{c2} is much higher than B_c in type-I material (Table 1.1). In this work, the focus is on type-II superconductors, which can be categorized in Low-Temperature Superconductor (LTS) or High-Temperature Superconductors (HTS) according to their critical temperature (Figure 1.1b). The first HTS superconductor was discovered in 1986 [8] and its critical temperature of 30 K set the threshold value above which a superconductor is defined as HTS.

It is important to distinguish clearly between the mixed state, which occurs in type-II superconductors and the intermediate state, which occurs in type-I superconductors. The intermediate state occurs in those type-I superconducting bodies, which have a non-zero demagnetizing factor, and its appearance depends on the shape of the body. However, the mixed state is an intrinsic feature of type-II superconducting material and appears even if the body has zero demagnetizing factor (e.g., a long rod in a parallel field).

1.1.3. Flux motions, $H - T$ phase diagram and resistivity regimes

Since each vortex carries a quantized magnetic flux, when both a transport current J and a magnetic field B are present in the superconductor, each vortex experiences the Lorentz force $F_L = J$xB as represented in Figure 1.2a.

The Lorentz force sets in motion the vortices, and thus, gives rise to an electric field and to net dissipation [11]. The presence of defects in the system (such as impurities, vacancies, interstitial atoms, dislocations, grain boundaries, precipitates) stops or attenuates the vortices' motion. In this regime ($F_L \leq F_p$), named flux-pinning, the vortices are anchored (or pinned) to the defects by the pinning force F_p, and no dissipation appears in the superconductor. If the

---

[3]There is a clear difference between the intermediate and mixed state. The intermediate state occurs due to geometrical factors in type I superconducting material, while the mixed state is an intrinsic feature of type-II superconducting material and appears even if the body has zero demagnetizing factors (e.g., a long rod in a parallel field) [7].
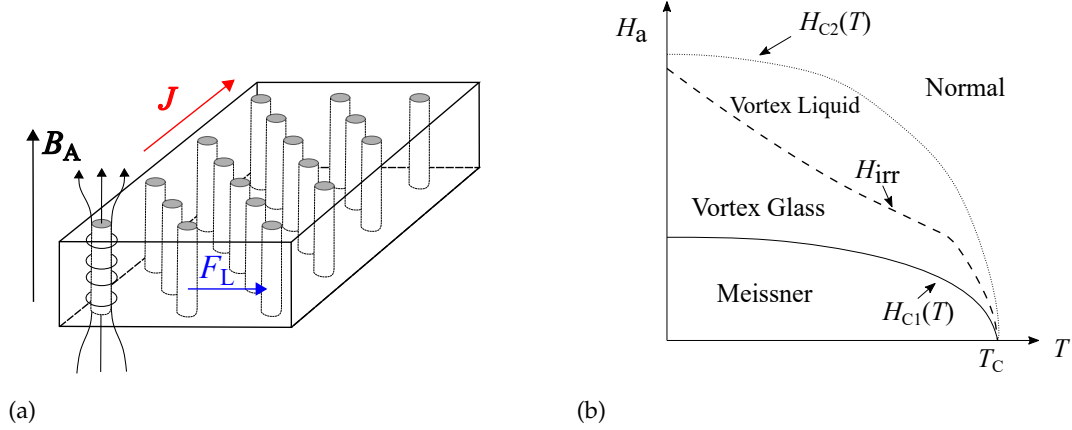
Figure 1.2: (a) Illustration showing a strip of superconductor in the mixed state. The external magnetic field B_A is able to penetrate the material through the vortices (cylinders) each carrying Φ_0. A Lorentz force F_L occurs when an external magnetic field is applied. (b) Phenomenological $H - T$ phase diagram for type-II superconductors. Above the irreversibility line (vortex liquid sub-state) vortices are all moving and dissipation occurs.

injected current density is large enough, the pinning force can be dominated ($F_L \geq F_p$), and all the pinned vortices are free to move. In this regime, named flux-flow, an onset of dissipation will appear. This behavior subdivides the mixed-state in two additional sub-states, represented in Figure 1.2b. In the vortex-glass state the vortices are held in place by defects ($F_L < F_p$) and mutual repulsion, while in the vortex-liquid state the vortices are moving freely ($F_L \geq F_p$). We can define the critical current density J_c as the current density at which the Lorentz force F_L exceeds the pinning force F_p. The vortex-glass state is the state where the superconductor's non-dissipative behavior manifests, while dissipation occurs in the vortex-liquid state. The line delimiting the two sub-states is named irreversibility field line H_{irr} [12]. Finally, the presence of inhomogeneities in superconducting compounds makes the pinning force not homogeneous. Therefore, the vortices unpin from the defects and start moving through the lattice gradually, not all at once. As a result, an intermediate and smoother regime between the flux-pinning and the flux-flow regime is present, named flux-creep.

1.2. Non-linear relation for superconductors
Different constitutive relations have been proposed in the literature to describe the resistivity regimes of the superconductor. The power-law is commonly used to describe the $E - J$ characteristic in the flux-creep regime [13, 14]:

$$E = E_c \left(\frac{J}{J_c(T, B)} \right)^{n(T, B)},$$

(1.2)

where E_c is the critical electric field, J_c is the critical current density and n is the power indicating the steepness of the characteristic (n-value). The higher the n-value is, the steeper $E(J, T, B)$ is. In LTS the n-value ranges from 40 to 50 [15], while in HTS(REBCO) the n-value ranges from 25 to 35 ([16]). In the case of REBCO tapes, the superconducting properties also depend on the tape's orientation with respect to the external magnetic field. It is possible that the amount of current carried under transverse field (wider flat face) is 1.5–4 times lower than under the same field amplitude but parallel to the tape. In Figure 1.4a it is represented the $E(J)$ relation for increasing n-value. The critical current J_c is usually defined as the value at which a voltage corresponding to an arbitrary electric field value (critical field) of $E_c = 1\,\mu V\,cm^{-1}$ to $10\,\mu V\,cm^{-1}$ is reached on the length of the measured sample. In the flux-flow regime, it has

Flux pinning   Flux creep   Flux flow
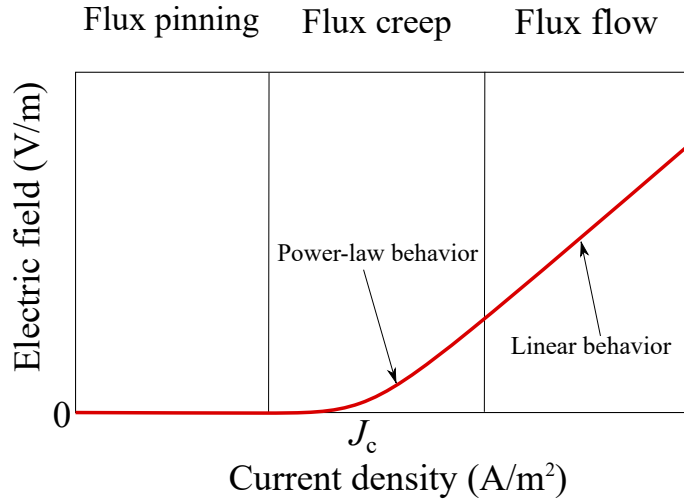
Figure 1.3: Behavioral representation of the three resistivity regimes in type-II superconductors. For type I superconductor the transition is much more rapid.

been shown that the $E - J$ relation is linear [11, 17–19]:

$$E = \rho_{ff}(B, T) \cdot (J - J_c) \qquad \rho_{ff}(B, T) = \rho_{NS} \frac{B}{B_{c2}(T)} \tag{1.3}$$

The electrical field is proportional to the number of vortices present in the superconductor up to the normal state, i.e., when the flux-flow resistivity (ρ_{ff}) equals the normal resistivity (ρ_{NS}). However, obtaining the fraction of conductor covered by flux-lines in motion is not straightforward [9]. For the sake of simplicity, most of the time, the electrical resistivity of the superconductor is described utilizing the power-law model only. In Figure 1.3, a behavioral representation of the three regimes, flux-pinning, flux-creep, and flux-flow, is shown. At this point, a remark is necessary about the physical meaning of Equation (1.2). The definition of critical current J_c is ambiguous since the flux-creep represents a regime where the vortices are not moving all at once, and the onset of an electric field due to their movement is difficult to determine experimentally. Despite this, the power-law model is simple to implement and widely used in modeling superconducting materials.

The power-law model can be expressed in terms of resistivity ρ (or conductivity $\sigma = 1/\rho$). A non-linear resistivity based on Equation (1.2) can be written as:

$$\rho_{PWL} = \frac{E(J)}{J} = \frac{E_c^{1/n}}{J_c} |E|^{(n-1)/n} + \rho_0, \tag{1.4}$$

where the temperature T and magnetic field B dependence of the critical current density $J_c(T)$ and the n-value are omitted. Equation (1.4) is used especially for numerical modeling. The parameter ρ_0, ranges between 10^{-16} and 10^{-15} $\Omega\,m^{-1}$, and it is added to avoid numerical divergences when the current is 0A ([20]). Besides, when large currents are injected in the superconductor, Equation (1.4) is not bounded, which can be an issue for the numerical solver. To bound the power-law and better reproduce the electrical behavior of the superconductor, a constant resistivity ρ_{NS} can be added in parallel ([21]). The resistivity power-law ρ_{SC} to be implemented in the numerical models can finally be expressed as:

$$\rho_{SC} = \frac{\rho_{PLW} \cdot \rho_{NS}}{\rho_{PWL} + \rho_{PWL}}. \tag{1.5}$$
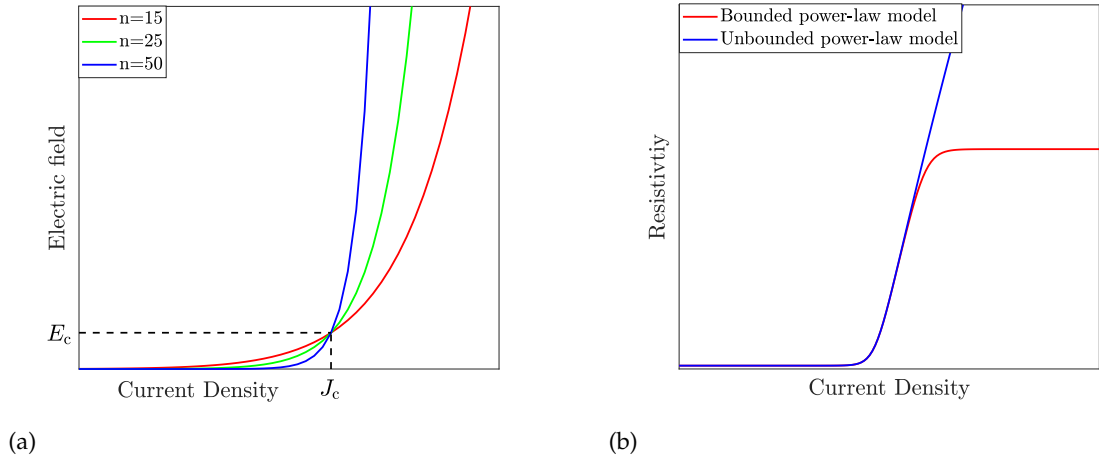
Figure 1.4: (a) The $E(J)$ power-law model increasing n-values. (b) Comparison between the unbounded and bounded power-law for $n-$value $= 50$.

Finally, in some cases, it is necessary to consider the temperature dependence of the normal-state resistivity of the superconducting material. To do this, a linear temperature dependence is described by:

$$\rho_{NS}(T) = \rho_{T_c} + \alpha \cdot (T - T_c),$$

where ρ_{T_c} is the normal state resistivity and α is the coefficient of the linear temperature-dependent resistivity. In Figure 1.4b, it is represented the comparison between the bounded and unbounded resistivity power-law model.

As mentioned earlier, Equation (1.2) is also used to describe the flux-flow regime. In some cases, the flux-flow in Equation (1.3) is treated similarly to the flux creep region by using a piecewise power-law with a lower n-value [22]. However, such relations are not always accurate in modeling superconductors. Despite the great interest in studying HTS super-conductors' resistivity, its electrical resistivity remains unknown for currents well above its critical current, i.e., in the flux-flow regime and in the superconducting-to-normal transition. Later in this manuscript, the lack of experimental data in the overcritical current regime will be discussed.

1.3. REBCO commercial tapes

The focus of this work is on the Rare Earth Barium Copper Oxide (REBCO). The REBCO belongs to the family of HTS compounds, and the rare earth used is typically Yttrium (Y) and Gadolinium (Gd), resulting in YBCO and GdBCO ([23, 24]). Figure 1.5 is a simplified depiction of the layered architecture of a commercial REBCO tape. REBCO tapes are manufactured in form of layers on a metallic substrate (50 μm to 100 μm thick [25]), which provide mechanical rigidity for the tape, the REBCO layer (1 μm to 5 μm thick [26, 27]) and an electrical stabilizer layer. The stabilizer, typically 1 μm to 5 μm thick silver, provides an alternative low resistive path in case of transition of the superconductor. Due to the high current that RE-BCO tapes can carry, a loss of superconductivity can lead to a destructive heat generation and thermal runaway in the tape, therefore a larger amount of stabilizer can be required. In some cases, therefore, the tape is coated with copper stabilizer. REBCO has better flux-pinning and irreversibility field properties than most superconductors, and they can carry a large amount of current in strong magnetic fields. The critical temperature is $T_c = 92\,\text{K}$ [28] in self-field conditions, and this allows the use of Liquid Nitrogen (77 K) as a coolant, which is cheaper and
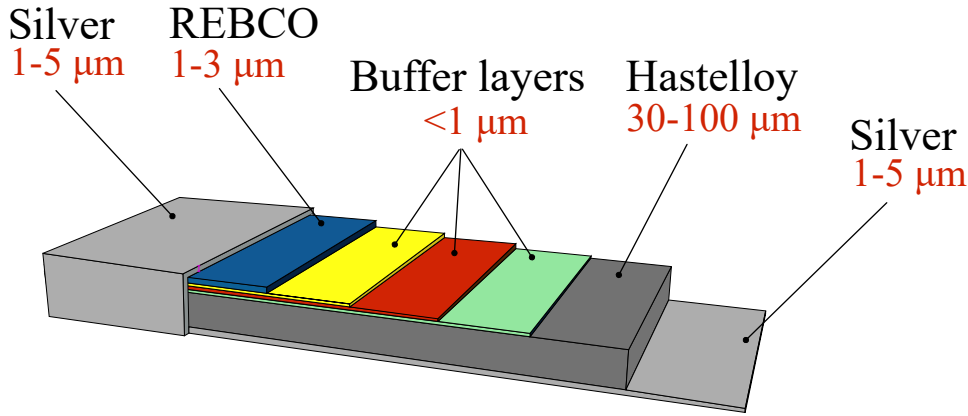
Figure 1.5: Architecture of a REBCO commercial tape. The representation it is not in scale.

easier to handle than other coolants such as Helium or Hydrogen.

In [29] it is reported that the overall critical current density of the wire at $4.2\,\mathrm{K}$[4] and $20\,\mathrm{T}$ show that REBCO tapes can carry more than $1200\,\mathrm{Amm^{-1}}$. REBCO tapes, therefore, reached impressive technical milestones compared to the samples produced at Los Alamos National Laboratory in 1995 [30], and their high performances in terms of carrying current at high magnetic field made them the most desirable choice for a plethora of applications. Such progress further stimulates the development of the current-carrying capabilities for REBCO tapes. Recently it has been reported the successful test of a REBCO based coil generating a magnetic field of $14.4\,\mathrm{T}$ inside a $31.1\,\mathrm{T}$ resistive background magnet to obtain a DC magnetic field of $45.5\,\mathrm{T}$, a record at the time of writing of this thesis [31]. However, the slow decrease in cost reduction of this technology since its inception is still a major obstacle in market penetration.

1.4. Characterization of REBCO tapes

Equation (1.2) and Equation (1.5) describe the behavior of a superconducting material using a few parameters that can be characterized experimentally. The REBCO $E-J$ characteristics' experimental characterization can be very challenging since mechanical aspects, field, temperature, and current dependence are involved. Many techniques have been developed to characterize specifics aspects of the superconductor, such as AC susceptibility measurements [32], magneto-optical imaging [33], and transport current. There is no interest in characterizing the whole behavior at once, however. For our goal, the $E-J$ characteristics of REBCO tapes from different manufacturers, especially in the overcritical current regime, are obtained utilizing transport current measurements between $77\,\mathrm{K}$ and $92\,\mathrm{K}$, and in magnetic field up to $400\,\mathrm{mT}$. Specifically, the experimental techniques described and used in this thesis work are DC transport current measurements and pulsed current measurements.

1.4.1. DC measurements

The most common technique to obtain the $E-J$ characteristics is by performing DC transport current measurements. The material is cooled down to an operational temperature T_0 (e.g. with liquid helium, liquid nitrogen, or conductive cooling) and an external magnetic field $\boldsymbol{B}$ is applied, if available in the setup. Afterward, an increasing transport current is injected until the chosen E_c criterion is reached. There are several disadvantages when using this technique. First of all, in Figure 1.4a, the critical current I_c is the same for all the n-values, but the electric

---

[4]Temperature of a boiling liquid helium bath at atmospheric pressure

field will develop sooner for lower n-value. This makes the E_c criterion ambiguous, and its arbitrary choice affects the determination of I_c, overall for materials with smaller n-value. Then, the gradual behavior of $\boldsymbol{E}(\boldsymbol{J})$ in REBCO materials makes it difficult to perform precise $I - V$ measurements with increasing transport current since the sample heats up during the measurement. Specifically, when characterizing the sample in conditions where the transport current exceeds the critical current ($I > I_c$), thermal instabilities can occur and quickly destroy the sample. Finally, no information is obtained on the rest of the superconducting-to-normal transition in the overcritical current regime.

1.4.2. Pulsed Current Measurements

A classic method to minimize heating effects in the tape and characterize the overcritical current regime of superconducting samples is using pulsed current measurements (PCM). The measured samples can be of various shapes, like the REBCO tapes, superconducting thin film grown on Sapphire substrate (to ensure thermal stability during the measurements), or REBCO bulks. The technique can be performed using different approaches. In [34, 35] a half-sine voltage wave is applied on a current limiting resistor in series with the HTS sample. Another approach uses an RLC circuit that generates a transient electrical impulse in the sample [36, 37]. With these techniques, the voltage signal is distorted by a high induced voltage. It is necessary to subtract the inductive contribution from the original measurement to measure the voltage drop exclusively on the tape. A solution is to use a loop voltage capable of measuring the inductive signal ([36, 37]) to be subtracted.

A method that helps reduce the issues due to the inductive signal is the use of squared current pulses that are sufficiently flat in the plateau region. Once the plateau is reached, and the current is stable, the measured signal is essentially due to the tape's voltage drop. Performing slow PCM (1 ms to 10 s), and for currents up to 10 kA [38–40] is fairly easy to achieve, but becomes challenging in the microseconds range. In [41] PCM in the micro-seconds range at substantial current density were performed on superconducting micro-bridges patterned on sapphire films. In [42, 43] $E - J$ measurements were conducted over more than four decades of electric field (0.1 mV m^{-1} to 10 mV m^{-1}) by a combination of DC current measurements at low voltages and of transient current measurements at higher voltages. In [42, 43], the measurements were performed on an etched REBCO tape, a process that may degrade or change the superconducting properties.

Despite the discrete number of studies involving PCM techniques, no system used in the studies mentioned above simultaneously combined high currents (hundreds of amps) and rise times in the scale of microseconds, with the possible exception of [44].

The articles [45, 46] outline the design of a PCM system developed at Polytechnique Montréal in collaboration with Ecole Polytechnique Fédérale de Lausanne, that allows applying squared current pulses with a duration as short as 15 μs, and currents between 60 A and 1600 A. This device enables characterizing commercial HTS materials at very high current densities without any preparation, such as cutting/etching operations to reduce cross-section. The geometrical and superconducting properties remain unaltered. The small amount of energy injected in the HTS material allows us to reach very high electric fields values on the tape without destroying the sample. In this work, PCM is performed with a setup with this design, of which there are two specimens (one at PM Montréal and one at EPFL).

Misura ciò che è misurabile, e rendi misurabile ciò che non lo è.

Measure what is measurable, and make measurable what is not so.

Galileo Galilei, Dialogo dei massimi sistemi

2
Experimental setup

2.1. Description of the experimental techniques and setups

The measurements were performed on commercially available REBCO coated conductors[1]. All the tapes were 4 mm to 12 mm wide and coated with silver stabilizer only and tapes with more complex architectures (e.g., with an additional layer of copper stabilizer) were not characterized. Since the PCM setup allows fast and non-destructive overcritical current measurements, the copper stabilizer was unnecessary. A representation of the cross section of REBCO tapes is depicted in Figure 2.1a, while a picture of the typical characterized samples is presented in Figure 2.1b. The techniques and setup used to characterize the REBCO tapes are presented in the next sections.

2.1.1. Pulsed current measurements setup

A PCM technique was used to perform non-destructive characterization of REBCO tapes at very high values of electric fields.

---

[1]We want to thank SuperOx, ShangHai, SuNAM, and THEVA for having provided samples for research purposes.

(a) (b)
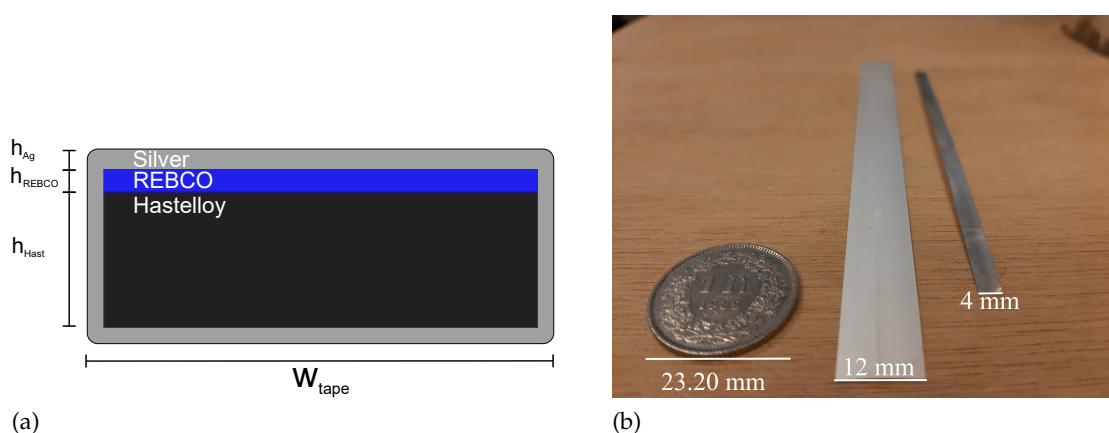
Figure 2.1: (a) Cross-section representation of the measured sample, not in scale. (b) REBCO samples of 12 mm and 4 mm, in comparison with a coin.

The setup can be divided into the following subsystems:

- Ultra-fast current source and current leads;

- Cryostat and normal-resistive dipole magnet;

- Sample holder and connections;

- Voltage amplifier and measuring system;

Ultra-fast current source and current leads: The PCM system, developed at Polytechnique Montréal in collaboration with École Polytechnique Fédérale de Lausanne, allows applying very short and constant (on the plateau) current pulses with a duration as short as ~ 15 µs, and currents between 60 A and 1600 A. The current pulses are generated by discharging one bank of capacitors, and their duration and amplitude are controlled by 8 Current Generation Modules (CGM Figure 2.2a) in parallel and driven by a low-power, pulsatile voltage source. Each module can generate a current pulse I_{pulse} ranging from 20 A to 200 A, operating its signal independently using a Micro-Controller Unit (MCU), provided with a feed-back stability loop and commanded by a single master MCU (Figure 2.2c). The reader can refer to [45, 46] for a more detailed description of the PCM system.

The CGMs are connected to a common point; specifically, a star-connection, screwed on the current leads. The current leads (Figure 2.2b), carrying the current from the star connection to the REBCO sample, consist of two bars, current injection and return. Each bar, reciprocally electrical insulated, is composed of a stack of copper tapes, 1.4 cm wide and 140 cm long, with Kapton tape as insulating filler to avoid high voltage arks during the pulses and minimize the overall inductance. Finally, to measure the pulsed current, we used a Rogowski coil with a gain of $G_{coil} = 2\,\mathrm{mVA}^{-1}$. The gain G_{coil} is used to convert an acquired voltage signal to current. If we measure $V_{coil} = 800\,\mathrm{mV}$, the effective current is $I_{coil} = V_{coil}/G_{coil} = 800\,\mathrm{mV}/2\,\mathrm{mVA}^{-1} = 400\,\mathrm{A}$.

Cryostat and normal-resistive dipole magnet: The cryostat in Figure 2.3 was 900 mm long, with a diameter of 50 mm and made out of glass. It allowed measurements under magnetic field (0 mT to 400 mT), at low pressure (0.1 atm to 1 atm), and in liquid nitrogen bath (between 65 K to 77 K, see Appendix A.3). The magnetic field was generated using a commercial magnetic dipole (μ-BEAM.Sàrl). The magnet, composed of 2 coils of 410 turns, was able to produce DC-magnetic flux as large as 400 mT for an air-gap of 60 mm. The cryostat was sealed with a Teflon© cap, elastomer, and vacuum grease. The Teflon© cap was traversed by the current leads, connecting the current source to the sample holder, which was placed along the length of the cryostat and between the poles of the magnetic dipole (Figure 2.3). The magnetic poles' orientation was fixed, such that the applied magnetic field was always perpendicular to the sample surface. In Appendix A.2, we report a simple 3D magnetostatics simulation in COMSOL, assessing the homogeneity of the applied magnetic field in the region of the sample. The field homogeneity was estimated to be within 1 % and 4 % along the width x and the length y of the sample holder, meaning 4 mm and 10 cm respectively.

Sample holder and connections: The mounting of the sample in Figure 2.4b, allowed measuring 14 voltage sections every 5 mm, plus one section that encompasses the whole length of the sample (7 cm). All the characterized samples were 10 cm long to ensure the electrical contact with the current leads in gold at the extremities of the sample holder. The samples were placed between the gold plated current contacts and fixed with a thin Kapton strip. The upper part of the sample holder was screwed to the sample holder's lower part, clamping the sample and Kapton strip. This ensures good electrical contact of the tape with the voltage
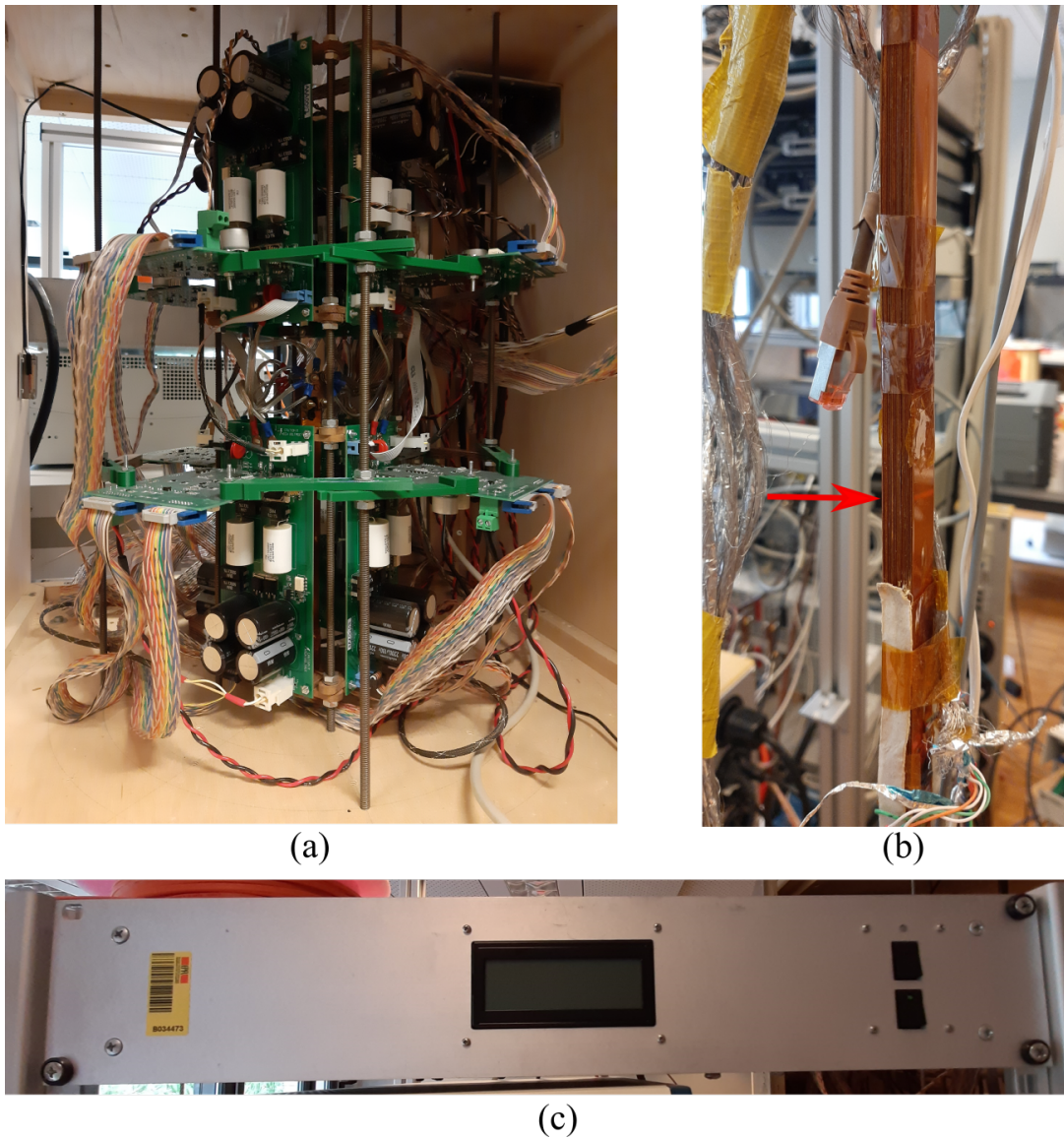
Figure 2.2: (a) One of the eight current generation modules (CGMs), the (b) current leads composed by a stack of copper tapes, and the (c) master controller unit.

taps. At the timescale (µs) and current amplitudes (hundreds of A) of the pulses involved, the inductive signals affect the measurements. The utilized sample holder was designed to minimize the inductive signals' effects and developed at Polytechnique Montréal. A PBC board with a SFM210-LPSE-D15-SP-BK connector (Figure 2.4b) can be plugged into the sample holder, routing twisted and shielded voltage pairs (Figure 2.4c) to the measuring system. The twisted pairs allowed reducing the effects of electromagnetic interference noise on the signal. Each twisted pair measures one of the section (A to O) and is soldered on the PCB board on one of the two ends. The other end is soldered to the positive and negative pins of a LEMO FGG.1B.303.CLAD connector (type male). In total, 15 LEMO connectors read the voltage signal and can be plugged into the measuring system. The signals are plugged in an attenuator (Figure 2.4d) box with a LEMO EXG.1B.303.HLN female sockets. By selecting between three attenuation values ($1x/10x/100x/1000x$), the attenuators ensure the correct dynamic of the DAQ measuring system.
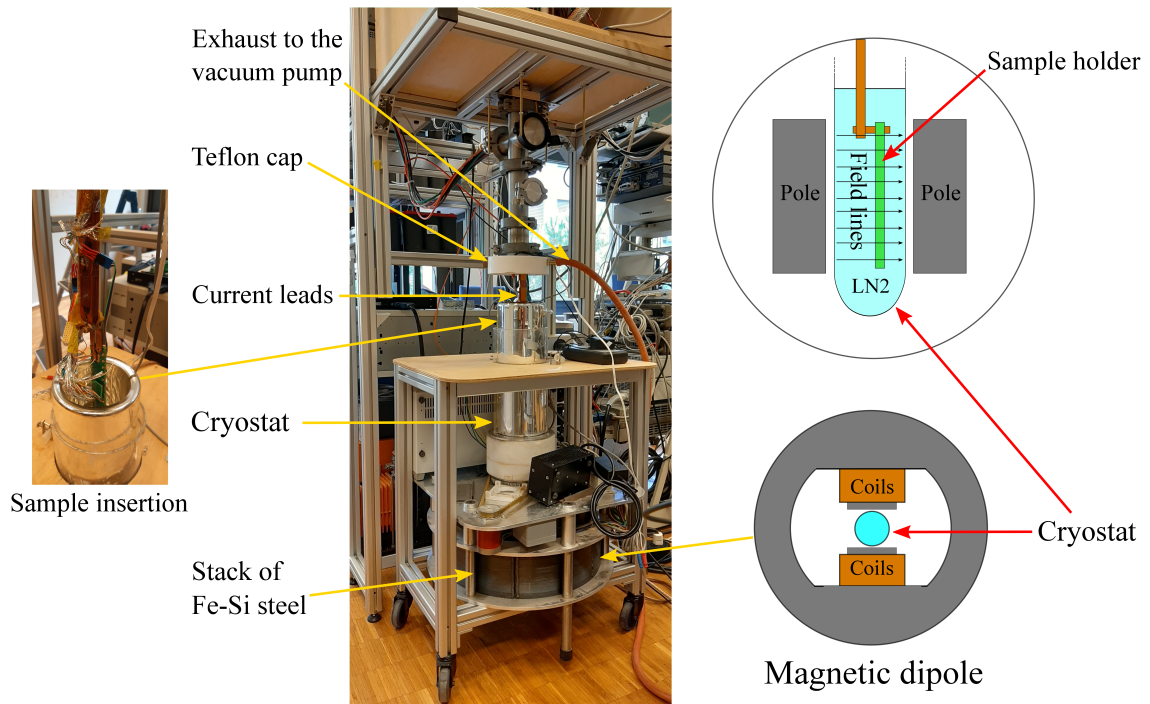
Figure 2.3: The current leads cross the Teflon cap, connecting the ultra-fast current source with the sample holder. The cryostat is connected to the vacuum pump utilizing an exhaust rubber tube. It crosses the air-gap of the dipole (inset bottom), which poles have approximately the same height as the sample holder (inset top). The resulting magnetic field-lines are homogeneous in the region of interest, i.e., where the voltage contacts are placed on the sample (see Appendix A.2).

Voltage amplifier and measuring system: When performing high current pulses (1600 A), the voltage between the sample and the ground can reach amplitudes up to 1000 V due to the impedance (resistance and inductance) of the measuring circuit [47]. The measuring system must handle at the same time voltage signals in the order of $milli-volts$ on the sample in presence of a common-mode of up to 1000 V. Also, the bandwidth of the measured signals is considerable, from ~ 0 Hz to ~ 20 MHz. The device that meets such requirements, the 8-Channel Isolated Amplifier System (8-CIAS), was commissioned and custom-built from SCI-Consulting [47] (company located in Lausanne).

The front-panel of the 8-channel Isolated Amplifier System is shown in Figure 2.5. Each channel contains a 3-pole input connector (In_+, In_- and $Earth$) and a 3-way gain selector[2] ($1x/10x/100x$). A single NI 68-pin connector is shared to transmit all channels' LF signals to a NI DAQmx compatible device. The amplifier separates the signal in low frequencies (LF) of the original signal (from ~ 0 Hz to ~ 49 kHz [47]) and high frequencies (HF) (from ~ 7.3 kHz to ~ 20 MHz) [47].

The LF and HF signals of the 8-CIAS no longer contain the common mode and can be measured by grounded acquisition cards. However, it is necessary to reconstruct the original signal from the LF and HF signals, using Fourier analysis. This step can be performed in MatLab or directly in a LabVIEW code supplied with the 8-CIAS [47]. During the reconstruction process, parasitic oscillations affecting the measurements were found, but in [48], a detailed analysis was allowed to correct them. In this work, the oscillations in the measurements reported are sufficiently low (for large signals, the error is below 10 %). The oscillations were mitigated by fine-tuning the transfer function implemented in the LabView code. The reader

---

[2]Note that the gain selector applies only to the LF signal, not the HF signal.
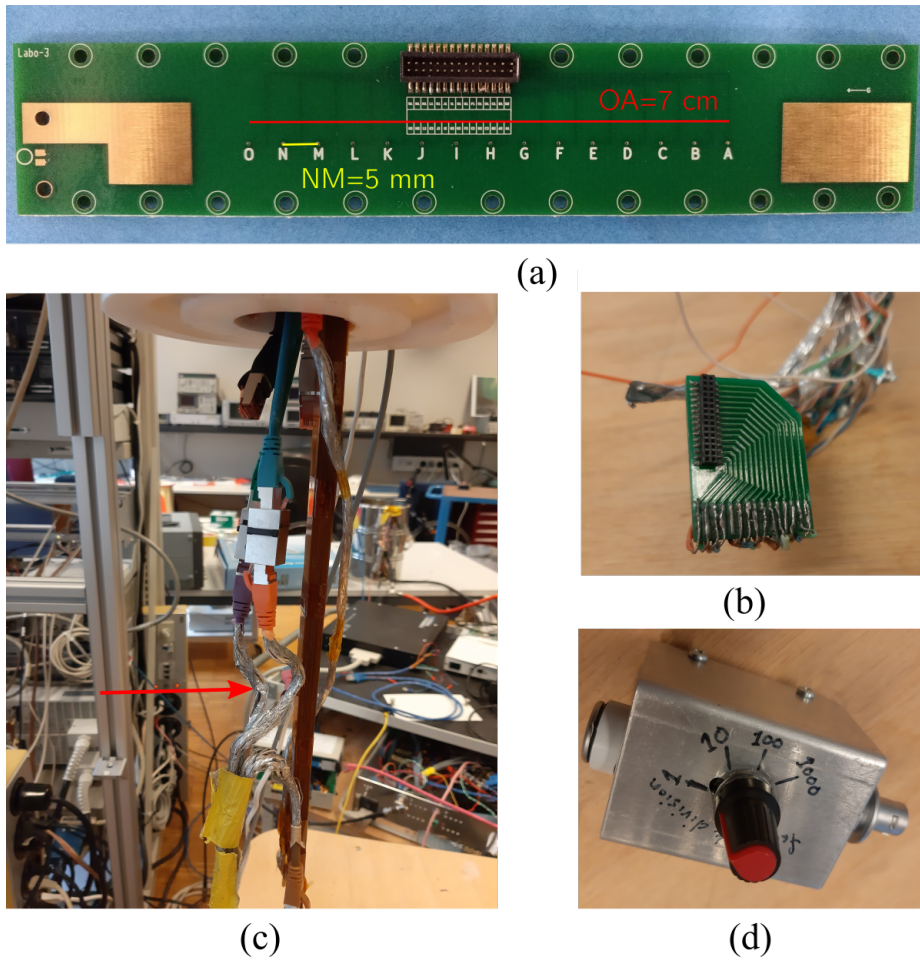
Figure 2.4: (a) Sample holder. The voltage was measured between the contacts (A to O) every 5 mm. The distance OA is 7 cm. The (b) PCB board connector routes the (c) twisted voltage pairs to the measuring system. The connection to the measuring system is made by means of LEMO connectors, plugged in a set of (d) attenuators.

can refer to [47, 48] for a more detailed description of the reconstructing algorithm and the parasitic oscillations that affect the signal and the Fourier analysis.

The LF signal acquisition was made using a NI PXIe 6341 card, while the HF signal was acquired with a NI PXIe 5105 model. With these acquisition cards, the uncertainty of the measurement is of the order of 0.2 mV. According to the electric field criterion $E_c = 10^{-4}\,\mathrm{V\,m^{-1}}$, when $I = I_c$, the voltage measured on the length of 7 cm (section A-O of the sample holder) is $V_c = E_c \cdot L_{A-O} = 10^{-4}\,\mathrm{V\,m^{-1}} \cdot 7.5\,\mathrm{cm} = 7.5\,\mu\mathrm{V}$. Since the uncertainty is much higher than this value, the system is too inaccurate to characterize the regime under and near I_c. For this reason, I-V curves and I_c measurements for some of the characterized samples, were performed at KIT with the experimental setup described in Paragraph 2.1.2. Finally, the subsystems described above were mounted on an aluminum frame, composed of T-slot aluminum 4040 rods, and arranged as represented in Figure 2.6. A part of the aluminum frame was designed to slide in the slots utilizing profile sliders. The current source, the measuring system, and the current leads with the sample holder were mounted on the frame's sliding section. In this way, the insertion and extraction of the sample holder in the cryostat were simple.
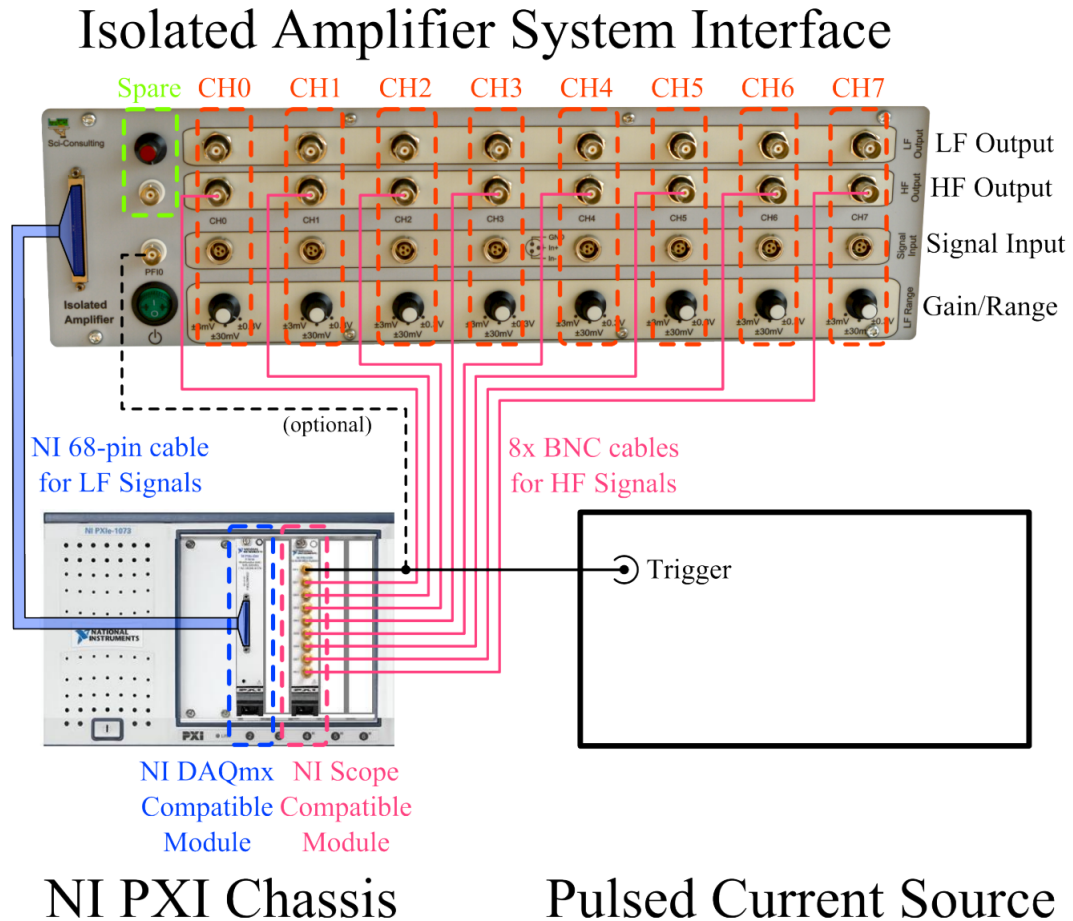
Figure 2.5: Connections between the Isolated Amplifier System Interface, the NI PXI Chassis and the Pulse Current Source (Courtesy of [47]).

2.1.2. DC transport current setup and measurements

DC current measurements were performed on the samples to obtain the critical current I_c in self-field condition, and the critical temperature T_c. Since part of the Ph.D. (about one year) was spent at KIT, some of the DC measurements were performed at KIT.

I-V curves

The critical current I_c of the samples was measured using electrical transport measurements, with the experimental setup described in [49]. The sample holder was placed in a helium-gas flow cryostat that provided stable temperatures between $1.8\,\mathrm{K}$ and $200\,\mathrm{K}$. The temperature was monitored with a Cernox sensor placed on the sample holder, while the current was injected in the sample up to the value at which the voltage corresponding to a critical electric field $E_c = 1\,\mathrm{\mu V\,cm^{-1}}$ was reached on the length of the measured sample, namely $10\,\mathrm{cm}$ (Figure 2.7a). The critical current at $77\,\mathrm{K}$ in self-field conditions of the characterized samples is reported in Table 2.1.

Resistance vs temperature setup and measurements

The critical temperature T_c of SuperPower and THEVA samples was measured at KIT, while the critical temperature of SuperOx, ShangHai and SUNAM samples was measured at EPFL. In both the experimental setups, the characterized tapes were clamped between two copper blocks immersed in liquid nitrogen. The experimental setup at KIT allowed to increase the
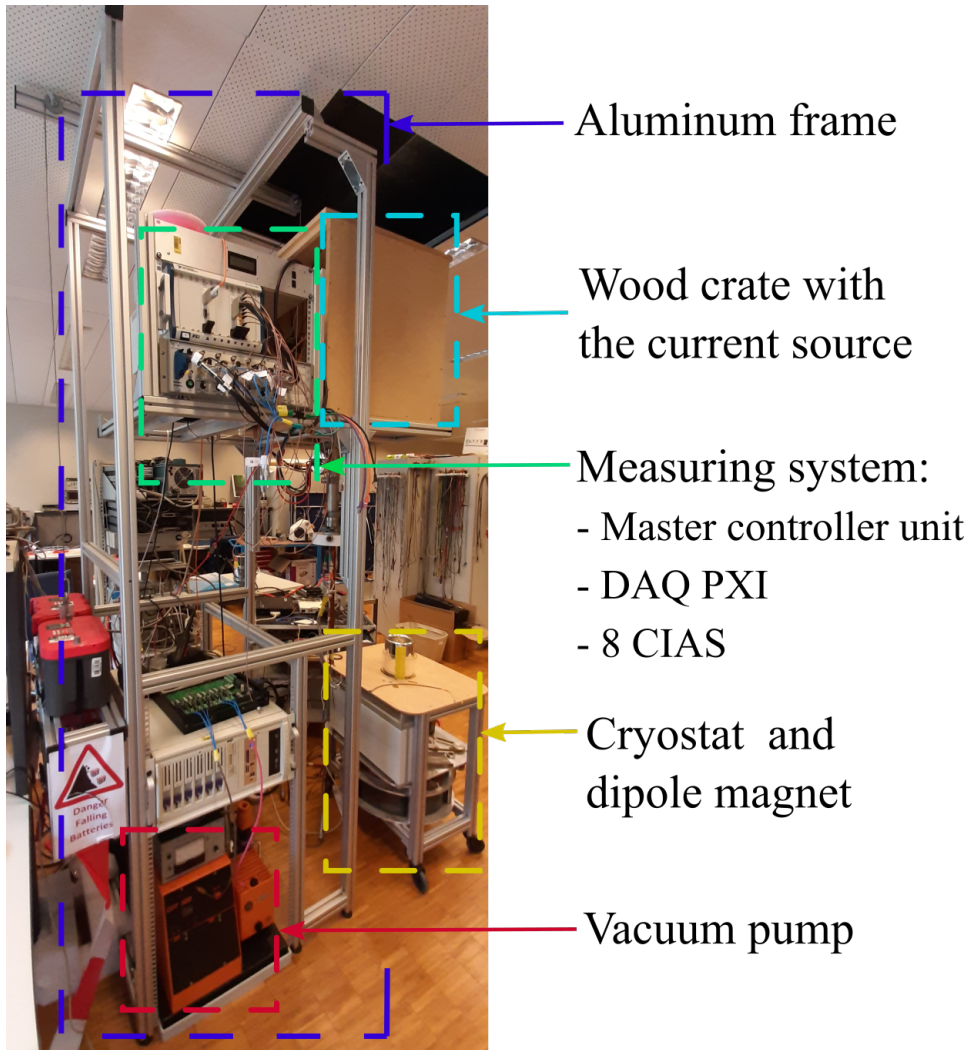
Figure 2.6: The current source, the measuring systems, the cryostat and the dipole are mounted on an aluminum frame, arranged as figure.

temperature of the copper block with a calibrated heating system while injecting 100 mA in the HTS tape. The measurements at EPFL were performed by leaving the sample to warm-up during the liquid-nitrogen evaporation ($\sim$ 12 h) while injecting 100 mA in the HTS tape. The resistance and temperature were recorded to determine $R_{\text{Tape}}(T)$[28]. The characteristics of the samples and the tags to which we will refer in this work are presented in Table 2.1. In Figure 2.7b are represented the measured tape resistance as a function of temperature for the selected samples SU02 and TH03, normalized with respect to the room temperature resistance R_{300}. A remark on the amount of silver surrounding the samples is necessary. In Section 3.2.1, we will describe a thermal model used to extract the overcritical resistivity data, and we will show how the knowledge of the exact amount of surrounding silver is critical for an exact execution of such model. In Table 2.1, the amount of surrounding silver is indicative, and to obtain its exact value, it has been necessary combining the measurements presented in Figure 2.7b with a MatLab script described in Paragraph 3.3.2.

15

(a)   (b)
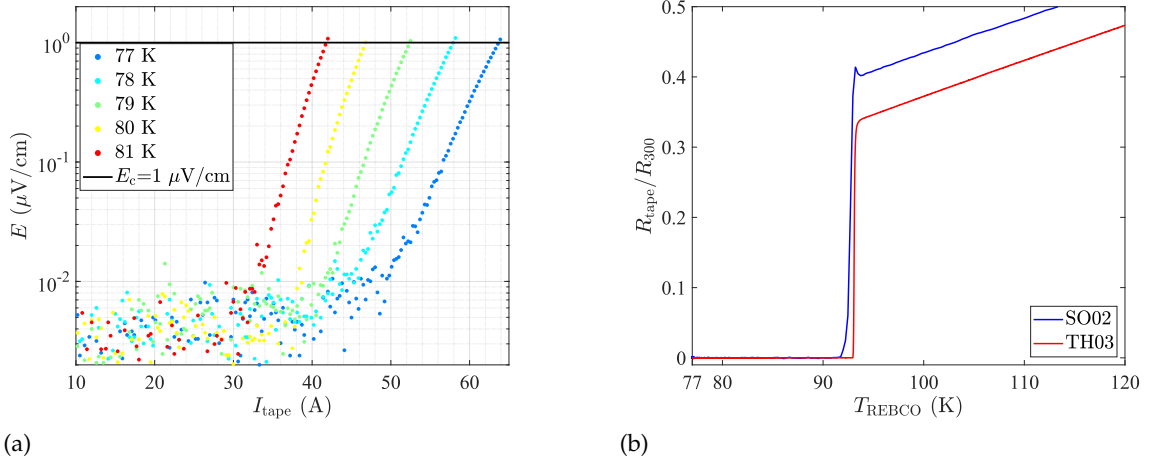
Figure 2.7: (a) Set of *I-V* curves for the SP02 sample. We want to thank Dr. Hänisch and his group for having performed those measurements. (b) *R-T* curves for selected samples. The room-temperature resistance (R_{300}) ranges from $0.009\,\Omega$ to $0.0887\,\Omega$ for the three samples.

Sample	Tag	Width	Thickness silver	Thickness REBCO	Thickness Hastel-loy	Critical current	Critical temperature	*n*-value
		w_{tape}	h_{Ag}	h_{REBCO}	h_{Hast}	I_{c}	T_{c}	
SuperPower	SP01	4 mm	2 µm	1 µm	50 µm	90 A	92 K	25
SuperPower	SP06	4 mm	2.2 µm	1 µm	50 µm	110 A	92 K	30
SuperOx	SO01	4 mm	4 µm	3 µm	50 µm	232 A	90 K	22
SuperOx	SO02	12 mm	2.2 µm	1 µm	97 µm	330 A	92 K	28
THEVA	TH03	4 mm	18 µm	3 µm	50 µm	270 A	92 K	30
SuNAM	SU01	4 mm	4 µm	2 µm	50 µm	241 A	92 K	25
ShangHai	SH03	4 mm	2.2 µm	1 µm	50 µm	177 A	92 K	24
ShangHai	SH05	4 mm	2.2 µm	1 µm	50 µm	177 A	92 K	23

Table 2.1: Characteristics of the two SuperPower samples. The critical current, critical temperature and *n*-value were measured in self-field condition at 77 K.

3

A procedure combining pulsed current measurements (PCM) on REBCO commercial tapes and numerical approaches to extract the resistivity of the superconductor material

In Figure 3.1 we represent the order of the contents followed in this Chapter. First, we present a qualitative analysis of the PCM, then we discuss a FEM-based approach developed to analyze the PCM and extract the electrical resistivity, and finally, we present the limits and validity of these approaches. Part of the work presented in this Chapter is also reported in:

- N. Riva, S. Richard, F. Sirois, C. Lacroix, B. Dutoit, F. Grilli - *Overcritical Current Resistivity of REBCO Coated Conductors through Combination of Pulsed Current Measurements and Finite Element Analysis*, IEEE TAS 2019, (Link to publication)
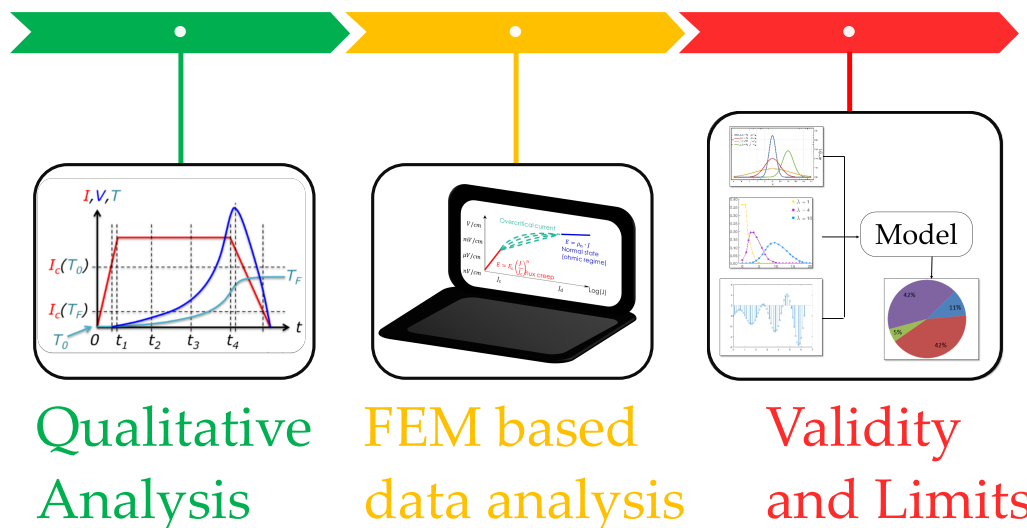
Figure 3.1: A qualitative data analysis of PCM is followed by a FEM-based data analysis of PCM. Lastly, the validity and limits of the method is discussed.

3.1. Qualitative PCM analysis

We present a qualitative analysis of the measurements performed in self-field condition for all the samples and in external magnetic field for the samples SO02 and SH05. We show that to analyze the PCM; it is not sufficient to calculate the quantity V_{meas}/I_{tot}, because the measured voltage can vary over time even when the current is constant. This sort of analysis does not allow to account for the sample's heating and the current sharing.

Self-field measurements: Pulses with current amplitudes ranging from $1.1\,I_c$ up to more than $5\,I_c$ were applied to the samples using the PCM system. Typical current pulses performed on the samples TH03 and SP01 are shown in Figure 3.2. It is worthwhile to notice that each pulse reaches the requested current in a remarkably short time. The constant current plateau of 1000 A in Figure 3.2a rose from zero to 95 % of its final value, in less than 15 µs (inset of Figure 3.2a) and remains within 5 % of the requested current. The current is flat, and the
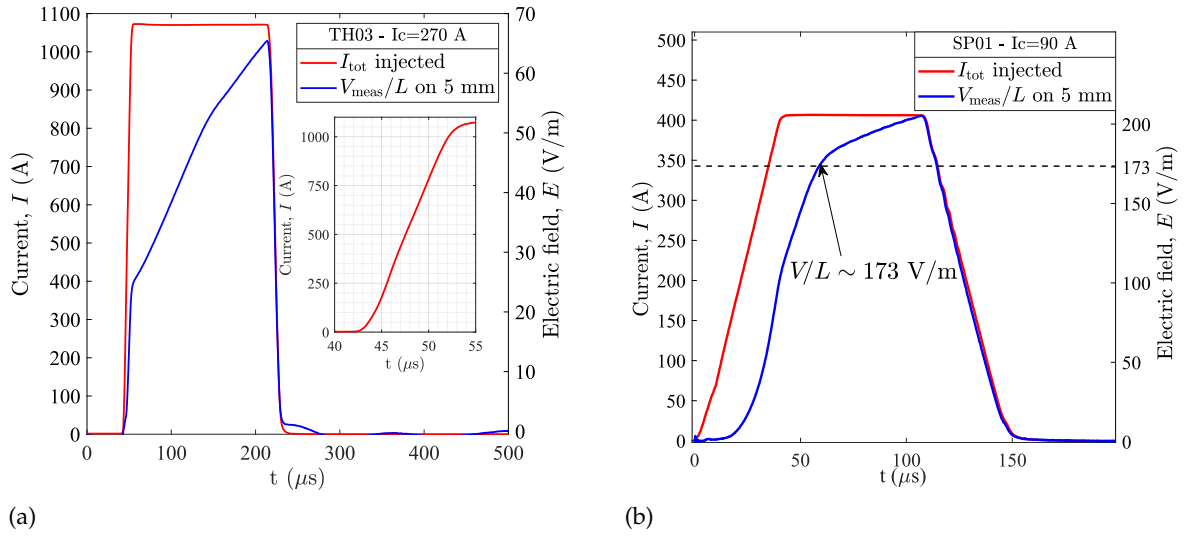
Figure 3.2: Typical current pulses generated with the PCM system on the samples (a) TH03 and (b) SP01.

sample holder is designed to minimize inductive signals. Consequently, the voltage's positive slope has to be attributed to the sample's joule heating effects. As a result, even with ultra-fast PCM, the sample's temperature rise cannot be neglected. In [50] a temperature rise from 77 K to 90 K was observed in less than 35 µs when a $I_{tot} = 3\,I_c$ was injected in a commercial REBCO tape.

The sample heating also leads to a progressive current transfer from the REBCO layer to the silver and Hastelloy layers. This makes the interpretation of the data, as well as the method to retrieve the resistivity of REBCO in function of the current and the temperature, somewhat complicated.

To have a better understanding of the complex electrothermal behavior occurring, we analyze a specific pulse in Figure 3.2b, performed on the SP01, where we have a high over-current pulse (i.e., $I > 4\,I_c$). In this plot, at about 60 µs, we observe an abrupt change in the slope of the voltage per unit length, which value is $173\,Vm^{-1}$. We show that the REBCO has reached its critical temperature at this instant, the superconducting properties are lost, and the current flows mostly in the silver and Hastelloy. To verify this hypothesis, we estimate the voltage drop per unit length when all the current flows in the silver and Hastelloy layers. We assume the critical temperature to be 92 K and to be uniform on the tape, a current $I_{tot} = 406\,A$, the following cross-sections $S_{Ag} = 0.008\,mm^2$ and $S_{Hast} = 0.188\,mm^2$, the resistivities

18

$\rho_{Ag}(T = 92\,K) = 3.5 \cdot 10^{-9}\,\Omega\,m$ and $\rho_{Hast}(T = 92\,K) = 1.23 \cdot 10^{-6}\,\Omega\,m$.

With the silver and Hastelloy to behave as resistors in parallel, the expected voltage drop per unit length is:

$$\frac{V_{meas}}{L} = I_{tot} \cdot \frac{\rho_{Hast} \cdot \rho_{Ag}}{\rho_{Ag} \cdot S_{Hast} + \rho_{Hast} \cdot S_{Ag}} \simeq 173\,\frac{V}{m}, \tag{3.1}$$

where L is the distance between the voltage taps. The value is shown in Figure 3.2b as a black dashed line. This simple calculation suggests that the change of slope corresponds to the time where the REBCO has reached its critical temperature and that the temperature rise occurring between the beginning of the pulse and $60\,\mu s$ is $15\,K$ only, which is remarkably low considering the high current injected in the samples.

Since we assessed that the current flows mostly in the silver and Hastelloy layers for $t > 60\,\mu s$, we can estimate the maximum temperature rise knowing the resistance of the stabilizer layers as a function of temperature. The resistance of the metallic layers of the SP01 sample expressed as a function of the temperature is:

$$R_{SP01}(T) = \left[2.59 + 0.0589 \cdot (T - 77\,K)\right] \frac{m\Omega}{cm} \tag{3.2}$$

The highest value of voltage per unit length reached in Figure 3.2b is $202\,V\,m^{-1}$, and the current is $406\,A$. The resulting resistance is $R_{SP01}(T_{fin}) = 4.97\,m\Omega\,cm^{-1}$. The linear relationship of Equation (3.2), allows estimating that the observed temperature rise T_{fin} was kept below $40\,K$. In Figure 3.3 we finally represent the measured voltage signals V_{meas} over $5\,mm$ for various characterized samples, where each subplot reports five pulses corresponding to increasing current amplitudes.

We can distinguish different heating regimes, occurring for low overcurrent pulse conditions (around $2\,I_c$), medium overcurrent pulse conditions (around $3\,I_c$) and high overcurrent pulse conditions (as high as $4\,I_c$). In [45] it was reported steady and linear heating occurring in similar overcurrent pulses, as in fact, we report in Figure 3.3 for the SP01 and TH03 samples. On the contrary, for the other samples, we observe a parabolic curvature in the voltage curves. Similar results were observed from *Antognazza*[1] *et al.* [55].

It is apparent that the heating cannot be neglected. However, it is valuable to analyze the PCM in order to obtain a preliminary set of $E - I$ curves. At this stage, we follow the same approach used in [45]: the value of the electric field is extrapolated from the measured voltage at the moment where the current pulse has attained $90\,\%$ of its final value. Ideally, this instant corresponds to zero energy injected in the sample, assuming a perfectly square current pulse [41]. The injected current I_{tot} is the value of the measured current at the top when the plateau was stable. In Figure 3.4(top) we present the $E - I_{tot}$ curves for selected samples. Because of the stabilizer layers constituting the REBCO tape, $I_{tot} \neq I_{REBCO}$ for $I_{tot} > I_c$. The effective $E - I_{REBCO}$ curve of the superconducting material, is overlapped to the stabilizer layers resistive sheath. A simple current sharing model allows estimating the amount of current in the REBCO layer [42, 43]. Assuming the current to be uniform along the sample's length and width, the current sharing model claims that the current carried by the superconductor is:

$$I_{REBCO}(T) = I_{tot} - I_{stab}(T) \tag{3.3}$$

---

[1]Yet, it is still not clear whether the reason of this parabolic behavior is given by a thermal runaway [51, 52], by the appearance of phase-slip lines [53] or by an instability of the vortices [54]. In any case, it indicates a gradual temperature rise. In fact, in the same work, *Antognazza et al.* observe that in thin REBCO films grown on sapphire, this behavior is not observed, probably due to the good thermal characteristic of the sapphire. In particular, when the thin film is grown on sapphire substrates, it is rather observed a sharp and quick transition into a high dissipative state.

The current in the matrix $I_{\text{stab}}(T)$ is the sum of the current in each stabilizer layers, and it can be calculated knowing the resistance $R_{\text{stab}}(T)$ of the metallic layers of the sample.

$$I_{\text{stab}}(T) = I_{\text{Ag}}(T) + I_{\text{Hast}}(T) = \frac{V_{\text{meas}}}{R_{\text{stab}}(T)} \tag{3.4}$$

In Figure 3.4(bottom), we present the $E - I_{\text{REBCO}}$ characteristics as a function of the super-conducting current. The inflecting curves confirm further the hypothesis of non-negligible heating in the measurements. Therefore, to use correctly Equations (3.3)-(3.4), we need to know the temperature rise accurately. However, it is impossible to perform a direct measure of the tape's temperature since the tape is clamped between the two plates of the sample holder, and we do not have direct access. A post-processing method proposed in [41], extrapolates the tilted voltage slope at top of the pulse to the time origin $t_0 = 0$ s, in order to obtain the initial electric field E_{t0} at the nominal bath temperature. This approach assumes that the resistivity is linear for low heating rates. In other words, that can be written as a first-order Taylor polynomial around the initial point T_0:

$$\rho(T - T_0) = \rho(T_0) + \frac{\partial \rho(T_0)}{\partial T}(T - T_0) + \dots \tag{3.5}$$

This method works for very short pulses and a limited temperature rise. For larger temperature rise and injected current, as in our case, Equation (3.5) is not valid, and another approach should be followed to analyze our data. Lastly, from this analysis, it is also clear that an accurate knowledge of architecture and material properties is fundamental.

External low field measurements: This section investigates the voltage and $E - I$ curves of REBCO tapes submitted to uniform and low external magnetic fields. The measurements were made on samples SO02 and SH05 (Table 2.1), using the magnetic system described in Paragraph 2.1.1. The applied field ranged from 0 mT to 300 mT, and the orientation of the applied field was always perpendicular with respect to the flat face of the tape, meaning perpendicular to the a-b plane. In Figure 3.5 and Figure 3.6, we represent the measured voltage signals V_{meas} over 5 mm, for the samples SO02 and SH05 (Table 2.1). Also, in this case, we can distinguish different heating regimes. Similarly to Figure 3.3, we observe a parabolic curvature in the voltage curves. Nevertheless, with increasing applied magnetic field, the curvature becomes more linear rather than parabolic, especially for sample SO02 (Figure 3.5).

The same qualitative data analysis described above was made for the PCM to obtain the $E - I$ curves in a low external magnetic field. In Figure 3.7(a-b/top) we present the $E - I_{\text{tot}}$ curves for selected samples. The presence of external field results in a reduction of the critical current, as also demonstrated in Figure 3.6. In Figure 3.7(a-b/bottom), we present the $E - I_{\text{REBCO}}$ characteristics as a function of the superconducting current. The inflecting curves confirm the hypothesis of non-negligible heating in the measurements. The rapid current dependence of the E_I characteristics tends to become flatter with increasing applied field.
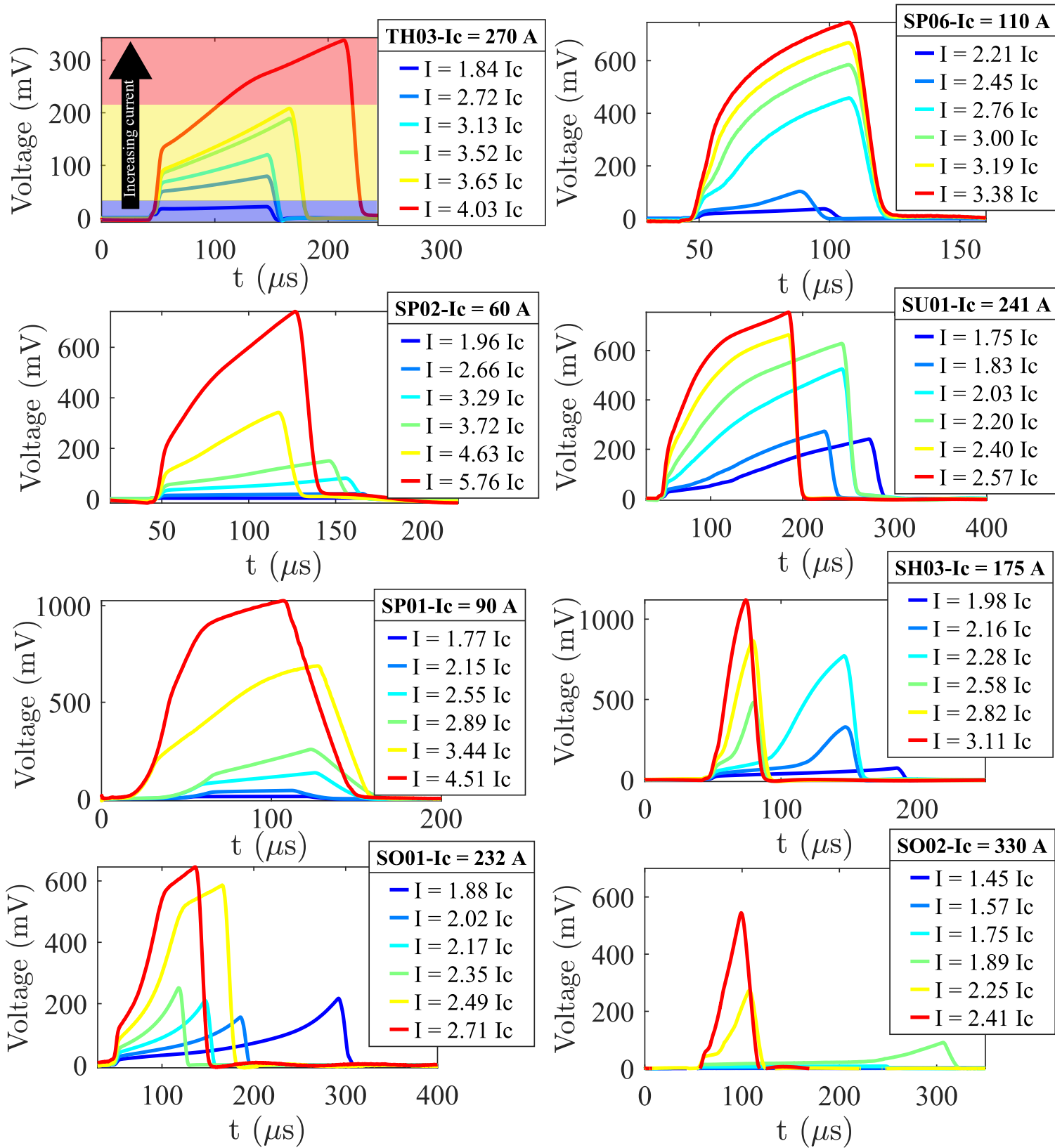
Figure 3.3: Voltage and current measurements for various samples. For a better understanding of the heating effects, we added coloured boxes on the TH03 voltage curves. It is possible to observe roughly three heating regimes: low overcurrent pulse conditions (blue), medium overcurrent pulse conditions (yellow) and high overcurrent pulse conditions (red). What is apparent, from this kind of curves, is that, even with ultra-fast PCM, the sample's temperature rise cannot be neglected.

21
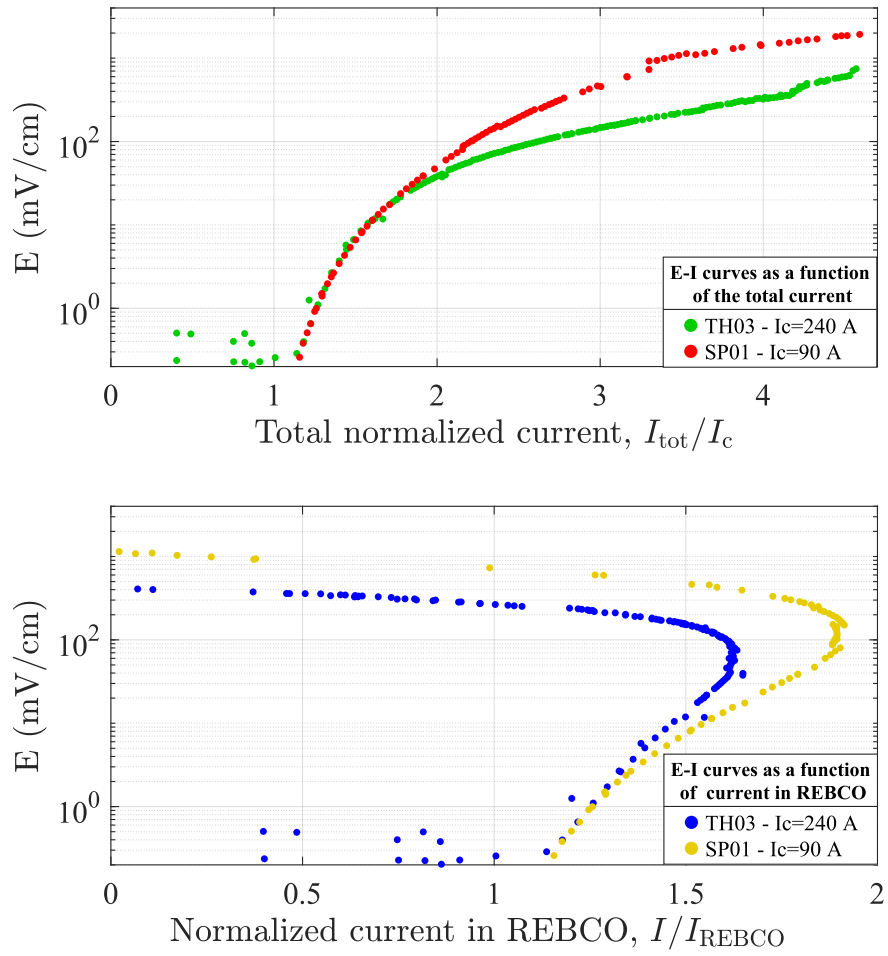
Figure 3.4: $E - I$ curves of the selected samples SP01 and TH03 represented as a function of the (top) total current I_{tot} and (bottom) current in the REBCO layer I_{REBCO}.
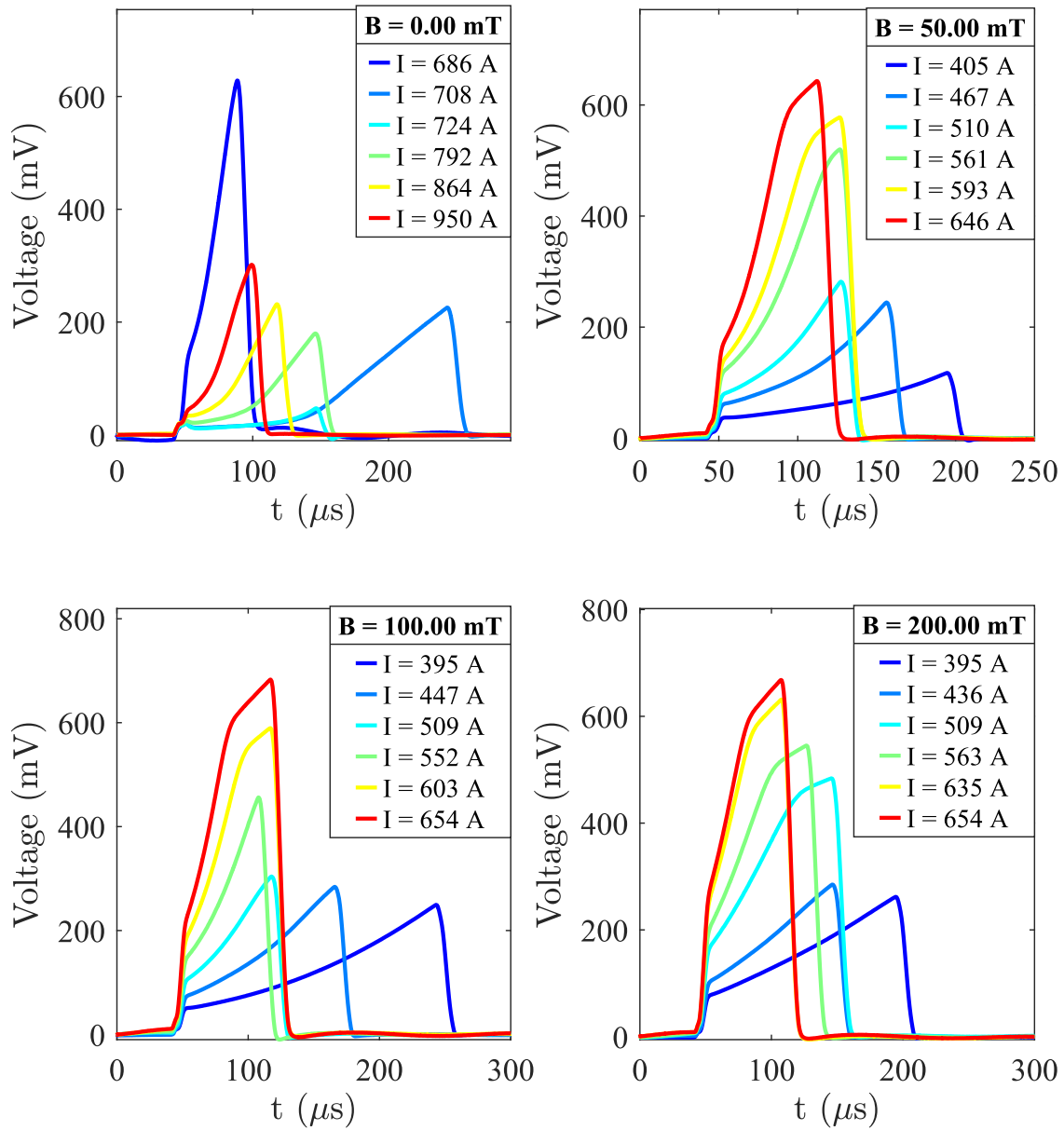
Figure 3.5: Voltage and current measurements for sample SO02 in low external applied magnetic field (0 mT to 300 mT). Heating effects are clearly observed.
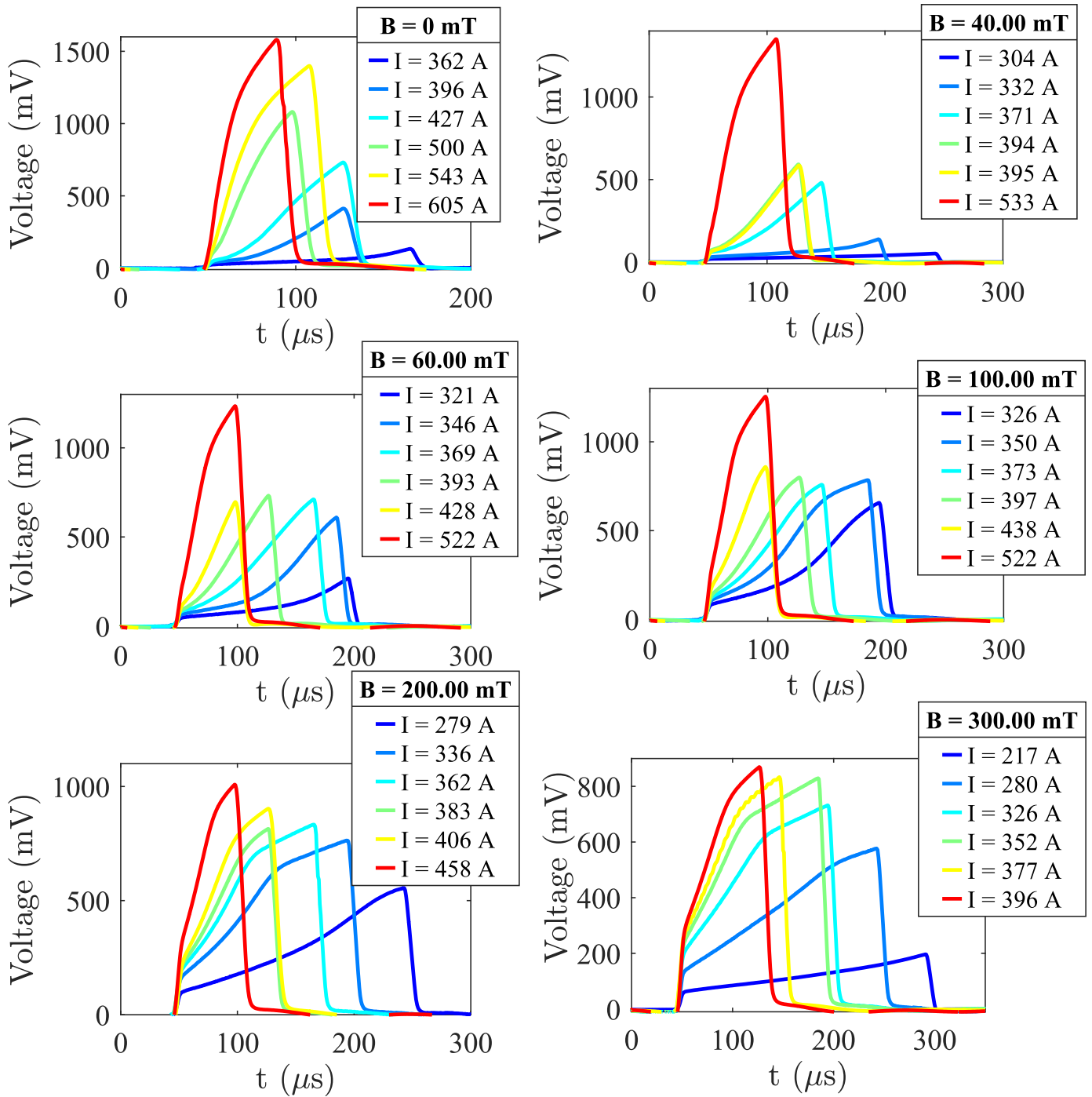
Figure 3.6: Voltage and current measurements for sample SH05 in low external applied magnetic field (0 mT to 300 mT). Heating effects are clearly observed.
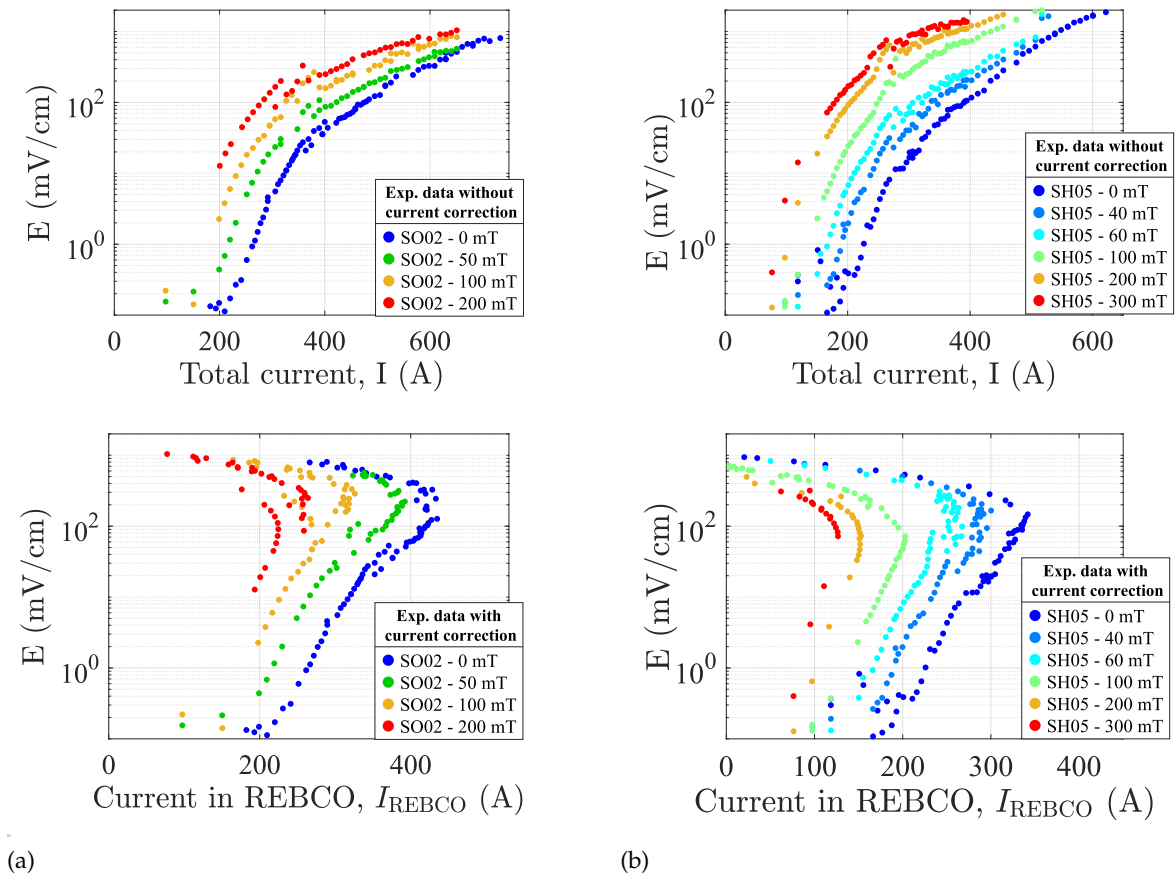
Figure 3.7: $E - I$ curves of the selected samples SO02 and SH05 represented as a function of the (top) total current I_{tot} and (bottom) current in the REBCO layer I_{REBCO}.

3.2. PCM data analysis based on FEM

The arguments above showed that due to the rapid heating occurring near and above the critical current, a correct interpretation of the data is rather complicated. To extract useful information, we need to know the amount of current in the REBCO layer as well as its temperature. The temperature rise is complicated to estimate, and accurate knowledge of architecture and material properties is of paramount importance.

Also, an incomplete magnetic relaxation in the sample at low injected currents (near or slightly above the critical current) adds a voltage contribution that affects the measurements and overlaps to the heating effects. The practical consequence of this relaxation is that the current distribution along the tape width is not uniform when this phenomenon occurs. Thus, we do not measure the same signal placing the voltage taps on the edge or in the center line of the tape [56], leading to an overestimation and mistaken extrapolated voltage [46].

To address these problems and analyze the data accurately, we used an approach based on FEA. In the next section, is presented the so-called "Uniform Current" (UC) model [56, 57], implemented in COMSOL [58]. This model allows us to estimate the temperature over time for each layer of the REBCO tape, as well as the amount of current flowing in each layer.

3.2.1. Uniform Current (UC) Model

The model, is a 2-D model based on the geometry represented in Figure 2.1a, on which the heat equation is solved, No external cooling is applied at the boundary of the tape (adiabatic regime).

$$\rho_{\mathrm{m}}(T)C_{\mathrm{p}}(T)\frac{\partial T}{\partial t} - \nabla \cdot (k(T)\nabla T) = Q(t), \tag{3.6}$$

where $\rho_{\mathrm{m}}(T)$ is the mass density, $C_{\mathrm{p}}(T)$ is the heat capacity and $k(T)$ is the thermal conductivity[2]. Due to the time scale involved, we assumed adiabatic conditions, as already done in previous works[45]. The heat source is $Q(t) = J(t)E(t)$, where $J(t)$ and $E(t)$ are derived from the experimental data:

$$E(t) = \frac{V_{\mathrm{meas}}(t)}{L}, \quad J_{\mathrm{mat}}(t) = \frac{E(t)}{\rho_{\mathrm{mat}}(T)}, \tag{3.7}$$

where $\rho_{\mathrm{mat}}(T)$ is the electrical resistivity of the material layer, which is known for every material except REBCO. The current in each material layer $I_i^{\mathrm{mat}}(t)$ is obtained by integrating the current density over the cross-section of each layer. Using the total measured current $I_{\mathrm{tot}}(t)$, the current in the REBCO is obtained as:

$$I_{\mathrm{REBCO}}(T(t)) = I_{\mathrm{tot}}(t) - I_{\mathrm{stab}}(T(t)) = I_{\mathrm{tot}}(t) - \sum_{i=1}^{n_{\mathrm{mat}}} I_i^{\mathrm{mat}}(T(t)). \tag{3.8}$$

Finally, the resistivity of REBCO is obtained knowing the cross section S_{REBCO} of the REBCO:

$$\rho_{\mathrm{REBCO}}(I, T) = \frac{V_{\mathrm{meas}}(t)}{I_{\mathrm{REBCO}}(T(t))} \cdot \frac{S_{\mathrm{REBCO}}}{L}. \tag{3.9}$$

The current density (and electric field) are assumed to be uniform on the cross-section of the REBCO layer, hence the name "Uniform Current" (UC) model.

An example of current sharing calculated with the UC model is presented in Figure 3.8 for sample SP01, where we present the measured voltage $V_{\mathrm{meas}}(t)$ (top), the measured current $I_{\mathrm{tot}}(t)$, and the current distribution in each layer (middle) calculated with the UC model. The temperature of REBCO (bot), is calculated as an average over the REBCO cross-section. From the simulation results, we observe that the current in the REBCO layer drops approximately

---

[2] All the thermal properties of the materials (silver, REBCO and Hastelloy) are known [59, 60].

to 0 A at about 60 μs, when the corresponding temperature is 92 K. The critical temperature in self-field for these tapes is close to 92 K [28, 61]. Therefore, the UC model seems to correctly estimate when the current in the REBCO layer drops to a minimum.
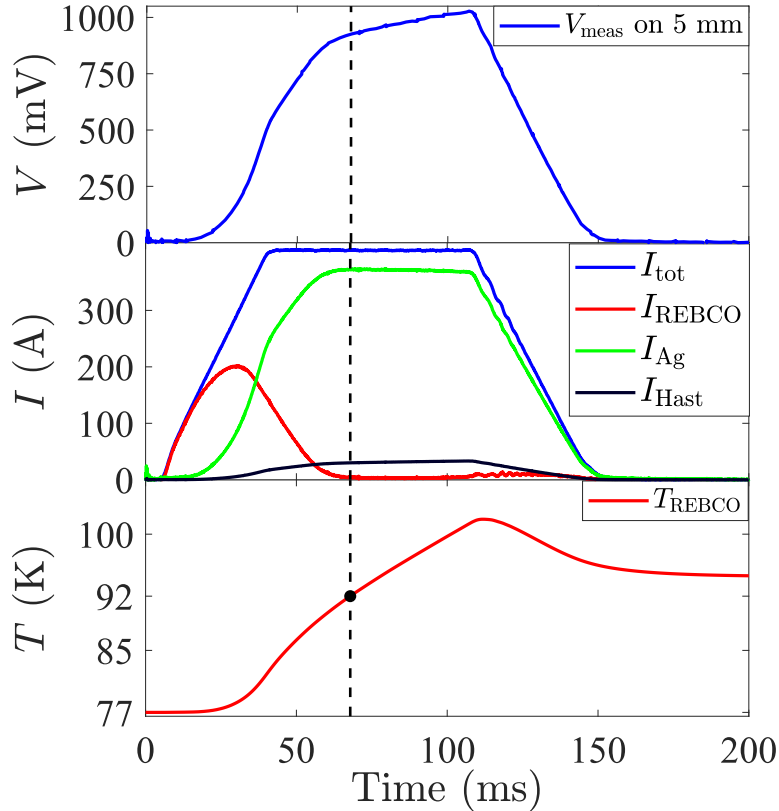
Figure 3.8: Example of current sharing between layers and temperature rise in REBCO for sample SP01.

3.2.2. Heat dynamics during PCM

Here, it is necessary to remark about the heat dynamics occurring during PCM. The UC model works under adiabatic condition. The temperature decrease in Figure 3.8 at the end of the pulse is caused by heat diffusion towards the substrate, and not due to any form of cooling of the tape. Is the adiabatic assumption valid in our experiments and modeling?

A first quantitative argument to characterize heat transfer in various time-scales is presented in *Sakurai et al* [62, 63]. They investigated the transient heat transfer for different heat inputs in liquid nitrogen showing that, for high input-rates, the heat transfer is associated with conduction to the nitrogen bath. However, at a certain threshold temperature T_{th} (called heterogeneous spontaneous nucleation temperature), the heat transfer changes abruptly to the film boiling regime. Quantitatively, *Sakurai et al* demonstrated that for heat pulses of duration smaller than $\tau < 50$ ms, the heterogeneous spontaneous nucleation temperature is approximately constant $T_{th} \simeq 107$ K.

Secondly, we recall that quenching of superconductors is thought to be an adiabatic phenomenon since the thermal diffusion is usually expected to be much smaller than the magnetic one (i.e. $D_{th} << D_m$) [64]. In other words, it takes longer for the heat to diffuse from one point to another rather than to have heat generation by Joule heating at the same location [64], which is also why heat transfer has negligible effects on the NZPV (tenths of ms) as shown

in [12]. In our experiments, the current pulses are in µs scale (much shorter than τ [62, 63] and of the ms time-scale), and the temperature grows rapidly toward the relatively small value of the transition temperature T_{th}. Therefore, the large amount of energy generated in the stabilizer prevents cooling of the conductor while it is heating (or quenching like in Figure 3.8). With these arguments, we can conclude that the adiabatic assumption is valid during our experimental conditions. However, further modeling and specific measurements need to be done to assess which is the energy /time threshold above which the adiabatic assumption is no more valid.

Finally, it is not possible to neglect the heating dynamic occurring on the cross-section of the tape. The heat diffusion coefficient of the Hastelloy at 77 K is $D = \frac{k}{c_k} = 4.26 \cdot 10^{-6} \mathrm{m}^2\,\mathrm{s}^{-1}$ and the diffusion length is $\lambda = 2\sqrt{Dt}$. The pulses we are analyzing have a length of 15 µs to 300 µs. However, at such length, the heat diffuses through 20 µm to 70 µm, and our tapes range in thickness from 50 µm to 100 µm. We can conclude that a 0-D UC model can not be used for the data analysis. On the other hand, a reduction to 1-D is reasonable, which can substantially reduce computational time. This possibility was explored in Appendix A.4.

3.2.3. Overcritical current resistivity calculated with the UC model

Using the data obtained from Equation (3.9), we can calculate the electrical resistivity of REBCO. The UC model assumes the electric field and the current distribution to be uniform on the REBCO layer's cross-section. As mentioned earlier, however, magnetic relaxation may invalidate this assumption. In fact, the model calculates an instantaneous temperature profile distribution and the current sharing between the various layers but does not allow accounting for magnetic relaxation and other inductive phenomena. Such phenomena may drive spatial inhomogeneities in the current density and electric field and impact the calculated quantities. In the work of *Richard et al.* [56], it was shown that the UC model works fine at high current amplitudes, while for lower current amplitudes (even if above the critical current I_c), it is necessary to wait a certain time, until magnetic relaxation effects disappear. Consequently, to extract meaningful data from the voltage PCM, the duration of the pulses must be chosen carefully. Too long pulses should be avoided since they can lead to a degradation or destruction of the sample.

A theoretical bound for the error committed and related to magnetic relaxation was derived and experimentally validated. The details of this method can be found in [48, 56], here we present only the results of the method applied to the PCM performed. According to work presented by *Richard et al.*, we estimated that the maximum error generated by the UC model is less than 10%. Given the input of the UC model (REBCO tape geometry, the properties of the material except that of REBCO which is unknown, the experimental voltage and current curves), the output of the UC model is the instantaneous triplet $(\rho_{REBCO}, I_{REBCO}, T_{REBCO})$.

Overcritical data in self-field conditions: The raw overcritical resistivity data $\rho_{OC}(I_{REBCO}, T_{REBCO})$ is shown in Figure 3.9. The scattered red-dots correspond to experimental points obtained with the PCM and post-processed with the UC model, while the blue points correspond to critical current measurements. From Figure 3.9 we realize that the amount of data in these plots is not sufficient to represent a complete resistivity $\rho_{REBCO}(I, T)$ surface. Some regions of the resistivity, i.e., high current and temperature, are not easily accessible. This is a consequence of the current sharing and heating, occurring during an overcritical current pulse: with a higher injected current, the heating rate and hence the temperature rise is higher. The higher temperature rise will lower the current in the REBCO layer, as the proportion of current in stabilizer (silver and Hastelloy) increases rapidly.

This trend can be better observed in Figure 3.10 and Figure 3.11, where we plot a projection on the (ρ,I), (ρ,T) and (I,T) planes for various selected samples. A representation of this sort in three different planes (Figure 3.10- 3.11) offers better insight into the extracted data. In the (ρ,I) plane (Figure 3.10-3.11 left) the resistivity as well as the temperature, increases with increasing current in the REBCO layer [3]. A similar trend is observed in the (ρ,T) plane (Figure 3.10-3.11 center), whilst in the (I,T) plane (Figure 3.10 3.11 right) the current in the REBCO layer decreases with increasing temperature of the REBCO. We recall that for all samples, we could not access the subcritical $(I < I_c)$ current data because of the limited accuracy of the measurements (Paragraph 2.1.1). In the (I,T) plane, we observe that the current in the REBCO drops to zero in a region comprised between 87 K to 92 K.

All the measurements start from 77 K, the temperature of the liquid nitrogen bath where the samples were immersed. The maximum value of resistivity represents the normal state resistivity ($30\,\mu\Omega\,cm^{-1}$ to $100\,\mu\Omega\,cm^{-1}$, in agreement with [66]). This can be observed in the temperature range spanning between 88 K to 92 K.

This way of representing the data offers a method to detect the spurious and unusable data. In Figure 3.10 and Figure 3.11 (center-left), we observe that for a few samples, the resistivity calculated presents spurious data: a few points follow an anomalous trend and do not lie with the majority of the others. It is complicated to interpret such behavior. However, such results are likely due to uncertainties of the input parameters. Later, in Section 3.3.2, we will discuss the sources of such uncertainties and their impact on our model.

It is also possible that the resistivity calculated with the UC model, utilizing high heating rate pulses[4], is very sensitive to the uncertainties of the input parameters (thermal properties, resistivity, geometry, voltage and current). A possible solution is to avoid performing too long pulses ($t_{pulse} < 100\,\mu s$), and thus reducing the excessive heating.

In this way, however, we would have limited access to high-temperature regions and an even smaller populated (ρ,T,I) surface. PCM with different initial temperatures should be done, but measurements at different initial temperatures were not performed because of time and technical constraints.

Finally, the sample TH03 in Figure 3.11(b) presents a different typology of problems. In the (ρ,T) and (I,T) planes, we can distinguish a progressive set of curves that increase and decrease respectively, indicating a possible degradation of the sample.

Here, it is necessary to comment about the source of the spread at high current I_{REBCO} upon the departure from 77 K (e.g., in Figure 3.9). This is also a consequence of the current sharing and heating occurring during an overcritical current pulse. For low overcurrent amplitudes, the heating effects are negligible. However, when the injected current is increased, the heating effects can not be neglected. The UC model allows estimating the heating effects and provides the temperature increase. The temperature increase explains why the extracted overcritical current data spread toward temperatures higher than 77 K. By further increasing the amplitude of the current pulses, the heating effects increase too, while it is possible to access higher I_{REBCO} regions. As a consequence, for higher current amplitudes, the spread in temperature will be larger. Finally, for very high current pulses, the sample will eventually quench, and the extracted data smoothly converge to the normal resistivity regime. in these regions ($T > 82$ K and $I_{REBCO} < 200$ A) the spread is reduced.

---

[3]Represented in terms of cividis colormap [65].

[4]In Appendix A.6 it is showed that the quantities calculated using FEA are very sensitive to the dynamic of the input voltage signal, namely to high heating rate pulses.
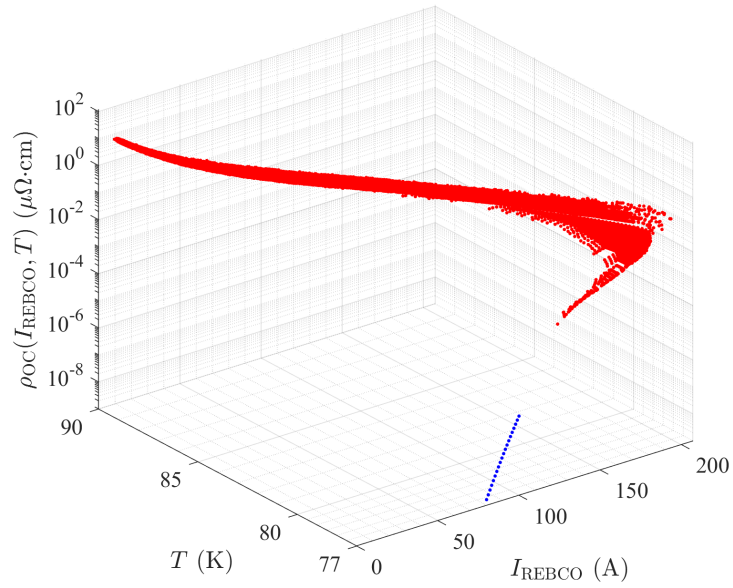
(a)
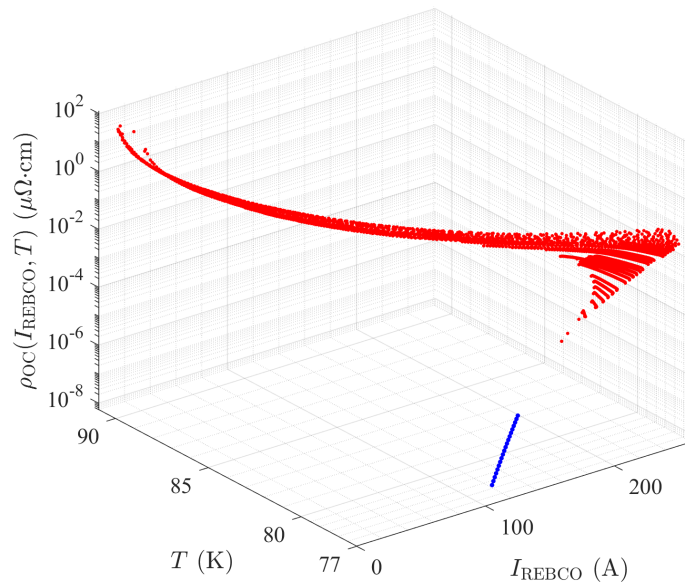
(b)

Figure 3.9: Raw resistivity data for samples (a) SP01 (I_c = 90A at 77 K self-field) and (b) SP06 (I_c = 110A at 77 K self-field). The scattered red dots correspond to experimental points obtained using PCM and post-treated using the UC model, while the blue points are from the critical current measurements.
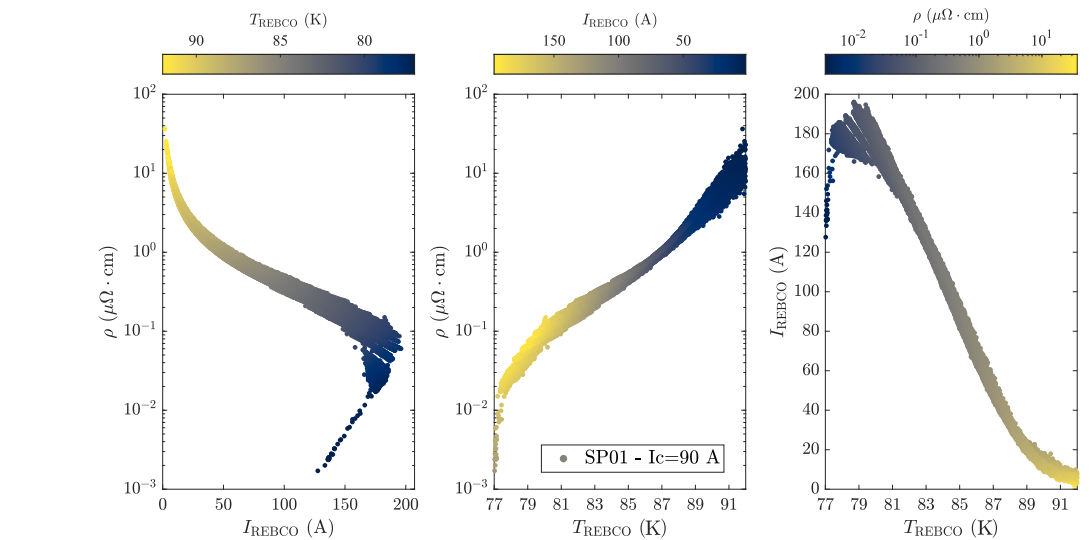
(a)
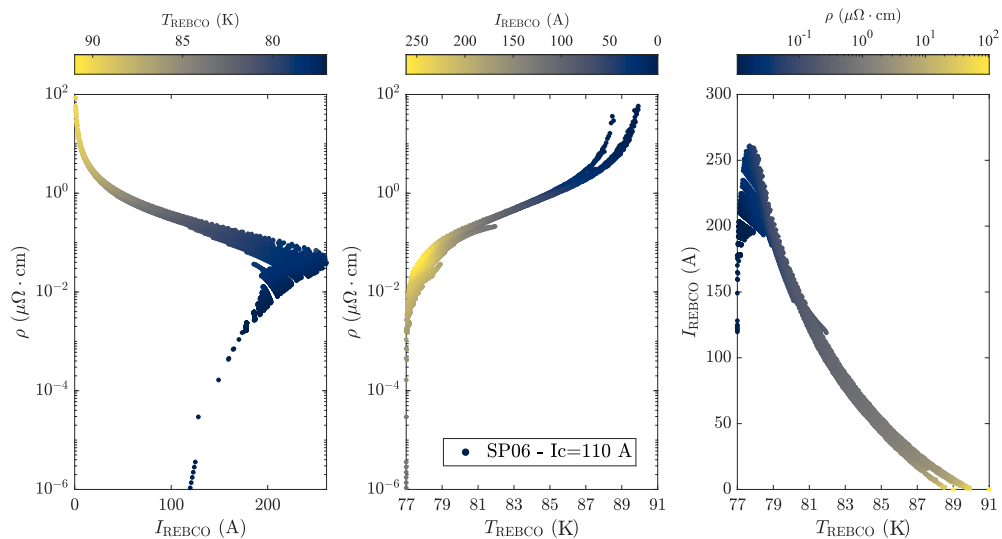
(b)
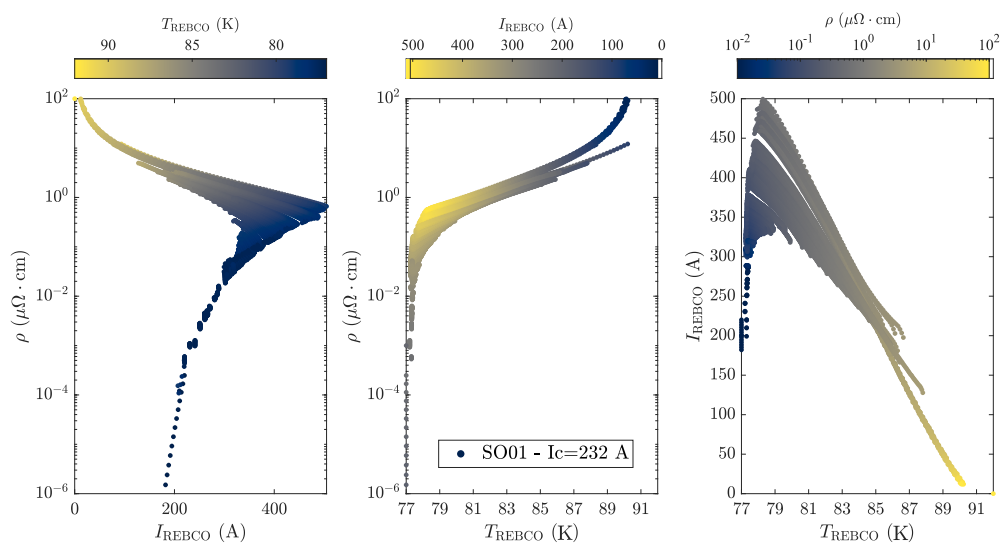
(c)

Figure 3.10: Representation on the (ρ,I), (ρ,T) and (I,T) planes of the resistivity calculated with the UC model for the SP01, SP06 and SO01 samples.
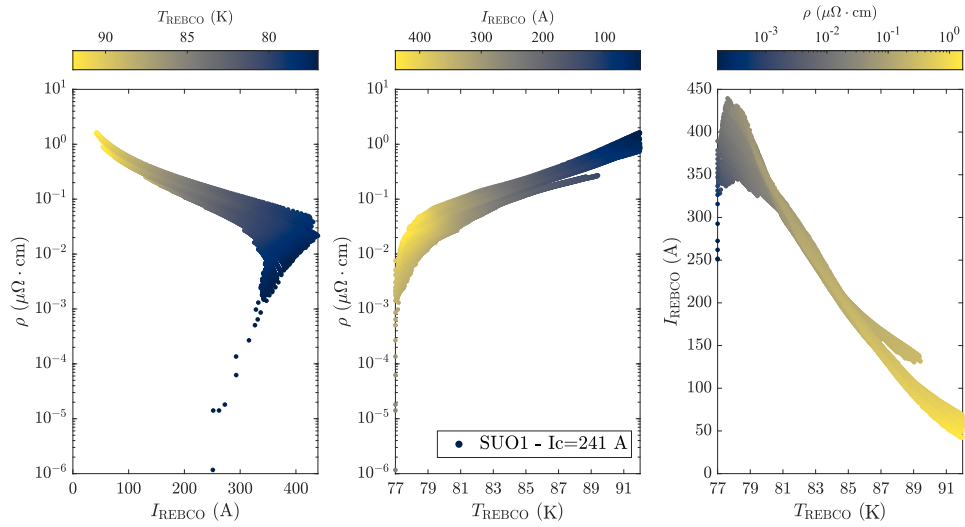
(a)
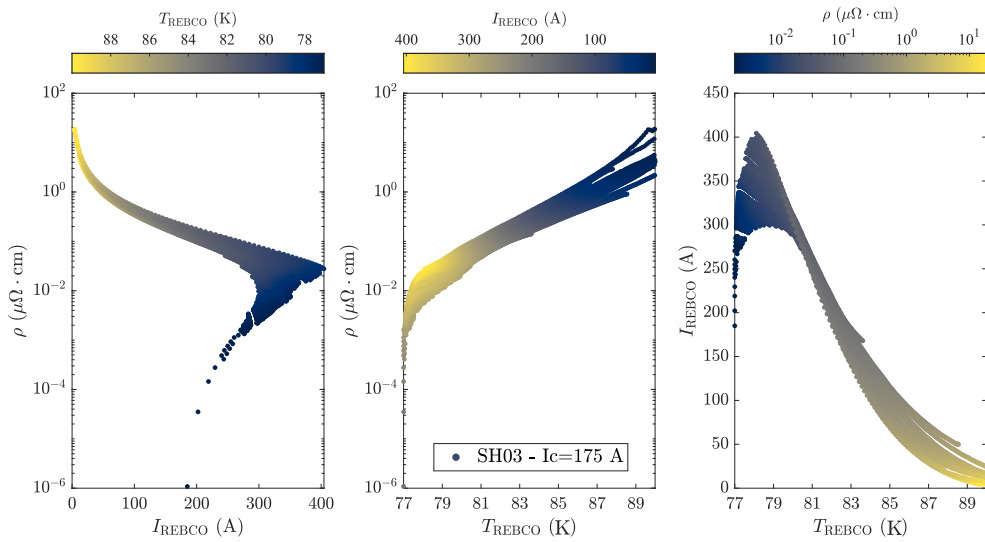
(b)
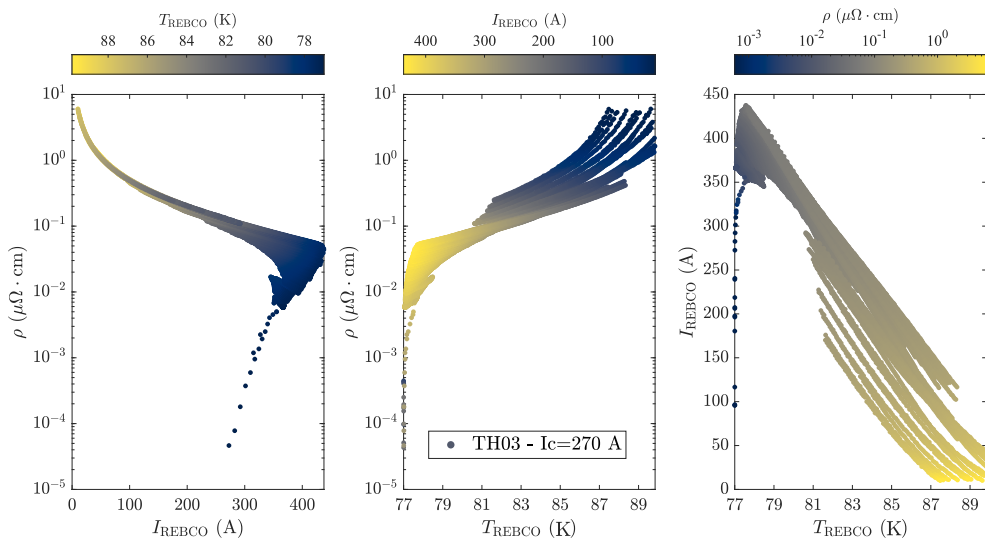
(c)

Figure 3.11: Representation on the (ρ,I), (ρ,T) and (I,T) planes of the resistivity calculated with the UC model for the SU01, SH03 and TH03 samples.

Overcritical data in external low field conditions: The measurements on the SO02 and SH05 samples were performed in self-field conditions and for the selected magnetic field values of 50/100/200 mT and 40/60/100/200/300 mT respectively. The magnetic field orientation was fixed; the magnetic field was applied perpendicularly to the $a-b$ plane (i.e. $B_{\perp,a-b}$, the flat face of the tape). This choice stems from the fact that the utilized data-analysis procedure outlined in [48, 57] is very time-consuming, and for the purpose of this work, we limited our analysis to $B_{\perp,a-b}$ only. We present the data obtained from sample SO01 and sample SH05 in Figure 3.12 and Figure 3.13 respectively. For the sake of brevity, only the representation in the (ρ, I) is provided.

The resistivity increases with an increasing current in the REBCO layer, as well as the temperature of the REBCO layer. We do not report the subcritical data for all samples for the same reasons mentioned in Paragraph 2.1.1 (accuracy). All the measurements start from 77 K, the temperature of the liquid nitrogen bath where the samples were immersed. All the measurements start from 77 K, the temperature of the liquid nitrogen bath where the samples were immersed. The maximum value of resistivity represents the normal state resistivity (30 $\mu\Omega\,cm^{-1}$ to 100 $\mu\Omega\,cm^{-1}$, in agreement with [66]). This can be observed in the temperature range spanning between 88 K to 92 K. Not surprisingly, the data shift toward left (lower current) is due to the reduction of the critical current with field. In agreement with [16, 49], the critical current value decreases very quickly from self-field up to 60 mT, and is followed by a more gentle drop above 60 mT.

3.2.4. General remarks on the extracted overcritical current data

At this stage, these results should be treated with considerable attention. No firm conclusions can be drawn, and investigating the underlying physical mechanism is outside the scope of this thesis work. However, it has been shown that with ultra-fast PCM and with the 2-D UC model, it is possible to retrieve the resistivity in the overcritical current regime.
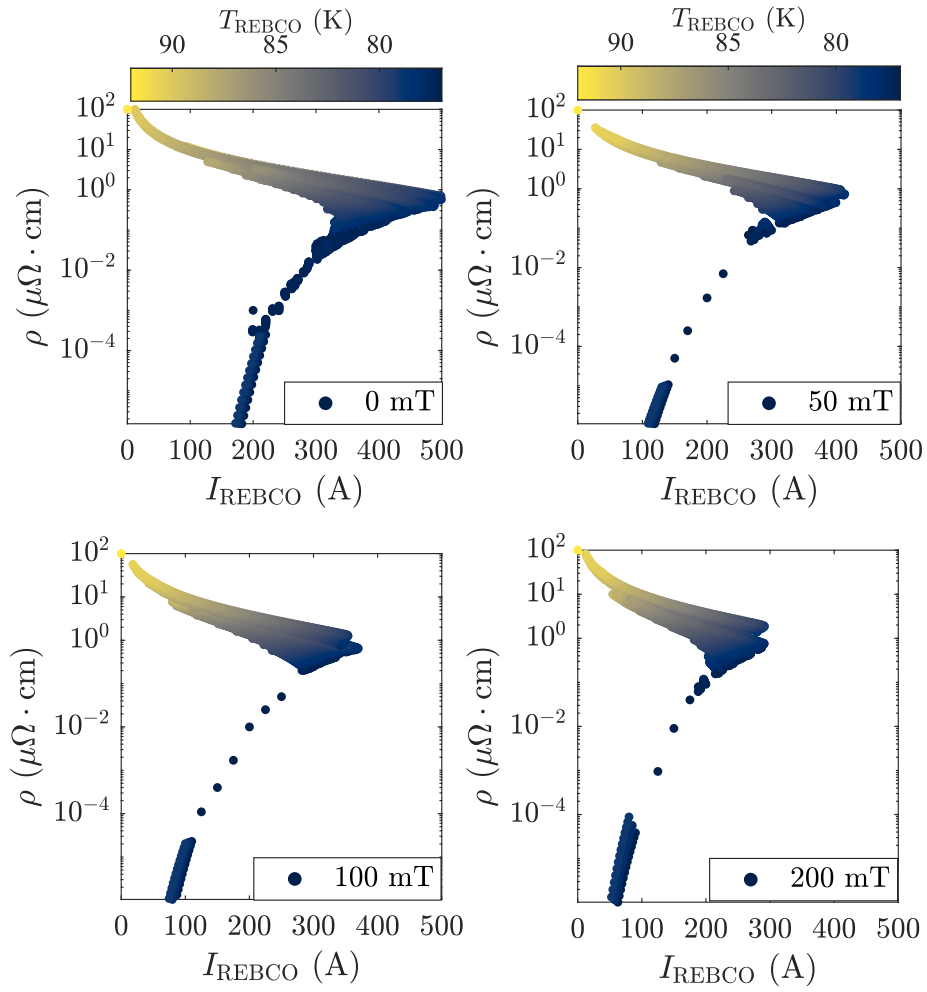
Figure 3.12: Representation on the (ρ,I) plane of the resistivity calculated with the UC model for the SO01 for increasing applied magnetic field (0 mT to 200 mT).
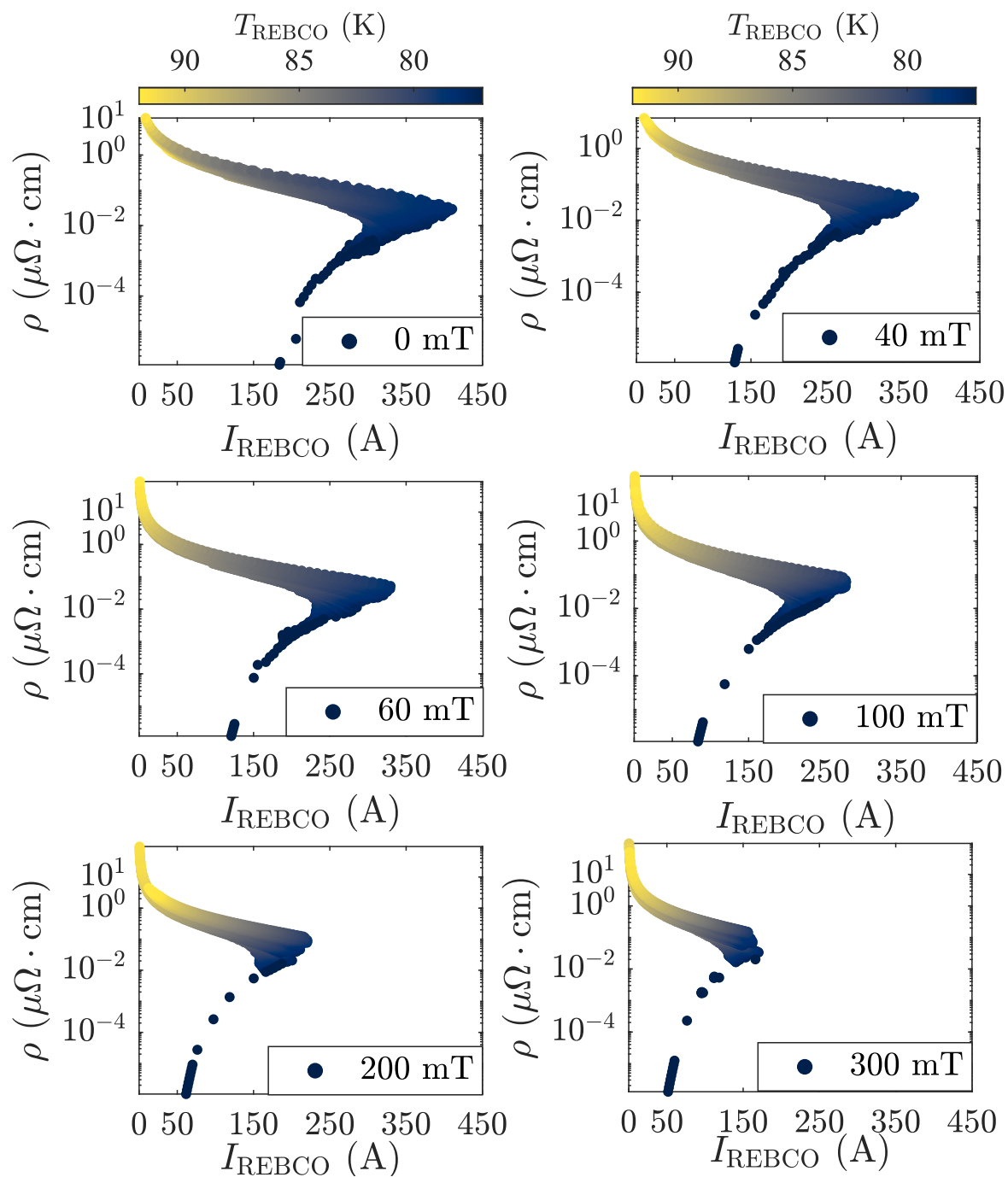
Figure 3.13: Representation on the (ρ, I) plane of the resistivity calculated with the UC model for the SH05 for increasing applied magnetic field (0 mT to 300 mT).

35

3.3. Validity and limits of the FEM-based data analysis

The numerical models and the experimental data can be affected by numerical errors, uncertainties, and experimental problems. In the next paragraphs, we discuss the validity and limitations of the UC model.

3.3.1. Validation of the magnetic relaxation criteria in self-field and low applied field

The first paragraph aims to address the validity and limits of the magnetic relaxation criteria in self-field and low applied external field.

Self-field conditions; magnetic relaxation criterion: It has been shown in [56] that magnetic relaxation is negligible for large current and when the heating is important. Further validation of the UC model and the measurement technique involves the reproducibility of the measurements obtained with current pulses on the REBCO samples. This verification ensures that assumptions such as that magnetic relaxation is negligible.

The experimental voltage curves, the temperature, and the current sharing calculated with the UC model were compared with the corresponding quantities calculated with the magnetothermal model. This model has the same geometry as the UC model, except for the surrounding air computational domain, within which we solve the magnetic field. Instead of modeling the REBCO resistivity with the power-law model, we use the post-processed experimental resistivity. The resistivity data were processed with a technique called data regularization, described in detail in Chapter 4. In this Chapter, we limit the discussion to the comparison of the simulations. The comparisons are shown in Figure 3.14, for a current pulse of $I = 286$ A. The agreement between the two models and the measured data is very good, with an error below 1%, except in the transient region of the pulse, where the error is 15% in the worst case. The transients' differences are due to magnetic induction in the voltage measurement realized with the sample holder, which was not modeled exactly with its real geometry (e.g., the current return path).
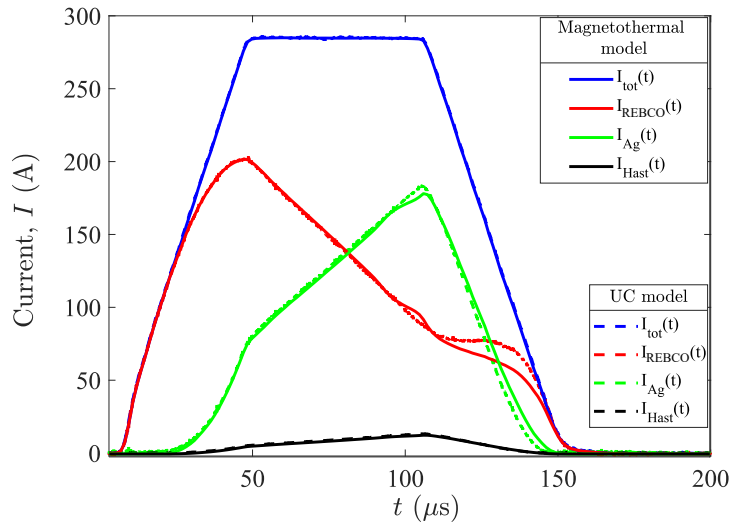
(a)
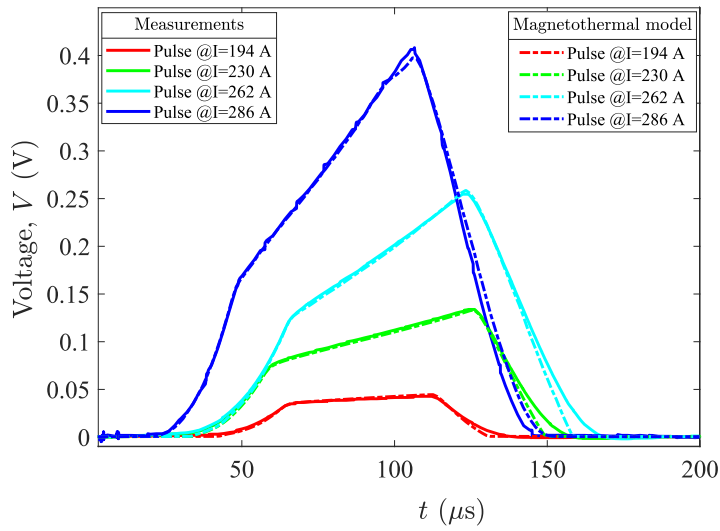
(b)
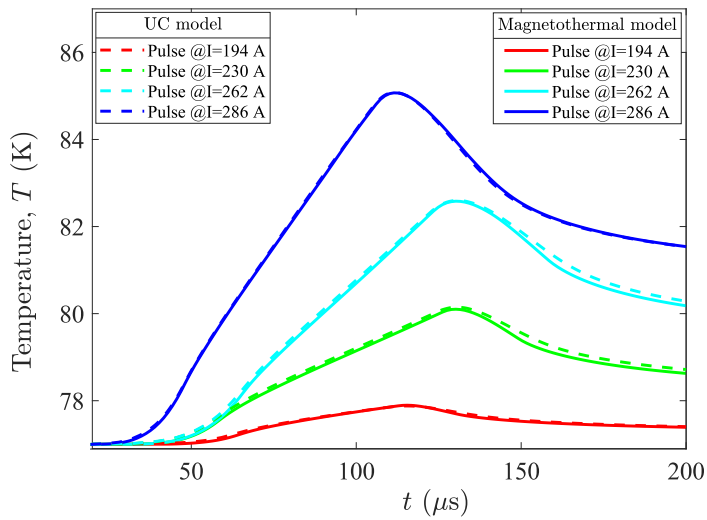
(c)

Figure 3.14: Comparison of the UC model with a magneto-thermal model for the SP01 sample. (a) Current sharing for a pulse of 286 A; (b) Voltage; (c) Temperature.

External low field conditions; magnetic relaxation criterion - tape magnetization/demagnetization:
The criterion developed in [56] to measure relaxation time and validate the extracted data needs to be verified in the presence of an external magnetic field. The method was developed in self-field conditions, and a validation of this sort requires an extensive measurement campaign and the use of another custom sample holder, described in [48]. In our work, we applied a heuristic strategy, which stems from the questions:

A) *Is the magnetic relaxation criterion, developed in self-field conditions, a conservative assumption in low/high applied field?*

B) *What is the impact of the magnetization of the tape on the measured signals, and thus, on the magnetic relaxation criterion?*

Specifically, according to the magnetic relaxation criterion, it is necessary to perform long pulses (i.e. wait a certain time) for the magnetic relaxation effects to disappear. The penetration depth of the magnetic field increases with the applied magnetic field [67, 68].
On the one hand, the magnetic field's increasing penetration depth may reduce the time to wait for the relaxation effects to disappear. This would make the self-field magnetic relaxation criterion a conservative assumption in the presence of a magnetic field.
On the other hand, the magnetization/demagnetization of the tape occurring when a field is applied/removed may affect the voltage signals' contribution, and thus the relaxation time.
In order to address such questions, we utilized two measurements strategies.
The first measurements strategy is depicted in Figure 3.15.
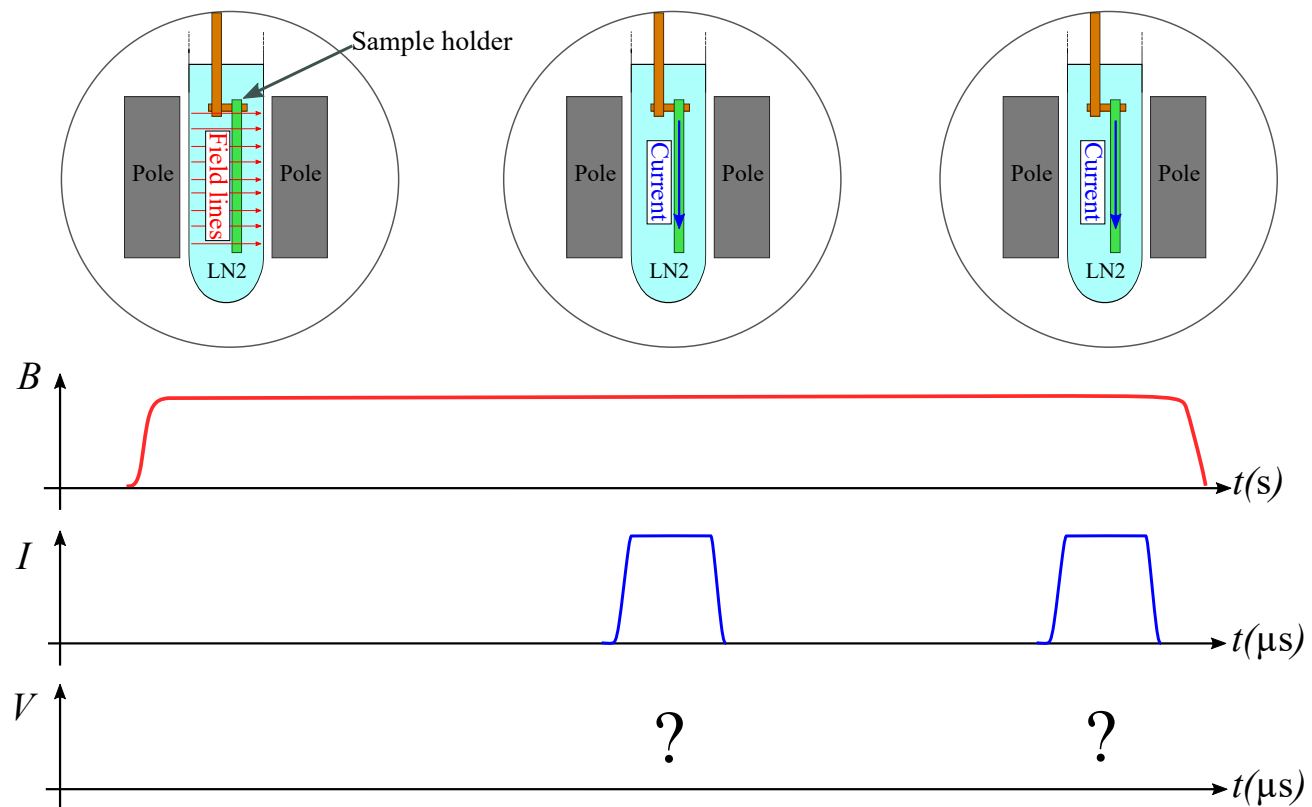
Figure 3.15: Experimental strategy to evaluate the impact of an external magnetic field, and of the magnetization/demagnatization effects on pulsed current measurements (and thus on the magnetic relaxation criterion). First an external field is applied on the tape, then two identical overcurrent pulses are applied. The voltage is recorded.

The sequence is performed as follows:

1. An external field B_{app} of increasing amplitude is applied to the REBCO tape and then kept constant;

2. A first current pulse above I_c is injected in the REBCO tape;

3. A second current pulse above I_c is injected in the REBCO tape;

We chose this sequence because, if the magnetization plays a role, we should see a difference between the first and the second pulse.

During the entire process, the samples are kept in a liquid nitrogen bath (77 K), acquiring the voltage on various sections of 5 mm of the tape, and applying the magnetic field perpendicularly to the flat face of the tape. The sample holder and the magnetic system utilized were the same presented in Chapter 2. In Figure 3.16, we show the voltage measurements obtained following the procedure outlined above for the same current pulse ($\simeq 249$ A) and increasing field amplitudes. After having magnetized the tape (or just after having increased the mag-
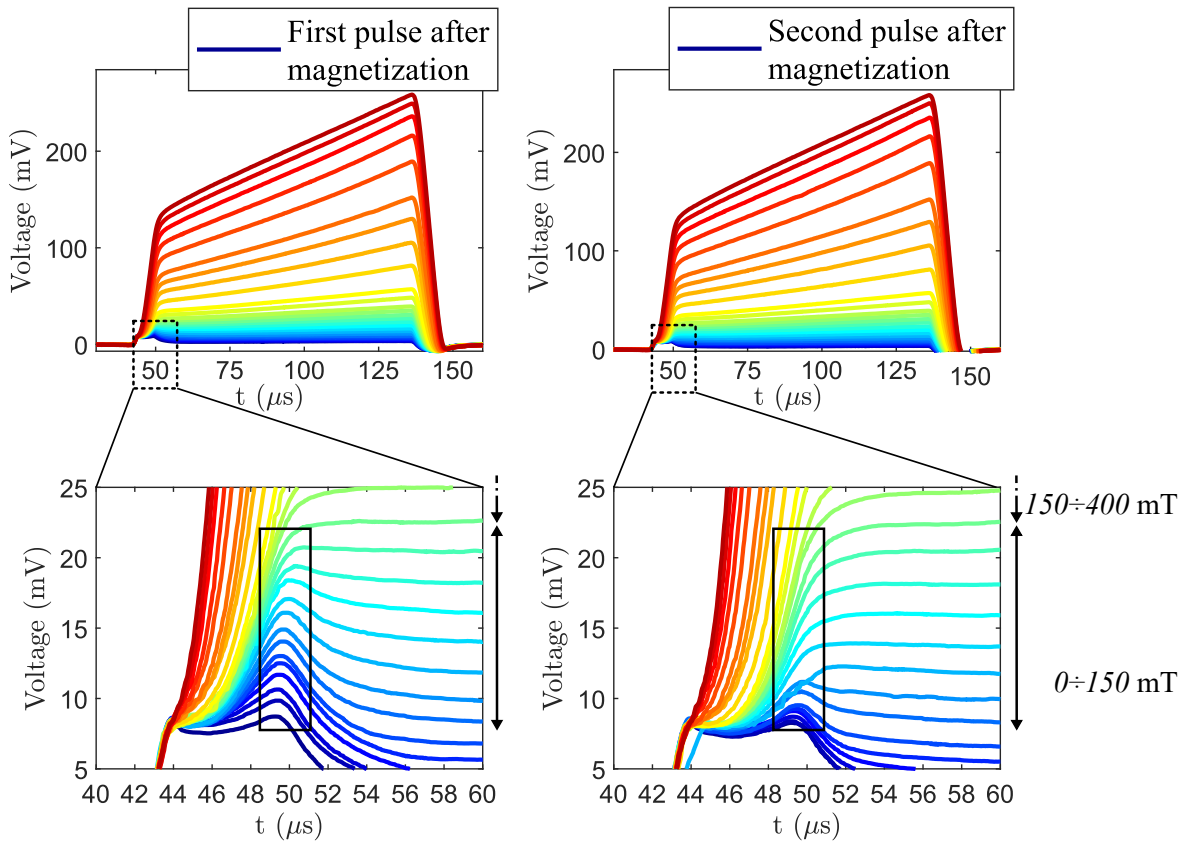
Figure 3.16: Voltage curves obtained by injecting PCM on a 4 mm ShangHai sample. The voltage curves were acquired on 5 mm sections following the field-pulse-pulse sequence. The right plot shows that the voltage curves exhibit a peak (between which origins cannot be attributed to the current transients, since there is a correlation with the applied magnetic field.

netic field), the first pulse presents an magnetization peak at the beginning. When a second pulse of the same current amplitude is applied, the measured signal changes shape, and the peak at 49 µs is reduced in amplitude. The difference between the two signals can be better appreciated in Figure 3.17, where we report the quantity R_{pk}, calculated as follows:

$$R_{pk} = \frac{V_{peak,1st}}{V_{peak,2nd}}, \tag{3.10}$$
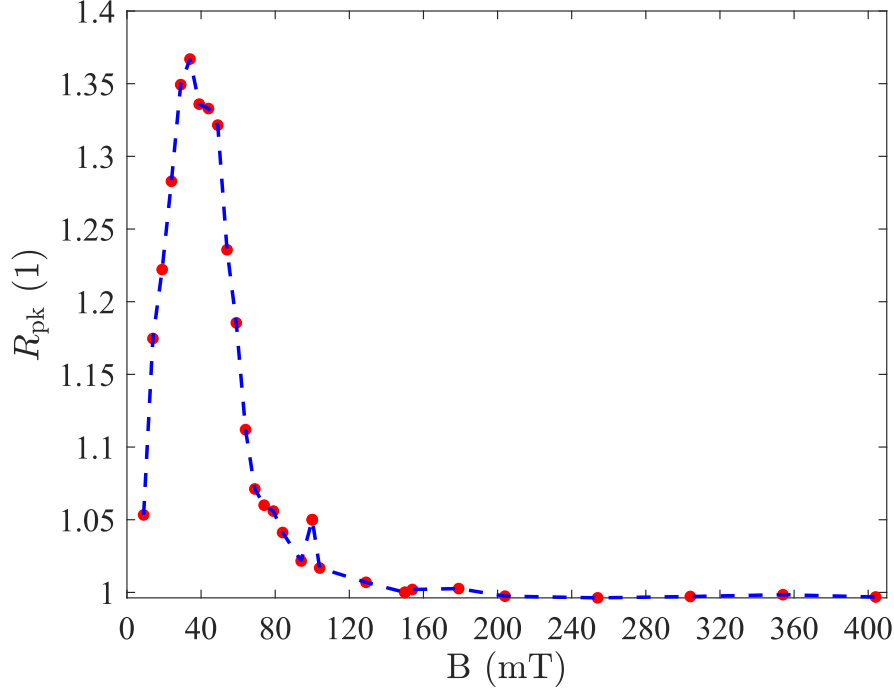
Figure 3.17: The quantity R_{pk}, calculated as indicated in Equation (3.10) is larger than 1 ($R > 1$) for $B < 150\,\text{mT}$. This indicates that the origin of the peak cannot be purely inductive.

where $V_{peak,1st}$ is the maximum voltage peak extracted from the first pulse after magnetizing the tape at about 49 µs) and $V_{peak,2nd}$ is the maximum voltage peak extracted from the second pulse after magnetizing the tape at about 49 µs. As $R_{pk} > 1$ for $B < 150\,\text{mT}$, it means that the two peaks (first/second pulse) are not identical, and thus the origin of these peaks cannot be attributed to inductive signals only. It is apparent that the magnetization of the tape occurring during plays a role in interpreting the data. The R_{pk} increases with the applied magnetic field from 0 mT to 42 mT, while above 42 mT it decreases, finally reaching 1 around 150 mT.

To further investigate this second aspect, we followed another measurement strategy aiming exclusively to address the magnetization/demagnetization of the tape. The strategy utilized is depicted in Figure 3.18 and was structured as follows:

1. A first current pulse above I_c is injected in the REBCO tape;

2. An external field B_{app} of increasing amplitude is applied to the REBCO tape and then removed;

3. A second current pulse (same amplitude of the first) above I_c is injected in the REBCO tape after removing the magnetic field;

4. A third current pulse (same amplitude of the first) above I_c is injected in the REBCO tape;

We chose this sequence because, if the magnetization plays a role, we should see a difference between the first, second, and third current pulse. The measurements were performed on sample SH05 ($I_c = 171\,\text{A}$ at 77 K in self-field conditions). During the entire process, the samples were in a liquid nitrogen bath (77 K). The sample holder and the magnetic system utilized were the same presented in Chapter 2. In Figure 3.19, we show the voltage measure-
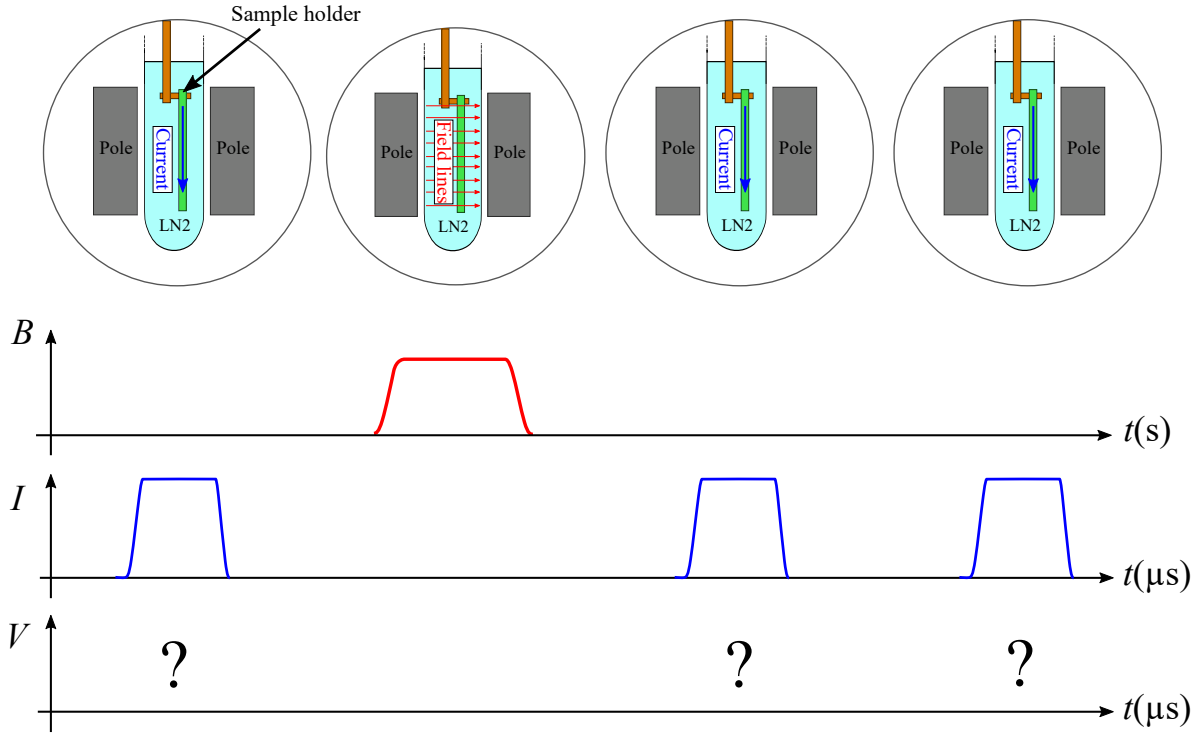
Figure 3.18: Experimental strategy to assess the magnetization role on the magnetic relaxation criterion. First, an overcurrent pulse, previous any magnetization of the tape is performed, then the tape is magnetized, and two more overcurrent pulses of the same duration and amplitude are performed on the tape. The voltage is acquired.

ments obtained following the procedure outlined above for the same current pulse ($\simeq 300\,$A) and increasing field amplitudes. The first pulse is the same for all cases since no magnetic field was applied. After removing the magnetic field (second pulse overall), the first pulse presents a very interesting magnetization peak at the beginning. The amplitude of the peak increases rapidly with the applied magnetic field from 0 mT to 42 mT, while above 42 mT its value is constant up to 400 mT. Finally, when the second pulse after removing the field is performed (third pulse overall), the anomalous peak disappears, and all the pulses resemble the first ones. The difference between the two signals can be better appreciated in Figure 3.20a, where we plot the maximum voltage peak calculated from the *first* pulse *after* removing the magnetic field (red dots), and the maximum voltage peak calculated from the *second* pulse *after* removing the magnetic field. Finally, as the two measuring strategies described in this paragraph are fundamentally different (in-field vs. self-field), it is not very easy to compare the results. However, there is a curious correlation between Figure 3.17 and Figure 3.20a. Specifically, above the field amplitude of 42 mT in Figure 3.17 the R_{pk} start decreasing until when it remains constant. Similarly, above the field amplitude of 42 mT, we see that in Figure 3.20a the maximum remains constant (around 20 mV). We need to remember, however, that these measurements were carried out in two very different conditions (i.e., with an external field and in self-field).

However, we can speculate that the magnetization peaks originate from the magnetic field penetrated in the tape after the magnetization. When a magnetic field is applied externally on the tape, the magnetic flux penetrates the tape in form of vortices. With an increasing applied field, the number of vortices (vortices density) increases as well. When PCM above I_c were performed and no magnetic field was previously applied, we have the situation represented in Figure 3.19 left, where the magnetization peaks are attributed to the rapid current
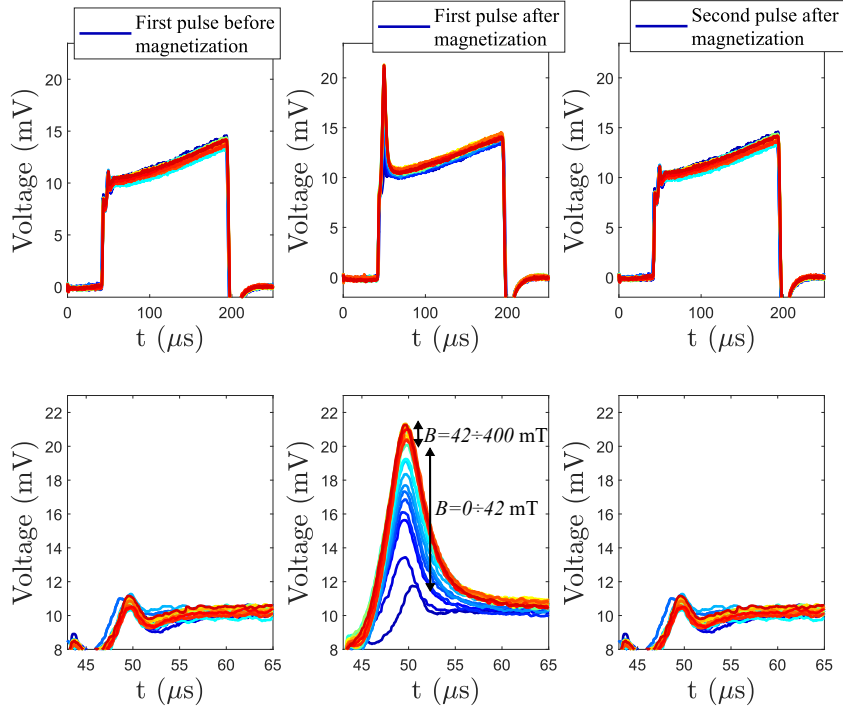
Figure 3.19: Voltage curves obtained by performing PCM on a 4 mm ShangHai sample and acquired on 5 mm sections following the pulse-field-pulse-pulse sequence. The middle plot shows that the voltage curves exhibit an magnetization peak which origins cannot be attributed to the current transients, since there is a correlation with the applied magnetic field.

transients only ($500\,\text{A}\,\mu\text{s}^{-1}$ [45]). When the same PCMs (above I_c) were performed after the tape was magnetized, a magnetization peak appeared (Figure 3.16 left or Figure 3.19 middle). A possible explanation is that the vortices penetrated during the tape's magnetization started moving all together when an overcurrent pulse was performed (flux-flow state). In fact, since the density of the vortices increases with the external applied magnetic field, and the electric field in the flux-flow state is proportional to the number of vortices present in the superconductor [9], also the voltage peak increases proportionally until the tape is fully penetrated. When a full-penetration of the tape is reached, the vortices are present over the tape's entire width, and the maximum voltage peak remains constant. In Figure 3.20a the red zone indicates the region where the field is completely penetrated, and the maximum voltage peak remains constant. We can verify the hypothesis described above by reproducing the experiment using a magnetothermal model and considering the magnetization phenomena occurring in a REBCO tape.

Modeling of the tape demagnetization in the μs **scale subjected to overcurrent pulses:** We used a $H-$formulation coupled with the Heat Equation, simulating the 2-D cross-section of the apparatus as represented in Figure 3.20b.
The magnetic field is applied along y using a Dirichlet boundary condition and the current pulse along z using a PointWise Constraint. The thermal dependence of the critical current density (linear decrease), as well as its magnetic field anisotropic dependence (Kim-Like
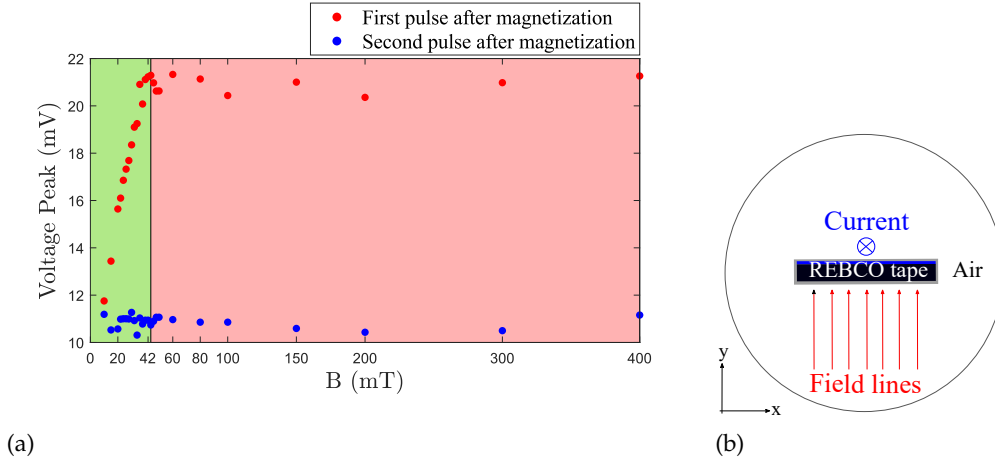
Figure 3.20: (a) Maximum voltage peak calculated from the first pulse (red dots) and the second pulse (blue dots) after removing the magnetic field, and (b) schematic representation of the FEM model used to investigate the magnetization peaks.

model [68, 69]), can be written in the following factorized form:

$$
J_c(B, T) = \frac{J_{c,77K}}{\underbrace{\left(1 + \dfrac{\sqrt{k^2|B_\perp|^2 + |B_\parallel|^2}}{B_0}\right)^\alpha}_{\text{Kim-Like model}}} \cdot \overbrace{\frac{T_c - T}{T_c - 77\,\text{K}}}^{\text{Thermal-dependence}}, \tag{3.11}
$$

where $J_{c,77K} = 2.8\text{x}10^{10}\,\text{Am}^{-2}$, $T_c = 92\,\text{K}$, $\alpha = 0.7$ [70–72], $k = 0.29515$ [72–74] and $B_0 = 42.65\,\text{mT}$ [69]. The variables $B_\perp$ and $B_\parallel$ are parallel and perpendicular components of the sample's local magnetic field. The values of B_0 and α are found in literature [69] and very interestingly reflects the experimental applied field above which the observed voltage peak remains constant (around 20 mV). Following a *field-pulse-pulse* simulation strategy, we obtain the results in Figure 3.21a. We observe that after having magnetized the tape (red pulse), the simulated voltage obtained after the first pulse presents a magnetization peak signal, while for the second pulse, it disappears. Similarly, following a *pulse-field-pulse-pulse* simulation strategy, in Figure 3.21b, we observe that after removing the magnetic field (red pulse), the simulated voltage resulting from the third pulse present a magnetization peak signal. The inset of Figure 3.21b shows that the magnetization peaks gradually increases with the magnetic field and remains the same (around 20 mV) above 40 mT. While this simulation does not provide an exact physical explanation, it provides evidence that a demagnetization phenomenon occurs in the µs scale and that the magnetic field-orientation anisotropy plays a role. Also, with this method, it is possible to measure the magnetic field relaxation time of REBCO tapes. In conclusion, when PCM in the microsecond scale are performed, it is necessary to pay attention to any voltage signal recorded since they can be affected by magnetization peaks originating by the magnetization of the tape:

- For relatively low applied field (above 40 mT) the magnetization effects play an important role on the magnetic relaxation criterion. Either a longer waiting time is needed, or a second "demagnetizing" pulse is required to remove such effects;

- For sufficiently large field (above 40 mT) the self-field relaxation criterion could be used and considered as conservative;

43

(a)

(b)
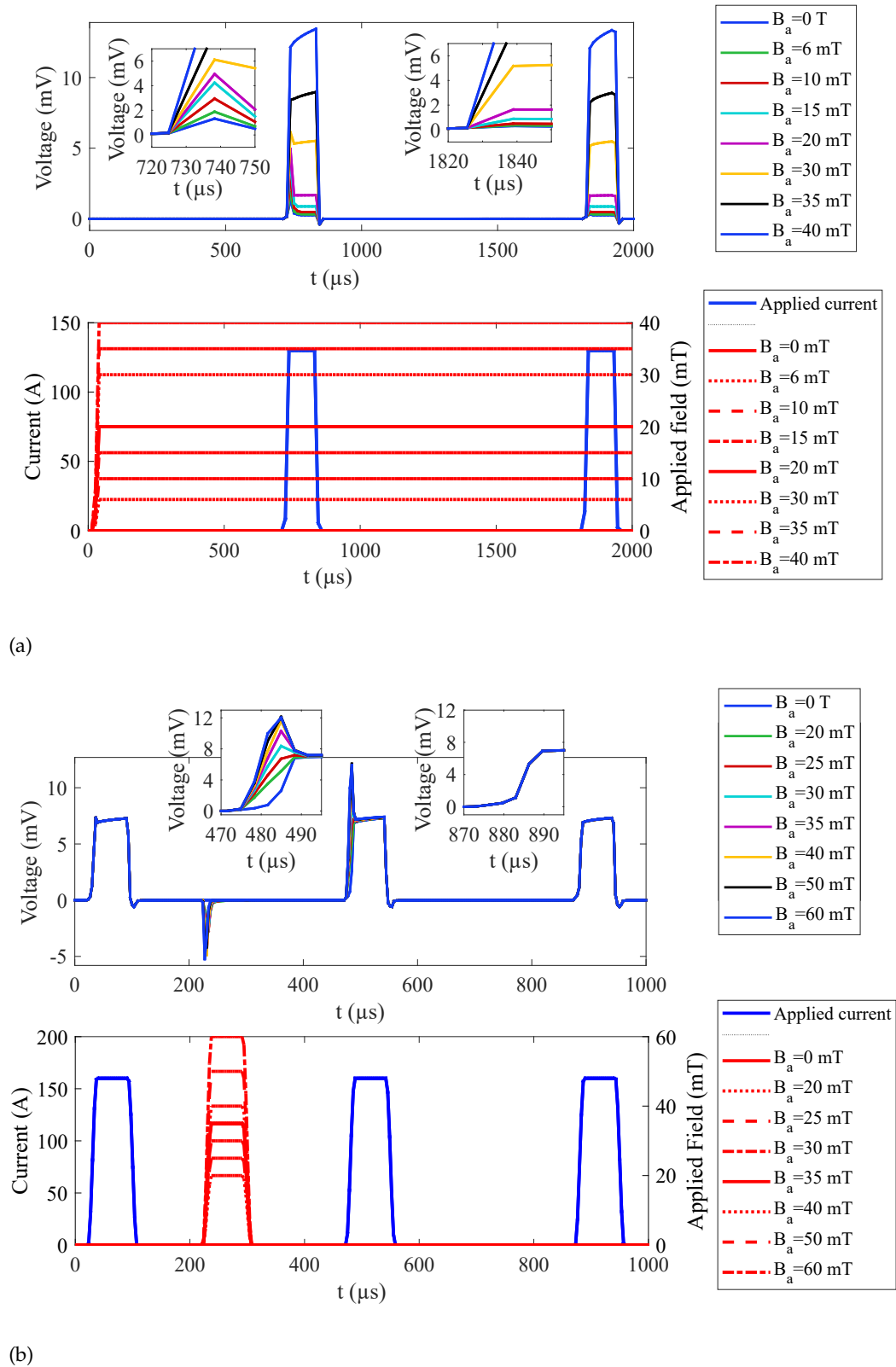
Figure 3.21: Simulated voltage curves obtained with a magnetothermal model implemented in COMSOL. The simulations reproduced qualitatively the results obtained with the (a) *field−pulse−pulse*, and (b) *pulse−field−pulse−pulse* procedure. The poor resolution during the transients has to be attributed to a relatively large stored time step. This, however, does not affect the simulation results quality.
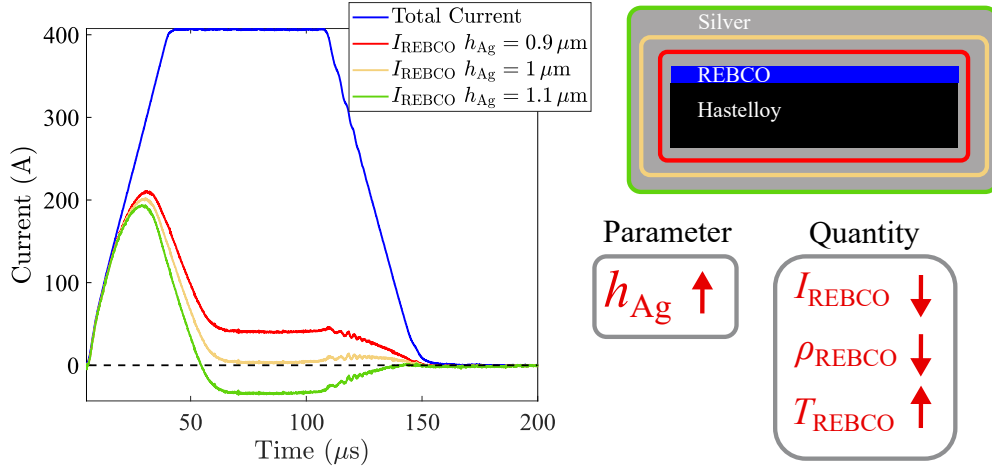
Figure 3.22: Sensitivity simulation of the UC model on a pulse performed on SP01. An error of the 10% on the amount of surrounding silver affects consistently a quantity like I_{REBCO}.

3.3.2. Uncertainty and sensitivity analysis: optimization method for extracting stabilizer geometry and properties of REBCO tapes

The need to calculate temperature, current, and resistivity using FEA makes such calculated quantities highly sensitive to the input parameters' uncertainties. The input parameters (geometry and material properties of the tape) impose limits on our confidence of the output (current sharing, the temperature in the UC model's domains, and resistivity). Hence, it is essential to perform sensitivity and uncertainty analysis.

A sensitivity analysis describes how the quantities of interest are sensitive to the variation of individual input parameters. Since there are multiple input parameters, a sensitivity analysis helped determine which ones drive most of the variation in the outcome and exclude others. Once individuated the most critical parameters affecting a model, it is necessary to perform an uncertainty analysis to describe the range of possible outcomes given a set of inputs (where each input has some uncertainty).

The details of the calculations are discussed in Appendix A.6, here we report the main results. The resistivity of the UC model calculated in Equation (3.9) is affected by several quantities, which can be categorized in measurements, geometry, and material properties:

$$\rho_{\text{REBCO,UC}} = f\left(V_{\text{tot}}, I_{\text{tot}}, [h_{\text{Ag}}, h_{\text{Hast}}, h_{\text{REBCO}}, ...], [\rho_{\text{Ag}}, \rho_{\text{Hast}}, ...]\right) \tag{3.12}$$

As a result of the sensitivity analysis (SA)[5], the parameters that mostly impact Equation (3.9) is the amount of surrounding silver and its resistivity. Consequently, an uncertainty analysis (UA) was performed using FEA[6], by varying the sensitive parameters within a uniform distribution of ±20% respect to the initial values. The UA allowed quantifying the variation of the quantities of interest (resistivity, temperature, and current) due to the variability of the sensitive parameters (resistivity and thickness of the silver). In the worst-case scenario, the quantities of interest were affected by an error up to 90%.

In Figure 3.22, we show that even the 10% of an error on the amount of surrounding silver affects an important calculated quantity such as I_{REBCO} considerably. For instance, if the nominal amount of surrounding silver is 1 μm, a variation of +10% (1.1 μm) of surrounding silver

---

[5]We used the partial derivatives method with respect to the inputs on Equation (3.9). This method allowed us to obtain an analytic estimation of the sensitivity of the results on the input parameters (Appendix A.6).

[6]In Appendix A.6 we also present a modified 2-D UC model that evaluates the sensitivities with respect to a geometric deformation of the silver layer and its electrical resistivity.

stabilizer implies a variation of -40% of I_{REBCO} ($-40\,\text{A}$). In other words, the current in the REBCO layer will be underestimated or without physical meaning (negative), as well as the estimated REBCO resistivity. The estimated temperature instead will increase. This aspect is critical, and it must be addressed.

However, the knowledge of the sample's exact geometry and its resistivity comes as a major problem due to its purity (hence RRR) and to the difficulty in measuring thin silver layers. To address this problem, we can follow two approaches.

The first approach relies on an extensive uncertainty analysis using FEA in order to find the correct parameters. This type of analysis can be computationally very demanding, and the possibility of using a 1-D or 0-D UC model (Appendix A.4) was explored. A 1-D model simplifies the data analysis, accurately captures the main behavior of the system of interest, but yields a CPU time reduction. Nonetheless, this way of proceeding is still computationally expensive.

Optimization method for extracting stabilizer geometry and properties of REBCO tapes:
To further reduce the computational efforts, the second approach does not rely on FEA. In this approach, experimental measurements of resistance vs temperature of the tape (R vs T) and quenched voltage PCM (all the current flows into the silver and Hastelloy matrix), are supported by the use of an algorithm developed to estimate geometry and resistivity of the silver layer correctly. This method was applied on several samples (SP01, SP06, TH03, and SH05). We present the selected case for the SP01 sample.

The first step requires a good initial guess of the involved quantities (namely h_{Ag} and $\rho_{\text{Ag}}(T)$). This is done by combining the characteristics provided by the manufacturer on the data-sheet with direct measurements of R vs T as described in Paragraph 2.1.2. The injected current to measure R vs T is very small ($100\,\text{mA}$), and we can assume that the acquired voltage signal is given by the silver layer only (as showed also in Equation (3.1)). Hence, it is possible to describe the electrical resistance of the tape as that of the silver with a temperature dependent linear fit:

$$R_{\text{Ag}}(T) = R_{\text{Ag},0} + \beta_{\text{Ag}} \cdot (T - T_{\text{c}}). \tag{3.13}$$

In Figure 3.23a, we report the measured resistance vs temperature. The electrical resistance of the tape embeds the information about both silver thickness and resistivity:

$$R_{\text{Ag}}(T) = (\widetilde{\rho}_{\text{Ag},0} + \widetilde{\alpha}_{\text{Ag}} \cdot (T - T_{\text{c}})) \cdot \frac{l_{\text{meas}}}{\widetilde{h}_{\text{tot,Ag}} \cdot w_{\text{tape}}}, \tag{3.14}$$

with $l_{\text{meas}} = 10\,\text{cm}$ being the length of the measured section for the R vs T measurements, and $w_{\text{tape}} = 4\,\text{mm}$ the width of the tape. The notation ~ (tilde) indicates the unknown parameters that we investigate with the optimization method. For the analyzed sample, the amount of silver declared on the data-sheet was of $\widetilde{h}_{\text{tot,Ag}} = 2.2\,\mu\text{m}$ ($1.1\,\mu\text{m}$ surrounding silver). The parameters in Equation (3.14) can be estimated by equating the fit calculated in Figure 3.23a (i.e. Equation (3.13)), and the datasheet:

$$\widetilde{\rho}_{\text{Ag},0} = \frac{R_{\text{Ag},0} \cdot \widetilde{h}_{\text{tot,Ag}} \cdot w_{\text{tape}}}{l_{\text{meas}}} = 0.3943\,\mu\Omega\,\text{cm}$$

$$\widetilde{\alpha}_{\text{Ag}} = \frac{\beta_{\text{Ag}} \cdot \widetilde{h}_{\text{tot,Ag}} \cdot w_{\text{tape}}}{l_{\text{meas}}} = 0.0049\,\mu\Omega\,\text{cm}\,\text{K}^{-1}. \tag{3.15}$$

With these values, the UC model predicts that the current in the REBCO drops below zero, as shown in Figure 3.24 (black line). This means that the set of used parameters overestimates the actual amount of silver (or underestimates its resistivity). The overestimation of silver
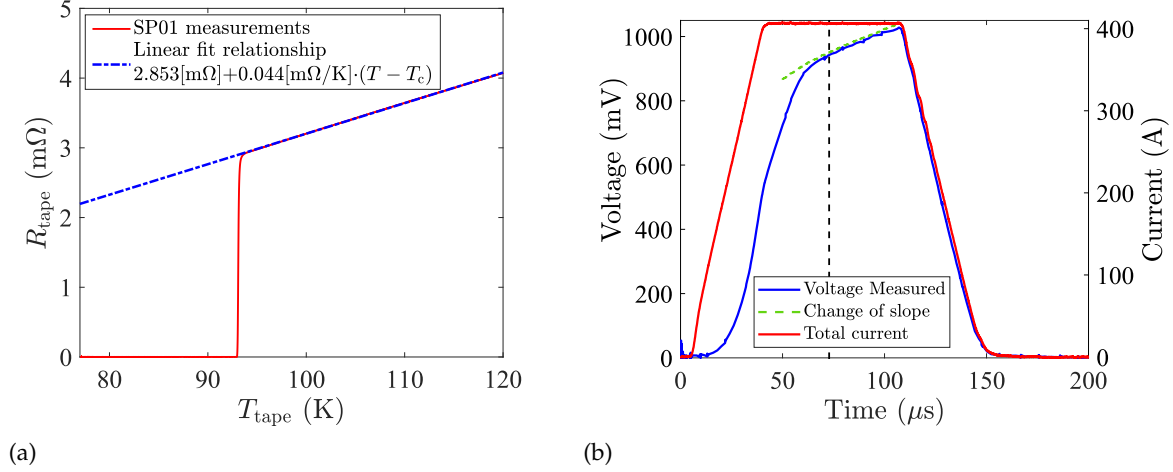
Figure 3.23: (a) Measured tape resistance vs temperature of the SP01 sample, and (b) example of selected pulse exhibiting a change of slope of the measured voltage.

thickness leads to an excessive value of current calculated for the silver layer, and thus a negative current in the REBCO layer. The initial guess need to be adjusted and optimized for a better result.

The second step of the optimization method involves the analysis of long PCM ($t > 100\,\mu s$) at large current amplitudes ($I_{tot} > 3\,I_c$), for which the sample quenches and the current flows entirely in the stabilizer matrix. In Figure 3.23b, we report the specific case of one pulse performed on the sample. When the pulsed current amplitude is as high as 400 A, we cannot neglect the contribution of the Hastelloy layer since part of the current flows in there. The overall resistivity of the sample can be represented as follows:

$$R_{tape}(T) \simeq \frac{R_{Ag}(T) \cdot R_{Hast}(T)}{R_{Ag}(T) + R_{Hast}(T)}, \tag{3.16}$$

where $R_{Ag}(T)$ and $R_{Hast}(T)$ are the resistance of the silver and Hastelloy, respectively. We can express $R_{Ag}(T)$ and $R_{Hast}(T)$ with a relationship similar to Equation (3.13).

If we assume that the Hastelloy's temperature-dependence resistivity is negligible ($\rho_{Hast}(T) =$ const $= 1.23 \cdot 10^{-6}\,\Omega\,m$) [25], then the electrical resistivity of the silver depends linearly on the temperature $\rho_{Ag}(T) = \rho_{Ag,0} + \alpha_{Ag} \cdot (T - T_c)$, so we can rearrange Equation (3.16) with the analytic expression:

$$R_{tape}(T) = \frac{l_{tape} \cdot \rho_{Hast}}{w_{tape}} \cdot \frac{\widetilde{\rho}_{Ag,0} + \widetilde{\alpha}_{Ag} \cdot (T - T_c)}{\left[\widetilde{\rho}_{Ag,0} + \widetilde{\alpha}_{Ag} \cdot (T - T_c)\right] h_{tot,Hast} + \rho_{Hast} \cdot \widetilde{h}_{tot,Ag}}, \tag{3.17}$$

where $l_{tape} = 5\,mm$, $w_{tape} = 4\,mm$ are the length and width of the measured section, $h_{tot,Hast} = 50\,\mu m$ to $90\,\mu m$ is the thickness of the Hastelloy layer. The parameter T_c, which varies from 89 K to 92 K, is the reference temperature (in this case the critical temperature of the analyzed tape). We have $\widetilde{h}_{tot,Ag}$ as the total thickness of the silver layer, i.e. if the surrounding silver layer is 1 μm, $h_{tot,Ag} = 2\,\mu m$. The parameter $\widetilde{\rho}_{Ag,0}$ is the silver resistivity at the reference temperature, and $\widetilde{\alpha}_{Ag}$ is the linear temperature coefficient ($\Omega\,m\,K^{-1}$).

With the analytic form in Equation (3.17) we can formulate and solve a non-linear least squares fitting problem, matching the quenched voltage curves with the analytic function (i.e., minimizing the residuals calculated as $|R_{exp} - R_{tape}|$).

47

The problem is defined as follows:

1. Given a set of n_{tot} experimental points $\{T_{exp,k}, R_{exp,k}\}$ (R vs T + quenched PCM);

2. Given the analytic model function in Eq. (3.17);

3. Find ($[\widetilde{\rho}_{Ag,0}, \widetilde{\alpha}_{Ag}, \widetilde{h}_{tot,Ag}]$) describing R_{tape} and matching the quenched PCM such that the following residuals are minimized:

$$\left\{ \sum_{n=1}^{n_{tot}} \left[R_{exp,k} - R_{tape}([\widetilde{\rho}_{Ag,0}, \widetilde{\alpha}_{Ag}, \widetilde{h}_{tot,Ag}], T_{exp,k}) \right]^2 \right\} \tag{3.18}$$

The algorithm formulated above is implemented in MatLab [75] and performs several iterations (non-linear least square fit) until the set of experimental points $\{T_{exp,k}, R_{exp,k}\}$ matches the analytic function in Equation (3.17). When fitting multiple parameters of a non-linear function, the χ^2 surface is likely to have multiple minima [76], possibly leading to mathematically correct but nonphysical solutions. A good initial guess and setting the right upper and lower limits of the searched parameters, is of paramount importance. Taking the values from Equation (3.15) as the initial guess, we assume the upper and lower bounds to vary by $\pm 20\%$ with respect to the initial guess (e.g. $\widetilde{\rho}_{Ag,0} = (2 \pm 0.4)\,\mu m$). The non-linear least squares fitting problem for this specific sample returns the optimal parameters $\widetilde{h}_{tot,Ag}^{op} = 1.92\,\mu m$, $\widetilde{\rho}_{Ag,0}^{op} = 0.3361\,\mu\Omega\,cm$, and, $\widetilde{\alpha}_{Ag}^{op} = 0.0052\,\mu\Omega\,cm\,K^{-1}$. If the UC model is rerun with such parameters, we obtain the results reported in Figure 3.24 (green line). Here the difference between using the optimized parameters with respect to the non-optimized parameters can be appreciated. Specifically, while the initial parameters poorly estimate the REBCO layer's current, with the new set of parameters the current in the REBCO layer reaches $\simeq 0\,A$ and remains constant afterwards. This result is a good indication that the set of parameters obtained with the algorithm of Equation (3.18), offer a better approximation of the actual thickness of the silver layer.

Here, it is necessary to comment about the general validity of this method. This method was applied on a limited number of characterized samples (4 samples overall). In Table 3.1, we report the optimal values obtained by applying the non-linear LSQ fitting problem, and the nominal amount of total thickness of the silver layer provided by the manufacturer on the data-sheet. The values are consistent with each other, especially as regards of $\widetilde{\rho}_{Ag,0}$. In the case of the sample from THEVA, even if the silver thickness was much higher than the other samples, the method seems to work adequately well. However, we note that $\widetilde{\alpha}_{Ag}$ is higher for that particular sample and this should be treated with caution. The reason for this discrepancy has to be further investigated. Overall, the obtained values are in good agreement with those reported in the literature [9, 12, 59]. Finally, the entire post-processing method relies

Sample	$\widetilde{\rho}_{Ag,0}^{op}$ [$\mu\Omega\,cm$]	$\widetilde{\alpha}_{Ag}^{op}$ [$\mu\Omega\,cm\,K^{-1}$]	$\widetilde{h}_{tot,Ag}^{op}$ [μm]	$h_{tot,Ag}^{nom}$ [μm]
SuperPower (SF4050)	0.3361	0.0052	1.92	2 to 3
SuperPower (SF4050)	0.4200	0.0060	2.2	2 to 3
THEVA (TPL1100)	0.3676	0.0082	18	15 to 19
SuperOx	0.3957	0.0048	1.8	2 to 3

Table 3.1: Optimal and nominal values.
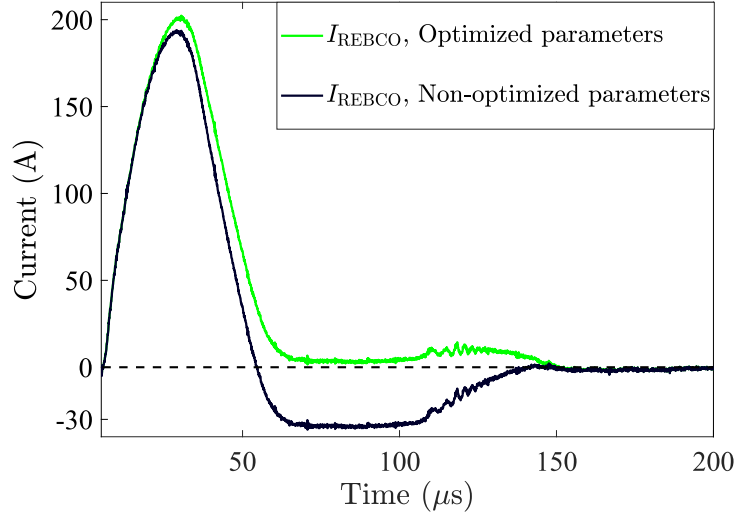
Figure 3.24: Comparison between I_{REBCO} calculated with the UC model and using the non-optimized and optimized parameters.

on the use of pulsed current measurements on the µs scale. In order to confirm the reliability of the method, other voltage curves obtained with different measurement systems should be tested (e.g., ms pulses). The main result of this method is the development of a reliable way to determine the parameters that mostly affect the UC model and help to minimize their uncertainties, hence estimating precisely the overcritical current resistivity.

3.3.3. Impact of silver layer thickness and REBCO layer inhomogeneities on the 2-D UC model (longitudinal cross-section)

Since the UC model is 2-D along the width, all the physical quantities are assumed to be uniform along the length. However, due to the possible inhomogeneity of the materials (e.g., silver thickness), the temperature and resistivity might not be the same along the sample's length, invalidating the 2-D UC model's assumptions. Measurements at different voltage taps along sample SP01 and SP06 were performed to verify this eventuality. In Figure 3.25a and Figure 3.25b, different voltage measurements on different sections of the selected samples are presented. The voltage curves belong to the same current pulse, $I_{\mathrm{tot,SP01}} = 260\,\mathrm{A}$ and $I_{\mathrm{tot,SP05}} = 320\,\mathrm{A}$ respectively, and the corresponding temperatures calculated with the UC model. Even though the voltages measured along the length of the sample SP01 (Figure 3.25a) present some differences, it does not result in a remarkable deviation of the calculated temperature (less then 1 K) over the sample length characterized (the distance between sections AB and FG it is about 4 cm). For sample SP05 (Figure 3.25b) the differences in voltage are more evident. Section JI (blue dash-dotted line) shows more rapid heating than the other sections at the beginning of the pulse. Around 140 µs, however, the slope changes abruptly, and the heating rate is drastically reduced with respect to the other sections. In this case, the differences in the measured voltage over the sample length characterized, result in a deviation of the calculated temperature of about 2 K. Since the error performed with the UC model was estimated at around 10 % according to the magnetic relaxation criteria, we can consider this deviation acceptable.

However, the voltage curves of Figure 3.25b present a shape noteworthy to be investigated, especially section JI. The marked difference between the voltage curves is most likely due to the silver thickness layer's inhomogeneities or the REBCO superconducting properties.

49
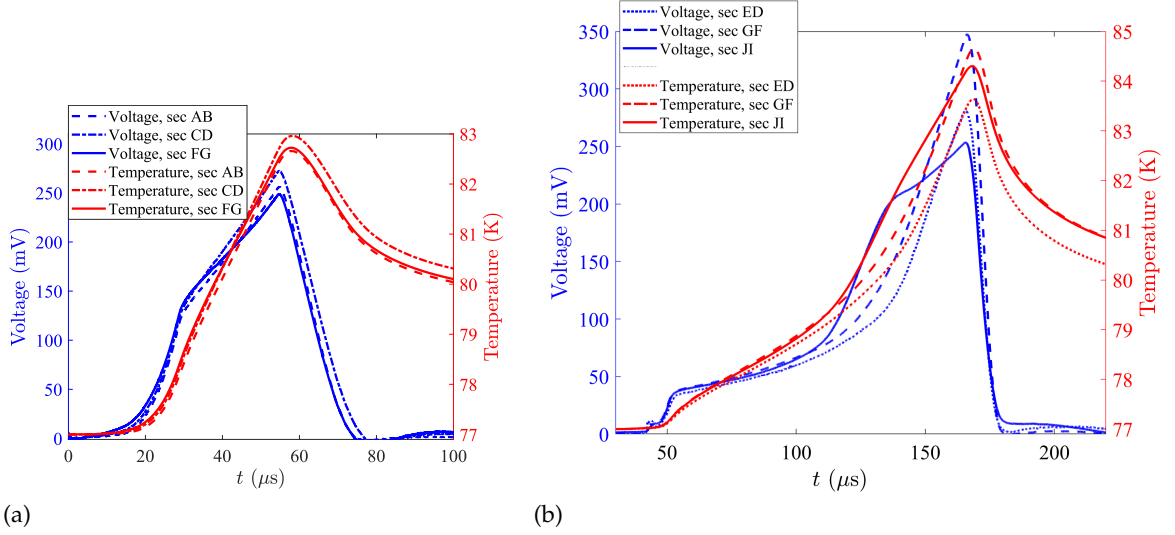
Figure 3.25: Voltage measurements and temperature calculations from the UC model for samples (a) SP01 and (b) SP06.

To verify one of the hypothesis and investigate the origin of the voltage signals, a 2-D longitudinal cross-section model electrothermal was developed (Appendix A.1). The conductivity model was based on the well-known power-law model (in terms of conductivity):

$$\sigma_{\mathrm{PWL}}(E, T) = \frac{J_{\mathrm{c(T)}}}{E_{\mathrm{c}}} \left(\frac{|\boldsymbol{E}|}{E_{\mathrm{c}}} \right)^{\frac{1-n}{n}} \tag{3.19}$$

where n is the n-value, $E_{\mathrm{c}} = 1\,\mu\mathrm{V\,cm}^{-1}$ is the critical electric field. The temperature-dependent critical current density $J_{\mathrm{c(T)}}$ is modeled as:

$$J_{\mathrm{c}}(T) = \begin{cases} J_{\mathrm{c,77K}} \cdot \left(\dfrac{T_{\mathrm{c}} - T}{T_{\mathrm{c}} - 77\mathrm{K}} \right) & \text{if } T \leq T_{\mathrm{c}} \\ 0 & T > T_{\mathrm{c}} \end{cases}$$

where $J_{\mathrm{c,77K}}$ is the critical current density at 77 K. The superconducting-to-normal transition was modeled assuming two resistances in parallel:

$$\sigma_{\mathrm{REBCO}} = \sigma_{\mathrm{PWL}}(E, T) + \sigma_{\mathrm{n}}$$

where $\sigma_{\mathrm{n}} = 1 \times 10^{6}\,\mathrm{S\,m}^{-1}$ is the normal state conductivity. The heat source Q is the term coupling the heat equation with the electric one expressed as:

$$Q = E \cdot J$$

where the critical current density is $J = \sigma \cdot E$. The current pulse/ground is imposed on the left/right boundaries, as showed in Appendix A.1. Finally, the heat exchange with the liquid nitrogen is taken into account using a boundary condition applied only on the top and the bottom layers (silver surfaces). The heat transfer coefficient $h_{\mathrm{LN_2}}(T_{\mathrm{i}} - T_0)$ is a function of the temperature [9]. The utilized models were two; the first one simulated the inhomogeneous superconducting properties of the REBCO (namely inhomogeneous critical current), while the second one simulated the influence of the silver layer's inhomogeneous thickness.

Influence of inhomogeneous critical current density (longitudinal cross-section): A space-dependent critical current density $J_c(T,x) = J_c(T) \cdot \Phi_x(x)$ was defined to reproduce the inhomogeneities of the superconducting properties. The spatial function $\Phi_x(x)$ is a piece-wise function:

$$\Phi_x(x) = \begin{cases} 1 & 0 \leq x < 1\,\text{cm} \\ 1.2 & 1\,\text{cm} \leq x < 2\,\text{cm} \\ 0.8 & 2\,\text{cm} \leq x < 3\,\text{cm} \\ 1.3 & 3\,\text{cm} \leq x < 4\,\text{cm} \\ 1 & 4\,\text{cm} \leq x \leq 5\,\text{cm} \end{cases}$$

The spatial inhomogeneity of the REBCO tapes usually is smoother and on a longer scale-lengths [77, 78]. Being a 2-D model, we assume the properties to be homogeneous along the width of the tape. However, this kind of analysis provides a reasonable investigation of what happens in such conditions (inhomogeneities, micro-second scale, and overcritical current pulses). We report the temperature profile for selected instants (Figure 3.26b), the temperature evolution calculated at selected points (Figure 3.26c), and the voltage drop every 1 cm (Figure 3.26d). As expected, the inhomogeneities play an important role in the electrothermal response of the tape. However, none of the samples' measurements presented voltage amplitudes as different as in the simulation.

If the scale on which the REBCO inhomogeneities occur is more significant than that one on which we measure (namely 5 mm), the temperature is reasonably uniform. In other words, if this condition is satisfied, we can apply the UC model on measurement performed on 5 mm.

Influence of inhomogeneous silver layer thickness: A space modulation of the silver thickness was made to reproduce its inhomogeneities along the length. The space modulation is represented in Figure 3.27a, where a variation of ±15 % is implemented using bezier curves, available in the geometry CAD of COMSOL. Since the solved model is in 2-D, it is important to recall that the properties of the REBCO in this simulation are homogeneous on both the width and the length. We report the temperature profile for selected instants (Figure 3.27b), the temperature evolution calculated at selected points (Figure 3.27c), and the voltage drop every 1 cm (Figure 3.27d). This fits with the results of the previous simulations, where we find different heating regime highlighted by abrupt changes of slope for the same current. This interesting analysis revealed that the reason of the rapid change of slope observed in Figure 3.25b might be due to the inhomogeneous silver thickness.

A better insight of what occurs in this situation can be observed in the set of Figures collected in Figure 3.28, where we represent, for the same selected times of Figure 3.27b, the temperature distribution in the domain (surface distribution plot), and the current density (arrow distribution plot). It appears that at 15 µs the current flows mostly in the REBCO layer, whilst for $t > 51$ µs the current is non-uniformly shared between the REBCO and silver layers. This is due to the inhomogeneous temperature distribution. Similarly to what we observed earlier, if the silver thickness inhomogeneities are on a relative large scale, we can apply the UC model on measurement performed on 5 mm.

Finally, this result can be seen with a more generic point of view: due to the inhomegeneities of the silver layer, there is a redistribution the current and the heat along the length. In the regions with a thinner silver layer, we have a smaller heat mass and bigger resistance. Hence, the temperature will rise faster in the regions with smaller amounts of silver, and the underneath REBCO layer might be degraded or damaged. In other words, a dishomogeneous silver thickness of the tape is a weakpoint, that can turn into a hotspot.
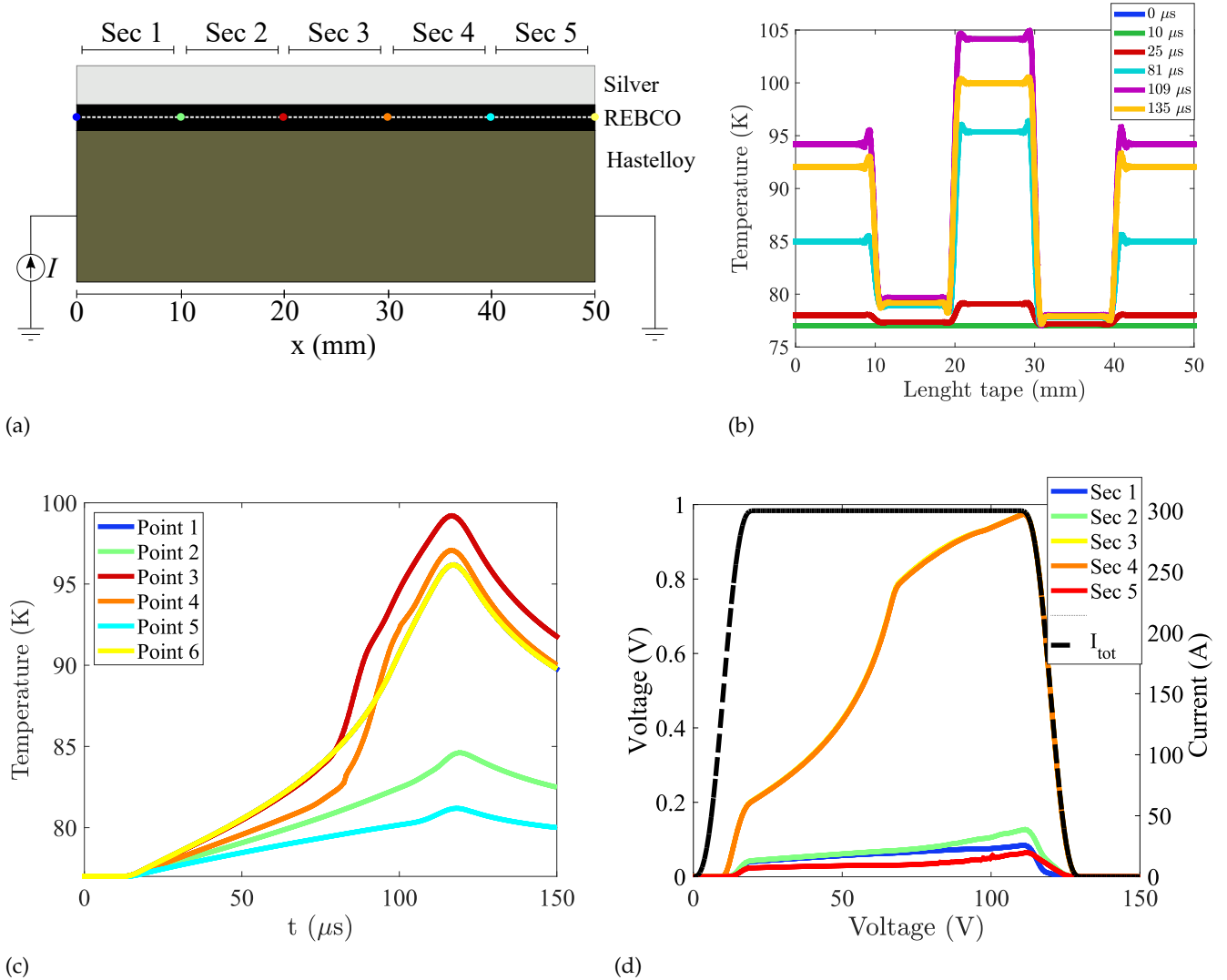
Figure 3.26: (a) Longitudinal cross-section of the REBCO tape with inhomogeneous properties. Here are also represented a white dashed line, and sections where the (b) temperature profile for selected instants, the (c) temperature evolution, and the (d) voltage drop every 1 cm are calculated.
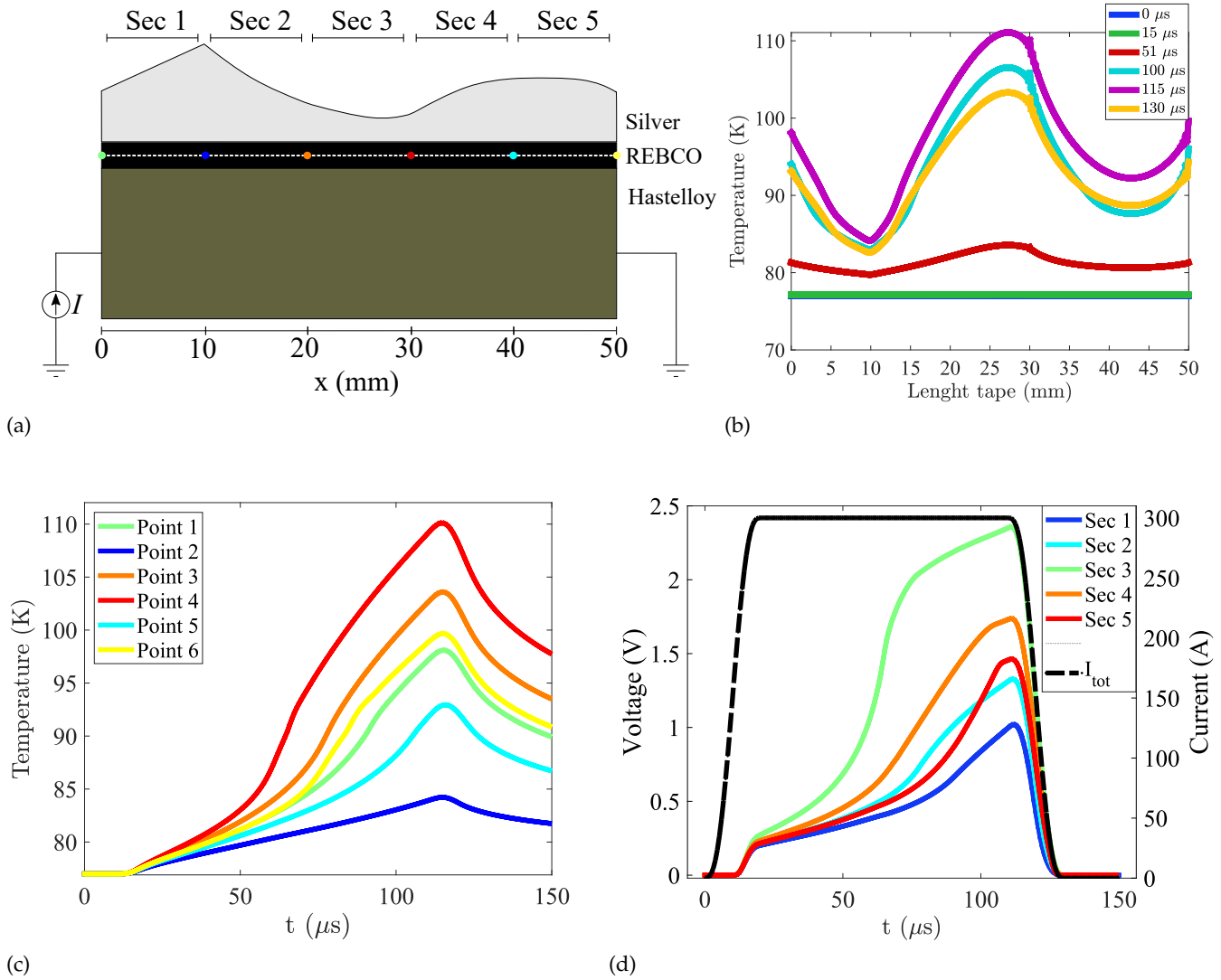
Figure 3.27: (a) Longitudinal cross-section of the REBCO tape with inhomogeneous silver thickness. Here are also represented a white dashed line, the points, and sections where the (b) temperature profile for selected instants, the (c) temperature evolution, and the (d) voltage drop every 1 cm are calculated.
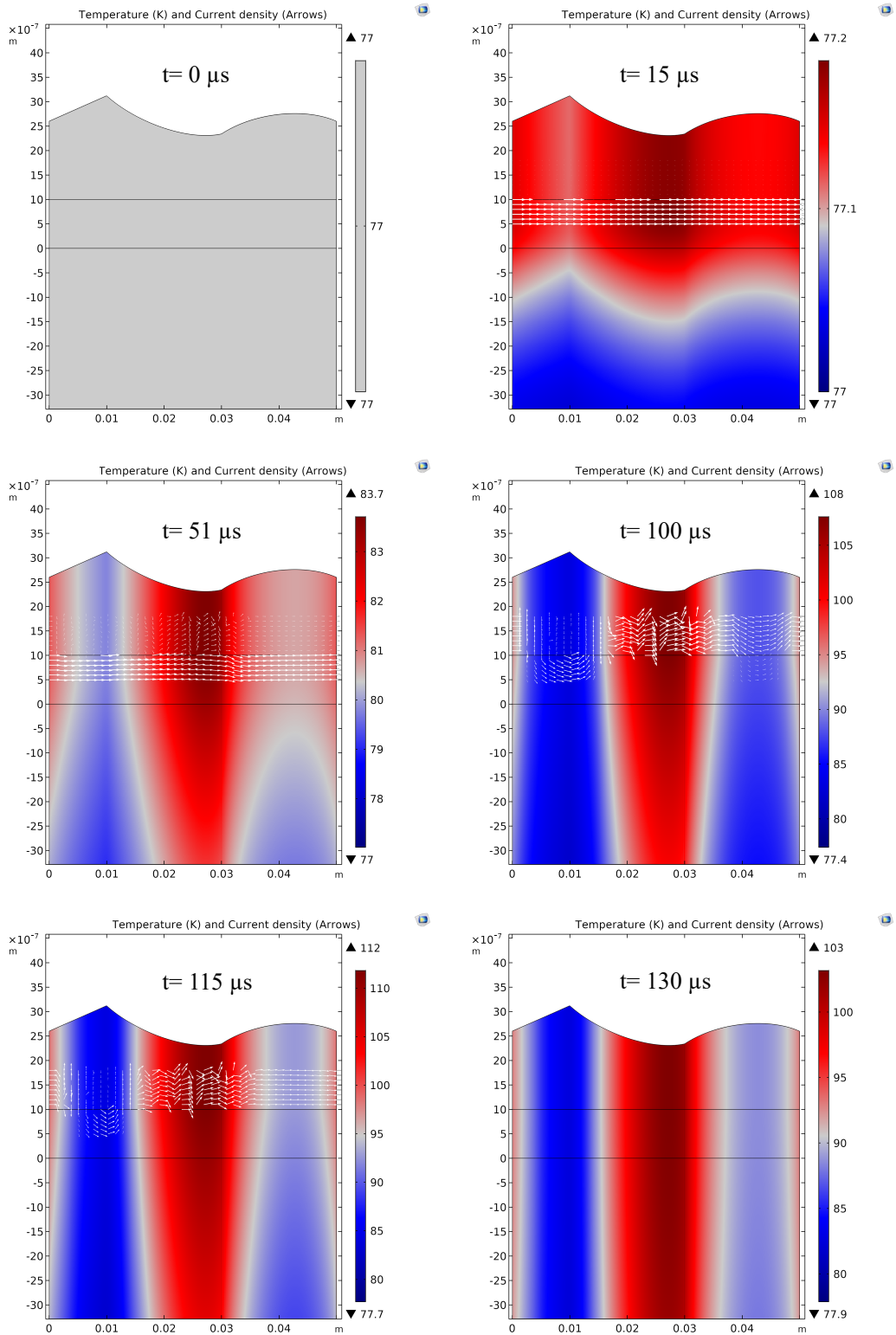
Figure 3.28: Temperature and current distribution (white arrows) for selected time. A inhomogeneous silver thickness in the tape can act as a hotspot.

3.4. Conclusions

In this Chapter, we have shown that with the combination of PCM and FEA, it is possible to retrieve the resistivity data of the superconducting layer in the overcritical current regime. More precisely, we developed a post-processing method (UC model) implemented COMSOL that allows correcting heating effects from the measurements with the so-called UC model, a thermal model plus current sharing model. The temperature estimated by the UC model and the calculated current sharing between the layers indicate that the current in the REBCO drops to $0\,\text{A}$ when its temperature reaches $92\,\text{K}$, which shows that the model correctly estimates the temperature of REBCO over time. Moreover, using a magneto-thermal model, we have shown that the surface obtained from the calculated $\rho(I_{\text{REBCO}}, T_{\text{REBCO}})$ is a very good estimation of the real resistivity, and it allowed us to model the thermal and electrical behavior of a REBCO commercial tape.

We also explored the major limits of this method:

- The UC model does not take into account the magnetic relaxation effects, and thus the complex magnetothermal behavior of the tape;

- The magnetic relaxation criterion was tested in self-field only. For PCM performed in an external field, we only provided a heuristic justification;

- The results calculated with this method are highly sensitive to the input parameters, especially the thickness of the silver layer as well as its electrical resistivity;

The great benefits of a good knowledge of the overcritical current model set this work's course to generate a model that can be implemented and used in numerical simulations for relevant case scenarios. In the rest of this thesis work, we will develop the overcritical current model and then assess its impact on numerical modeling for the simple but relevant case scenario of an SFCL.

Entia non sunt multiplicanda praeter necessitatem.
Pluralitas non est ponenda sine necessitate.
Frustra fit per plura quod fieri potest per pauciora.
  William of Ockham, *Occam's razor principles*

4

Electrical resistivity data of REBCO tapes post-processed with non-parametric constrained regularization methods

This Chapter provides a simplistic overview of the non-parametric constrained regularization techniques used to post-process the experimental overcritical current. The work presented in this Chapter will be reported in:

- J. Nicholson, N. Riva, B. Dutoit, F. Grilli - *Non-parametric constrained regularization method applied to the electrical resistivity data of REBCO tapes for finite element modeling*, Under preparation, draft and regularization code available upon request

4.1. Applying Occam's Razor to the overcritical current data

The quotations inserted at the beginning of this Chapter are different formulations of the *Occam's Razor* principle credited to 14th-century friar William Ockham (or Occam). The English translation states: "*Do not multiply the elements more than necessary. Do not consider plurality if it is not necessary. It is useless to do with more what you can do with less*".

In short, all that Occam's Razor states is "*simple (but not easy) solutions are more likely to be correct than complex ones*" [79]. This became a guiding principle in scientific fields [79, 80]. How does it relate to our research? When we extracted the set of overcritical current data with the UC model (i.e., I_{REBCO}, T_{REBCO} and ρ_{REBCO}) it was desirable to process them in order to obtain an interpolating table to use in FEA afterwards. However, when conventional interpolating techniques were utilized, we encountered a few problems that can be summarized as follows:

1. If an interpolation process is applied to complex *n*-dimensional data-sets, problems such as *overfitting* and *ill-posed problems* [1] generate non-smooth and non-physical surfaces typically, i.e., the model is too complicated.

2. A simple interpolation may lead to a *loss of monotonicity* and, therefore, local oscillations of the resulting interpolation. In our specific case, we can assume that the resistivity

---

[1]Problems that are not well-posed in the sense of Hadamard [81] are termed ill-posed. Inverse problems are often ill-posed. For instance, the inverse heat equation, deducing a previous temperature distribution from the final data, is not well-posed. The solution is highly sensitive to changes in the final data.
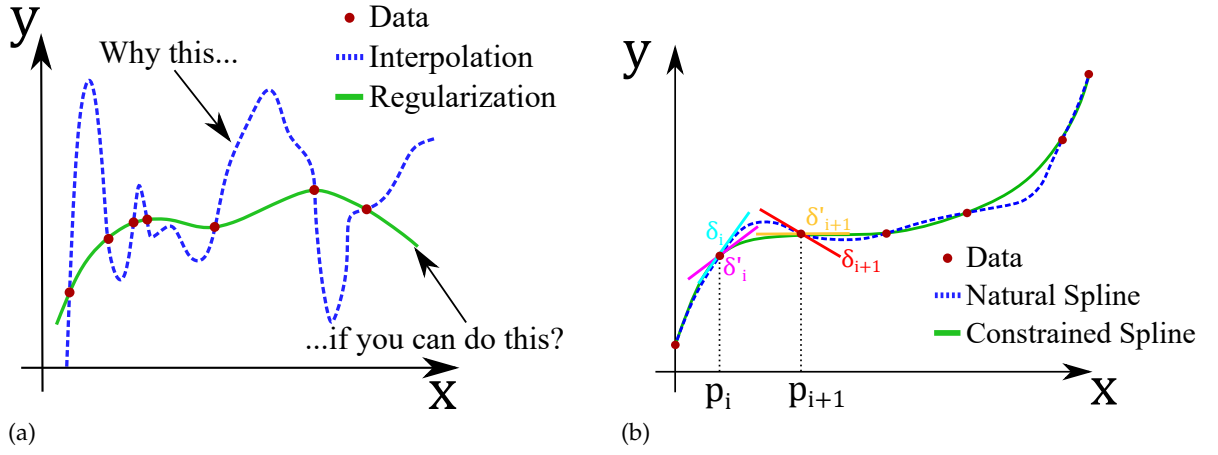
Figure 4.1: (a) Regularization of data relies on the "Occam's Razor" approach; it's a trade-off between how well the model fits the training data (blue dashed) and how "simple" that model is (continuous green). It can be seen as constructing a numerical data-set similar to the data (red dots) but with better smoothing and resolution. (b) To ensure the monotonicity, prevent overshooting (blue dashed) and obtain a constrained spline (continuous green), the tangents δ_i and δ_{i+1} of each successive point p_i and p_{i+1} are constrained.

increases with both temperature/current. Therefore, a loss of monotonicity is problematic since it generates non-physical oscillating behavior of the resistivity interpolating spline.

3. As discussed in Paragraph 3.2.3 the choice to measure in liquid nitrogen affects the population density of the (I, T, ρ) surface. Specifically, all the data start from 77 K, which limits the range of experimental temperature and current. Most interpolating techniques do not guarantee that the regressed model will give reasonable extrapolation where there is a lack of data.

In [57], we reported a $\rho_{OC}(I, T)$ data set whose validity was restricted to a limited range of currents and temperatures. This was because data interpolation had the limitation mentioned above for reconstructing surfaces from experimental measurements suitable for FEA afterwards.

Problems such as overfitting and ill-posed problems (1) are common problems in mathematics, data analysis and finance [82, 83], optoacoustic tomography [84] and equivalent dipole moment source model [85]. Machine learning, advanced statistical methods, and non-parametric regression [86–89] have all advanced in ways that greatly benefit these field in addressing them. In this thesis work, to address overfitting and ill-posed problems, we used a new non-parametric regression technique called *regularizeNd*, which relies on the so-called *regularization of data* and leverages the very Occam's Razor principle. If the model is *too simple*, it will make useless predictions. If the model is *too complex*, it will not generalize well.

The problem of loss of monotonicity (2) can be addressed by imposing *monotonic constraints*. In short, to ensure the monotonicity and prevent overshoot of the resulting resistivity spline, the tangents of each successive point of the spline are constrained. Both concepts can be visualized by the simplistic representation in Figure 4.1. Another approach is the use of *constrained least-squares methods*, where a linear least-squares problem with an additional constraint on the solution is solved.

4.2. Non-parametric constrained data regularization techniques

In the next sections, we will show the consequences of using conventional interpolating techniques on the overcritical current data and the necessity of approaching data regularization

techniques. Afterwards, we will provide an intuitive interpretation of the underlying mathematics.

4.2.1. Overfitting and loss of monotonicity of the overcritical current interpolating splines

This paragraph demonstrates how classical interpolation methods applied to the overcritical current data produce splines and surfaces affected by overfitting and monotonicity loss. For this purpose, we selected the SP02 sample. In Figure 4.2 we represent the extracted overcritical current data with the UC model ρ_{UC} in function of the current in the REBCO I_{REBCO} and for the selected temperature of 77 K. We compare the interpolating splines performed on the data (red-dots) with a *piecewise Hermite interpolating polynomial* (black-dashed) and with a *cubic spline interpolation* (green-dashed). The consequences of overfitting and loss of monotonicity are apparent, utilizing graphical methods. They can be intuitively interpreted as when the model (or the algorithm) fits the data too well. In Figure 4.3 we present an attempt to reconstruct a 3-D $\rho_{\mathrm{OC}}(I, T)$ surface with the interpolating technique available in the commercial software MatLab, namely $Interp2$ and $griddata$ [75]. Also, in this way of representing the data, it is apparent how the problems mentioned above heavily affect reconstructing a surface using conventional interpolating techniques.
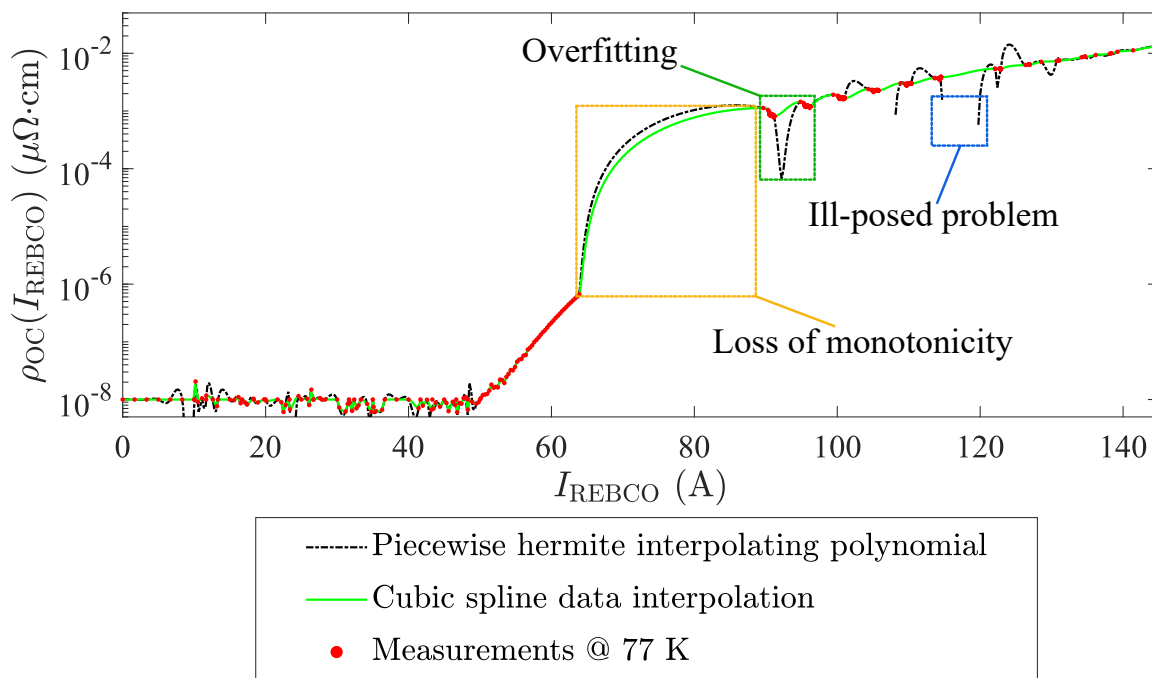
Figure 4.2: Interpolating techniques in comparison applied to the selected sample SP02 at 77 K. We compare the experimental overcritical current data (red-dots) with a *piecewise hermite polynomial interpolation* (black-dashed), and with a *cubic spline interpolation* (green-dashed).

4.2.2. *regularizedNd*: a MatLab script for non-parametric constrained regularization methods

In this thesis, we tested a new non-parametric regression algorithm called *regularizeNd* [90] in collaboration with the developer, Jason Nicholson[2]. regularizeNd generates a look-up table non-affected by overfitting or loss of monotonicity, utilizing additional constraints in the interpolator-solver. Besides, regularizeNd can allow for reasonable linear extrapolation from

---

[2]Former Danfoss Power Solutions employer, and now employed at John Deere.
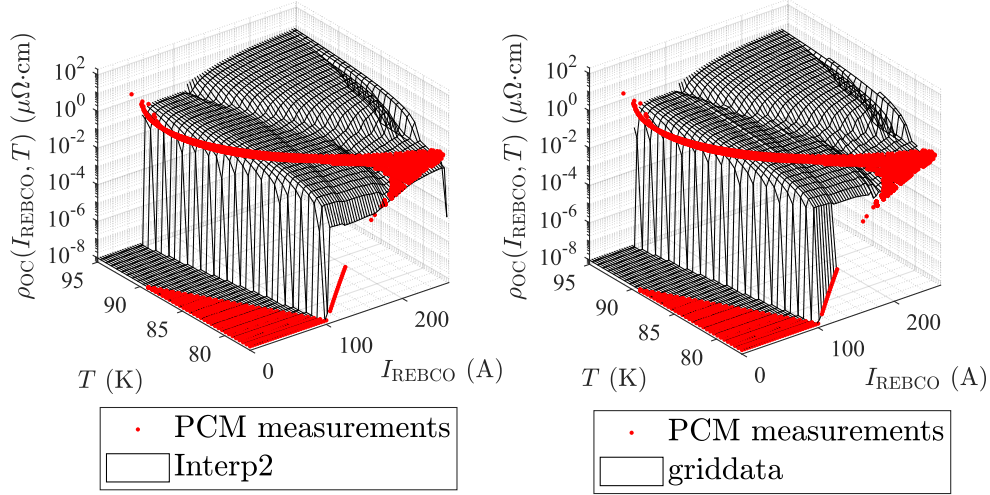
Figure 4.3: Attempt to reconstruct a 3-D $\rho_{OC}(I, T)$ surface with the interpolating technique available in the commercial software MatLab, namely *Interp2* and *griddata*.

the test data (despite we recall that *no first-physics* principle should be inferred).
Intuitively, we need to generate a numerical data-set similar to the measurements but with custom spacing[3] (better resolution) on the independent variables[4] (x, y) (i.e., T_{REBCO} and I_{REBCO}) and smoothing on z (i.e., ρ_{REBCO}) [90]. A system of linear equations named "fidelity" (checking that the agreement of the output points agrees with the measured data) and "smoothness" (checking whether the output points oscillate wildly or not) is solved. The special feature of this method is to scale the linear equations in a way that balances the *goodness* of fit against its *smoothness*, so that the output data-set embodies the best compromise between fidelity and smoothness [90].
For the sake of simplicity, we will consider a 2-D example as described in [90]. Afterwards, the necessary steps to apply this technique to a 3-D data set will be shortly discussed.

Experimental 2-D data-set and regularized data: Let's consider an experimental 2-D data-set:

$$(\underline{x}, \underline{y}) = (x_0, x_1, ..., x_n, y_0, y_1, ..., y_n), \tag{4.1}$$

where $x_i < x_{i+1}$, and n is the number of measured points. The points x_i are not regularly spaced, which possibly means $|x_{i+1} - x_i| \neq |x_{l+1} - x_l|$ for $i \neq l$.
The regularized data 2-D data-set that we want to obtain is:

$$(\underline{x}^{reg}, \underline{y}^{reg}) = (x_0^{reg}, x_1^{reg}, ..., x_m^{reg}, y_0^{reg}, y_1^{reg}, ..., y_m^{reg}), \tag{4.2}$$

where $x_i^{reg} < x_{i+1}^{reg}$, and m is the number of regularized points such that $m \geq n$[5]. The points x_i^{reg} are regularly (and custom) spaced, which means $|x_{i+1} - x_i| = |x_{l+1} - x_l|$ for any i, l.
The vector $\underline{x}^{reg}$ can be generated as a linearly spaced vector starting from $\underline{x}$. In MatLab this can be done by defining $x_{reg} = linspace(min(x), max(x), m)$.

---

[3]If we have an irregularly spaced (as in our case) data-set on (x, y), its utilization in numerical modeling should be avoided. As a matter of fact, the numerical solver's interpolator may encounter the issues discussed above (overfitting, oscillations, etc).
[4]regularizedNd can be easily applied to n-dimensions.
[5]Such condition is necessary because choosing $m < n$ we would contribute to the ill-conditioning of the problem.

Fidelity matrix: The fidelity matrix is one part of the system of linear equations we need to solve. It can be thought of as the conventional interpolation technique since it checks the "agreement of the output points with the measured data". As a consequence, we can apply the *linear*, *cubic* or *nearest – neighbour* interpolation methods. For the sake of simplicity, we consider a *linear* interpolation method. It is possible to show that the desired output points y_i^{reg} points can be represented as a linear combination of the experimental points y_i as follows:

$$y_j^{\text{reg}} = y_i \cdot \left(1 - \frac{x_j^{\text{reg}} - x_i}{x_{i+1} - x_i}\right) + y_{i+1} \cdot \left(\frac{x_j^{\text{reg}} - x_i}{x_{i+1} - x_i}\right) \tag{4.3}$$

$$= \sum_{k=i}^{i+1} b_{k,j} \cdot y_k, \tag{4.4}$$

where $b_{k,j}$ are *weights* used to represent the output points, and they should sum to 1 for each row[6]. Similarly (or by inverting Equation (4.4)), we can demonstrate that the experimental points y_i can be represented as a linear combination of y_i^{reg} as follows:

$$y_i = \sum_{j=1}^{m} a_{i,j} \cdot y_j^{\text{reg}}, \tag{4.5}$$

where $a_{i,j}$ are *weights* used to represent the output points, and they should sum to 1 for each row. Combining the set of n linear equations, we obtain the set of linear equations in Equation (4.5), in matrix form:

$$A_{\text{Fid}}\,\underline{y}^{\text{reg}} = \underline{y}, \tag{4.6}$$

where A_{Fid} is a sparse matrix that contains the weights obtained by linear interpolations, and has n rows (experimental input points) and m columns (desired output points).

Smoothness matrix: The smoothness matrix is the second part of the system of linear equations that we need to solve. These equations address the "smoothness" of the interpolating spline, and thus, its differentiability. The minimum differentiability order that ensures a smooth function is C^2, namely the second derivative. It is possible to show that, with the *three-point formula* [91, 92], the *numerical second derivative* of the points $(x_{i-1}^{reg}, x_i^{reg}, x_{i+1}^{reg})$ can be written as:

$$\frac{\mathrm{d}^2 y_i^{\text{reg}}}{\mathrm{d}x^2} = \begin{bmatrix} \dfrac{2}{\left(x_i^{reg} - x_{i-1}^{reg}\right) \cdot \left(x_{i+1}^{reg} - x_{i-1}^{reg}\right)} \\[2.5em] \dfrac{-2}{\left(x_{i+1}^{reg} - x_i^{reg}\right) \cdot \left(x_i^{reg} - x_{i-1}^{reg}\right)} \\[2.5em] \dfrac{2}{\left(x_{i+1}^{reg} - x_i^{reg}\right) \cdot \left(x_{i+1}^{reg} - x_{i-1}^{reg}\right)} \end{bmatrix}^{\mathsf{T}} \begin{bmatrix} y_{i-1}^{reg} \\[2em] y_i^{reg} \\[2em] y_{i+1}^{reg} \end{bmatrix}. \tag{4.7}$$

For m points we can obtain $m - 2$ numerical second derivatives. In matrix form is written as follows:

$$A_{\text{2nd}}\,\underline{y}^{\text{reg}} = \frac{\mathrm{d}^2\underline{y}^{\text{reg}}}{\mathrm{d}x^2}. \tag{4.8}$$

---

[6]For instance, the value $y_i = 0.55$ can be represented as a weighted average of $y_l^{\text{reg}} = 0.5$ and $y_{l+1}^{\text{reg}} = 1$. In this case the weights are $a_{i,l} = 0.9$ and $a_{i,l+1} = 0.1$, respectively.
This results into $y_i = a_{i,l} \cdot y_l^{\text{reg}} + a_{i,l+1} \cdot y_{l+1}^{\text{reg}} = 0.9 \cdot 0.5 + 0.1 \cdot 1 = 0.55$

The core of regularization lies in the next steps. Let's note the *zero vector* as $\underline{0}$ ($m - 2$ elements). If we impose the following condition:

$$A_{\text{2nd}}\,\underline{y}^{\text{reg}} = \underline{0} = (0, 0, ..., 0)^{\mathsf{T}}, \tag{4.9}$$

we constrain the output points (spline) to be perfectly smooth (namely to be a *straight line*, a linear function), which is certainly unwanted. We need a more gentle approach to penalize large variations in the output points (spline) and adjust the severity of the penalty in Equation (4.9). This can be done by scaling the magnitude of A_{2nd}[7].

Overall matrix: First, we need to concatenate A_{Fid} and A_{2nd} into one single matrix (fidelity and smoothness requirements), and also the experimental points $\underline{y}$ and $\underline{0}$ as follows:

$$\boldsymbol{A}_{\text{tot}} = \begin{bmatrix} A_{\text{Fid}} \\ \Gamma \cdot A_{\text{2nd}} \end{bmatrix} \qquad\qquad \underline{b} = \begin{bmatrix} \underline{y} \\ \underline{0} \end{bmatrix}$$

where A_{2nd} is scaled by a factor Γ, defined as follows:

$$\Gamma = \psi_{\text{smooth}} \sqrt{\frac{n}{m - 2}}, \tag{4.10}$$

where n is the number of "fidelity" equations (experimental input points), and m is the number of "smoothness" equations (desired output points). The parameter ψ_{smooth} is a constant chosen by the user, always greater than 0, and dictates the degree of the *smoothness* (or "stiffness") relative to the *fidelity*.

The smaller is ψ_{smooth}, the closer is to the experimental input points (i.e., $\underline{y}$). An extremely large value, such as $\psi_{\text{smooth}} = 1000$, will cause the output points $\underline{y}^{\text{reg}}$ (spline) to be practically a straight line. In practice, ψ_{smooth} ranges from 10^{-5} to 10^{-2}. Finally, with $\psi_{\text{smooth}} = 1$ we have equal importance to *fidelity* and *smoothness*. In *regularizedNd* the ψ_{smooth} value can be intuitively represented the so-called **L-curve** [89, 93, 94], although it is not its rigorous definition. The **L-curve**, however, provides a graphical method to assess what is the compromise between minimization of the regularized solution vs the corresponding residual, which is the very core of any regularization method.

The value Γ is necessary to produce consistent results: a given value of ψ_{smooth} will always produce the same answer independently of m, the number of chosen output points.

Finally, the overall linear system equations are written as follows in matrix form:

$$\boldsymbol{A}_{\text{tot}}\,\underline{y}^{\text{reg}} = \underline{b}. \tag{4.11}$$

This system, however, is overdetermined and has $n + m - 2$ equations but only m variables.

Linear least squares method for overdetermined systems: We can use the *least squares method* (once more) to find an approximate solution to overdetermined systems. For the system:

$$\min_{\underline{y}^{\text{reg}}} \| \boldsymbol{A}_{\text{tot}}\,\underline{y}^{\text{reg}} - \underline{b} \|, \tag{4.12}$$

the solution of which can be written with the normal equations [95]:

$$\boldsymbol{A}_{\text{tot}}^{\mathsf{T}} \boldsymbol{A}_{\text{tot}}\,\underline{y}^{\text{reg}} = \boldsymbol{A}_{\text{tot}}^{\mathsf{T}}\underline{b}, \tag{4.13}$$

---

[7]A scaling of the magnitude of A_{2nd} is necessary when if we want to compare the residuals of "fidelity" and "stiffness" matrices.

The system in Equation 4.13 in this form are called the *normal equations* [96, 97]. The quantity $A_{tot}^T A_{tot}$ generates a sparse, symmetric, band matrix[8].
The regularized output data is obtained as:

$$\underline{y}^{reg} = \left(A_{tot}^T A_{tot}\right)^{-1} A_{tot}^T \underline{b}. \tag{4.14}$$

The quality of the resulting regularized spline can be evaluated using the residuals as follows:

$$Residuals = A_{tot}\,\underline{y}^{reg} - \underline{b}. \tag{4.15}$$

Least square problem and monotonic constraints: The regularization of data is iteratively solved through a least-squares curve fitting problems in the form:

$$\min \frac{1}{2} \left\| A_{tot}\underline{y}^{reg} - \underline{y} \right\|_2^2 \tag{4.16}$$

Finally, we want our output points to lie on a monotonically increasing [9] spline such that $y_i^{reg} \le y_{i+1}^{reg}$. We chose the constrained least-squares method to express the monotonic constraints problem.

It is fairly simple to add this requirement to the regularization problem [94, 100], since it becomes an additional constraint solved as follows:

$$\min \frac{1}{2} \left\| A_{tot} \cdot \underline{y}^{reg} - \underline{y} \right\|_2^2 \qquad \text{such that} \qquad \begin{cases} C \cdot \underline{y}^{reg} \le \underline{g} \\ \underline{lb} \le C \cdot \underline{y}^{reg} \le \underline{ub} \end{cases}.$$

where A_{tot} is the composite of fidelity and smoothness matrix, C and $\underline{g}$ are respectively matrix and vector to solve and set the constraint, $\underline{lb}$ and $\underline{ub}$ are the constraints.

Regularize data in 3-D: For the sake of brevity, we will provide a general idea. The steps to follow are similar to what discussed above, except that:

A) **Bilinear interpolation** [101]:
   In short, a bilinear interpolation is performed first by doing a linear interpolation in x, and then again in the y. Note that, although each step is linear in the sampled values, the bilinear interpolation has a quadratic term, i.e., $z(x,y) \approx a_0 + a_1 x + a_2 y + a_3 x y$;

B) **Numerical second derivative for two variables:**
   The second derivatives are calculated similarly as the 2-D case (three-point formula), except that they are calculated separately for both axes, x and y. If we want an output regularized look-up table z of mxn, then the number of the second derivatives[10] is $Num_{2nd} = m(n-2) + n(m-2)$;

The scaling factor Γ, as well as the factor ψ_{smooth}, have the same meaning as in 2-D. Also, in this case, we will have an overdetermined matrix that can be solved and written as follows:

$$z^{reg}(x,y) = \left(A_{tot}^T A_{tot}\right)^{-1} A_{tot}^T \boldsymbol{b}. \tag{4.17}$$

---

[8]In mathematics, particularly matrix theory, a band matrix is a sparse matrix whose non-zero entries are confined to a diagonal band, comprising the main diagonal and zero or more diagonals on either side [98, 99].

[9]This is because we can assume that the resistivity increases with both temperature/current.

[10]For instance, a $5 \wedge 4$ grid has 22 derivative equations. There are $(5-2)$ second derivatives to take within each column, and there are 4 columns. Additionally, there are $(4-2)$ second derivatives that you can take in each row with 5 rows. That gives a total of $3 \cdot 4 + 2 \cdot 5 = 22$.

4.3. Post processing of the overcritical current data with *regularizedNd*

In this section we present the results of constrained regularization data applied to the 3-D case of $\rho_{OC} = \rho_{OC}(I_{OC}, T_{OC})$.

First of all, the experimental measurements are noted as ρ_{OC} while the variables to solve (the regularized data) are ρ_{reg}. In both quantities, a base-10 logarithm ($\log_{10}$) was applied. This can help the solver since a polynomial-like output will be smoother and change slower in log space, reducing the computational efforts and number of iterations of the process described above. To retrieve the actual data will be sufficient to reverse the logarithm.

The regularization of the data and the application of the monotonic constraint is solved through a least-squares curve fitting problems in the form:

$$\min \frac{1}{2} \left\| C \cdot \log_{10}(\rho_{reg}) - \log_{10}(\rho_{OC}) \right\|_2^2 \qquad \text{such that} \qquad \begin{cases} A \cdot \rho_{reg} \le b \\ lb \le A \cdot \rho_{reg} \le ub \end{cases},$$

where C is the composite of fidelity and smoothness matrix, A and b are respectively matrix and vector to solve and set the constraint, lb and ub are the constraints.

In Figure 4.4a we compare the experimental data (red-dots) with a *piecewise hermite polynomial interpolation* (black-dashed), with a *cubic spline interpolation* (green-dashed) and finally with the regularized data (blue-dashed). In the rest of this work of thesis, we indicate the regularized overcritical current data $\rho_{OC}(I_{REBCO}, T)$ as $\rho_{OC}(I, T)$.

The abrupt and non-physical oscillations have been removed, and the algorithm works adequately also when we have a limited amount of information (i.e., for $60\,A \le I_{REBCO} \le 100\,A$. This is different from an extrapolation process, however. Having a small information of data does not imply having a lack of data, i.e., between $60\,A \le I_{REBCO} \le 100\,A$ we do not have data but for the external intervals, $I_{REBCO} \le 60\,A$ and $I_{REBCO} \ge 100\,A$, we have actual data that weigh the choice of the correct spline. This is different for $I_{REBCO} \ge 150\,A$, above which no resistivity data could be retrieved experimentally[11]. As a consequence, we should not rely on the regularized data for such a high current regime. However, the critical current at 77 K and self-field conditions is $I_c = 57\,A$ only (for SP02), and such high current regime ($I_{REBCO} > 2.5\,I_c$) normally it is not explored at all in practical application.

Finally, the resulting regularized look-up tables obtained by applying *regularizedNd* to the overcritical current data are presented in Figure 4.4 (b-f). The regularized look-up tables are presented for samples SP02, SP06, SH05, SU01, and SO02. The scattered red-dots correspond to experimental points obtained with the PCM and post-processed with the UC model (see [56, 57]), while the blue points correspond to critical current measurements.

4.4. Conclusions

The advantages of these techniques are apparent: both overfitting and loss of monotonicity have been addressed. As a result, the reconstructed surface $\rho_{OC}(I, T)$ can be used in numerical simulation. We will demonstrate this possibility in Chapter 6, where we checked the validity of the look-up tables $\rho_{OC}(I, T)$, renamed overcritical current model. Specifically, we compared AC and DC fault current measurements carried out at EPFL and KIT on commercial REBCO samples, with the simulation results obtained with a simple 1-D electrothermal FEM model.

---

[11] As a recall, a lack of data in this region was due to the excessive heating and current sharing occurring during the measurements.
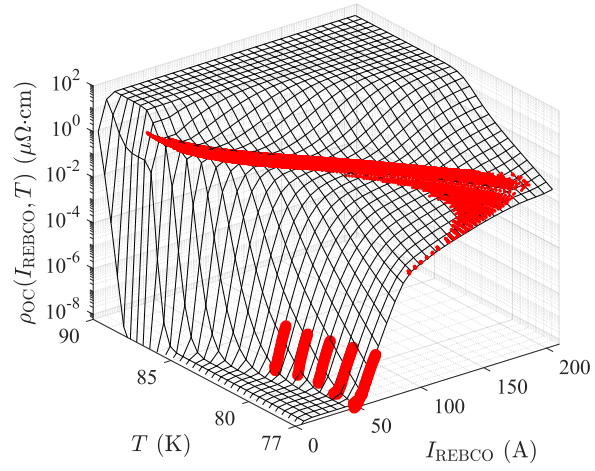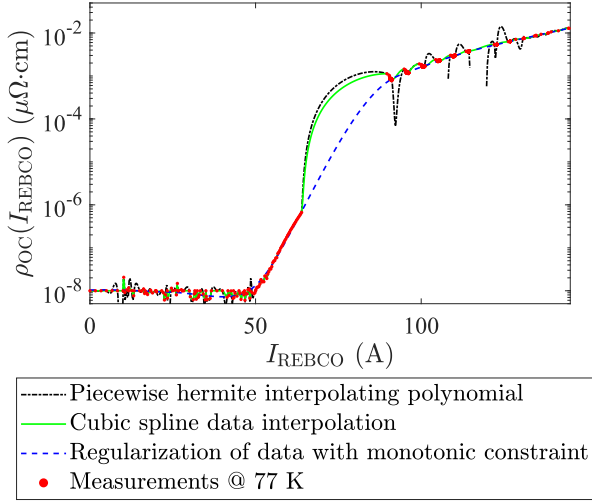
(a) Interpolating vs regularization techniques

(b) SP02 sample
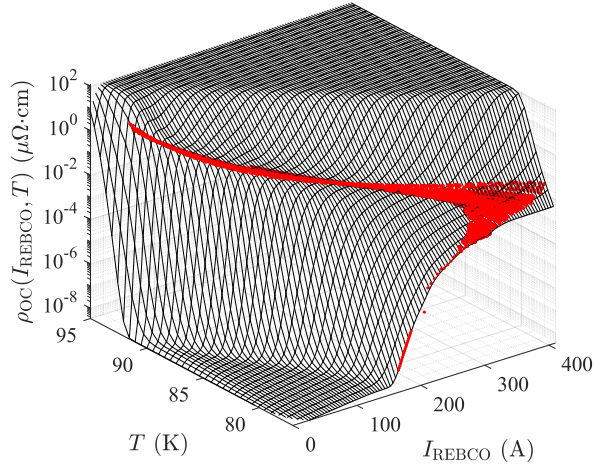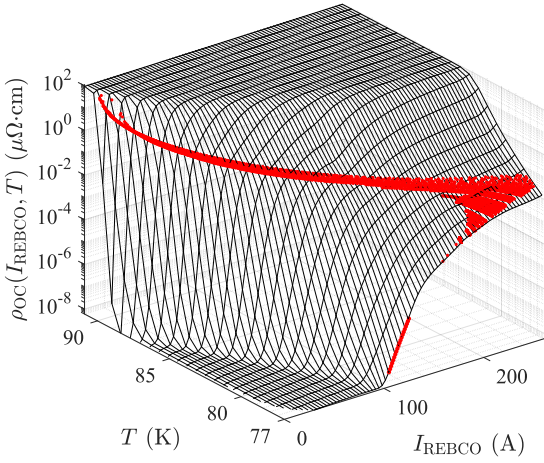
(c) SP06 sample

(d) SH05 sample
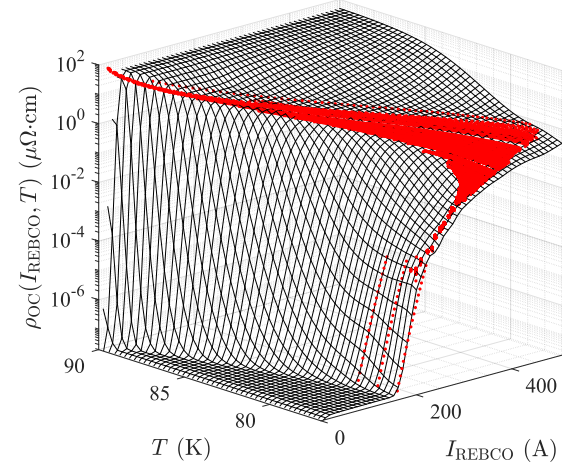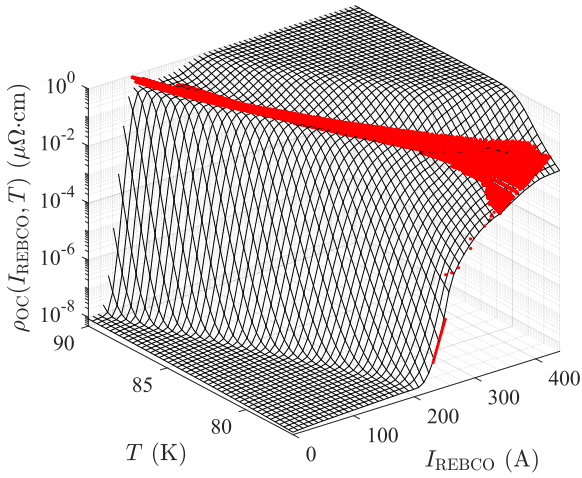
(e) SU01 sample

(f) SO02 sample

Figure 4.4: (a) Comparison between interpolating techniques and regularization on the overcritical data and (b-f) regularized look-up tables for samples. The scattered red-dots correspond to experimental points obtained with the PCM and post-processed with the UC model (see [56, 57]), while the blue points correspond to critical current measurements.

5

The overcritical current model: A modified resistivity relationship for numerical simulations of REBCO tapes

The provocative statement of George Pelham Box recalls Occam's Razor concept and re-proposes the dilemma of choosing between complex models and more straightforward but less representative models. Specifically, in [102], he says that "*[...] following William of Occam he (the scientist) should seek an economical description of natural phenomena*". On the other hand, he also suggests that "*Since all models are wrong the scientist must be alert to what is importantly wrong. It is inappropriate to be concerned about mice when there are tigers abroad*".

In the effort to find the right balance between "*an economical description*" and what is "*importantly wrong*", we present a mathematical expression of the overcritical current model (indicated as $\rho_{\eta\beta}(I,T)$). The $\rho_{\eta\beta}(I,T)$ model is based on measurements performed between $77\,\mathrm{K}$ and $90\,\mathrm{K}$ in self-field conditions for several samples (SP01, SP06, SO01, SO02, SH05 and SU01). We also present the model in external low field conditions for sample SH05 subjected to magnetic field values of $40/60/100/200/300\,\mathrm{mT}$.

The work presented in this chapter will be reported in:

- N. Riva, F. Sirois, C. Lacroix, J. Giguere, F. Grilli, B. Dutoit - *Modified resistivity model of REBCO tapes for numerical simulations in the overcritical current regime*, Under preparation, draft available upon request

5.1. The overcritical current model: a deviation from the power-law

In [103] we presented the overcritical current model $\rho_{\mathrm{OC}}(I_{\mathrm{REBCO}}, T_{\mathrm{REBCO}})$ in form of look-up tables. In the rest of this work, we indicate $(I_{\mathrm{REBCO}}, T_{\mathrm{REBCO}})$ simply as (I,T). The data-set was obtained by applying a regularization [90, 104] of the raw overcritical current data. In this Section, we propose a heuristic model describing the dissipative behavior in the overcritical current regime. The model we propose is based on the *collective pinning* theory reported in [105] and discussed in [42, 43]. The overcritical current model proposed in this work was obtained by fitting the data acquired as described in Chapter 3, and has the following form:

$$\rho_{\mathrm{OC},\eta\beta}^{\mathrm{SC}}(I,T) = \rho_{\min} + \rho_{\mathrm{c}} \exp\left[\eta(T)\cdot\left(1 - \left[\frac{I_{\mathrm{c}}(T)}{I}\right]^{\beta(T)}\right)\right], \tag{5.1}$$

where $\rho_{\min} = 1 \cdot 10^{-17}\,\Omega\,\mathrm{m}$ is added to avoid numerical divergences when the current is 0 A, $\rho_c = 1 \cdot 10^{-15}\,\Omega\,\mathrm{m}$, $I_c(T)$ is the critical current, and $\eta(T)$ and $\beta(T)$ are the temperature-dependent fitting parameters of the model. For sake of simplicity we tried to limit the number of fitting parameters to two[1], namely $\eta(T)$ and $\beta(T)$.

The overall standard deviation of the fitting model was calculated for each temperature as:

$$\sigma_{\eta\beta} = \sqrt{\frac{\mathrm{RMSD}}{\rho_{\mathrm{UC,max}} - \rho_{\mathrm{UC,min}}}},$$

where RMSD is the root-mean-square deviation, and $\rho_{\mathrm{UC,max}}$ and $\rho_{\mathrm{UC,min}}$ are the maximum and minimum values of resistivity obtained from the UC model for a selected temperature (e.g. 78 K). The quantity $\rho_{\mathrm{UC,max}} - \rho_{\mathrm{UC,min}}$ is the range of data used to normalize the RMSD [93]. The values of the standard deviation $\sigma_{\eta\beta}$ range between 1 % to 12 %.

For the purpose of comparison, we also use the power-law model with a temperature dependent critical current $I_c(T)$. The power-law relation is written as follows:

$$\rho_{\mathrm{PLW}}^{\mathrm{SC}}(I, T) = \rho_{\min} + \frac{\Sigma \cdot E_c}{I_c(T)} \left(\frac{|I|}{I_c(T)} \right)^{n-1}, \tag{5.2}$$

where Σ is the cross section of the REBCO layer, $E_c = 1\,\mu\mathrm{V\,cm}^{-1}$ is the electric field criterion and n is the constant power-law exponent. The critical current value $I_c(T)$ for both models decreases linearly with the temperature and has a relationship of the form:

$$I_c(T) = I_{c,77\,\mathrm{K}} \cdot \frac{T_c - T}{T_c - 77\,\mathrm{K}}, \tag{5.3}$$

where $I_{c,77\,\mathrm{K}}$ is the critical current at 77 K and self-field conditions, and T_c the critical temperature. Finally, the normal state resistivity of REBCO $\rho_{\mathrm{NS}}(T)$ is added in parallel to both models [21], i.e.:

$$\rho_k = \frac{\rho_k^{\mathrm{SC}}(I, T) \cdot \rho_{\mathrm{NS}}(T)}{\rho_k^{\mathrm{SC}}(I, T) + \rho_{\mathrm{NS}}(T)}, \tag{5.4}$$

where k indicates the two models, namely the power-law model (ρ_{PWL}) and the overcritical current model ($\rho_{\eta\beta}$). The temperature dependence of the normal-state resistivity of REBCO is modeled with a simple linear relationship, i.e.:

$$\rho_{\mathrm{NS}}(T) = \rho_{T_c} + \alpha \cdot (T - T_c),$$

where ρ_{T_c} ranges from $30\,\mu\Omega\,\mathrm{cm}$ to $100\,\mu\Omega\,\mathrm{cm}$ and $\alpha = 0.47\,\mu\Omega\,\mathrm{cm\,K}^{-1}$ [66, 106].

In the remaining part of this Section, we compare the overcritical current model $\rho_{\eta\beta}(I, T)$ with the power-law model $\rho_{\mathrm{PWL}}(I, T)$, while in the next Section we provide a detailed discussion of the fitting parameters $\eta(T)$ and $\beta(T)$, as well an analysis of the continuity of Equation (5.1).

5.1.1. Self-field conditions

Since the qualitative results remain the same for all samples, we report the measurements performed in self-field conditions for samples SP02 and SO01 only. In Figure 5.1 (left) we present the raw overcritical current data (red-scattered dots) extracted with the UC model (see [56, 57]) and the resistivity surface obtained with the $\rho_{\eta\beta}(I, T)$ model. All the measurements start from 77 K, the temperature of the liquid nitrogen bath, where the samples were immersed during the characterization. The maximum value of resistivity ranges from $30\,\mu\Omega\,\mathrm{cm}^{-1}$ to $100\,\mu\Omega\,\mathrm{cm}^{-1}$ at corresponding temperatures varying from 88 K to 92 K. These values represent

---

[1]According to John von Neumann *"With four parameters I can fit an elephant, with five I can make him wiggle his trunk".*

the normal state resistivity $\rho_{\text{NS}}(90\,\text{K})$ (in agreement with [66, 106]) and the critical temperature T_c respectively (in agreement with [28]). In Figure 5.1 (right) we compare, for selected temperatures, the raw overcritical current data (scattered black-dots) with the overcritical current model $\rho_{\eta\beta}(I, T)$ (dashed lines), and with the power-law model $\rho_{\text{PWL}}(I, T)$ (continuous lines). The difference between the experimental overcritical current data (thus the $\rho_{\eta\beta}(I, T)$ model) and the ρ_{PWL} is remarkable. The data presents a marked softening of the n-value for $I_{\text{REBCO}} > I_c$. Such results are in line and corroborate the work done by *Falorio et al.* [42, 43], where a similar deviation from power-law model was observed for four etched samples and across a very large range of temperature (15 K to 86 K).
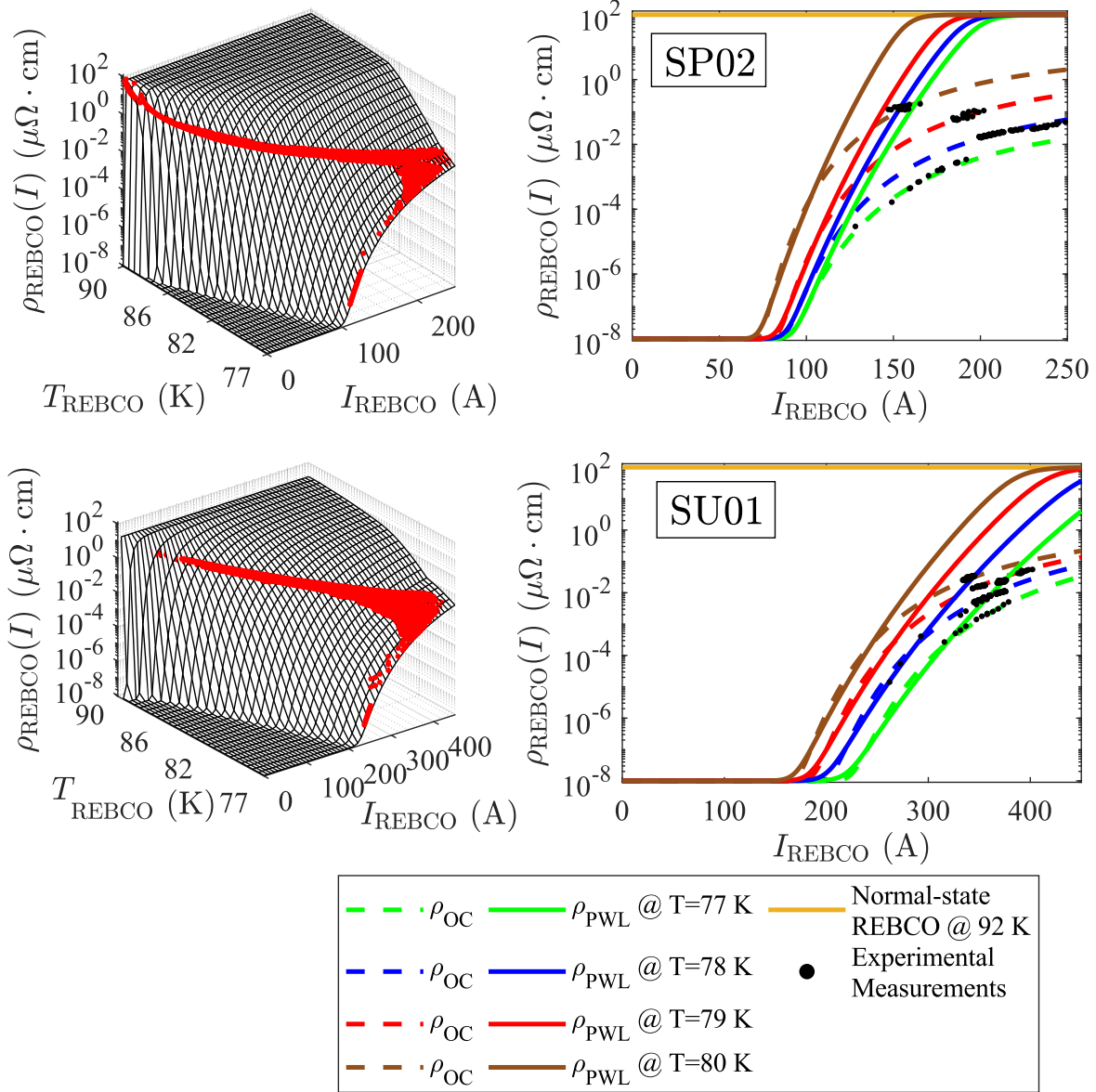
Figure 5.1: Results for samples SP01 and SO01. (left) Resistivity surfaces obtained from the $\rho_{\eta\beta}(I, T)$ model. The scattered dots correspond to experimental points obtained using PCM and post-treated using the UC model. (right) Comparison between the experimental measurements (black dots), the $\rho_{\eta\beta}(I, T)$ model (dashed line) and $\rho_{\text{PWL}}(I, T)$ (continuous line) for selected temperatures.

5.1.2. External field conditions (SH05 sample)

The SH05 samples' measurements were performed in self-field conditions and for the selected magnetic field values of 40/60/100/200/300 mT. The magnetic field orientation was fixed; the magnetic field was applied perpendicularly to the $a-b$ plane (i.e., $B_{\perp,a-b}$, the flat face of the tape). This choice stems from the fact that the utilized data-analysis procedure outlined in [56, 57] is very time-consuming, and for this work, we limited our analysis to $B_{\perp,a-b}$ only[2]. In Figure 5.2 we compare the raw overcritical current data (scattered black-dots) with the overcritical current model $\rho_{\eta\beta}(I, T)$ (dashed lines), and with the power-law model $\rho_{\text{PWL}}(I, T)$ (continuous lines) for selected temperatures and increasing level of field amplitude. Consistently with the results in self-field conditions, the overcritical current model presents a softer n-value for $I_{\text{REBCO}} > I_{\text{c}}$.

Not surprisingly, both the power-law and overcritical current models shift toward left (lower current) with an increasing field due to the reduction of the critical current. In agreement with [16, 49], the critical current value decreases very quickly from self-field up to 60 mT, while it is followed by a reduction more gentle above 60 mT. The critical current value decreases linearly with the temperature as in Equation (5.3) while the n-value decreases with increasing field, going from 28 in self-field conditions to about 15 with an externally applied field of 300 mT (in good agreement with [16]). The overall standard deviation $\sigma_{\eta\beta}$ of the fitting model ranges between 1 % to 10 %.

---

[2]The computing time of the UC models per pulse ranges from 30 s to 200 s per pulse. When analyzing a large number of pulses (up to 100), it is desirable to reduce this calculation time. In Appendix A.4, a reduction to 1-D has been explored. We show that the quantities of interest (current sharing and temperature) calculated with the 1-D approach are equivalent to those calculated with the 2-D approach, making the 1-D approach a valid alternative. A further improvement of the computational time can be achieved through an analytical formula. It is possible to solve the Heat Equation in 2-D or 1-D using the Green's Function, obtaining an analytic formulation of the UC model.
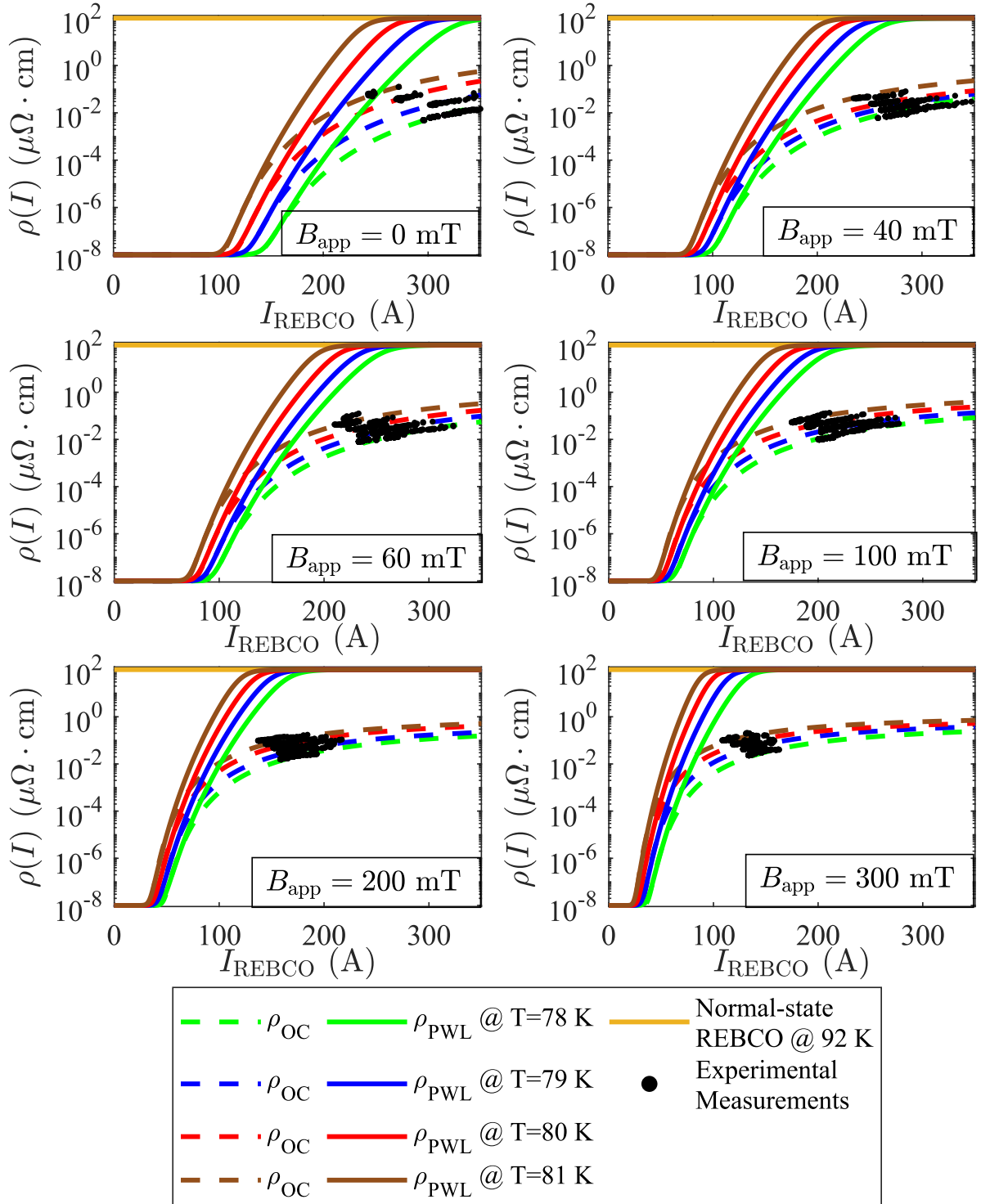
Figure 5.2: Results for the SH05 sample. Comparison between power-law model ($\rho_{\mathrm{PWL}}(I, T)$ continuous line), overcritical resistivity model ($\rho_{\eta\beta}(I, T)$ dashed line) and experimental measurements (black dots) for selected temperatures and increasing applied magnetic field.

5.2. Analysis of the fit-parameters

In this Section we discuss the parameters $\eta(T)$ and $\beta(T)$ constituting the $\rho_{\eta\beta}(I, T)$ model. After that, we discuss the data's scaling properties when represented in terms of electric field vs. current $(E - I)$.

5.2.1. Fit-parameters in self-field conditions

In Figure 5.3 we present the temperature dependence of the fitting parameters $\eta(T)$ and $\beta(T)$ for all samples in self-field condition. Since the fitting parameters for all samples show a common trend, we can fit a piece-wise polynomial function of $2nd$ and $1st$-degree on $\eta(T)$ and $\beta(T)$ respectively. The temperature-dependence of $\eta(T)$ for samples SO01 and SH05 remains
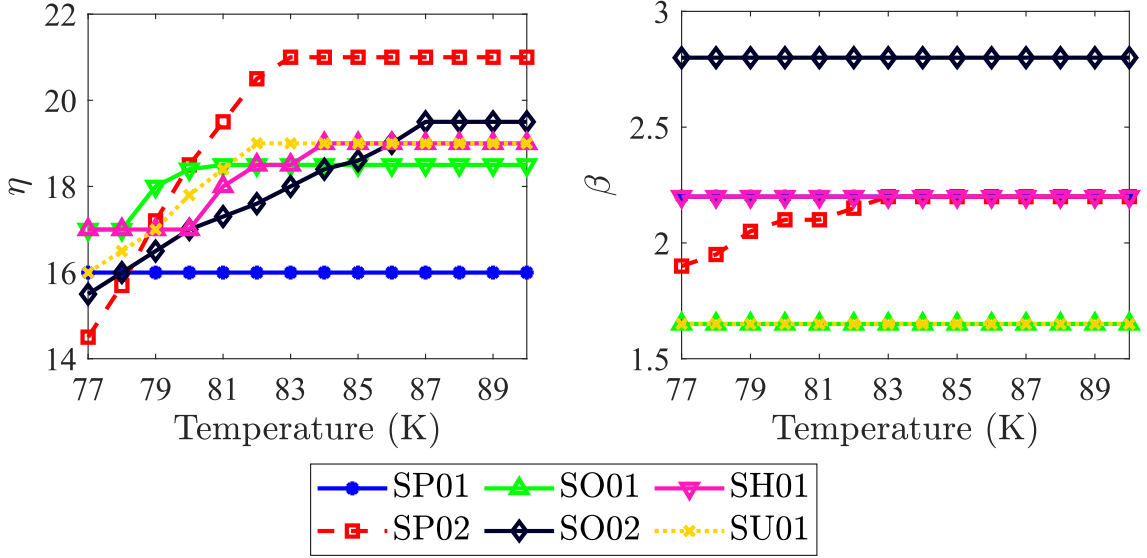
Figure 5.3: Temperature dependence and piece-wise polynomial relationships of the fitting parameters (left) η and (right) β of the $\rho_{\eta\beta}(I, T)$ model for samples SP01, SP02, SO01 and SH05.

constant until a specific value of temperature, then for all samples, it increases in a not-strictly-monotonic way and eventually reaches a constant plateau. Sample SP01, on the contrary, presents a constant η within all the temperature range. The parameter $\beta(T)$ has been kept as constant as possible with the temperature (for the sake of simplicity). This operation was possible for most of the samples between $77\,\text{K}$ and $90\,\text{K}$, except for sample SP02.
The piece-wise polynomial relationship for $\eta(T)$ can be written as follows:

$$\eta(T) = \begin{cases} \eta_{\text{pt},1} & 77 \leq T < T_{\text{pt},1} \\ \eta_2(T - T_{\text{pt},1})^2 + \eta_1(T - T_{\text{pt},1}) + \eta_0 & T_{\text{pt},1} \leq T < T_{\text{pt},2} \\ \eta_{\text{pt},2} & T \geq T_{\text{pt},2}, \end{cases} \qquad (5.5)$$

where T is the temperature of the REBCO material, $T_{\text{pt},1}$ and $T_{\text{pt},2}$ are the threshold temperatures below and above which η remains constant, and η_i (with $i = 0, 1, 2$) are the polynomial coefficients. The parameters $\eta_{\text{pt},1}$ and $\eta_{\text{pt},2}$ are determined by imposing a continuity condition such that $\eta(T)_{T \to T_{\text{pt},i^-}} = \eta(T)_{T \to T_{\text{pt},i^+}}$.
The piece-wise polynomial relationship for $\beta(T)$ is the following:

$$\beta(T) = \begin{cases} \beta_1(T - T_0) + \beta_0 & 77 \leq T < T_{\text{pt}} \\ \beta_{\text{pt}} & T \geq T_{\text{pt}}, \end{cases} \qquad (5.6)$$

where T is the temperature of the REBCO material, T_0 is the temperature of the liquid nitrogen bath, T_{pt} is the threshold temperature above which β remains constant, and β_i (with $i = 0, 1$) are the polynomial coefficients. The parameter β_{pt} is determined by imposing a continuity condition such that $\beta(T)_{T \to T_{pt^-}} = \beta(T)_{T \to T_{pt^+}}$.

Table 5.1 contains a summary of the fit parameters (η and β), and the standard deviation in percentage ($\sigma_{\eta,T}$ and $\sigma_{\beta,T}$) for all samples. For sample SP02 it was attempted a linear fit too. This further simplifies a practical implementation of the $\rho_{\eta\beta}(I, T)$ model.

						Fitting parameters						
Sample	$\eta_{pt,1}$ [1]	η_2 [K^{-2}]	η_1 [K^{-1}]	η_0 [1]	$\eta_{pt,2}$ [1]	$\sigma_{\eta,T}$ [%]	β_1 [K^{-1}]	β_0 [1]	β_{pt} [1]	$\sigma_{\beta,T}$ [%]	$T_{pt,1}$ [K]	$T_{pt,2}$ [K]
SP01	-	-	-	16	16	-	-	-	2.2	-	-	-
SP02	-	-0.087	1.233	16.23	23.65	2	0.048	1.92	2.2	0.1	-	83
SP02$_{lin}$	-	-	1.1233	16.23	23.65	11.5	0.048	1.92	2.2	0.1	-	83
S001	17	-0.225	1.615	15.63	18.5	0.5	-	-	1.65	-	78	81
S002	-	-	0.38	15.68	19.48	2	-	-	2.80	-	78	81
SH01	-	-	0.615	15.91	18.9	0.7	-	-	1.65	-	-	82
SU01	17.03	-0.1364	1.036	17.03	19	0.5	-	-	2.2	-	80	84

Table 5.1: Fitting parameters of the $\rho_{\eta\beta}(I, T)$ model and standard deviation values in percentage.

Having provided the mathematical relation of $\eta(T)$ and $\beta(T)$ with Equations (5.5)-(5.6), it is possible to analyze the continuity of Equation (5.1). We need to assess if Equation (5.1) is continuous in the space explored by the variables (I, T), i.e. $\rho_{\eta\beta} \in C^0([I, T])$.

Since $T \in ([77, T_{fin}])$ and $I \in ([0^+, I_{fin}])$, where both T_{fin} and I_{fin} are a finite values, the only discontinuity may occur in $I = 0^+$ A, $I_c(T) = 0^+$ A or $I = I_c(T) = 0^+$ A. The limit of two variables approaching the potential discontinuity is written as follows:

$$\lim_{(I,T) \to (0^+, T_{fin})} \rho_{min} + \rho_c \exp\left[\eta(T_{fin}) \cdot \left(1 - \left[\frac{I_c(T_{fin})}{0^+} \right]^{\beta(T_{fin})} \right) \right]. \tag{5.7}$$

Both $\eta(T_{fin})$ and $\beta(T_{fin})$ are finite and non-zero. If $I_c(T_{fin}) > 0$ A, the two-variable limit tends to a finite value. If $I_c(T_{fin}) = 0$ A the limit presents an indeterminate form (0/0), and leads to a potential unbounded behavior of the function. Although such problem can be addressed by tools such as a multi-variable Taylor expansion (or an application of the multi-variable Hôpital's Rule), we need to remember that also the power-law model present a similar problem.

Moreover, $I_c = 0$ only for $T \geq T_c$. Therefore this kind of issue can be addressed by imposing that for $T \geq T_c$ the REBCO is in its normal state, and thus $\rho_{REBCO} = \rho_{NS}(T)$. Other strategies involve the addition of a negligible perturbation such that the current in the circuit (or the applied voltage) is never identically zero:

$$I(t) \longrightarrow I(t) + 0.01 \, \text{A}.$$

The physical interpretation of this operation can be though as the addition of a small "shunt" resistor that maintains a minimum current flow in the REBCO layer, and thus, avoids numerical issues. This strategy, however, is prone to other physical errors and not mathematically rigorous.

5.2.2. Fit-parameters in external field

For sample SH05 we present the fitting parameters η and β as a function of both temperature and applied magnetic field (Figure 5.4). The overcritical current regime's behavior in mag-
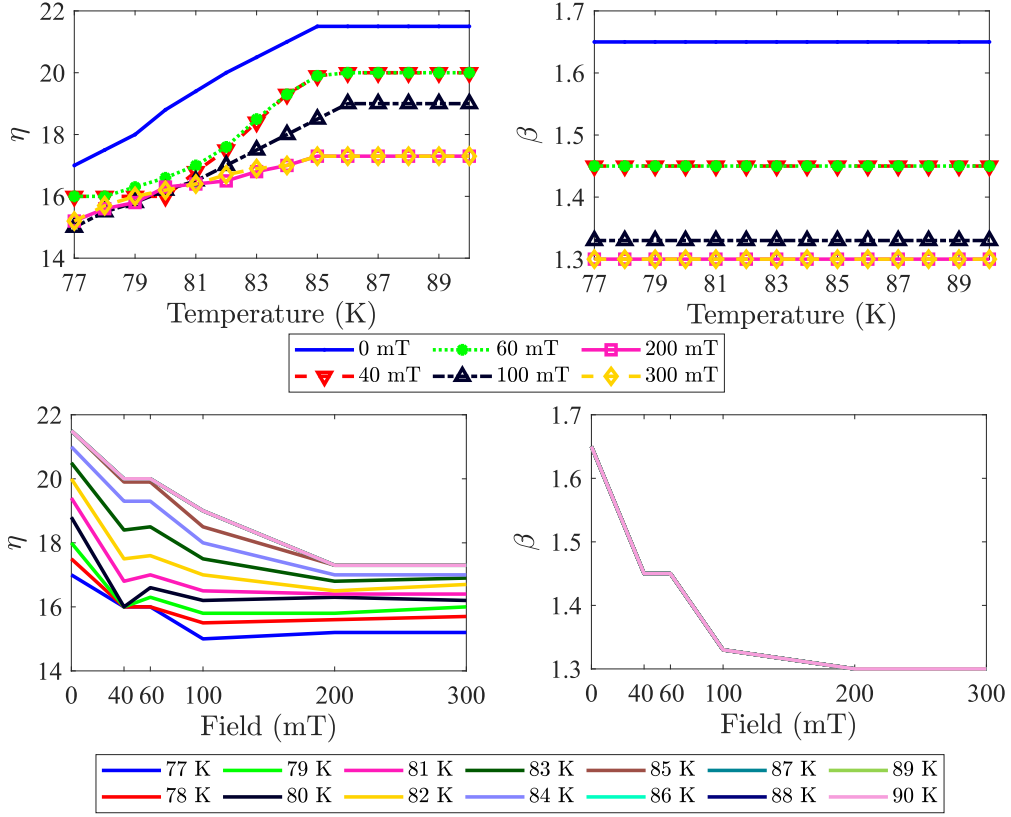
Figure 5.4: Temperature and magnetic field dependence of the fitting parameters (left) η and (right) β of the $\rho_{\eta\beta}(I, T)$ model for sample SH05.

netic field was studied on a limited number of characterized samples (only SH05). Further data collection would be needed to provide a mathematical function for $\eta(B)$ and $\beta(B)$. For this reason, we limit our work to a qualitative analysis of the fitting parameters.

The parameter $\eta(B)$ increases with the temperature (non-strictly-monotonic) while it decreases with the applied field. The parameter $\beta(B)$ is constant within the entire temperature range, however it decreases with the applied field. Due to experimental constraints, the data was collected in a limited magnetic field-range. However, superconducting properties like the critical current show a very quick decrease from self-field up to 60 mT, which is then followed by a more gentle drop. Similarly, we can speculate that both parameters $\eta(B)$ and $\beta(B)$ will not drastically change for a higher applied magnetic field. A possible result, which is in agreement with the results observed for flux-flow measurements at high current and magnetic field [11, 41, 44], is that the the resistivity curve shape will become flatter and less sharp for an increasing applied magnetic field until the measured resistivity $\rho(I)$ will present an independent-I plateau. Despite the limited data collected, our findings sustain the previous observations (a deviation from the power-law) in the case of an applied field.
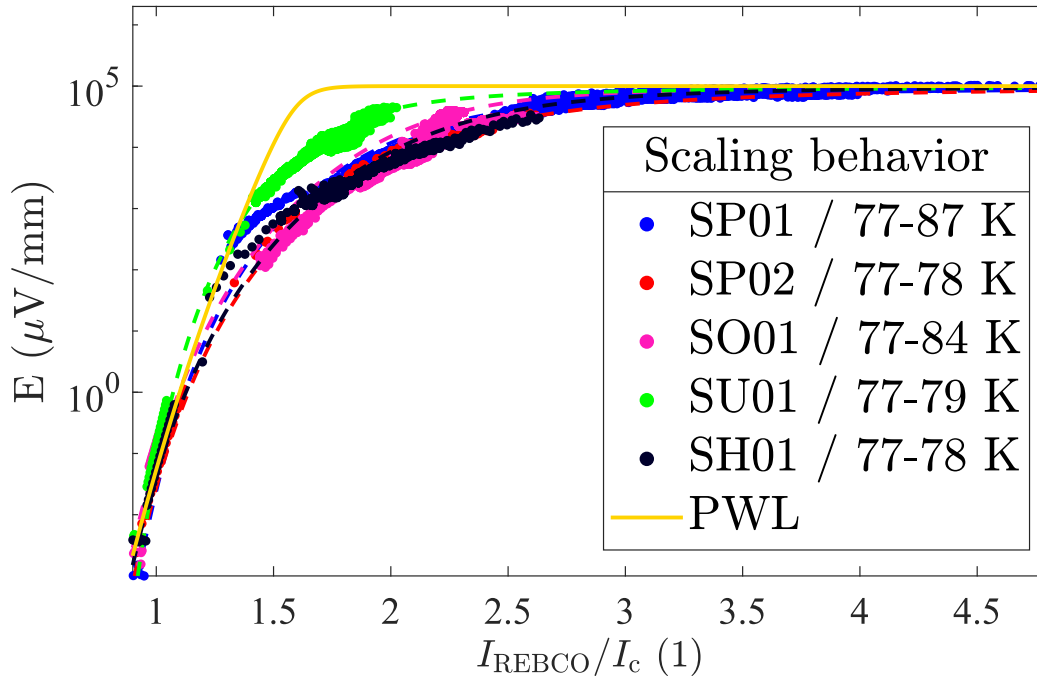
Figure 5.5: Scaling behavior of the overcritical current data for different manufactured samples.

5.3. A common scaling behavior

Finally, very intriguing results can be obtained when plotting the experimental data showed above in terms of the electric field, and as a function of the I_{REBCO} scaled by $I_c(T)$. The electric field is obtained from the relation $E = \rho_{\mathrm{UC}} \frac{I_{\mathrm{UC}}}{\Sigma}$, where ρ_{UC} and I_{UC} are the data obtained with the UC model [56, 57], and Σ is the cross-section of the superconductor. The results for samples SP01, SP02, SO01, SU01, and SH05 at different temperatures range (indicated in the legend) are presented in Figure 5.5.

The extracted overcritical current data represented as $E - I/I_c$ presents a scaling behavior, and thus, a common trend is observed in a specific range of temperature, regardless of the manufacturer. Our results corroborate previous findings presented in [42, 43], where this sort of scaling behavior was observed. However, while in Figure 5.5 the scaling behavior occurs in a broad temperature range for sample SP01 (i.e., 77 K to 87 K), for others samples, the scaling properties are limited to a much smaller temperature range (i.e., 77 K to 78 K). When a broader range of temperature is plotted for such samples, the common trend, and thus the scaling properties, disappear.

To clarify the origin of the differences in the scaling properties, one should consider the various manufacturing techniques that each company uses. Companies such as SuperPower, SuperOx and SuNAM all rely on Ion Beam Assisted Deposition (IBAD) [107] to generate a biaxially textured template, whilst the epitaxial REBCO film is grown by metal-organic chemical vapor deposition (MOCVD) [108] for SuperPower, by pulsed laser deposition (PLD) [109–111] for SuperOX and ShangHai Superconductor, and by reactive co-evaporation (RCE) for SuNAM [112, 113].

However, the most significant difference, rather than among other manufacturers, is observed between sample SP01 and all the other samples. For SP01 we observe a scaling behavior over a larger temperature range with respect to the other samples. Interestingly, the year of manufacturing of SP01 is 2009 while for the remaining samples are 2018/2019 (both SP01 and

SP02 were manufactured by SuperPower). Although such findings are based on a limited number of characterized samples, we can speculate that the reason for this difference lies in the advances in manufacturing achieved by SuperPower between 2009 and 2019. In 2012, in the framework of the project *Quadrupling critical current in HTS superconductor wires* [114], ARPA-E funded two teams[3] to develop advanced HTS magnet wire with high critical current. Eventually, a critical current enhancement was achieved by introducing defects into the REBCO thin-film [115]. As of April 2016, the UH/SuperPower team generated several scientific publications [114] and patents demonstrating the success of this project.

This remarkable improvement in terms of high critical current, and thus pinning scenario, may play a role in the difference when comparing samples recently manufactured with older samples.

A physical interpretation of the data presented and the underlying physics of the overcritical current model goes beyond the scope of this work (which instead aims to provide a model for numerical simulations), and these findings need to be interpreted with caution. The interested reader can refer to the research carried out by *Falorio et al.* [42, 43]. In this work, a statistical model [116] was used to correlate the overcritical current dissipation described using a collective pinning model to the flux-flow resistance of Bardeen-Stephen [17]. Further evidence of the flux-flow resistance was provided by *Kunchur et al.* [41], where the authors reported that, at sufficiently large current density resulting in rapid displacement of the vortex, the measured resistivity $\rho(J)$ had independent-J plateau (i.e., Ohmic behavior). Such measurements were performed on over three decades of the applied magnetic field ($B/B_{c2}(T) = 0.001$ to 1), and the behavior was found to follow the Bardeen-Stephen model and consistent with the values in literature [19, 117].

5.4. Conclusions

The advantage of the $\rho_{\eta\beta}(I, T)$ model, with respect to the look-up tables obtained with the regularization method in Chapter 4 is apparent; the model can be implemented in a model without the need of the raw overcritical data or the regularization code. This model can be used in numerical simulations for scenarios where the current sharing plays an important role such as during a hotspot in superconducting devices, in a non-insulated coil, during pulsed field magnetization, or in Superconducting Fault Current Limiters.

In the next Chapter we will provide the experimental validation of both overcritical regularized look-up tables ($\rho_{OC}(I, T)$) and the overcritical current model ($\rho_{\eta\beta}(I, T)$).

---

[3]The teams were Brookhaven National Lab (BNL) with American Superconductor AMSC, and the University of Houston (UH) with SuperPower respectively.

6

Impact of the overcritical current curves on SFCL modeling

In this Chapter, we evaluate to what extent using the overcritical current model instead of the power-law model impacts the electrothermal response of a REBCO tape. For this purpose, we used the overcritical current model developed in Chapter 4 and Chapter 5 to study the simple case of a superconducting fault current limiter (SFCL).
The work presented in this Chapter is also reported in:

- N. Riva, F. Grilli, F. Sirois, B. Dutoit, C. Lacroix, W.B.T. de Sousa - *Resistivity of HTS tapes in overcritical current regime: impact on Superconducting Fault Current Limiter modeling*, Superconductor Science and Technology, (Link to publication)

- N. Riva, F. Grilli, B. Dutoit - *A stand-alone executable App to teach about superconductors for power applications: The Superconducting Fault Current Limiter*, Under preparation - Draft and App available upon request

6.1. Self-consistency check of the overcritical resistivity model

We first describe a FEM model implemented in COMSOL Multiphysics, used to verify the overcritical resistivity model's consistency with both AC and DC fault measurements performed on SuperPower samples. The same FEM model is used to evaluate the SFCL behavior in typical AC and DC fault current limitation scenarios and the impact of using the overcritical current resistivity model instead of the widely used power-law $\rho_{\mathrm{PWL}}(I, T)$.

6.1.1. Numerical models

In order to verify the correctness of the overcritical resistivity model obtained above, and also to study the behavior of REBCO tapes in various quench scenarios, we used a 1-D thermal finite element model (temperature variation across the thickness of the tape) coupled with an electric circuit model (current sharing between the various layers of the tape).
We assume that the simulated tape's electrical and thermal properties do not vary significantly along its width and length. This means that the simulated tape has uniform properties (width and length) and that with this simple model, one cannot investigate the impact of defects and hot-spots on the RSFCL behavior. The model is nevertheless sufficiently accurate
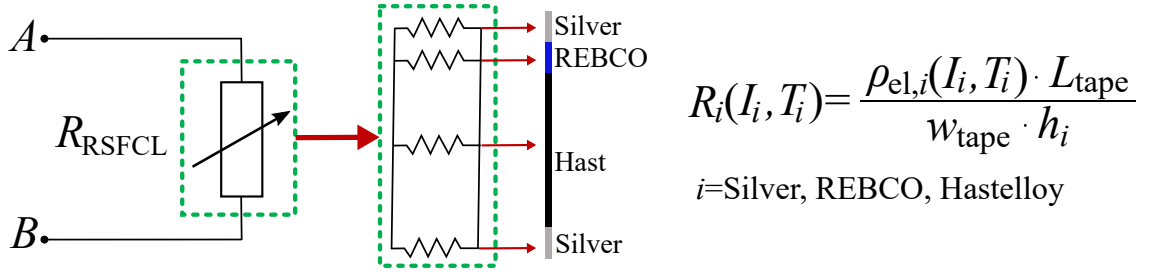
Figure 6.1: Schematic representation of the electrical REBCO tape model implemented in COMSOL Multiphysics.

to study short samples. The equivalent electrical model of the RSFCL is represented in Figure 6.1.

The RSFCL is modeled as a set of resistors in parallel, representing the stabilizer (in this case silver), the Hastelloy and the REBCO layers, respectively. Each resistor $R_i(I_i, T_i)$ is defined by the electrical resistivity $\rho_{\text{el},i}(I_i, T_i)$, the length of the the tape L_{tape}, its width w_{tape} and the thickness of the single layer h_i, where the subscript i stands for the layer of the tape (i.e. silver, REBCO, etc.). A voltage V_{app} or a current I_{app} can be applied across the tape terminals A and B. The model is implemented in COMSOL Multiphysics. The heat equation, modeled in the Heat Transfer Module (ht), is coupled with the equivalent circuit model of the RSFCL, modeled in the Electric Circuit Module (cir) [58]. The heat equation is solved on each 1-D domain, schematically represented in Figure 6.1, and reads as follows:

$$\rho_{\text{mass},i}(T_i) C_{\text{p},i}(T_i) \frac{\partial T_i}{\partial t} + \frac{\partial}{\partial x}\left(-k_i(T_i)\frac{\partial T_i}{\partial x}\right) = \frac{R_i(I_i, T_i) \cdot I_i^2}{\Omega_i} - h_{\text{LN}_2} \cdot (T_i - T_0)\Big|_{\partial\Omega}, \qquad (6.1)$$

where on the left side we have the mass density $\rho_{\text{mass},i}(T_i)$, the specific heat capacity $C_{\text{p},i}(T_i)$ and the thermal conductivity $k_i(T_i)$. On the right side of equation, there is the heat source term and a cooling term. The heat source comes from Joule's first law, i.e. $P = R_i \cdot I_i^2/\Omega_i$, and the volume of the conductor is noted as $\Omega_i = w_{\text{tape}} \cdot L_{\text{tape}} \cdot h_i$. The heat exchange with the liquid nitrogen is taken into account applying a boundary condition applied only on the top and the bottom layers of the tape (silver surfaces), indicated by $\partial\Omega$. In Equation (6.1), the heat transfer coefficient $h_{\text{LN}_2}(T_i - T_0)$ is a function of the temperature [9].

For better readability, the temperature dependence of $h_{\text{LN}_2}(T_i - T_0)$ is omitted and the transfer coefficient is simply written as h_{LN_2}. The temperature dependence of all the thermal and electrical material properties are taken into account. For R_{REBCO}, we consider the dependence of its resistivity with temperature and current using the overcritical resistivity models introduced above. The overcritical current model was implemented with both look-up tables and the mathematical expression. For comparison, we also use a power-law model with a temperature-dependent critical current $I_{\text{c}}(T)$. We write the power-law as follows:

$$\rho_{\text{PLW}}^{\text{SC}}(I, T) = \frac{E_{\text{c}}}{I_{\text{c}}(T)}\left(\frac{|I|}{I_{\text{c}}(T)}\right)^{n-1},$$

where $E_{\text{c}} = 1\,\mu\text{V}\,\text{cm}^{-1}$ is the electric field criterion, n is the power-law exponent and $I_{\text{c}}(T)$ is given by a relationship of the form:

$$I_{\text{c}}(T) = I_{\text{c},77\,\text{K}} \cdot \frac{T_{\text{c}} - T}{T_{\text{c}} - 77\,\text{K}}. \qquad (6.2)$$

The normal state resistivity of REBCO $\rho_{NS}(T)$ is added in parallel to both models [21], i.e.:

$$\rho_k = \frac{\rho_k^{SC}(I,T) \cdot \rho_{NS}(T)}{\rho_k^{SC}(I,T) + \rho_{NS}(T)}, \tag{6.3}$$

where k indicates the two models, namely the power-law model (ρ_{PWL}) and the overcritical current model ($\rho_{\eta\beta}$). The temperature dependence of the normal-state resistivity of REBCO is modeled with a simple linear relationship, i.e.:

$$\rho_{NS}(T) = \rho_{T_c} + \alpha \cdot (T - T_c),$$

where ρ_{T_c} ranges from $30\,\mu\Omega\,\text{cm}$ to $100\,\mu\Omega\,\text{cm}$ and $\alpha = 0.47\,\mu\Omega\,\text{cm}\,\text{K}^{-1}$ [66, 106].

Finally, as a side note, the model described above was implemented in a COMSOL-Java App and was used as a demonstrating exercise for the 2019 course *Superconducting Materials for Energy Applications* at KIT. With a simulation App we can incorporate complex concepts behind a user-friendly interface, without the students having to deal with unnecessary jargon. The potential benefits are beyond this: the development of Apps of this sort leverages the power of easy accessible modeling and simulation with the aim to arouse interest in students or generate valuable business tools for companies.

We furthered the App's development, creating a license-free executable for all the OS, downloadable from the HTS Modeling Website. A detailed description of the App can be found in Appendix A.5 and will be published in the future [118].
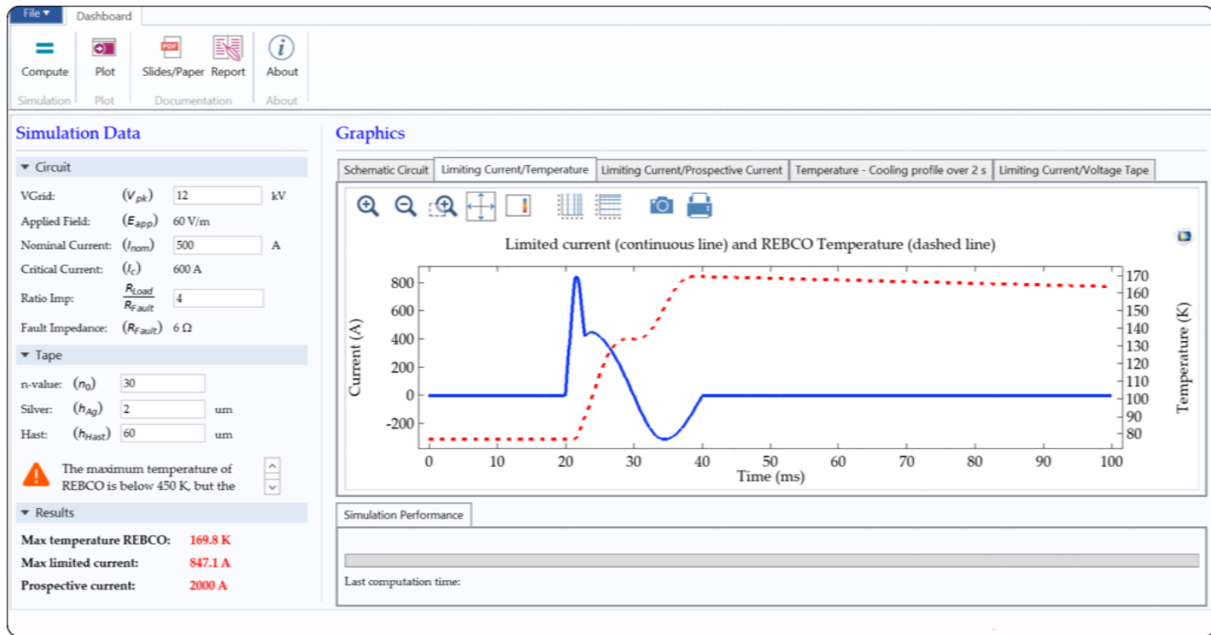
Figure 6.2: Snapshot of the App.

6.1.2. Fault current measurements

Fault current measurements in a liquid nitrogen bath (77 K) were performed at KIT (AC faults) and EPFL (DC faults) on SuperPower samples coming from the same batch of the SP06 sample. The overcritical resistivity look-up tables ρ_{OC} were implemented using the regularized surface of sample SP06 (Chapter 4, Figure 4.4). The mathematical expression of the overcritical current model $\rho_{\eta\beta}(I, T)$ was implemented for sample SP06 as discussed in Section 5.2, and according to the parameters $\eta(T)$ and $\beta(T)$ in Table 5.1. We used the linear representation of $\eta(T)$ for sample SP02 reported in Table 5.1, at which we will refer as $\eta_{1st}(T)$.

Simulations vs. measurements (AC Measurements - KIT)

AC fault current measurements ranging from $1.4\,I_c$ to $5\,I_c$ and in a liquid nitrogen bath (77 K) were performed on a tape called SP06b at KIT. The SP06b sample was 30 cm long, obtained from the same spool as the SP06 sample (1.1 µm of surrounding silver stabilizer). The critical current of SP06b was $I_c = 118\,$A at 77 K in self-field conditions. The measurements were carried

(a)

(b)
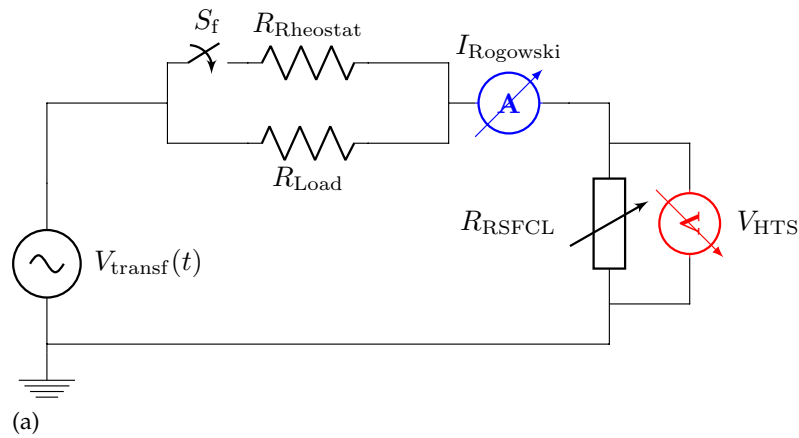
Figure 6.3: (a) Schematic representation of the experimental setups used and (b) picture of the sample holder and experimental setup utilized at KIT.

out with the help and collaboration of Dr. Kudymow and Dr. Batista De Sousa. The experimental setup[1] is schematically represented in Figure 6.3a. A low impedance transformer provided the voltage source V_{transf}, while the fault resistance value of $R_{Rheostat}$ was controlled

---

[1] The interested reader can refer to [119, 120] for a detailed description of the experimental setup.
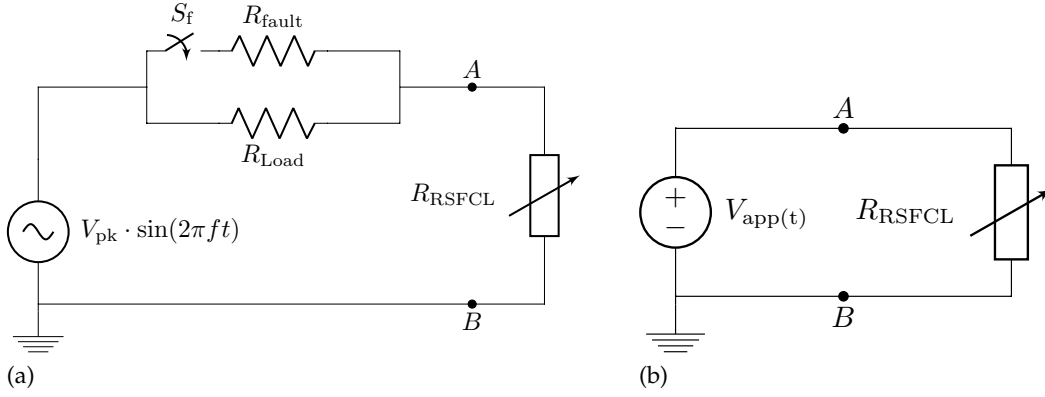
Figure 6.4: Signal excitations used in the model of Figure 6.1 to check the self-consistency of the overcritical resistivity model for (a) AC fault measurements (KIT), and (b) DC fault current measurements (EPFL).

using a rheostat. We measured the current in the circuit I_{Rogowski} with a Rogowski coil (indicated with a white arrow in Figure 6.3a). Finally, we measured the voltage V_{HTS} with the help of voltage taps installed on the sample, separated by a distance of 20 cm each. The voltage taps were located on the top of the copper block, as shown in Figure 6.3a.

The 1-D thermal + circuit model is rather flexible, as both voltage or current excitation can be applied across the tape terminals A and B in Figure 6.1. The electric-circuit used for self-consistency in case of AC fault check is illustrated in Figure 6.4b. The current limitations tests, for increasing prospective fault, are presented in Figure 6.5. In Figure 6.5 (a) the prospective current was $I_{\text{peak}} = 1.52\, I_c = 168\,\text{A}$, while the limited peak current was of $I_{\text{peak}} = 162\,\text{A}$. In Figure 6.5 (e) the prospective current was $I_{\text{peak}} = 3.70\, I_c = 406\,\text{A}$, while the limited peak current was of $I_{\text{peak}} = 189\,\text{A}$. It is noteworthy to observe that the tape worked as a very good SFCL.

For comparison, we also calculated the current with the power-law model using both a constant and temperature-dependent n-value. A value of $n_0 = 30$ was sued for the constant n-value, while the temperature-dependent $n(T)$-value reads as follows [121]:

$$n(T) = \begin{cases} (n_0 - 1) \cdot \left(\dfrac{T_c - T}{T_c - T_0} \right)^{1/4} + 1 & T \leq T_c \\ 1 & T \geq T_c, \end{cases} \tag{6.4}$$

where $n_0 = 30$ is the n-value at T_0, $T_0 = 77\,\text{K}$ is the liquid nitrogen temperature and $T_c = 92\,\text{K}$ is the critical temperature. Unlike the ρ_{OC} model, the ρ_{PWL} model does not always reproduce the experimental curves adequately. The most significant difference between the models is present for low overcurrent transients (low prospective, current fault). Specifically, for $I_{\text{peak}} = 1.52\, I_c$ (Figure 6.5 (a)), using the power-law model the voltage signal is largely overestimated with respect to the real measurements. As a consequence, the Joule losses are overestimated and the power-law model predicts a faster quench than the overcritical current model (red region highlighted in the Temperature REBCO plot (a) on the right).

For high prospective fault current, the overcritical current model and the power-law model have similar behaviors. The motivation for this difference will be discussed later in this Chapter. Finally, the difference when using a constant or a temperature dependent $n(T)$-value it is very small. For low overcurrent transients, in particular, the difference in terms of the calculated quantities does not change the qualitative results, especially in terms of temperature for the REBCO (faster quench). This means that, in the remaining part of this work, we can further simplify the model by using a constant n-value.

Overall, the model based on ρ_{OC} reproduces the temporal profile of the measured current accurately for the prospective fault considered. Nevertheless, not all the simulations reached a

satisfactory level of accuracy. In Figure 6.5 (b-e), especially the simulated voltage drop over the tape, does not represent the real experiments very well. One hypothesis is that, since the current regime explored in these measurements is near or above the tape's critical current, the inhomogeneous critical current distribution leads to the onset of localized normal resistive zones, hence to the abrupt change of slope in the observed voltage. Other issues can arise due to the experimental setup. During the experience, we observed that several spurious harmonics were present in the voltage source. This can be observed from the experimental measurements, when the injected current signal crosses 0A. Due to time constraints, during the experience we could not characterize the impedance of the overall circuit (inductance and contact resistance). Since we lacked this knowledge, it was not possible to further validate the experimental results with our model, and we decided to perform other measurements with another experimental setup.
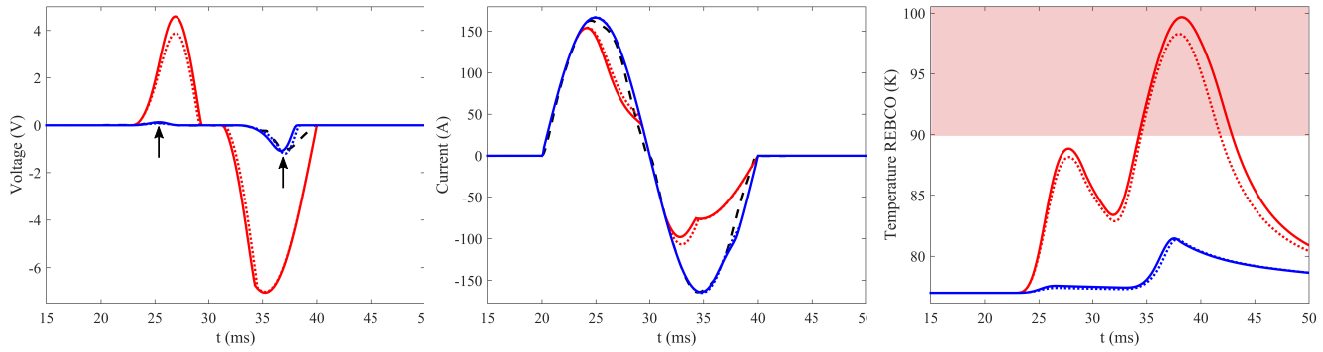
a) I_{prosp}=168 A = 1.52 Ic
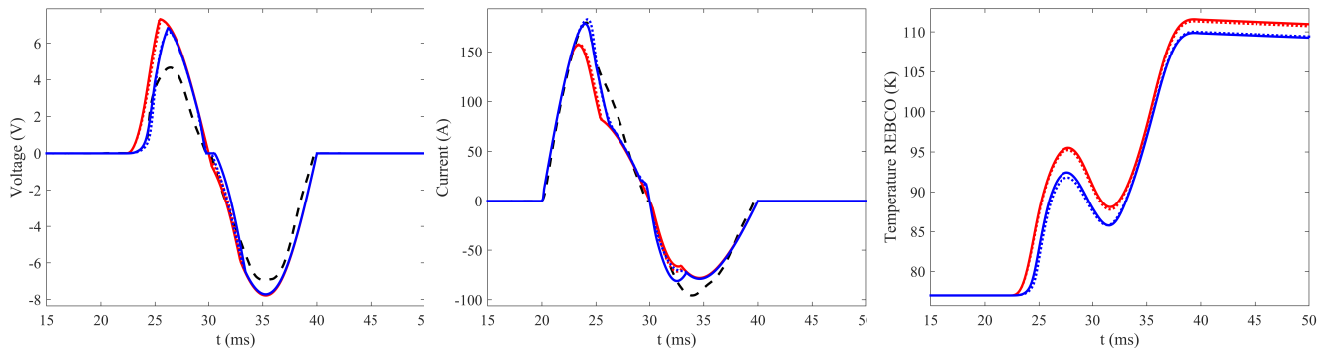
b) I_{prosp}=195 A = 1.78 Ic
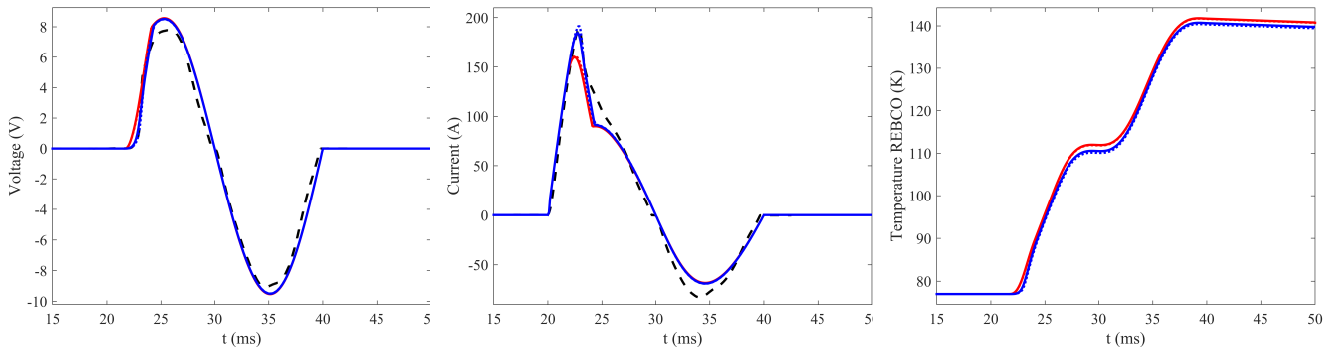
c) I_{prosp}=264 A = 2.40 Ic

d) I_{prosp}=406 A = 3.70 Ic

- - - Experimental measurements
—— Power-law, n constant
······ Power-law, n(T)
—— OC (fit)
······ OC (look-up tables)
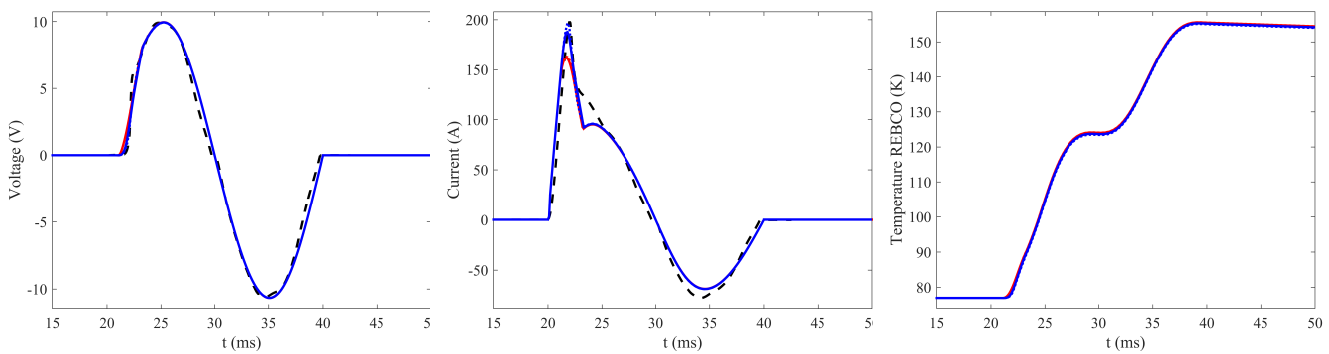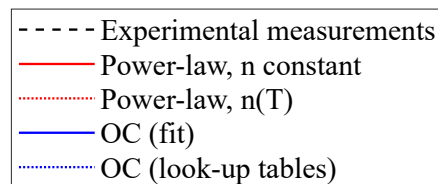
SuperPower (SP06)
I_c=110 A @ 77 K self-field

Figure 6.5: Measurements and simulations of an HTS tape undergoing AC fault current limitation for four levels of prospective current
. The measurements were performed on one sample (SP06b) coming from the same batch as SP06.
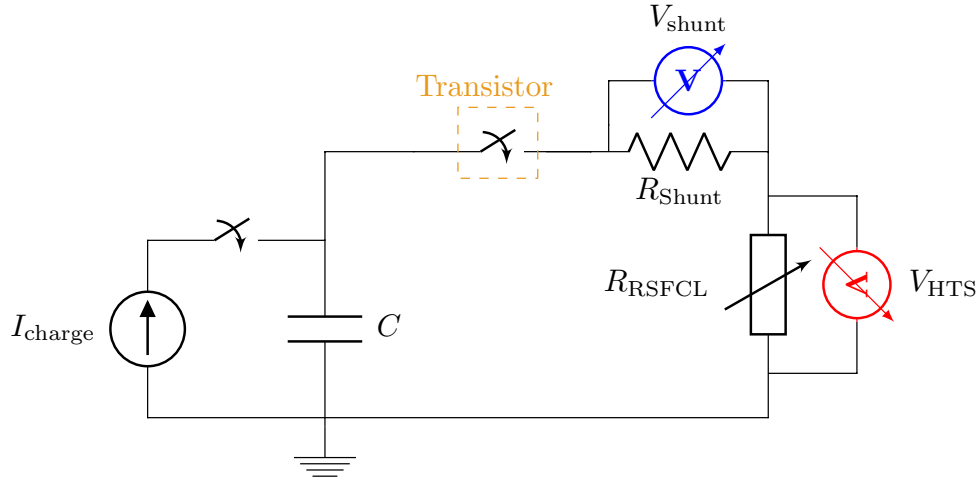
Figure 6.6: Schematic representation of the experimental setups used at EPFL.

Simulations vs. measurements (DC Measurements - EPFL)

At EPFL, DC fault current measurements in a liquid nitrogen bath (77 K) were performed on a tape called SP06c. The SP06c sample was 13.5 cm long, obtained from the same spool as the SP06 sample (1.1 μm of surrounding silver stabilizer, I_c = 110A at 77 K in self-field conditions). The experimental setup used is schematically represented in Figure 6.6. The voltage was applied to the sample with a capacitor previously charged with a current source. A transistor was used as a switch to trigger the discharge. The capacitor could generate currents as high as 1600A in the circuit. We measured the voltage drop V_{shunt} across a calibrated resistor R_{shunt} in order to determine the current in the circuit as $I_{app} = V_{shunt}/R_{shunt}$. Finally, we measured the voltage V_{HTS} with the help of voltage taps installed on the sample, separated by a distance of 9.5 cm. Each voltage tap was located 1 cm away from the copper terminals, which was sufficient to allow the current transfer into the superconducting layer. The electric field and current for two limitations tests are presented in Figure 6.7. In Figure 6.7(left), the voltage applied on the sample was 3.02 V, which generated a peak current of I_{peak} = 184.5A. In Figure 6.7(right) the voltage applied on the sample was 3.23 V, which generated a peak current of I_{peak} = 189A. In this figure $E_{app} = V_{app}(t)/L$, where L is the spacing between voltage taps (9.5 cm), is represented in green on the right axis of the figure. We observe that the behavior can not be explained by spurious inductive signals and heating only. One hypothesis is that, since the current regime explored in these measurements is near or above the critical current of the tape (110 A), the inhomogeneous critical current distribution leads to the onset of localized normal resistive zones, hence to the abrupt change of slope in the observed voltage. In Figure 6.7, the results of the experimental measurements and the COMSOL simulations are compared. The measured voltage V_{HTS} was used as the voltage excitation $V_{app}(t)$, across the terminals A and B in Figure 6.1. The electric-circuit used for self-consistency check is illustrated in Figure 6.4b. Overall, both models (ρ_{OC} and $\rho_{\eta\beta}$) reproduce the temporal profile of the measured current accurately for the two electric fields level considered, especially the current peak at the beginning. For comparison, we also calculated the current with the power-law model. Unlike the overcritical current models, the ρ_{PWL} model does not reproduce the experimental curves adequately. Finally, observing the simulations in Figure 6.7, we can say that the models ρ_{OC} and $\rho_{\eta\beta}$ are practically equivalent.
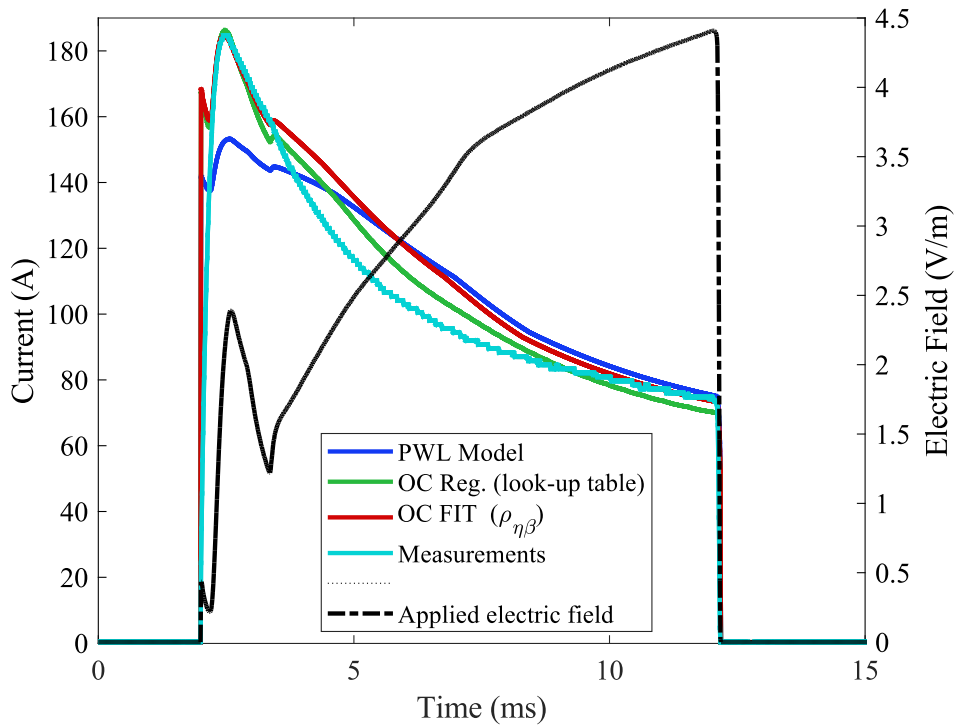
(a)
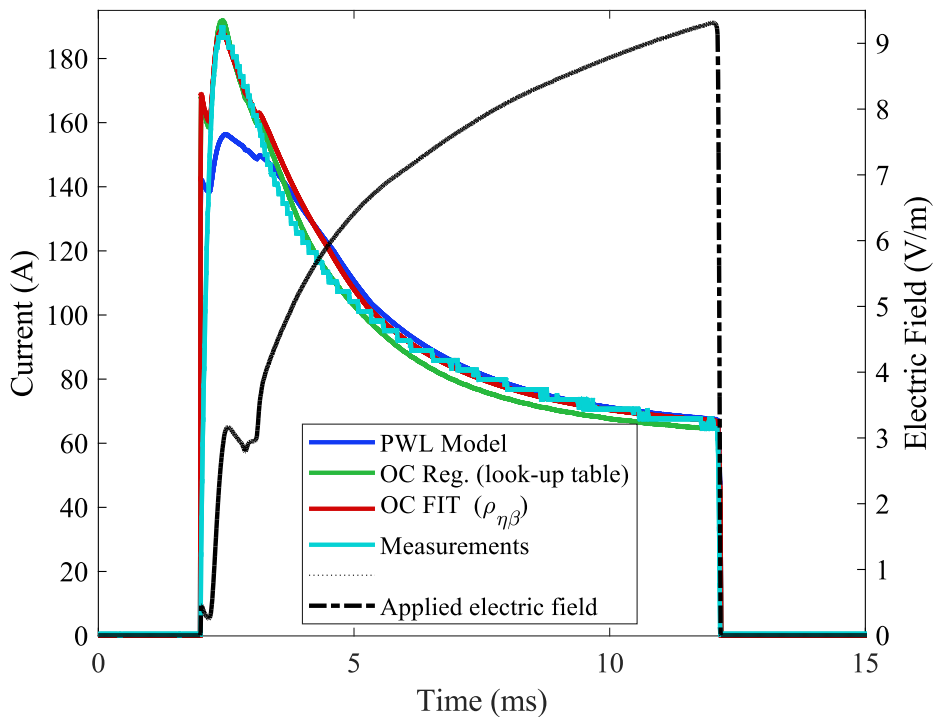
(b)

Figure 6.7: Measurements and simulations of an HTS tape undergoing fault current limitation under an increasing applied electric field. The current peak at the beginning which is very similar for the two electric fields level considered, $I_{peak} = 184.5$ A (left) and $I_{peak} = 189$ A (right) respectively. The measurements were performed on one sample (SP06c) coming from the same batch as SP06.

6.2. Impact of resistivity model on SFCL behavior

This section analyzes the impact of using the overcritical current model instead of the power-law model. In particular, we calculate by simulation the temporal evolution of current and temperature in the tape for different homogeneous DC and AC fault current limitation conditions. In the previous Section we assessed that the $\rho_{\eta\beta}(I, T)$ (mathematical expression) and $\rho_{oc}(I, T)$ (look-up table) are practically equivalent. Therefore, to evaluate the impact of the overcritical current model with respect to the power-law model we used only the mathematical expression, namely $\rho_{\eta\beta}(I, T)$. The $\rho_{\eta\beta}(I, T)$ model was implemented for sample SP06 as discussed in Section 5.2, and according to the parameters $\eta_{1st}(T)$ and $\beta(T)$ in Table 5.1.

6.2.1. Impact on DC fault current limitation

Various fault conditions were generated by applying different values of DC voltage pulses, noted $V_{app}(t)$ (Figure 6.4b). Two representative cases are plotted in Figure 6.8. We deliberately chosen two electric field values ($28.21\,\mathrm{Vm^{-1}}$ and $28.26\,\mathrm{Vm^{-1}}$), where the recovery of the tape was significantly different, to verify if using $\rho_{OC}(I, T)$ instead of $\rho_{PWL}(I, T)$ would have a significant impact. Figure 6.8 we can conclude that there is not much difference for homogeneous DC fault conditions. Since the heating occurs quickly at the beginning of the fault, the tape is no longer superconducting within a few ms, hence the stabilizer dominates the resistive behavior. However, similarly to what reported in Figure 6.7, a remarkable difference is present at the beginning of the pulse, where the peak of the limited current I_{OC} is larger than that of I_{PWL} (inset in Figure 6.8).
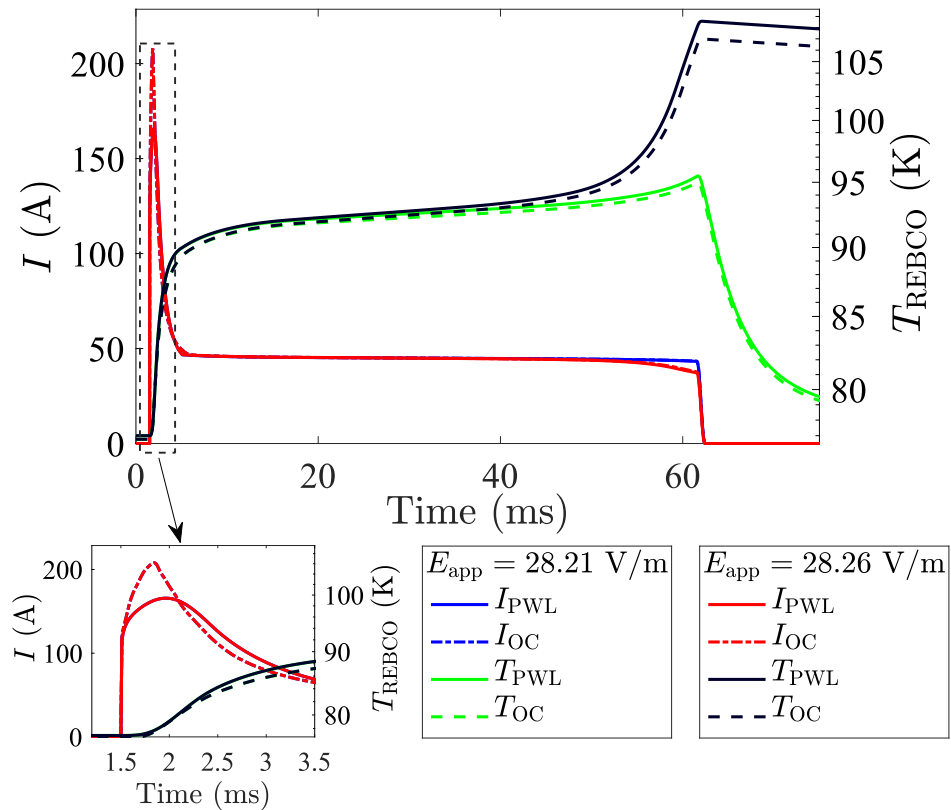
Figure 6.8: Simulated DC faults on SP06 with the overcritical resistivity model and the power-law model, for $E_{app} = 28.21\,\mathrm{Vm^{-1}}$ and $E_{app} = 28.26\,\mathrm{Vm^{-1}}$. The small difference between the two values of E_{app} leads to a drastic change in the recovery of the tape.

(a) $I_{\text{fault}} = 1.63\,I_{\text{c}}$
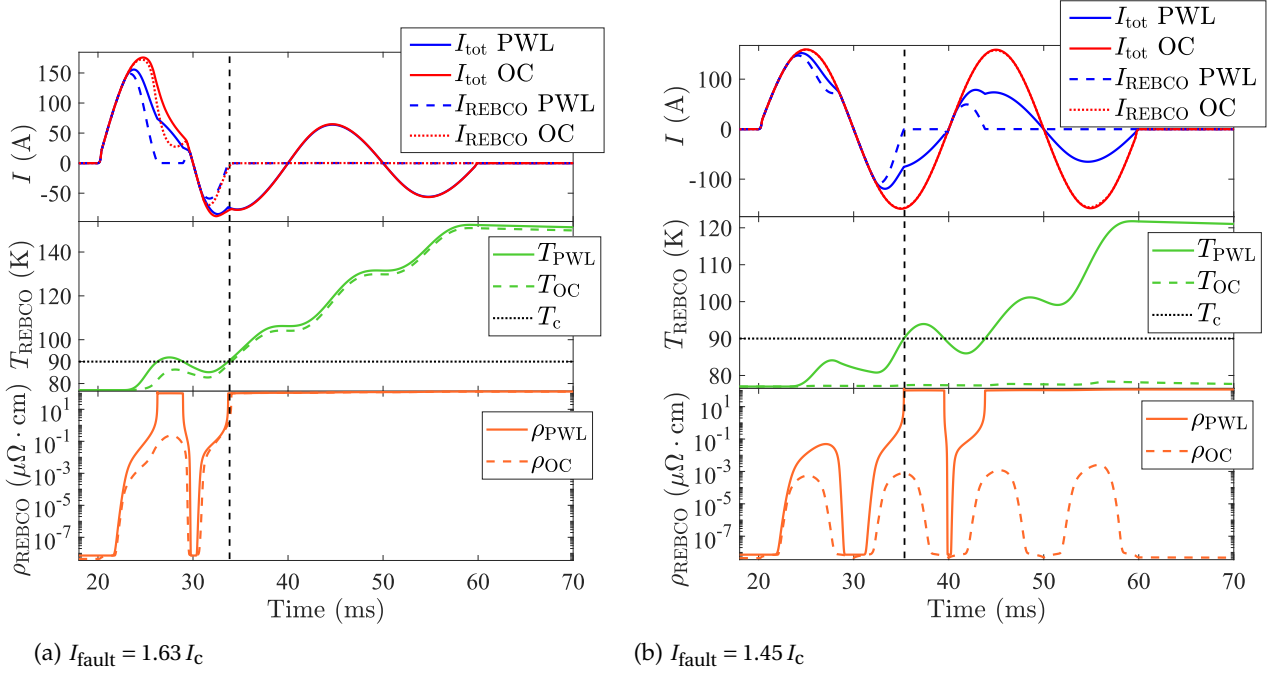
(b) $I_{\text{fault}} = 1.45\,I_{\text{c}}$

Figure 6.9: Simulated AC faults on SP06 with the overcritical resistivity model ρ_{OC} and the power-law model ρ_{PWL}, for (a) $I_{\text{fault}} = 1.63\,I_{\text{c}}$ and (b) $I_{\text{fault}} = 1.45\,I_{\text{c}}$. The black dashed lines indicate the moment where the quench occurs (a) for both models and (b) for ρ_{PWL}.

6.2.2. Impact on AC fault current limitation

The model used to simulate AC fault current limitation is presented in Figure 6.4a. A sinusoidal voltage signal is imposed on the circuit, while a load resistor R_{Load} draws the nominal current from the source. A switch in parallel to the load resistor, when closed, simulates the fault occurring at a given time and draws the fault current through a resistor R_{fault}. In the simulations, $V_{\text{peak}} = 12\,\text{V}$ and $f = 50\,\text{Hz}$. The switch operates at $t = 20\,\text{ms}$ and the short-circuit is cleared after two periods of the sinusoidal voltage source, i.e. $t = 60\,\text{ms}$. Finally, the prospective current is calculated as $I_{\text{fault}} = V_{\text{peak}}/R_{\text{fault}}$. In Figure 6.9, we present the evolution of the total current in the circuit and the current in the REBCO layer (top), the temperature (middle), and the REBCO layer resistivity (bottom). The difference in the simulations of the fault current when using $\rho_{\text{OC}}(I, T)$ instead of $\rho_{\text{PWL}}(I, T)$ is very small, except during the first peak, when $I_{\text{fault}} = 1.63\,I_{\text{c}}$, as shown in Figure 6.9a. As in the case of DC faults, the heating occurs rapidly at the beginning of the fault, and the device is no longer superconducting after a few ms, hence the stabilizer dominates the resistive behavior. Figure 6.9b shows the results for $I_{\text{fault}} = 1.45\,I_{\text{c}}$. In this case, the difference in simulation results is remarkable. Even if the first current peak does not change considerably using $\rho_{\eta\beta}(I, T)$ instead of $\rho_{\text{PWL}}(I, T)$, the temperature rise is significantly different. The power-law model predicts a faster quench than the overcritical current model, i.e. its temperature reaches $T_{\text{c}} = 90\,\text{K}$ in less than one cycle (see Figure 6.9b).

The difference in the temperature rise obtained when using the overcritical current model instead of the power-law model can be understood by comparing the electrical resistance per unit of length of the of REBCO layer ($R_{\text{REBCO}}(I, T)/L_{\text{tape}}$), the total resistance per unit of length of the tape ($R_{\text{tape}}(I, T)/L_{\text{tape}}$) and the total Joule losses ($\sim R \cdot I^2$).

In Figure 6.10a, we plot $R_{\text{REBCO,PWL}}/L_{\text{tape}}$ described by the power-law model (full lines), compared with $R_{\text{REBCO,OC}}/L_{\text{tape}}$ described by the overcritical resistivity model $\rho_{\eta\beta}(I, T)$ (dashed
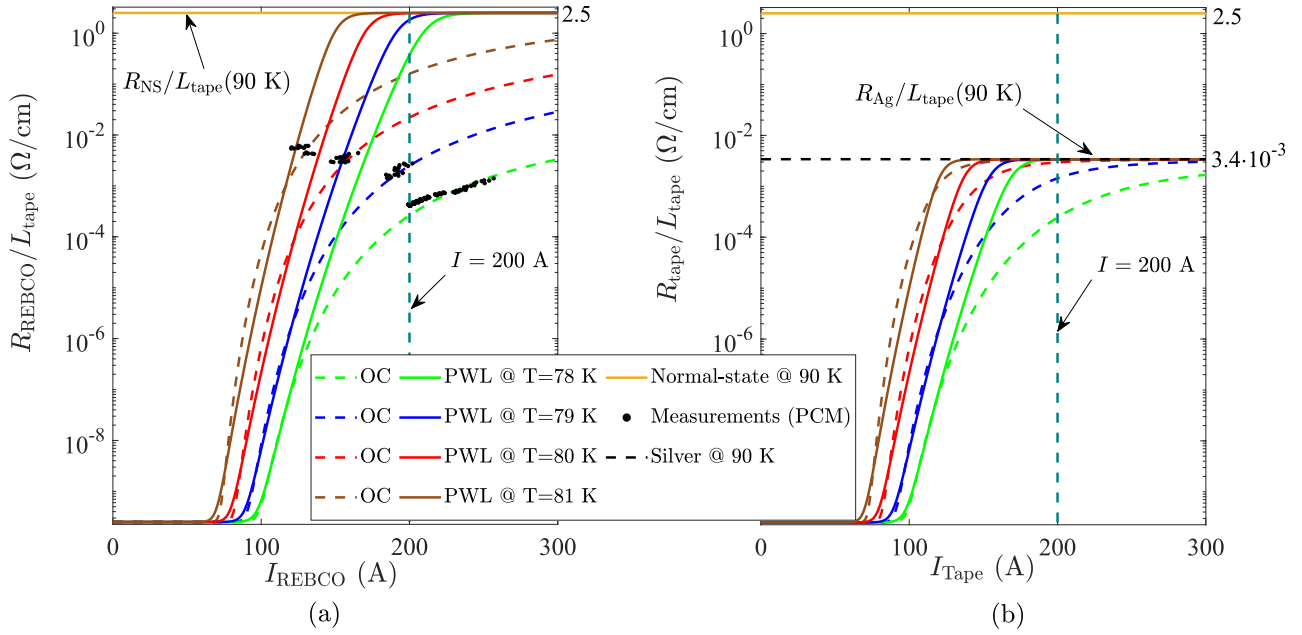
Figure 6.10: (a) Comparison between the power-law and the overcritical resistivity models in term of resistance per unit length. The normal state resistance of REBCO is considered in the model. (b) Comparison between the global resistance per unit length of the tape, using the power-law and the overcritical current model, in parallel with the resistance of silver at 90 K.

lines). The constant line at $2.5\,\Omega\,cm^{-1}$ is the normal state resistance per unit length of RE-BCO at 90 K, while the black scattered points correspond to the experimental measurements. The difference between $R_{REBCO,PWL}(I,T)/L_{tape}$ and $R_{REBCO,OC}(I,T)/L_{tape}$ for the same current is striking. If we consider $I_{REBCO} = 200\,A$ and $T = 78\,K$, the ratio between the two resistances is:

$$\frac{R_{REBCO,PWL}(200\,A, 78\,K)/L_{tape}}{R_{REBCO,OC}(200\,A, 78\,K)/L_{tape}} = \frac{0.32\,\Omega\,cm^{-1}}{2\cdot 10^{-4}\,\Omega\,cm^{-1}} \simeq 1600.$$

When looking at the tape as a whole, this difference is mitigated by the presence of a stabilizer such as silver. In Figure 6.10b, the resistance per unit length of silver is represented as a constant line at $3.4\cdot 10^{-3}\,\Omega\,cm^{-1}$. The silver acts as a parallel resistor, and the effective resistance per unit length of the tape are lower than that of a single REBCO layer. In this case, the ratio between the two resistances is:

$$\frac{R_{tape,PWL}(200\,A, 78\,K)/L_{tape}}{R_{tape,OC}(200\,A, 78\,K)/L_{tape}} = \frac{3.4\cdot 10^{-3}\,\Omega\,cm^{-1}}{2\cdot 10^{-4}\,\Omega\,cm^{-1}} \simeq 17.$$

Therefore, when the prospective current is $I_{fault} = 1.63\,I_c$ (Figure 6.9a), the high current pushes the device in the normal state, far from the regime where the differences between the resistances are important. Since the temperature reaches the critical temperature $T_c = 90\,K$ at the beginning of the fault, what we are simulating is the current flowing in the silver stabilizer and the Hastelloy, which have the same properties in the two simulations. The situation for $I_{fault} = 1.45\,I_c$ is different. A better insight of the role played by the different resistivity models is given by the total Joule losses in the tape. The total losses can be written as $P_i = R_{tape}\cdot J_i^2$. In Figure 6.11 we compare the total current, the resistance per unit length of the tape and the total Joule losses obtained with the power-law and overcritical current resistivity models. In the gray-shaded area between 23 ms and 29 ms, when the tape is still superconducting, we see that the total current $I_{tot,PWL}$ is not too different from $I_{tot,OC}$. However, we see that
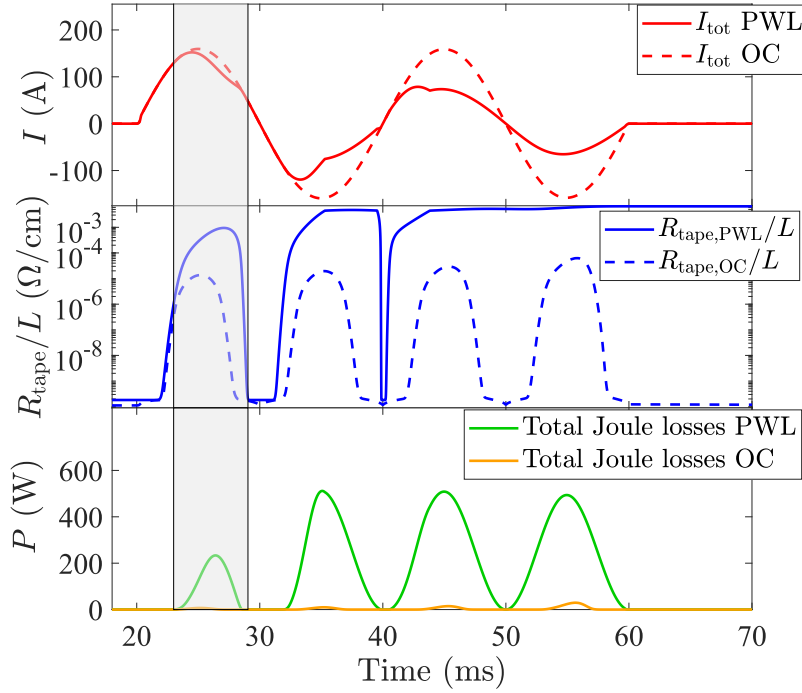
Figure 6.11: Comparison between the total current (top), resistance per unit length (middle) and Joule losses (bottom) in the RSFCL model using the power-law and overcritical current resistivity models in the AC current limitation case with $I_{fault} = 1.45\,I_c$. The gray-shaded area shows the remarkable difference in term of Joule losses.

$R_{tape,PWL}$ is considerably larger than $R_{tape,OC}$ ($R_{tape,PWL} \simeq 100 \cdot R_{tape,OC}$). As a consequence, we have $P_{PWL} > P_{OC}$ and the temporal evolution of the temperature in the SFCL in the two case is very different. For $t > 45\,\text{ms}$, $R_{tape,PWL} \simeq R_{Ag} = 3.4 \cdot 10^{-3}\,\Omega\,\text{cm}^{-1}$ and the stabilizer dominates the resistive behavior. However, $R_{tape,OC}$ remains low, the device is still in the superconducting state. This situation clearly demonstrates that scenarios where low overcurrent transients are involved are highly impacted by the correct choice of resistivity model. Low overcurrent transients play an important role in the design of SFCL, since it's the regime where hotspot and defects impact the design of the device [122]. In this case, using the $\rho_{PWL}(I, T)$ model leads to a wrong estimation of the temporal evolution of the temperature.

6.3. Conclusions and possible improvements

In this Chapter, we demonstrated how an accurate knowledge of the overcritical current resistivity as a function of current and temperature is essential when studying the electrothermal behavior of RSFCL. Through numerical simulations, we evaluated the impact of using the overcritical current model $\rho_{OC}(I, T)$ and $\rho_{\eta\beta}(I, T)$ (validated with AC and DC fault current measurements) instead of the power-law model in the simple case of an RSFCL constituted of a silver-stabilized tape. We demonstrated that, for low AC overcurrent faults, the power-law model leads to a wrong estimation of the temperature's temporal evolution, largely overestimating the maximum temperature at the end of the AC fault. When using the overcritical current model, the temperature is much lower. The major limitation of the models utilized in this Chapter is that the models assume uniform material properties in the REBCO tape. Thus, such models cannot be used to investigate the impact of defects and hot-spots. The distribution of the defects can be simulated using a 2-D electrothermal model, where we consider a space dependent critical current distribution $I_c(T, x)$, assuming the defect distribution to be gaussian around a mean-value $I_{c,0}$ and with a root-mean-square (RMS) width σ_{I_c}.

...Though I'm past 100,000 miles
I'm feeling very still
And I think my spaceship knows which way to go
Tell my wife I love her very much
She knows...

David Bowie, *Space Oddity*

7
General conclusions and necessary improvements

High-Temperature Superconductor (HTS) materials, especially REBCO commercial tapes, are an emerging technology holding immense potential for future applications such as medical and energy applications. Even though superconductivity was discovered over 100 years ago, the penetration in the market of this alluring material is hindered by technological complexities, acceptance, and costs.

Cost reductions are also achieved thanks to numerical modeling. The non-linear resistivity is usually described using models such as the power-law model. Such models poorly describe the overcritical current regime of REBCO.

This research's main goal was to study the electrothermal behavior and HTS coated conductor's resistivity in the overcritical current regime ($I > I_c$). The experimental challenge to retrieve the electrical resistivity in the overcritical current regime $\rho_{OC}(I, T)$ is due to the excessive overheating that can destroy the tapes as soon as the current injected in the tapes is above the critical current ($I > I_c$). Thanks to a unique experimental technique developed at Polytechnique Montreal (PM) and Ecole Polytechnique Fédérale de Lausanne (EPFL), we can perform Pulsed Current Measurement (PCM) injecting currents up to 10 times the critical current of commercial wires (up to 1600 A) for a period as short as 20 µs. The small energy injected enables a characterization of the superconductor's electrical resistivity at high current densities and electric fields without destroying the samples.

The challenges in interpreting the raw data are the heating and electrothermal effects occurring during a pulse. The heating effects and the current sharing between the layers make difficult to know the amount of current carried by the superconducting layer and its temperature, and thus, its resistivity.

In the framework of the Ph.D. research, the major scientific achievements include:

- The development of a post-processing method based on the so-called Uniform Current (UC) model to estimate the resistivity of the HTS in the overcritical current regime from experimental measurements with an accuracy below 10 %;

- The formulation of a Non-Linear Least Squares optimization method. This method aimed to find the silver layer thickness's best-approximated values and its electrical

resistivity temperature dependence. The method was used to minimize the uncertainties on such parameters and reduce the error of the calculated quantities (temperature, current, resistivity) related to such uncertainties.

- The use of *non-parametric constrained regularization methods* to treat the experimental measurements extracted in the overcritical current regime. The output of this technique is a look-up table that can be shared with interested partners and used in numerical modeling afterward;

- The proposal of the *overcritical current model*, an alternative to the power-law model, to describe the overcritical current regime ($I > I_c$), based on experimental measurements obtained as outlined above. The model was validated experimentally with measurements performed at EPFL and KIT, and it was used to show that for the case of a superconducting fault current limiter when the power-law model is used to model its electrothermal response, the device quenches faster than with the overcritical model;

The lack of good knowledge in the overcritical current regime is a major issue in developing quality simulation tools for optimizing the design of superconducting devices working near and above the critical current. This work can be very useful to optimize the use of superconducting material as well as the amount of stabilizer. More interestingly, it opens the study of the overcritical current regime, a new exciting aspect of REBCO commercial tapes.

In the near future, we plan to assess the impact of using the overcritical current model in other relevant case scenarios like a hotspot scenario in superconducting devices, quench in magnets, or non-insulated coil, or also for coolant optimization. We are also considering characterizing the REBCO overcritical current regime for other sample typologies like bulks, stacks of tapes, or thin films.

Finally, significant work in the physical interpretation of the results should be done. Before doing this, however, future improvements need to be considered.

Future improvements

In the future, an extensive measurement campaign will be necessary, exploring several experimental conditions. A significant limitation of this work in fact, is that only a few experimental conditions were explored. Although many samples from different manufacturers were characterized, no comparative work was carried out (samples with different pinning force/scenarios, higher magnetic field ($B > 300$ mT, wider temperature range $T < 77$ K). In order to accomplish this, a few steps must be undertaken.

Improvements for the experimental setup: The cryostat at EPFL is challenging to control in temperature and relatively limited in field (450 mT). The other PCM system is mounted at PM (Montreal), where the applied external field can be up to 5 T. In this setup, the cooling system consists of a vacuum chamber connected to a helium compressor that cools by conduction the sample down to 15 K. Nevertheless, as discussed in detail in [48], the measurements campaign led at PM was hindered by a few experimental issues of the utilized cryostat. Such issues were finally addressed in recent times.

In order to perform even faster pulses, it is possible to use higher voltage capacitors. However, the use of some capacitors and the different triggers of the fast source created noise in the voltage measurements [45, 46, 48]. According to the PCM system designers, it is necessary to improve the communication between the computer, the master controller unit, and the CGMs. This improvement can be made by substituting the LabVIEW VIs with code in Python that the researchers at PM have begun to develop (at the time of this writing).

Sample treatment and processing: As previously mentioned, populating a complete (ρ,T,I) surface is complex. Several methods can help to explore other regions of the resistivity surface. For instance, we can perform the measurements with different starting temperatures (e.g., from 65 K to 77 K). Another method to populate the (ρ,T,I) surface, is to etch the sample and remove the silver selectively in some sections of the sample [42, 43]. In fact, between the Hastalloy and the REBCO, there are insulating buffer layers. If the silver is removed by a local etch, the proportion of the current flowing through the REBCO layer will increase consistently, enabling the characterization of higher resistivities. However, it would also increase the rate of heating, risking damaging the samples. An insulating layer that acts as a heat sink can be added to the etched sample, but this would increase the sample's preparation time.

Improvements of the post-processing methods: It is important to specify that the adiabatic assumptions we made in our analysis, does not limit the validity of the UC model. However, further tests are needed to assess the validity of the adiabatic approximation for pulses of several hundred microseconds, particularly in liquid nitrogen.

The utilized finite element models should be improved in terms of both computational time and accuracy in the future. The optimization method to extract the correct silver geometry and electrical resistivity should be further investigated and validated. A common problem faced when using FEA is the cost in terms of computational time. The computing time of the UC models per pulse ranges from 30 s to 200 s per analyzed pulse. When analyzing a large number of pulses (up to 100), it is desirable to reduce this calculation time. In Appendix A.4, a reduction to 1-D has been explored. We show that the quantities of interest (current sharing and temperature) calculated with the 1-D approach are equivalent to those calculated with the 2-D approach, making the 1-D approach a valid alternative. A further improvement of the computational time can be achieved through an analytical formula. It is possible to solve the Heat Equation in 2-D or 1-D using the Green's Function, obtaining an analytic formulation of the UC model. It is possible to show that a Green's Function always exists if the domain can be decomposed into one-variable problems [123]. This is the case of the REBCO tape for both the 2-D and 1-D approximations. During this work of thesis, the possibility of using the Green functions was discussed with Mr. Richard (PM) and partially developed afterward. Due to time constraints, this work was not accomplished but remained an exciting method to explore.

Finally, a *drastic* reduction of the UC model's computational efforts can be obtained by reducing its computational complexity by applying techniques such as Model Order Reduction (MOR) [124, 125]. Also this method was partially explored, but it needs further development.

Finally, it is necessary a generalization to 3-D of the UC model. As shown in Paragraph 3.3.2, in fact, the inhomogeneities of the material properties make the quantities of interest calculated by the UC model (current, temperature, resistivity) susceptible to errors and inaccuracy. In addition, if etched samples will be characterized in the future, the UC model must be modified accordingly.

As a result of both aspects, the assumption of uniformity along the length would not be valid anymore. To address both the complexities, a complete 3-D electrodynamic model must be used, i.e. also including the electrical interface resistance between the superconductor and the silver, in order to evaluate the impact of the etching on the heat generated and to see if it is possible to use a 2-D analysis model also in such a case.

A

Appendices

A.1. Superconductor modeling

Many physical formulations can be used to solve Maxwell's equations for superconductors. The approaches used in this work of thesis are based on the H-formulation and the electric potential V, with the names referring to the electromagnetic state variables.

H-formulation: The formulation is based on the Faraday's equation, using the magnetic field components as state variables:

$$\nabla \times E = -\frac{\partial H}{\partial t},$$ (A.1)

where $B = \mu_r \mu_0 H$. In this work the magnetic permeability is $\mu_r = 1$. In order to express Equation A.1 in term of H, we use the following relations:

$$E = \rho J \qquad J = \nabla \times H.$$

We obtain therefore the following Equation:

$$\nabla \times (\rho \times H) = -\frac{\partial(\mu_0 H)}{\partial t},$$ (A.2)

where the magnetic field needs also to obey Gauss's law:

$$\nabla \cdot (\mu_0 H)|_{t=t_0} = 0.$$ (A.3)

The condition at $t = t_0$ in Equation (A.3) avoids an over-constrained problem.
A transport current on a conductor can be constrained using a Dirichlet boundary condition as follows:

$$\int_k J \cdot dS = I_t(t),$$

where S is any open surface that completely intersects the conductor alone [126] and I_t the transport current used as an input.

Electric potential V: The formulation is based on the Gauss' law without source term, using the electric vector potential as state variables:

$$\nabla \cdot (-\sigma \nabla V) = 0, \tag{A.4}$$

where V is the electric scalar potential and σ the electrical conductivity.

A transport current on a conductor can be conduced through the conductor by applying proper Dirichlet boundary conditions. In particular, on one boundary $\partial\Omega_t$ it is applied:

$$\int_{\partial\Omega_t} (-\sigma \nabla V) \mathrm{d}S = I_t(t), \tag{A.5}$$

with $I_t(t)$ being the transport current used as an input. On another boundary $\partial\Omega_0$ is imposed:

$$V = 0 \quad \text{on} \quad \partial\Omega_0. \tag{A.6}$$

On the remaining boundaries of the conductor we have:

$$\mathbf{n} \cdot \nabla V = 0. \tag{A.7}$$

A.2. 3-D magnetostatic simulation of EPFL resistive dipole

In this Appendix, the homogeneity of the applied magnetic field on the sample was evaluated. A real dipole is limited in length and width, and this has a consequence on the homogeneity of the field on the sample. The dipole magnet has a rectangular H-type structure (Figure A.1a). The CAD was reconstructed according to the specs present in the user manual, as well as the saturation curve (μ-BEAM.Sàrl). The magnet is composed of 2 coils of 410 turns, able to produce DC-magnetic flux as large as 500 mT for an air-gap of 60 mm. The simulation was carried out in COMSOL (mf module), and the model domain is constituted of the dipole, the copper coils and the surrounding air computational domain. With a nominal current of 28 A (11480 $ampere \cdot spire$), the simulation results are presented in Figure A.1. In Figure A.1b, we present the magnetic field profile along the width (x) and the length (y) of the sample holder. The field homogeneity was calculated by numerical simulations as $\Delta B(x) \, B(0)$ (or $\Delta B(y) \, B(0)$). The value $B(0) = 494$ mT is the field at the center of the sample holder $(x, y) = (0, 0)$. The field homogeneity was estimated to be within 1 % and 4 % along the width x and the length y of the sample holder respectively. In Figure A.1c and Figure A.1d we have the magnetic flux and streamline representation on the $x - y$ and $x - z$ plane respectively.

(a)

(b)

(c)

(d)
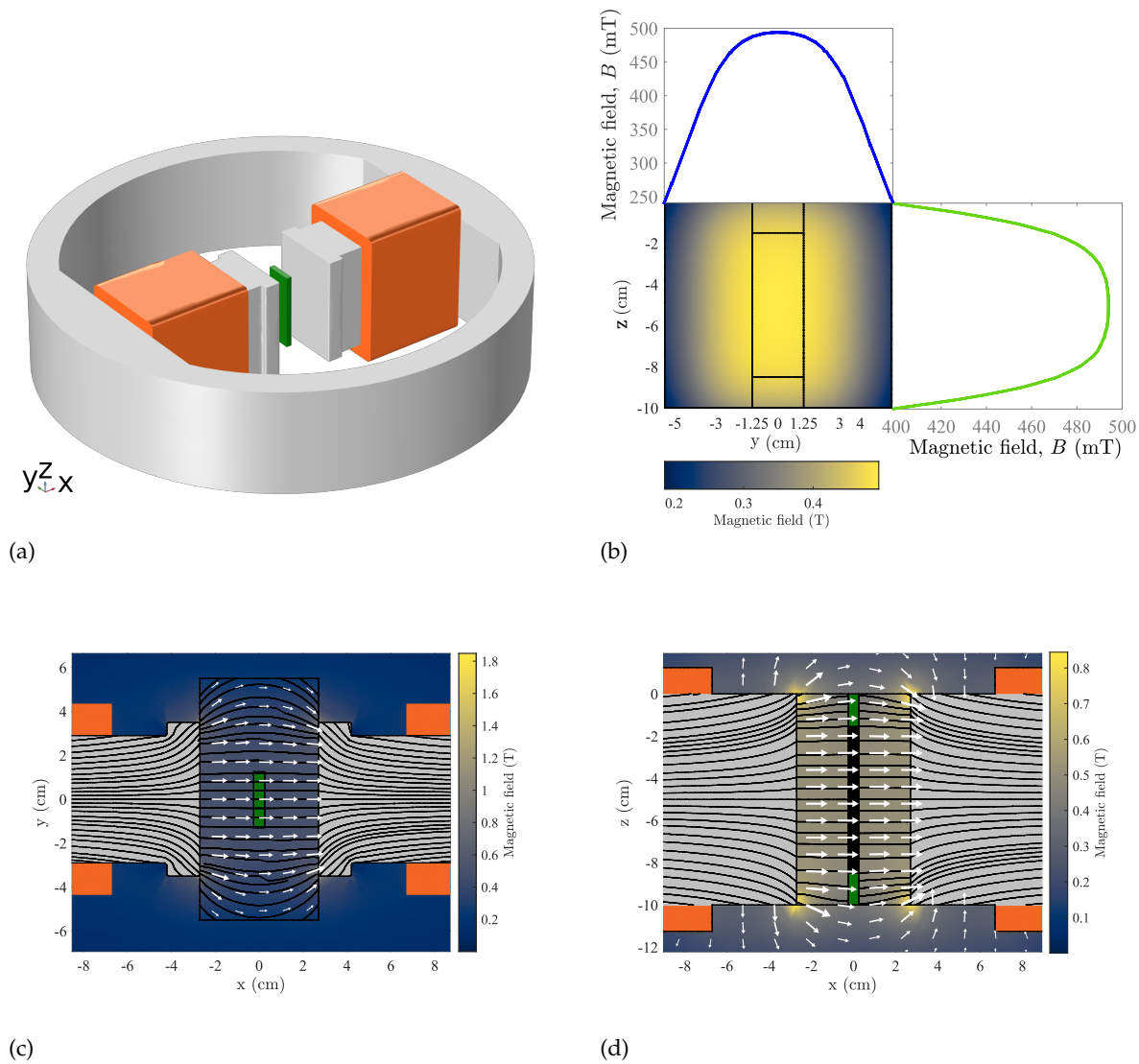
Figure A.1: (a) Dipole in 3-D and (b-c-d) magnetic flux on the sample on the various planes.

A.3. EPFL glass cryostat: temperature control methods

In this Appendix, we discuss of the cryostat utilized at EPFL to measure in liquid nitrogen bath between 65 K to 77 K. The cryostat is connected to the vacuum pump through an exhaust vacuum tube. The temperature was controlled by vacuuming the cryostat with an Alcatel CFF 100 Turbo Molecular vacuum pump. Control the pressure level in the cryostat was necessary to set the temperature of the liquid nitrogen bath in the cryostat [1]. To control the pressure, and thus to set the temperature, two approaches were used:

- Temperature control based on thermal inertia;

- Temperature control system based on hysteresis;

A.3.1. Temperature control based on thermal inertia

The cryostat was vacuumed, and once the selected temperature T_{set} was reached, we used to restore the atmospheric pressure in the cryostat. Depending on the volume of liquid nitrogen contained in the cryostat, the bath used to get slowly back 77 K. Since the cryostat volume was tiny, we assumed the liquid nitrogen bath to be isothermal within the cryostat. However, during one set of measurements, it was noticed that once the temperature sensor reached 77 K (after rising slowly from 65 K), the voltage shape was not behaving as expected. Specifically, while pulsing the same current at the same temperature (read from the sensor), the voltage kept changing his shape and increasing in magnitude. This can be better understood by observing the current pulse and the voltage curves measured for one section (Figure A.2).
For the same current and slightly different temperatures, we have a remarkably different be-
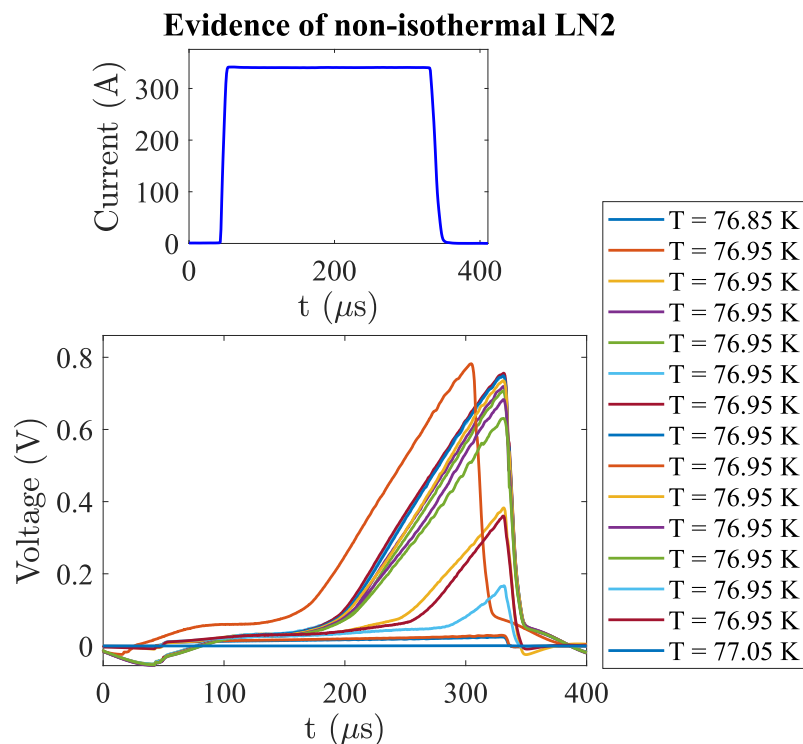
Figure A.2: For the same current and slightly different temperature, we have a remarkably different behavior of the voltage drop over 5 mm.

---

[1]The boiling point of the liquid nitrogen (77 K at sea level) changes accordingly to the vapor pressure.

havior of the voltage drop over 5 mm. This means that the temperature read probably was not be the same as the sample, and as a consequence, the liquid nitrogen bath was not uniform, having the liquid nitrogen in a non-isothermal fluid state.

The sample holder is vertically aligned with respect to the cryostat (Figure A.3a). The distance between the temperature sensor and the sample holder is $\simeq 10$ cm only, but there is possibly a temperature gradient along this length. Due to convection, boiling point variation, and
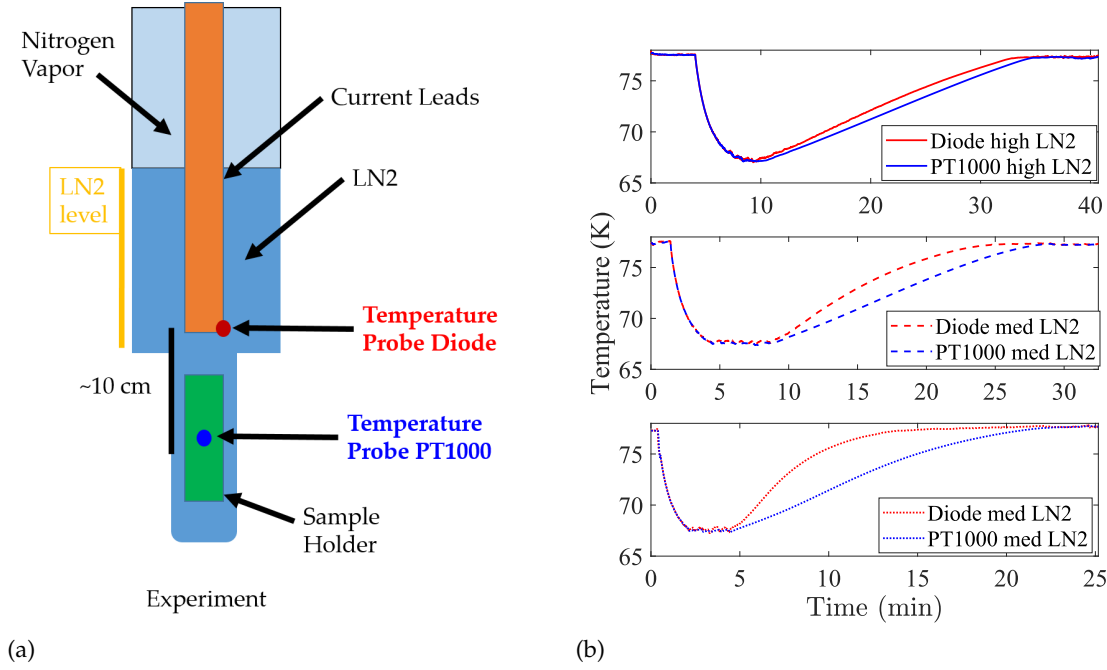
Figure A.3: (a) Schematic representation of sample holder and temperature sensors positioning in the cryostat and, (b) direct experimental measurements with a Cernox PT1000 and a Diode.

stratifications [127], the fluid can be in non-isothermal flow conditions in the cryostat. Stratification results because the warmer layer has a lower density, and the fluid itself is a poor heat conductor. To verify this, we can mount a second temperature sensor. Measurements: mounting a second temperature sensor closer to the sample holder, as shown in Figure A.3a, and then recorded the temperature changing during the cryostat warming-up. Three sets of measurements were performed:

1. **High level of LN2**: Between the sample holder and the LN2 surface, there were about 60 cm.

2. **Middle level of LN2**: Between the sample holder and the LN2 surface, there were about 30 cm.

3. **Low level of LN2**: Between the sample holder and the LN2 surface, there were about 10 cm.

Afterwards, we pumped vacuum on the cryostat until we reached 67 K. Once the temperature was reached, the atmospheric pressure was restored, and then we waited for the temperature to rise and set back to 77 K.

In Figure A.3b we show the experimental temperature measurements. Once we restore the atmospheric pressure, the gradient is clearly present and depends on the volume of evaporating mass. We can estimate the maximum temperature gradient (inset Figure A.3b) by recording

99

the maximum value of the difference $|T_{PT1000} - T_{Diode}|$, which in the worst-case scenario is around 4.13 K. To further investigate this phenomenon, we developed a model simulating the non-isothermal flow (at this moment without phase change).

These simulations aim to show that the temperature is not constant during the boil-off of the LN2. The atmospheric pressure set the triple point at 77 K, and there is not turbulent convection, but only natural buoyancy due to external heat loads and stratification. Applying the correct heat loads, we can, in the first instance, neglect the change of phase and evaluate if there is a temperature gradient. Finally, by changing the amount of LN2 mass, we change the total heat loads from the external, and thus, the gradient between the two points will be affected. In Figure A.3a, we present the experiment and the simulations settings. The model is 2-D axisymmetric. The major heat loads are the external loads (coming from the current leads), the convective cooling due to the external flowing air at T_{ext}, and the radiating heat loss of the cryostat, with an emissivity of $\epsilon = 0.06$. We applied the force of gravity to the LN2 mass to simulate the buoyancy effect and its stratification. A sweep parameter allowed to
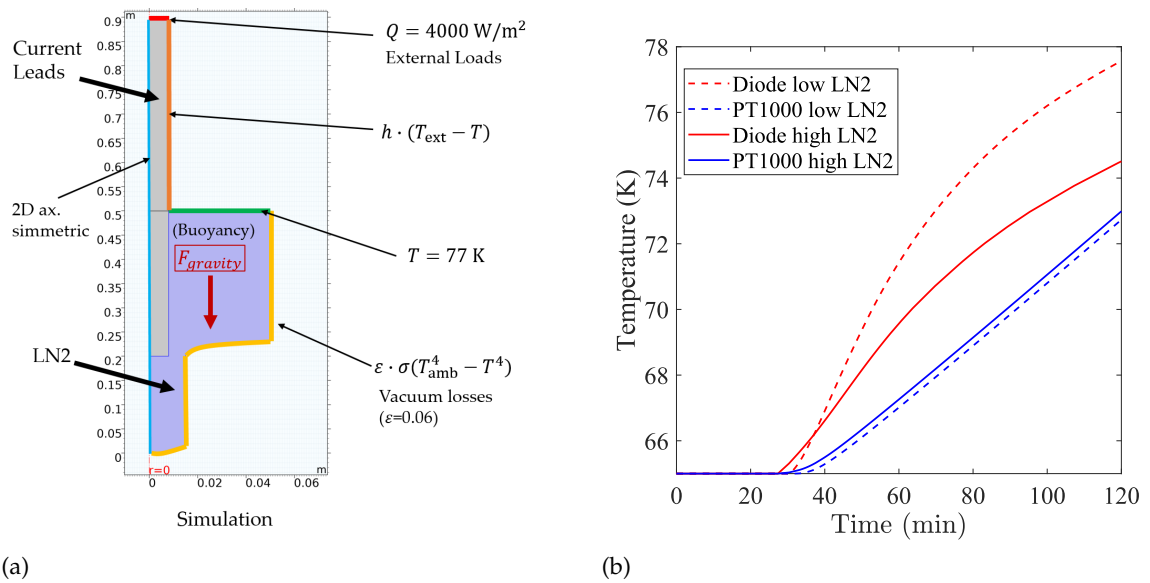
Figure A.4: (a) Schematic representation of the simulation implemented in COMSOL and, (b) Simulation results. The temperature was calculated using a probe point in the lower part and middle region of the cryostat.

change the height of LN2, and the temperature probes showed the temporal evolution in the selected points (Figure A.3b). The simulation results confirm that the gradient is present, and it depends on the heat loads such as the current leads, some radiation towards the external environment, and the amount of cold mass.

A.3.2. Temperature control system based on hysteresis

The cryostat was connected to the vacuum pump through an exhaust vacuum tube. A vacuum valve (SMC VXD240KGLXB) was added to set the pressure level. The valve could be open (allowing a pump to evacuate the cryostat) or closed (insulating the cryostat from the external environment and setting the pressure level). The decision to open/close the valve was controlled by a hysteresis method implemented in LabView.

The theoretical desired temperature T_{set} was set as control value, and the corresponding theoretical vapor pressure $P_{vap,press}(T_{set})$ was extracted from a look-up table implemented in LabView. A pressure sensor reads the pressure level P_{meas} in the cryostat. If the measured pressure dropped below or above the theoretical one, the valve was open, otherwise, the valve

was kept closed. To prevent unwanted rapid switching of the valve, and allow the pressure to stabilize in the cryostat, some amount of hysteresis P_{hyst} was added in terms of pressure (typically $P_{\text{hyst}} = 10\%$ of $P_{\text{vap,press}}(T_{\text{set}})$). The state of the valve can be expressed as follows:

$$\text{Valve state} = \begin{cases} \text{Close} & \text{if } |P_{\text{meas}} - P_{\text{vap,press}}(T_{\text{set}})| \leq P_{\text{hyst}} \\ \text{Open} & \text{otherwise} \end{cases} \tag{A.8}$$

Once the electrovalve (and thus the temperature) was set, we repeated the initial set of measurements that evidenced a thermal gradient's presence. In Figure A.5, we observe that the voltage curves present the expected behavior. The curves are much more similar within a change of 0.5 K.
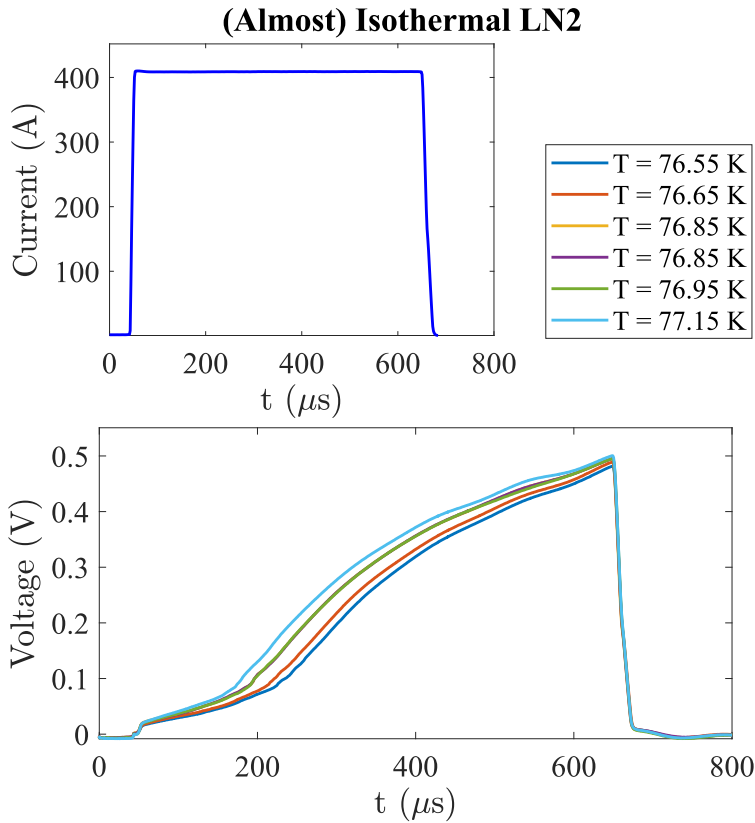
Figure A.5: For the same current and slightly different temperature, we have practically the same voltage drop over 5 mm.

A.3.3. Conclusion

The practical consequences of our findings pointed out that if we want to perform temperature-controlled measurements with the system described above, we need to pay attention to the way we cool down the bath. Specifically, it is not possible to cool down the bath at 65 K and then wait for the entire volume to get back to 77 K, as we would have a thermal gradient across the volume (and across the sample). Even with the temperature control system, we can not ensure that no thermal gradient would appear.

The correct procedure involves cooling the liquid nitrogen temperature bath gradually by a few degrees (e.g. 77 K to 76.5 K, then 76.5 K to 76 K, etc...) and then carry out the measurements for each temperature step. In such a way, the liquid nitrogen bath temperature is more uniform, and we avoid having much colder layers at the bottom with respect to the surface.

A.4. UC model: 1-D and 0-D formulation

A common problem faced when using FEA, is the cost in terms of computational time. The computing time of the UC models per pulse ranges from 30 s to 200 s per analyzed pulse on an Intel(R) Core(TM) i5-7Y57 CPU @ 1.30 GHz). Even if the period of time is reasonable, a large number of pulses and run is required to obtain a complete resistive surface. It is desirable to reduce the calculation time of the UC model. This can be achieved with several approaches. It is possible to develop an analytical model (based on Green's function method), or use advanced computational techniques known as Reduced Order Models [124, 125] for linear thermal problems. The simplest way, however, is to replace the 2-D geometry in the UC model with a 1-D geometry, which means neglecting the influence of silver on the sides of the sample[2]. A further simplification foresees the reduction to a 0-D model. Here we present the formulation and limits of the two approaches.

A.4.1. Formulation and limits of the 0-D and 1-D UC model

In the 0-D approach, all the quantities are homogenized, simplifying the data analysis and significantly improving computational time. Nevertheless, due to the combination of high
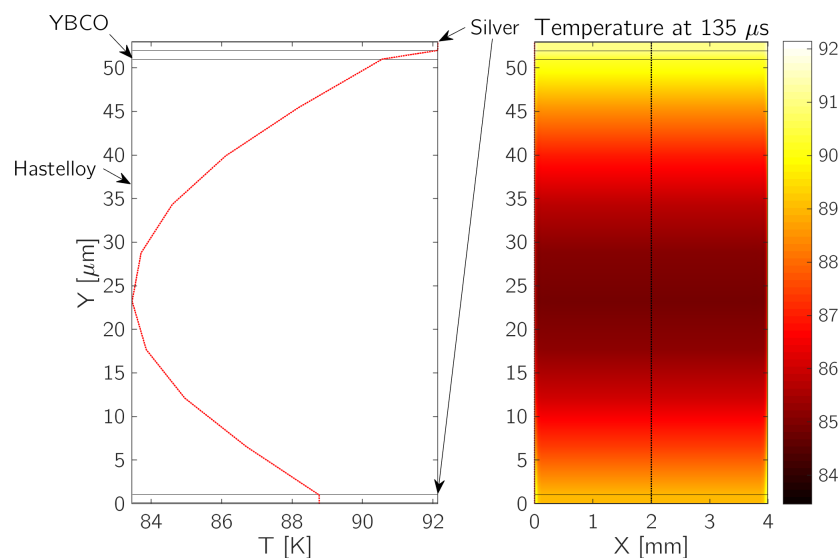
Figure A.6: Temperature at 135 μs calculated on a line crossing the tape from bottom to top of the sample (left) and cross-section heat map (right).

heat generation and short timescale, it is not possible to neglect the dynamic occurring on the cross-section of the tape. The heat diffusion coefficient of the Hastelloy at 77 K is $D = \frac{k}{c_k} = 4.26 \cdot 10^{-6} \mathrm{m^2\,s^{-1}}$ and the diffusion length is $\lambda = 2\sqrt{Dt}$. The pulses we are analyzing have a length of 15 μs to 300 μs. However, at such length, the heat diffuses through 20 μm to 70 μm, and our tapes range in thickness from 50 μm to 100 μm. To verify that the heat can not diffuse in such a short scale, we can show the temperature profile due to the heat generation occurring in the pulses performed on the cross-section of the tape (Figure A.6). In this Figure it is represented the evaluation of the temperature along a line that crosses all the layers from bottom to top, at the center of the tape and the heat map on the cross section for a given time (135 μs). This simulation shows that, for this particular pulse, the temperature distribution is not uniform on the cross-section (The cross-section is not represented in real scale). With the previous evaluations, we can conclude that a 0-D approach can not be used for the data

---

[2]The impact of the silver at the edges in the tape should be further investigated

analysis.

The 1-D UC model is constituted by 4 segments representing the bottom-to-up layered struc-
ture of the tape [e.g. silver(1 μm)-Hastelloy(47 μm)-REBCO(1 μm)-silver(1 μm)]. In Figure A.7a
and Figure A.7b we can see the comparison between temperature distribution and the current
layer sharing. The results are very similar, and we can consider to analyze the data with a 1-D

(a)

(b)
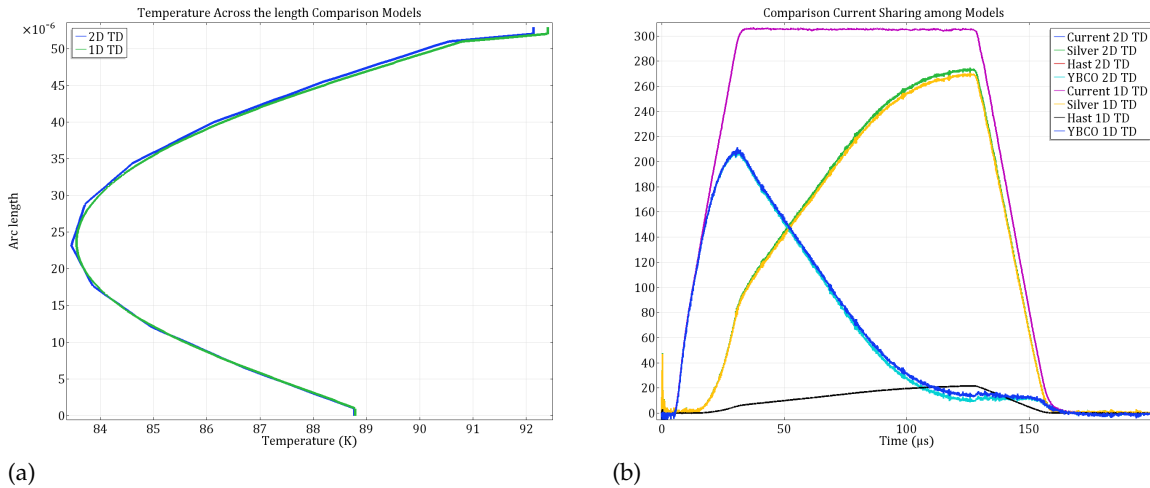
Figure A.7: Comparison between the 2-D and 1-D model. (a) Temperature distribution and (b) current distribu-
tion.

UC model.

However, in Figure A.8a we show the temperature at 135 μs calculated on a line crossing the
tape from left to right (a) and the line along which it has been calculated (b). The effects due
to the silver edges impact the local heating, and this aspect should be further investigated
before choosing as a final approach to the 1-D UC model.

(a)

(b)
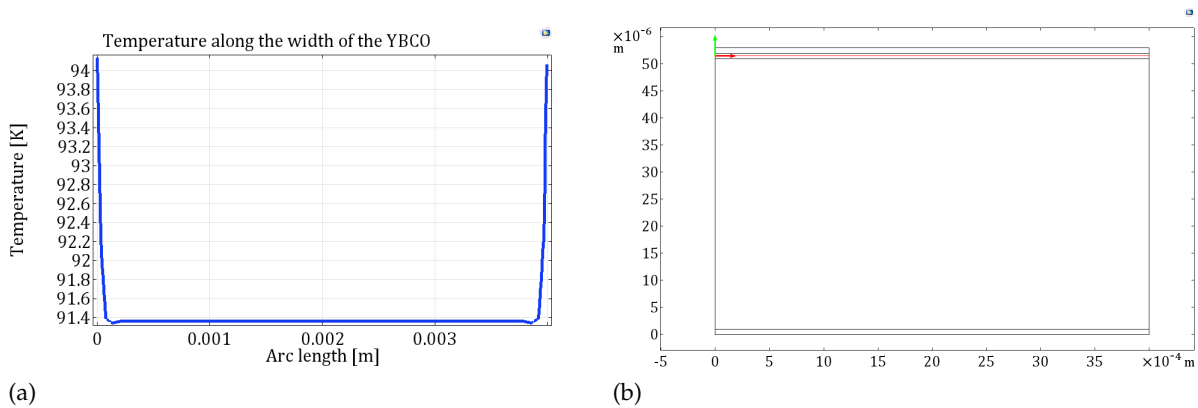
Figure A.8: Temperature at 135 μs calculated on (a) a line crossing the tape from left to right, and line (b) upon
which it has been calculated.

A.5. Superconductors for power applications: an executable and web application to learn about resistive fault current limiters

Given the ever increasing role of electricity in our society, protecting electric grids from faults and surges has become of paramount importance. For this purpose, different technologies have been developed: these include explosive I_s-limiters, high-voltage fuses and air-core reactors. These technologies, while effective, present important limitations, for example added circuit impedance during normal operation, limited scalability, and high maintenance efforts. High-Temperature Superconductors (HTS) can be superconducting in liquid nitrogen (77 K), holding immense promises for our future, such as nuclear fusion and power applications. For instance, in a power system, high short-circuit currents can exceed the current power system's operational current by more than ten times, putting at risk much equipment in the system. The Superconducting Fault Current Limiters (SFCL) can limit the prospective fault current without disconnecting the power system, becoming more important in future grids. With a growing interest in modeling and commercializing SFCLs, a requested challenge is teaching and explaining their operation to students. To help them visualize the potential use and benefits of a SFCL, we created a stand-alone executable app and a web application using COMSOL Multiphysics. The aim of this work is to introduce the readers to the use of RE-BCO coated conductors for SFCL application, with particular focus on the role of the tape's structure and physical parameters on the current limiting behavior. For this purpose, we developed a finite-element model for the electro-thermal behavior of the tape in fault-current limiting applications. The model is implemented in the COMSOL Multiphysics environment and distributed as a COMSOL application, as an executable (HTS modeling website or upon request), and as a web application within the project AURORA (le**a**rning s**u**pe**rc**onductivity th**r**ough **a**pps). With a simulation application, complex concepts can be incorporated behind a user-friendly interface, so that users do not have to deal with unnecessary jargon. In addition, this type of applications enables an easy access to simulation tools that can generate interest in students and provide values to companies.
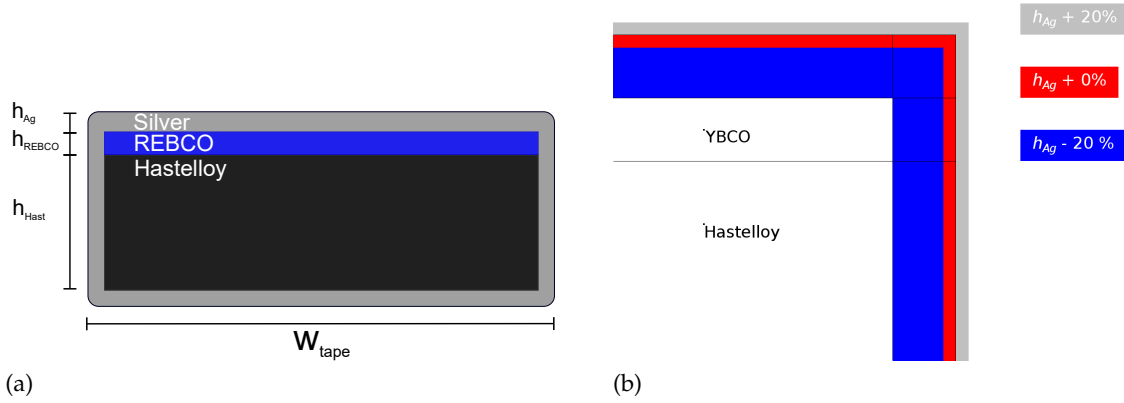
Figure A.9: (a) Cross section of the sample with the geometrical parameters, and (b) modification of the silver thickness.

A.6. Uncertainty and sensitivity analysis by means partial derivatives and numerical tools

The uncertainties related to the input parameters of the UC model are multiple. Experimental measurements, geometry, and material properties contribute significantly to the evaluation of the final results. Sensitivity analysis helps determine which ones drive most of the outcome's variation, helping exclude the others.

An uncertainty analysis conducted using FEA is consequently performed on the major affecting parameters. The simulations are carried out by varying such parameters within a uniform distribution and evaluating the UC model's robustness results in the presence of uncertainty.

A.6.1. Sensitivity Analysis on the UC Model Upon Input Parameters: Resistivity and Current Sharing

The first analysis was carried out on the UC Model in order to evaluate the sensitivity of quantities such as the current or the resistivity on the input parameters.

Regarding the temperature, there is no direct analytical formula to estimate the impact of the uncertainties in a PDE. This work will be carried out in future works.

Analysis on the Resistivity and the current into the REBCO
The resistivity calculated accordingly to the UC model can be written as follows:

$$\rho_{\text{UC}} = \frac{V_{\text{meas}}(t)}{I_{\text{REBCO}}(t)} \cdot \frac{\Sigma_{\text{REBCO}}}{L}. \tag{A.9}$$

The current in the REBCO is calculated as:

$$I_{\text{REBCO}}(t) = I_{\text{tot}}(t) - I_{\text{Ag}}(t) - I_{\text{Hast}}(t), \tag{A.10}$$

where the current in each layer k (see Fig A.9a) can be written as:

$$I_k(t) = J(t) \cdot \Sigma_k = \frac{E(t)}{\rho_k(T)} \cdot (h_k \cdot w_k). \tag{A.11}$$

This equation assumes that the current density is homogenized on the cross-section of the

layers. Since we have $E(t) = V_{\text{meas}}(t)/L$, we obtain the following relation for the resistivity into the REBCO:

$$\rho_{\text{UC}} = V_{\text{meas}}(t) \cdot \frac{h_{\text{REBCO}} w_{\text{REBCO}}}{L} \cdot \frac{1}{\left[I_{\text{tot}}(t) - \frac{V_{\text{meas}}(t)}{L} \left(\frac{h_{\text{Ag}} w_{\text{Ag}}}{\rho_{\text{Ag}}(T)} + \frac{h_{\text{Hast}} w_{\text{Hast}}}{\rho_{\text{Hast}}(T)} \right) \right]}. \tag{A.12}$$

Equation A.12 allows individuating the parameters which uncertainties affects the resitivity curves[3].

As an example of the calculation, we assume that the uncertainties affecting the most the resistivity and current sharing calculation are the following:

- The thickness of the silver h_{Ag};

- The resistivity of the silver $\rho_{\text{Ag}}(T)$;

We will discuss shortly in the next paragraph the impact of other parameters such as h_{Hast}, and we will see how to discriminate whether a parameter affects the quantities of interest significantly or not.

Analytical prediction to perform a sensitivity analysis of the quantities of interest upon the input parameters
One of the methods to perform a sensitivity analysis, knowing the analytical formula, is to differentiate the equations Equation A.10 and Equation A.12, with respect to the input of interest.

$$\frac{\partial I_{\text{REBCO}}}{\partial h_{\text{Ag}}} = -\frac{V_{\text{meas}}(t) w_{\text{Ag}}}{L \rho_{\text{Ag}}(T)}, \tag{A.13}$$

$$\frac{\partial \rho_{\text{UC}}}{\partial h_{\text{Ag}}} = +V_{\text{meas}}^2(t) \cdot \frac{w_{\text{Ag}} h_{\text{REBCO}} w_{\text{REBCO}}}{\rho_{\text{Ag}}(T) L^2} \cdot \frac{1}{\left[I_{\text{tot}}(t) - \frac{V_{\text{meas}}(t)}{L} \left(\frac{h_{\text{Ag}} w_{\text{Ag}}}{\rho_{\text{Ag}}(T)} + \frac{h_{\text{Hast}} w_{\text{Hast}}}{\rho_{\text{Hast}}(T)} \right) \right]^2}. \tag{A.14}$$

From Equation A.13 and Equation A.14, we can see that the variations of the physical quantities of interest with respect to h_{Ag} also depends on the involved dynamics, namely the amplitude of the measured voltage (and also from the measured current).
Consequently, the higher the voltage's amplitude, the more sensitive the current and resistivity variation under variation of the silver thickness.
The differentiation with respect to the resistivity of the silver $\rho_{\text{Ag}}(T)$ is:

$$\frac{\partial I_{\text{REBCO}}}{\partial \rho_{\text{Ag}}} = \frac{V_{\text{meas}}(t) w_{\text{Ag}}}{L \rho_{\text{Ag}}^2(T)}, \tag{A.15}$$

$$\frac{\partial \rho_{\text{UC}}}{\partial \rho_{\text{Ag}}} = -V_{meas}^2(t) \cdot \frac{w_{Ag} h_{\text{REBCO}} w_{\text{REBCO}}}{\rho_{\text{Ag}}^2(T) L^2} \cdot \frac{1}{\left[I_{\text{tot}}(t) - \frac{V_{\text{meas}}(t)}{L} \left(\frac{h_{\text{Ag}} w_{\text{Ag}}}{\rho_{\text{Ag}}(T)} + \frac{h_{\text{Hast}} w_{\text{Hast}}}{\rho_{\text{Hast}}(T)} \right) \right]^2}. \tag{A.16}$$

From Equation A.15 and Equation A.16, we can see that also in this case the variation of the physical quantities of interest (respect to ρ_{Ag}) depends on the involved dynamics (namely the amplitude of the measured voltage and the measured current).
From Equation A.13 - Equation A.14 we observe that with an increase of h_{Ag}, I_{REBCO} decreases while the ρ_{UC} increases. In a similar fashion, from Equation A.15 - Equation A.16, with an

---

[3]Note that $w_{Ag} = w_{Hast} = w_{Tape}$

increasing ρ_{Ag}, I_{REBCO} will increase and the ρ_{UC} will decrease.

From Equation A.10, we can roughly claim that a thicker layer of silver results in a larger amount of current in the silver. As a consequence, less current will flow in the REBCO, and a higher resistivity will be esteemed.

Additionally, a larger resistivity of the silver layer results in less current into the silver, therefore higher current in the REBCO and a lower resistivity of the REBCO.

Quantitative impact of the parameters on the quantities of interest

To evaluate properly the impact of uncertainties on I_{REBCO} and ρ_{UC} one should derive them respect to all the parameters susceptible to variation, meaning:

- h_{Ag} - h_{Hast} - h_{REBCO} - w_{tape}

- $\rho_{\text{Ag}}(T)$ - $\rho_{\text{Hast}}(T)$ - $C_{\text{p,Hast}}(T)$ - etc...

However, to reduce simulations time and avoid too many calculations, we should understand which parameters impact the calculated quantity of interest and respect to the others.

A possible approach, it is to evaluate the ratio between the quantities such as $\partial_{h_{\text{Ag}}} I_{\text{REBCO}}$ and $\partial_{h_{\text{Hast}}} I_{\text{REBCO}}$, or $\partial_{\rho_{\text{Ag}}} I_{\text{REBCO}}$ and $\partial_{\rho_{\text{Hast}}} I_{\text{REBCO}}$ etc. Defining as it follows:

$$\alpha_{I,h_{\text{Ag}}} = \frac{\partial I_{\text{REBCO}}}{\partial h_{\text{Ag}}} = -\frac{V_{\text{meas}}(t) w_{\text{Ag}}}{L\rho_{\text{Ag}}(T)} \qquad \alpha_{I,h_{\text{Hast}}} = \frac{\partial I_{\text{REBCO}}}{\partial h_{\text{Hast}}} = -\frac{V_{\text{meas}}(t) w_{\text{Hast}}}{L\rho_{\text{Hast}}(T)}$$

We can evaluate the quantity:

$$\frac{\alpha_{I,h_{\text{Ag}}}}{\alpha_{I,h_{\text{Hast}}}} = \frac{w_{\text{Ag}}}{\rho_{\text{Ag}}} \frac{\rho_{\text{Hast}}}{w_{\text{Hast}}} \approx \frac{1.2 \cdot 10^{-6}}{2 \cdot 10^{-9}} \approx 600 \tag{A.17}$$

Similarly for the resistivity ρ_{UC}, we obtain:

$$\beta_{\rho,h_{\text{Ag}}} = \frac{\partial \rho_{\text{UC}}}{\partial h_{\text{Ag}}} = \frac{V_{\text{meas}}^2(t) w_{\text{Ag}} h_{\text{REBCO}} w_{\text{REBCO}}}{I_{\text{REBCO}}^2 \cdot L^2 \cdot \rho_{\text{Ag}}(T)} \qquad \beta_{\rho,h_{\text{Hast}}} = \frac{\partial \rho_{\text{UC}}}{\partial h_{\text{Ag}}} = \frac{V_{\text{meas}}^2(t) w_{\text{Hast}} h_{\text{REBCO}} w_{\text{REBCO}}}{I_{\text{REBCO}}^2 \cdot L^2 \cdot \rho_{\text{Hast}}(T)}$$

We can evaluate the quantity:

$$\frac{\beta_{\rho,h_{\text{Ag}}}}{\beta_{\rho,h_{\text{Hast}}}} = \frac{w_{\text{Ag}}}{w_{\text{Hast}}} \frac{\rho_{\text{Hast}}}{\rho_{\text{Ag}}} \approx \frac{1.2 \cdot 10^{-6}}{2 \cdot 10^{-9}} \approx 600 \tag{A.18}$$

From Equation A.17 and Equation A.18 we observe that the height of the silver has a larger impact on the calculation of I_{REBCO} then the height of the Hastalloy, therefore we can neglect the analysis on h_{Hast} for a first evaluation.

With the same method, it is possible to obtain the following table.

$\alpha_{I,h_{\text{Ag}}}/\alpha_{I,h_{\text{Hast}}}$	$\alpha_{I,h_{\text{Ag}}}/\alpha_{I,h_{\text{REBCO}}}$	$\alpha_{I,h_{\text{Ag}}}/\alpha_{I,w_{\text{tape}}}$	$\alpha_{I,\rho_{\text{Ag}}}/\alpha_{I,\rho_{\text{Hast}}}$
$\dfrac{\rho_{\text{Hast}}}{\rho_{\text{Ag}}} \approx 600$	(N.A.)	$\dfrac{w_{\text{Ag}}}{h_{\text{Ag}}} \approx 4000$	$\dfrac{\rho_{\text{Hast}}^2 h_{\text{Ag}}}{\rho_{\text{Ag}}^2 h_{\text{Hast}}} \approx 10^5$
$\beta_{\rho,h_{\text{Ag}}}/\beta_{\rho,h_{\text{Hast}}}$	$\beta_{\rho,h_{\text{Ag}}}/\beta_{\rho,h_{\text{REBCO}}}$	$\beta_{\rho,h_{\text{Ag}}}/\beta_{\rho,w_{\text{tape}}}$	$\beta_{\rho,\rho_{\text{Ag}}}/\beta_{\rho,\rho_{\text{Hast}}}$
$\dfrac{\rho_{\text{Hast}}}{\rho_{\text{Ag}}} \approx 600$	$\dfrac{h_{\text{REBCO}} w_{\text{Ag}}}{\rho_{\text{Ag}} L} \cdot \dfrac{V_{\text{meas}}(t)}{I_{\text{REBCO}}(t)}$	$\dfrac{h_{\text{REBCO}}}{L} \cdot \dfrac{I_{\text{tot}}(t) V_{\text{meas}}(t)}{I_{\text{REBCO}}^2(t)}$	$\dfrac{\rho_{\text{Hast}}^2 h_{\text{Ag}}}{\rho_{\text{Ag}}^2 h_{\text{Hast}}} \approx 10^5$

Table A.1: Impact comparison of the parameters on I_{REBCO} and ρ_{UC}.

In most of the results, we can easily estimate which is the impact of the various parameters. Nevertheless, in some of the evaluations, this impact depends upon the dynamic of the system, and in particular, upon $V_{\mathrm{meas}}(t)$, $I_{\mathrm{tot}}(t)$ and $I_{\mathrm{REBCO}}(t)$. An approximation can be obtained by observing the order of magnitude of such quantities.

$V_{\mathrm{meas}}(t)$ depends on the region of resistivity explored and on the sample used, i.e. 4 mm to 12 mm wide, copper/no copper stabilizer etc. In our case $V_{\mathrm{meas}}(t)$ can ranges from few mV up to 1 V on the length of 5 mm. The $I_{\mathrm{meas}}(t)$ ranges from few A up to 800 A. The $I_{\mathrm{REBCO}}(t)$, calculated by the software, ranges from few A up to 200 A.

In the case of the parameter that impacts the dynamic of the inter-layer current sharing, we

must distinguish the case as represented in the following tables. From the Table, we see that

Pulse regime	Voltage	Current range	Current in REBCO	$\beta_{\rho,h_{\mathrm{Ag}}}/\beta_{\rho,h_{\mathrm{REBCO}}}$	$\beta_{\rho,\rho_{\mathrm{Ag}}}/\beta_{\rho,w_{\mathrm{tape}}}$
Low current	60 mV	200 A	170 A	≈ 0.2	$\approx 8 \cdot 10^{-9}$
Medium current	300 mV	280 A	128 A	≈ 1	$\approx 2 \cdot 10^{-6}$
High current	1 V	400 A	1 A	≈ 26	$\approx 1 \cdot 10^{-3}$

Table A.2: Dynamic dependent impact parameters.

the width plays a big role in the resistivity calculation. However, since w_{tape} can be considered less uncertain than the h_{Ag}, we can neglect it for the first analysis.

The impact of the uncertainty of the REBCO layer becomes less important for higher currents. Consequently, since the current regime we explore is $I > I_c$, we can consider neglecting its influence. However, we performed a sensitivity study on this parameter to verify its impact on every current range.

A.6.2. Modelling Uncertainties through Finite Element Analysis

The outcome of the previous sensitivity analysis is the parameters' choice, mostly affecting the quantities of interest and, therefore, the parameters that perform an uncertainty analysis. The chosen parameters are namely h_{Ag}, h_{REBCO} and $\rho_{\mathrm{Ag}}(T)$.

For the resistivity, multiple simulations have been run, varying the resistivity curve of a certain percentage. For the geometric parameters, the solver will perform a displacement normal to the boundaries. In Figure A.9b, there is an example of the modified geometry where the colored regions represent a change in percentage of the nominal thickness (i.e. $h_{\mathrm{Ag}} = 1\,\mu\mathrm{m}$). In particular, here the variation of the thickness is of the 20 %, where every boundary has been displaced of $d_{\mathrm{Ag}} = \pm 0.2\,\mu\mathrm{m}$. Time-Dependent simulations have been done for three pulses in different current regimes. The goal is to validate the dependence of the variation of outputs such as temperature and current in REBCO and resistivity.

We expect, in fact, that the uncertainty on such quantities depends on the amplitude of the voltage from Equation A.13 and Equation A.14, therefore by the regime of resistivity and by the length on which the measurements is done.

Regarding the temperature, further studies on an analytic estimation of the sensitivity of temperature upon the input parameters' uncertainty will be done in future works.

(a)

(b)

(c)
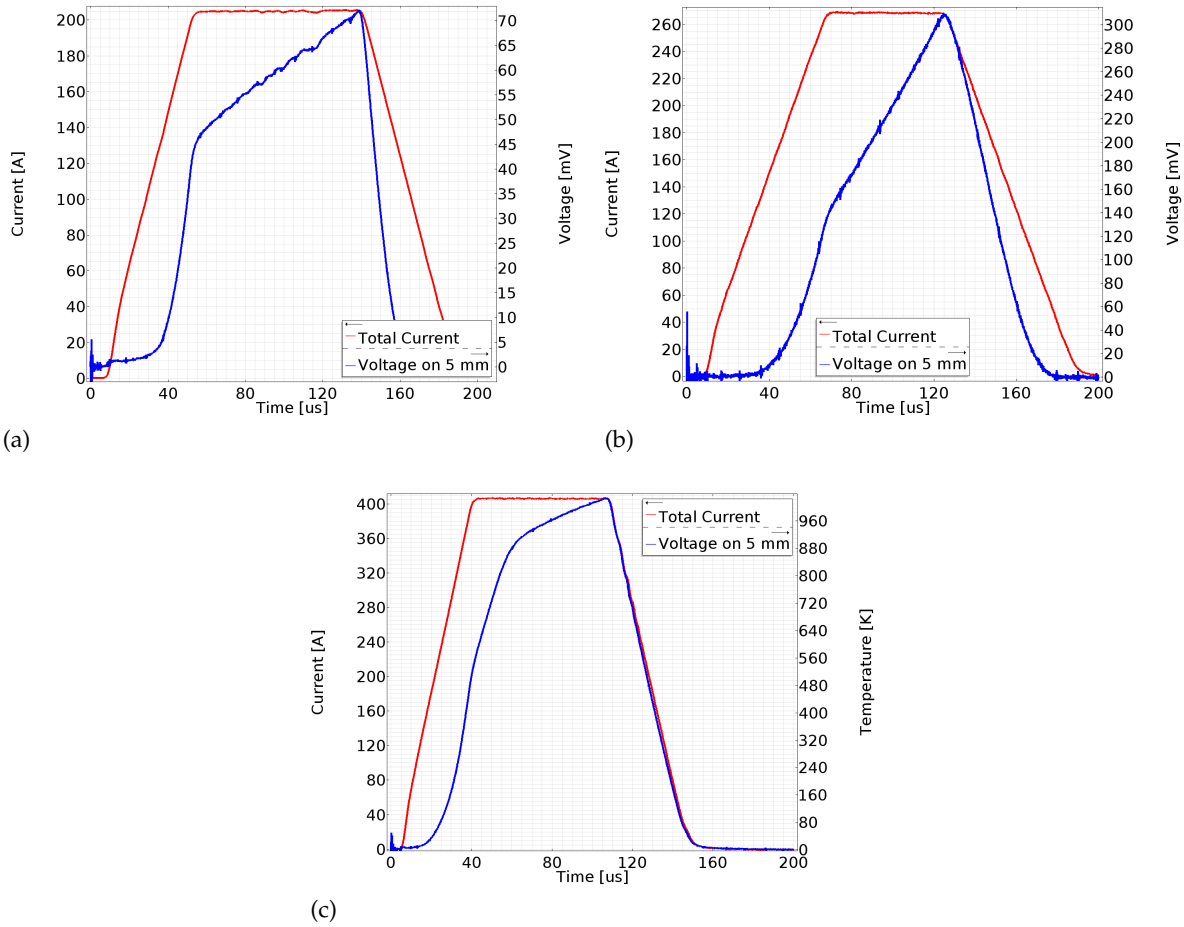
Figure A.10: Voltage and current for (a) low, (b) medium, and (c) high current level.

A.6.3. Current regime explored

The current regime explored are distinguished into:

- Low current regime Figure A.10a

- Medium current regime Figure A.10b

- High current regime Figure A.10c

The thickness of the silver layer has been modified all around the tape. In case of low and medium current regime, the boundaries of the silver layer have been displaced of between $d_{Ag} = -0.3\,\mu m$ and $d_{Ag} = +0.3\,\mu m$ (with a step of $\Delta d_{Ag} = 0.1\,\mu m$, resulting into a maximum percentage variation of 30 %.

In case of high current regime the displacement has been of $d_{Ag} = \pm 0.3\,\mu m$ ($\Delta d_{Ag} = 0.1\,\mu m$ - 10 %).

(a)

(b)

(c)
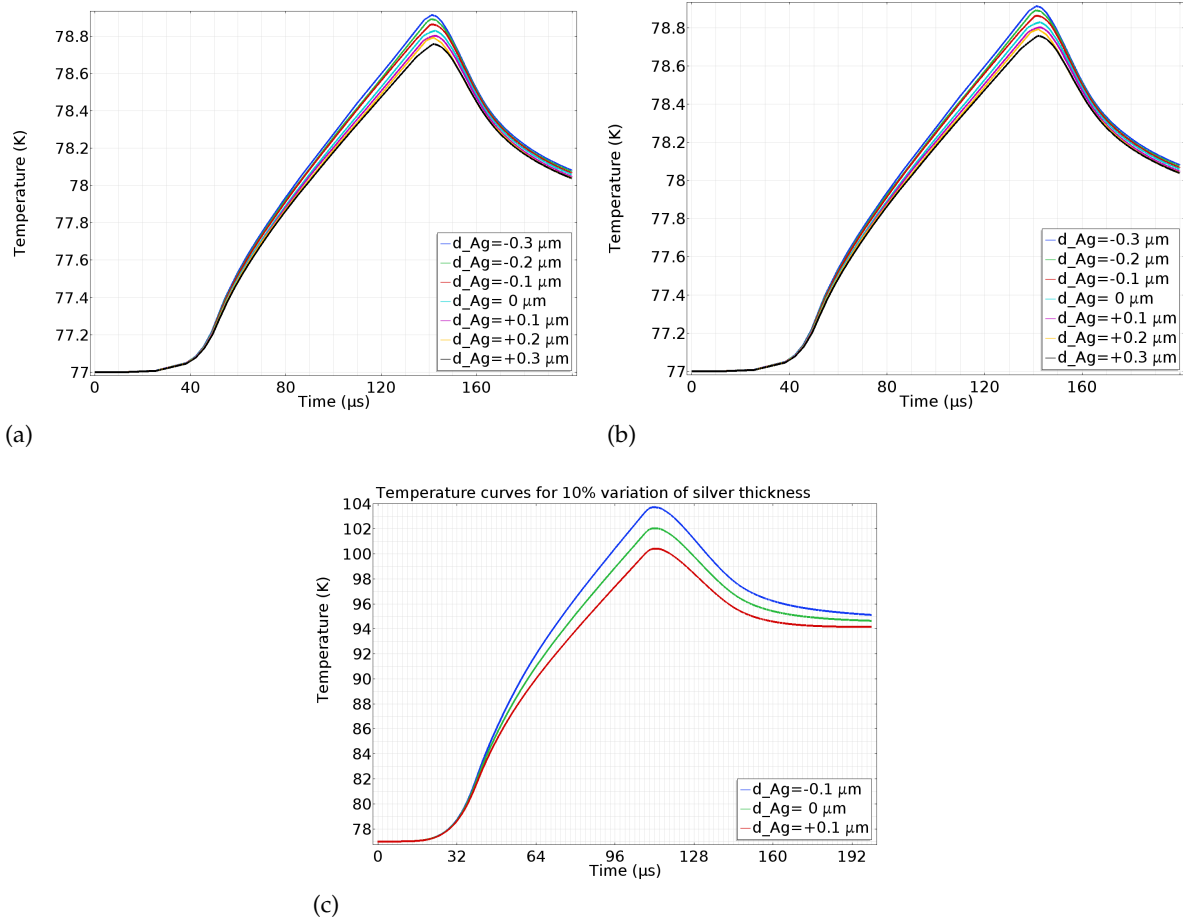
Figure A.11: Temperature profile of the REBCO layer for (a) low, (b) medium, and (c) high current level.

Temperature sensitivity

Only the results obtained by FEM are available, and from Figure A.11a to Figure A.11c, we can see how the error depends on the current regime we are performing the simulations. The analysis shows that when the silver thickness is varied of 30 %, the temperature is not heavily affected (low and medium current regime).

In a high current regime, we avoided varying the silver thickness more than 10 % due to the already dramatic sensitivity at such current amplitude and heating rate.

Furthermore, the error due to the numerical solver here it is not estimated, but it is clear that the higher the heating rate and the temperature rise it is, the higher the error we commit.
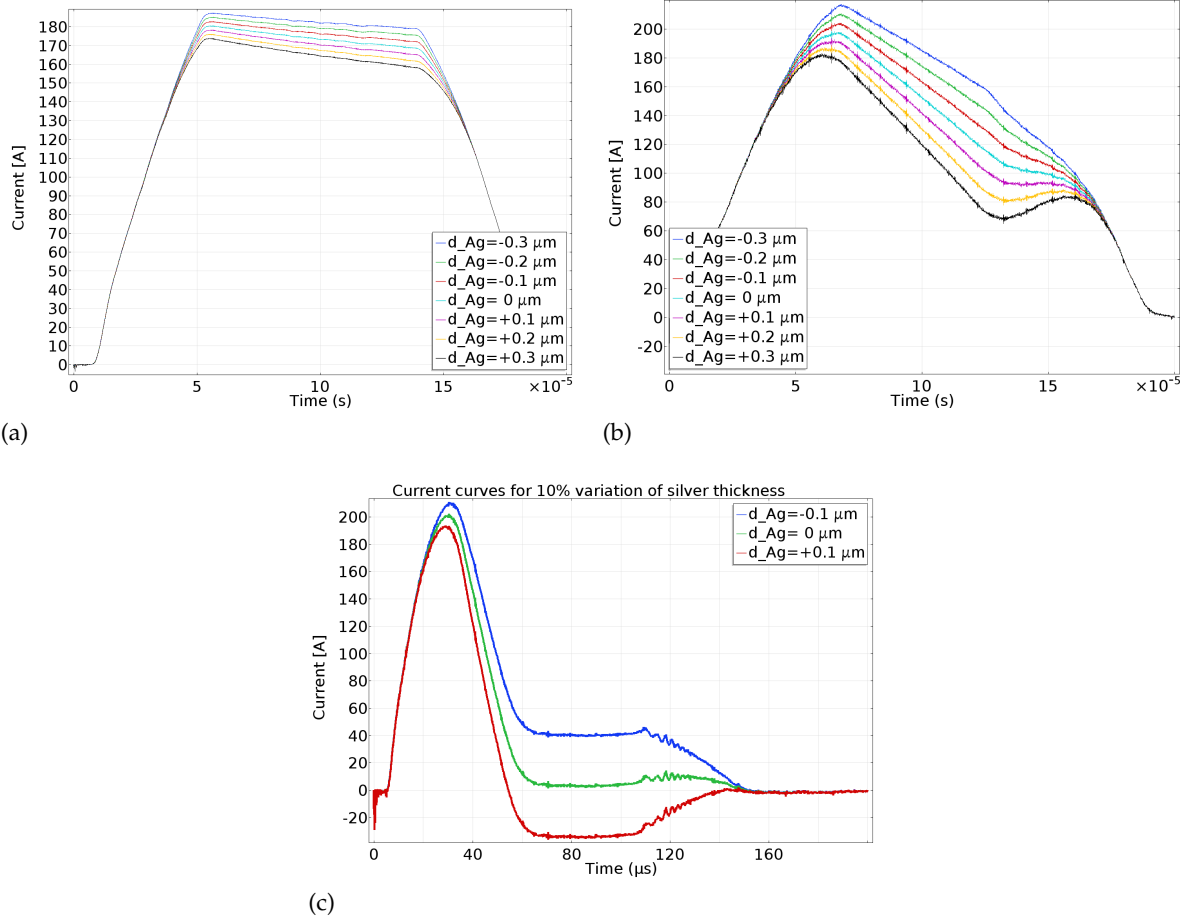
Figure A.12: Current in the REBCO layer for (a) low, (b) medium, and (c) high current level.

Current sensitivity

The results obtained by FEM are plotted from Figure A.12a to Figure A.12c. Also, here the error depends on the current regime where we are performing the simulations. The analysis shows that when the silver thickness is varied of 30 % (low and medium current regime), the temperature presents a remarkable for the medium current regime error.

In the high current regime, the result is again dramatic, being that the current flowing into the REBCO for less silver results to be negative.

111
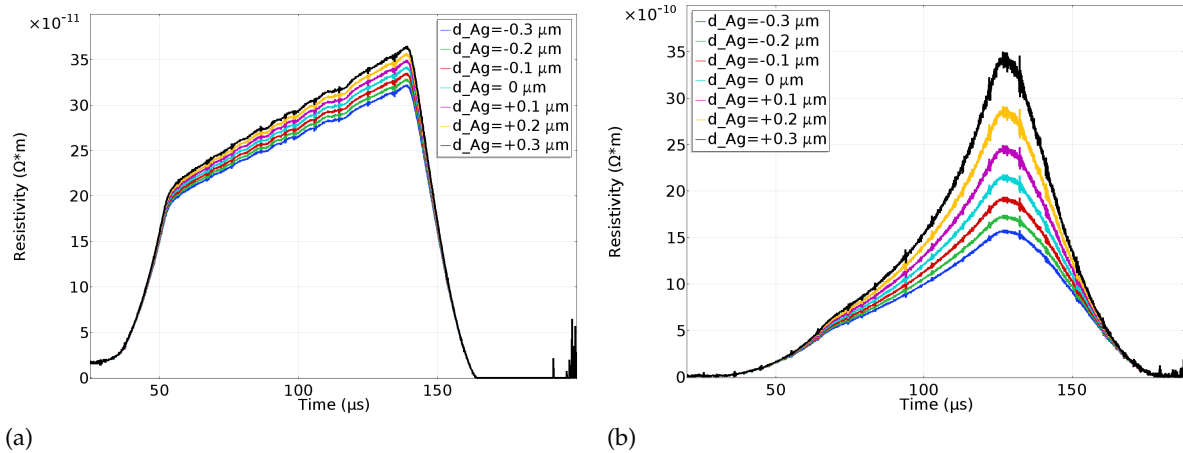
Figure A.13: Resistivity of the REBCO layer for (a) low, (b) medium current level.

Resistivity sensitivity

The results obtained by FEM are plotted in Figure A.12a and Figure A.13b. Also, here the error depends on the current regime where we are performing the simulations. The analysis shows that when the silver thickness is varied by 30 % (low and medium current regime), the temperature presents a remarkable error. If on the one side the 30 % it is a high variation, the 10 % of variation in the thickness of silver it is more likely to occur, and the error (overall for the medium current regime) it is already higher then the error committed with the magnetic relaxation criteria.

In the case of a high current regime, we avoided reporting the results because of the negative current into the REBCO. The resistivity curves were varying in fact of more than 100 %, and plot them together was not meaningful.

A.6.4. Impact of the uncertainties on the extracted resistivity data $\rho_{OC}(I_{REBCO}, T)$

The physical reason for this strong dependence comes to the regime of resistivity. For higher current and voltage, the current component of silver prevails on the current component of the REBCO. As a result, more or less silver will majorly affect the current amount in the silver layer and therefore the other quantities such as temperature and resistivity.

A mesh sensitivity analysis might benefit accuracy as well, but this aspect has a lower priority. The highest priorities are given by:

- Further studies will be done to estimate the presence of uncertainties in the PDE and, in particular, in the Heat Equation.

- A quantitative sensitivity analysis must be done. So far, only a qualitative analysis has been possible. This will be possible implementing the Sensitivity Analysis in the solvers node with a Time-Dependent simulation (apparently it is possible, but I have not managed yet).

- As previously showed, multiple inputs might affect the resistivity calculated. Further analysis of such properties will be performed.

List of Figures

113

List of Tables

Bibliography

[1] David Goodstein and Judith Goodstein. Richard Feynman and the History of Super-conductivity. *Physics in Perspective*, 2(1):30–47, 2000. (see page: 1)

[2] Kamerlingh Onnes. Further experiments with liquid helium. On the change of electric resistance of pure metals at very low temperatures, etc. V. The disappearance of the resistance of mercury.". *Comm. Phys. Lab. Univ. Leiden*, 122b, 1911. (see page: 1)

[3] Michael Tinkham. *Introduction to Superconductivity*. Dover Publications, 2 edition, jun 2004. (see pages: 1, 2)

[4] W Meissner and R Ochsenfeld. Ein neuer Effekt bei Eintritt der Supraleitfähigkeit. *Die Naturwissenschaftenn*, 21(September):787–788, 1933. (see page: 1)

[5] J Bardeen, L Cooper, and J R Schrieffer. Theory of Superconductivity. *Physical Review*, 108(5):1175–1204, 1957. (see page: 2)

[6] John David Jackson. *Classical Electrodynamics (Second ed.)*. John Wiley & Sons, 1975. (see page: 2)

[7] A.C. Rose-Innes and E.H. Rhoderick. *Introduction to Superconudctivity*. Pergamon, second edition, 1978. (see page: 3)

[8] J G Bednorz and K A Müller. Possible highTc superconductivity in the BaLaCuO system. *Zeitschrift für Physik B Condensed Matter*, 64(2):189–193, 1986. (see page: 3)

[9] François Roy. *Modeling and Characterization of Coated Conductors Applied to the Design of Modeling and Characterization of Coated Conductors Applied to the Design of Superconducting Fault Current Limiters*. Phd thesis, EPFL, 2010. (see pages: 3, 5, 42, 48, 50, 78, and 119)

[10] Hideo Hosono, Akiyasu Yamamoto, Hidenori Hiramatsu, and Yanwei Ma. Recent advances in iron-based superconductors toward applications. *Materials Today*, 21(3):278–302, 2018. (see pages: 3, 119)

[11] G. Blatter, M. V. Feigel'Man, V. B. Geshkenbein, A. I. Larkin, and V. M. Vinokur. Vortices in high-temperature superconductors. *Reviews of Modern Physics*, 66(4):1125–1388, 1994. (see pages: 3, 5, and 74)

[12] F. Roy, B. Dutoit, F. Grilli, and F. Sirois. Magneto-thermal finite element modeling of 2nd generation HTS for FCL design purposes. *Journal of Physics: Conference Series*, 97(1), 2008. (see pages: 4, 28, and 48)

[13] Igor Aranson, Alex Gurevich, and Valerii Vinokur. Vortex Avalanches and Magnetic Flux Fragmentation in Superconductors. *Phys. Rev. Lett.*, 87(6):67003, 2001. (see page: 4)

[14] M Prester. Current transfer and initial dissipation in high- superconductors. *Superconductor Science and Technology*, 11(4):333–357, apr 1998. (see page: 4)

[15] Arup K Ghosh. V–I transition and n-value of multifilamentary LTS and HTS wires and cables. *Physica C: Superconductivity*, 401(1):15–21, 2004. (see page: 4)

[16] X Zhang, Z Zhong, J Geng, B Shen, J Ma, C Li, H Zhang, Q Dong, and T A Coombs. Study of Critical Current and n-Values of 2G HTS Tapes: Their Magnetic Field-Angular Dependence. *Journal of Superconductivity and Novel Magnetism*, 31(12):3847–3854, 2018. (see pages: 4, 33, and 70)

[17] J Bardeen and M J Stephen. Theory of the motion of vortices in superconductors. *Physical Review*, 140(4A):A1197–A1207, 1965. (see pages: 5, 76)

[18] J R Clem. Local temperature-gradient contribution to flux-flow viscosity in superconductors. *Physical Review Letters*, 20(14):735–738, 1968.

[19] M Tinkham. Viscous flow of flux in type-ii superconductors. *Physical Review Letters*, 13(26):804–807, 1964. (see pages: 5, 76)

[20] S Stavrev, F Grilli, B Dutoit, N Nibbio, E Vinot, I Klutsch, G Meunier, P Tixador, Y Yang, and E Martinez. Comparison of Numerical Methods for Modelling of Superconductors. *IEEE Transactions on Magnetics*, 38(2):849–852, 2002. (see page: 5)

[21] Joseph Duron, Francesco Grilli, Bertrand Dutoit, and Svetlomir Stavrev. Modelling the E – J relation of high- T c superconductors in an arbitrary current range. *Physica C: Superconductivity*, 401(1-4):231–235, 2004. (see pages: 5, 68, and 79)

[22] W Paul, M Chen, M Lakner, J Rhyner, D Braun, and W Lanz. Fault current limiter based on high temperature superconductors ± di erent concepts , test results , simulations , applications. *Physica C: Superconductivity*, 354:27–33, 2001. (see page: 6)

[23] Xavier Obradors and Teresa Puig. Coated conductors for power applications: materials challenges. *Superconductor Science and Technology*, 27(4):44003, mar 2014. (see page: 6)

[24] H W Weijers, U P Trociewitz, W D Markiewicz, J Jiang, D Myers, E E Hellstrom, A Xu, J Jaroszynski, P Noyes, Y Viouchkov, and D C Larbalestier. High Field Magnets With HTS Conductors. *IEEE Transactions on Applied Superconductivity*, 20(3):576–582, jun 2010. (see page: 6)

[25] J Lu, E.˜S. Choi, and H.˜D. Zhou. Physical properties of Hastelloy C-276 at cryogenic temperatures. *Journal of Applied Physics*, 103(6):64906–64908, mar 2008. (see pages: 6, 47)

[26] V Selvamanickam, M Heydari Gharahcheshmeh, A Xu, Y Zhang, and E Galstyan. Critical current density above 15 MA cm2 at 30 K, 3 T in 2.2 um thick heavily-doped (Gd,Y)Ba2Cu3Oxsuperconductor tapes. *Superconductor Science and Technology*, 28(7):72002, may 2015. (see page: 6)

[27] Goran Majkic, Rudra Pratap, Aixia Xu, Eduard Galstyan, and Venkat Selvamanickam. Over 15MA/cm(2) of critical current density in 4.8μm thick, Zr-doped (Gd,Y)Ba(2)Cu(3)O(x) superconductor at 30K, 3T. *Scientific reports*, 8(1):6982, may 2018. (see page: 6)

[28] M. K. Wu, J. R. Ashburn, C. J. Torng, P. H. Hor, R. L. Meng, L. Gao, Z. J. Huang, Y. Q. Wang, and C. W. Chu. Superconductivity at 93 K in a new mixed-phase Y-Ba-Cu-O compound system at ambient pressure. *Physical Review Letters*, 58(9):908–910, mar 1987. (see pages: 6, 15, 27, and 69)

[29] V Braccini, A Xu, J Jaroszynski, Y Xin, D C Larbalestier, Y Chen, G Carota, J Dackow, I Kesgin, Y Yao, A Guevara, T Shi, and V Selvamanickam. Properties of recent IBAD-MOCVD coated conductors relevant to their high field, low temperature magnet use. *Superconductor Science and Technology*, 24(3):35001, dec 2010. (see page: 7)

[30] Robert F Service. New Superconductor Stands Up to Magnetic Fields. *Science*, 268(5211):644, 1995. (see page: 7)

[31] Seungyong Hahn, Kwanglok Kim, Kwangmin Kim, Xinbo Hu, Thomas Painter, Iain Dixon, Seokho Kim, Kabindra R Bhattarai, So Noguchi, Jan Jaroszynski, and David C Larbalestier. 45.5-tesla direct-current magnetic field generated with a high-temperature superconducting magnet. *Nature*, 570(7762):496–499, 2019. (see page: 7)

[32] Martin Nikolo. Superconductivity: A guide to alternating current susceptibility measurements and alternating current susceptometer design. *American Journal of Physics*, 63(1):57–65, 1995. (see page: 7)

[33] Frederick S. Wells, Alexey V. Pan, Stephen Wilson, Igor A. Golovchanskiy, Sergey A. Fedoseev, and Anatoly Rozenfeld. Dynamic magneto-optical imaging of superconducting thin films. *Superconductor Science and Technology*, 29(3), 2016. (see page: 7)

[34] Yusheng Zhou, Yuejin Tang, Jingdong Li, Bin Wei, and Jing Shi. Quench and recovery behaviors of Bi-2223/Ag HTS tapes under pulsed over-currents with different durations. *Physica C: Superconductivity*, 433(1):37–42, 2005. (see page: 8)

[35] D Bourgault, S Pavard, R Tournier, L Porcar, N Caillault, and L Carbone. Current limitation capability of bulk Bi2223 material. *Physica C: Superconductivity*, 372-376:1598–1601, 2002. (see page: 8)

[36] V Meerovich, V Sokolovsky, L Prigozhin, and D Rozman. Dynamic response of {HTS} composite tapes to pulsed currents. *Superconductor Science and Technology*, 19(4):267–275, feb 2006. (see page: 8)

[37] L Frolek, J Oravec, and J S\uouc. Impulse measurement of dynamic current-voltage curves of superconducting tape at various lengths and shapes of current waves. *Journal of Physics: Conference Series*, 97:12085, feb 2008. (see page: 8)

[38] A Ishiyama, T Iwata, H Ueda, S Mukoyama, and Y Shiohara. Transient Stability Characteristics of Parallel-Connected YBCO Coated Conductors for Power Transmission Cables. *IEEE Transactions on Applied Superconductivity*, 17(2):1672–1675, jun 2007. (see page: 8)

[39] J W Lue, M J Gouge, and R C Duckworth. Over-current testing of HTS tapes. *IEEE Transactions on Applied Superconductivity*, 15(2):1835–1838, jun 2005.

[40] M T González, S Vidal, J Viña, M R Osorio, J Maza, and F Vidal. Electric field versus current density curves in melt-textured samples of YBa2Cu3O7δ under currents well above the critical current. *Physica C: Superconductivity*, 372-376:1852–1854, 2002. (see page: 8)

[41] Milind N Kunchur, David K Christen, and Julia M Phillips. Observation of free flux flow at high dissipation levels in YBa2Cu3O7 epitaxial films. *Physical Review Letters*, 70(7):998–1001, 1993. (see pages: 8, 19, 20, 74, and 76)

[42] I Falorio, E A Young, and Y Yang. E-J Characteristic of 2G YBCO Coated Conductor Tapes at Different Temperatures. *Physics Procedia*, 36:1462–1467, 2012. (see pages: 8, 19, 67, 69, 75, 76, and 93)

[43] Iole Falorio, Edward A Young, and Yifeng Yang. Flux pinning distribution and E-J characteristics of 2G YBCO Tapes. *Journal of Physics: Conference Series*, 507(2):22004, may 2014. (see pages: 8, 19, 67, 69, 75, 76, and 93)

[44] Milind N. Kunchur, D. K. Christen, C. E. Klabunde, and Kamel Salama. Exploring the dissipative regime of superconductors for practical current-lead applications. *Applied Physics Letters*, 67(6):848, 1995. (see pages: 8, 74)

[45] Frédéric Sirois, Jonathan Coulombe, and Antoine Bernier. Characterization of the superconducting to normal transition of HTS coated conductors by fast pulsed current measurements. *IEEE Transactions on Applied Superconductivity*, 19(3):3585–3590, 2009. (see pages: 8, 10, 19, 26, 42, and 92)

[46] Frédéric Sirois, Jonathan Coulombe, François Roy, and Bertrand Dutoit. Characterization of the electrical resistance of high temperature superconductor coated conductors at high currents using ultra-fast regulated current pulses. *Superconductor Science and Technology*, 23(3):3–8, 2010. (see pages: 8, 10, 26, and 92)

[47] Sci-Consulting Sàrl. 8-channel Isolated Amplifier System. Technical report, SCI Consulting, 2015. (see pages: 12, 13, 14, and 113)

[48] Simon Richard. *Caracterisation de rubans supraconducteurs en regime sur critique a l'aide de pulses de courant dans les microsecondes*. PhD thesis, Polytechnique Montreal, 2019. (see pages: 12, 13, 28, 33, 38, and 92)

[49] M. Lao, J. Hänisch, S. Kauffmann-Weiss, R. Gehring, H. Fillinger, A. Drechsler, and B. Holzapfel. High current variable temperature electrical characterization system for superconducting wires and tapes with continuous sample rotation in a split coil magnet. *Review of Scientific Instruments*, 90(1), 2019. (see pages: 14, 33, and 70)

[50] M. Therasse, M. Decroux, L. Antognazza, M. Abplanalp, and O. Fischer. Electrical characteristics of DyBCO coated conductors at high current densities for fault current limiter application. *Physica C: Superconductivity*, 468(21):2191–2196, 2008. (see page: 18)

[51] Mauricio Ruibal, Gonzalo Ferro, Manuel R. Osorio, Jesús Maza, José A. Veira, and Félix Vidal. Size effects on the quenching to the normal state of YBCO thin-film superconductors. *Physical Review B - Condensed Matter and Materials Physics*, 75(1):1–5, 2007. (see page: 19)

[52] A. Lehner, A. Heinrich, K. Numssen, and H. Kinder. Probing the temperature during switching of YBCO films. *Physica C: Superconductivity and its Applications*, 372-376:1619–1621, 2002. (see page: 19)

[53] S. Reymond, L. Antognazza, M. Decroux, E. Koller, P. Reinert, and Fischer. Current-induced highly dissipative domains in high-(formula presented) thin films. *Physical Review B - Condensed Matter and Materials Physics*, 66(1):1–7, 2002. (see page: 19)

[54] M. Decroux, L. Antognazza, N. Musolino, E. De Chambrier, S. Reymond, J. M. Triscone, O. Fischer, W. Paul, and M. Chen. Properties of YBCO films at high current densities: fault current limiter implications. *IEEE Transactions on Applied Superconductivity*, 11(1 II):2046–2049, 2001. (see page: 19)

[55] Louis Antognazza, Mathieu Therasse, Michel Decroux, Frangois Roy, Bertrand Dutoit, Markus Abplanalp, and Øystein Fischer. Comparison between the behavior of hts thin film grown on sapphire and coated conductors for fault current limiter applications. *IEEE Transactions on Applied Superconductivity*, 19(3):1960–1963, 2009. (see page: 19)

[56] Simon Richard, Frederic Sirois, and Christian Lacroix. Post-processing method for extracting the resistivity of Rare-Earth Barium Copper Oxide (REBCO) coated conductors in over-critical current conditions from ultra-fast V-I pulsed current measurements. *Journal of Applied Physics*, 126(023902):023902, 2019. (see pages: 26, 28, 36, 38, 64, 65, 68, 70, 75, and 116)

[57] N Riva, S Richard, F Sirois, C Lacroix, B Dutoit, F Grilli, A Pulsed Current, and Measurements Pcm. Overcritical Current Resistivity of YBCO-Coated Conductors Through Combination of PCM and Finite-Element Analysis. *IEEE Transactions on Applied Superconductivity*, 29(5):6601705, 2019. (see pages: 26, 33, 58, 64, 65, 68, 70, 75, and 116)

[58] COMSOL Multiphysics® v. 5.4. (Website). (see pages: 26, 78)

[59] Shengnan Zou, Víctor M R Zermeño, A Baskys, A Patel, Francesco Grilli, and B A Glowacki. Simulation and experiments of stacks of high temperature superconducting coated conductors magnetized by pulsed field magnetization with multi-pulse technique. *Superconductor Science and Technology*, 30(1):014010, 2017. (see pages: 26, 48)

[60] HTS MODELING WORKGROUP. HTS Modelling Website, 2012. (see page: 26)

[61] Drew W Hazelton. 2G HTS Wire Development at SuperPower. Technical report, SuperPower, 2016. (see page: 27)

[62] A Sakurai and M Shiotsu. Transient Pool Boiling Heat TransferPart 1: Incipient Boiling Superheat. *Journal of Heat Transfer-transactions of The Asme*, 99:547–553, 1977. (see pages: 27, 28)

[63] A Sakurai, M Shiotsu, and K Hata. Boiling heat transfer characteristics for heat inputs with various increasing rates in liquid nitrogen. *Cryogenics*, 32(5):421–429, 1992. (see pages: 27, 28)

[64] Dresner Lawrence. *Stability ofsuperconductors*. Plenum Press, Ney-York, 1995. (see page: 27)

[65] Jamie R. Nuñez, Christopher R. Anderton, and Ryan S. Renslow. Optimizing colormaps with consideration for color vision deficiency to enable accurate interpretation of scientific data. *PLoS ONE*, 13(8):1–14, 2018. (see page: 29)

[66] Charles-henri Bonnard, Frédéric Sirois, Christian Lacroix, and Gaëtan Didier. Multi-scale model of resistive-type superconducting fault current limiters based on 2G HTS coated conductors. *Supercond. Sci. Technol.*, 30(014005):014005, 2017. (see pages: 29, 33, 68, 69, and 79)

[67] Ernst Helmut Brandt and Mikhail Indenbom. Type-II-superconductor strip with current in a perpendicular magnetic field. *Physical Review B*, 48(17):12893–12906, 1993. (see page: 38)

[68] Ernst Helmut Brandt and Grigorii P. Mikitik. Why an ac Magnetic Field Shifts the Irreversibility Line in Type-II Superconductors. *Physical Review Letters*, 89(2):1–4, 2002. (see pages: 38, 43)

[69] Y. B. Kim, C. F. Hempstead, and A. R. Strnad. Critical persistent currents in hard super-conductors. *Physical Review Letters*, 9(7):306–309, 1962. (see page: 43)

[70] Bright Chimezie Robert, Muhammad Umar Fareed, and Harold Steven Ruiz. How to Choose the Superconducting Material Law for the Modelling of 2G-HTS Coils. *Materials*, 12(2679):1–19, 2019. (see page: 43)

[71] S C Wimbush and N M Strickland. A Public Database of High-Temperature Superconductor Critical Current Data. *IEEE Transactions on Applied Superconductivity*, 27(4):1–5, jun 2017.

[72] Super Power. Super Power 2G HTS CC Material Safety Data Sheet. (see page: 43)

[73] Victor M R Zermeno, Asger B Abrahamsen, Nenad Mijatovic, Bogi B Jensen, and Mads P Sørensen. Calculation of alternating current losses in stacks and coils made of second generation high temperature superconducting tapes for large scale applications. *Journal of Applied Physics*, 114(17):173901, 2013.

[74] Kailash Prasad Thakur, Ashish Raj, Ernst Helmut Brandt, Jozef Kvitkovic, and Sastry V. Pamidi. Frequency-dependent critical current and transport ac loss of superconductor strip and Roebel cable. *Superconductor Science and Technology*, 24(6), 2011. (see page: 43)

[75] MatLab. *MATLAB R2019b*. The Mathworks, Inc., Natick, Massachusetts, 2017. (see pages: 48, 59)

[76] E J Schlossmacher. An Iterative Technique for Absolute Deviations Curve Fitting. *Journal of the American Statistical Association*, 68(344):857–859, 1973. (see page: 48)

[77] T Nakamura, Y Takamura, N Amemiya, K Nakao, and T Izumi. Longitudinal inhomogeneity of DC current transport properties in Gd-system HTS tapes – Statistical approach for system design. *Cryogenics*, 63:17–24, 2014. (see page: 51)

[78] X Li, A B Yahia, G Majkic, M Kochat, S Kar, and V Selvamanickam. Reel-To-Reel Critical Current Measurement of REBCO Coated Conductors. *IEEE Transactions on Applied Superconductivity*, 27(4):1–5, jun 2017. (see page: 51)

[79] Jonathan Schaffer. What Not to Multiply Without Necessity. *Australasian Journal of Philosophy*, 93(4):644–664, 2015. (see page: 57)

[80] C.M. Barry. Who sharpened the Occam's Razor?, 2015. (see page: 57)

[81] Hadamard Jacques. Sur les Problèmes aux Dérivées Partielles et Leur Signification Physique. *Princeton University Bulletin*, 13:49–52, 1902. (see page: 57)

[82] D. Ormoneit. A regularization approach to continuous learning with an application to financial derivatives pricing. *Neural Networks*, 12(10):1405–1412, 1999. (see page: 58)

[83] Jonathan L. Ticknor. A Bayesian regularized artificial neural network for stock market forecasting. *Expert Systems with Applications*, 40(14):5501–5506, 2013. (see page: 58)

[84] Xipan Li, Li Qi, Shuangyang Zhang, Shixian Huang, Jian Wu, Lijun Lu, Yanqiu Feng, Qianjin Feng, and Wufan Chen. Model-Based Optoacoustic Tomography Image Reconstruction With Non-local and Sparsity Regularizations. *IEEE Access*, 7:102136–102148, 2019. (see page: 58)

[85] Wei Liu, Zhaowen Yan, Jianwei Wang, Zheng Min, and Zhangqiang Ma. An Improved Equivalent Dipole Moment Source Model Based on Regularization Optimization Method for near Field-Far Field Conversion. *IEEE Access*, 8:42504–42518, 2020. (see page: 58)

[86] John D'Errico. Understanding Gridfit. Surface Fitting using Gridfit, 2020. (see page: 58)

[87] Garcia Damina. smoothn, 2020.

[88] Peter Goldstein. RegularizeData3D, 2020.

[89] Damien Garcia. Robust Smoothing of Gridded Data in One and Higher Dimensions with Missing Values. *Comput. Stat. Data Anal.*, 54(4):1167–1178, apr 2010. (see pages: 58, 62)

[90] Jason Nicholson. Introduction to Regularizing with 2D and 3D Data and Monotonic Constraints (Website), 2019. (see pages: 59, 60, and 67)

[91] R. L. Burden and J. D. Faires. *Numerical Analysis*. PWS Publishing Co. Boston, MA,, fifth edit edition, 1957. (see page: 61)

[92] Peter Goldstein. A Numerical Second Derivative from Three Points. (see page: 61)

[93] R James, G., Witten, D., Hastie, T., Tibshirani. *An Introduction to Statistical Learning - with Applications in R*. Springer, 2013. (see pages: 62, 68)

[94] C. P. Hansen. Regularization Tools - A Matlab Package for Analysis and Solution of Discrete Ill-Posed Problems. *Numerical Algorithms*, 6(March):1–35, 2008. (see pages: 62, 63)

[95] James E Gentle. *Numerical Linear Algebra for Applications in Statistic*, volume 53. Springer, 2013. (see page: 62)

[96] W. Vogt. Negative Binomial Distribution. *Dictionary of Statistics & Methodology*, 2015. (see page: 63)

[97] Eric W Weisstein. Normal Equation. (see page: 63)

[98] A. J. Moakes and M. V. Wilkes. *A Short Introduction to Numerical Analysis*. Wiley, 1967. (see page: 63)

[99] Gene H Golub and Charles F Van Loan. *Matrix Computations (3rd Ed.)*. Johns Hopkins University Press, USA, 1996. (see page: 63)

[100] Stephen Boyd and Lieven Vandenberghe. *Introduction to Applied Linear Algebra*. Cambridge University Press, 2018. (see page: 63)

[101] H. Press William, A. Teukolsky Saul, T. Vetterling William, and P. Flannery Brian. *Numerical recipes: The Art of Scientific Computing*. Cambridge University Press, third edition, 2007. (see page: 63)

[102] George E P Box. Science and Statistics. *Journal of the American Statistical Association*, 71(356):791–799, 1976. (see page: 67)

[103] N Riva, F Sirois, C Lacroix, W T B de Sousa, B Dutoit, and F Grilli. Resistivity of REBCO tapes in overcritical current regime: impact on superconducting fault current limiter modeling. *Superconductor Science and Technology*, 33(11):114008, oct 2020. (see page: 67)

[104] Jason Nicholson, Nicolò Riva, and Francesco Grilli. Non-parametric constrained regularization method applied to the electrical resistivity data of REBCO tapes for finite element modeling, Under preparation. *Under preparation*, 2020. (see page: 67)

[105] A. I. Larkin and Yu N. Ovchinnikov. Pinning in type II superconductors. *Journal of Low Temperature Physics*, 34(3-4):409–428, 1979. (see page: 67)

[106] T. A. Friedmann, M. W. Rabin, J. Giapintzakis, J. P. Rice, and D. M. Ginsberg. Direct measurement of the anisotropy of the resistivity in the a - b plane of twin-free, single-crystal, superconducting YBa2Cu3O7. *Physical Review B*, 42(10):6217–6221, 1990. (see pages: 68, 69, and 79)

[107] J. R. Groves, P. N. Arendt, S. R. Foltyn, Q. X. Jia, T. G. Holesinger, L. A. Emmert, R. F. DePaula, P. C. Dowder, and L. Stan. Improvement of ibad mgo template layers on metallic substrates for ybco hts deposition. *IEEE Transactions on Applied Superconductivity*, 13(2):2651–2654, 2003. (see page: 75)

[108] V. Selvamanickam, G. B. Galinski, G. Carota, J. Defrank, C. Trautwein, P. Haldar, U. Balachandran, M. Chudzik, J. Y. Coulter, P. N. Arendt, J. R. Groves, R. F. Depaula, B. E. Newnam, and D. E. Peterson. High-current Y-Ba-Cu-O superconducting films by metal organic chemical vapor deposition on flexible metal substrates. *Physica C: Superconductivity and its Applications*, 333(3):155–162, 2000. (see page: 75)

[109] T. Nagaishi, Y. Shingai, M. Konishi, T. Taneda, H. Ota, G. Honda, T. Kato, and K. Ohmatsu. Development of REBCO coated conductors on textured metallic substrates. *Physica C: Superconductivity and its Applications*, 469(15-20):1311–1315, 2009. (see page: 75)

[110] M. Igarashi, K. Kakimoto, S. Hanyu, C. Tashita, T. Hayashida, Y. Hanada, S. Fujita, K. Morita, N. Nakamura, Y. Sutoh, H. Kutami, Y. Iijima, and T. Saitoh. Remarkable progress in fabricating RE123 coated conductors by IBAD/PLD technique at Fujikura. *Journal of Physics: Conference Series*, 234(PART 2), 2010.

[111] Alexander Usoskin, Herbert C. Freyhardt, Alexander Issaev, Juergen Dzick, Juergen Knoke, Marijn P. Oomen, Martino Leghissa, and Heinz W. Neumueller. Large area YBCO-coated stainless steel tapes with high critical currents. *IEEE Transactions on Applied Superconductivity*, 13(2 III):2452–2457, 2003. (see page: 75)

[112] S. S. Oh, H. S. Ha, H. S. Kim, R. K. Ko, K. J. Song, D. W. Ha, T. H. Kim, N. J. Lee, D. Youm, J. S. Yang, H. K. Kim, K. K. Yu, S. H. Moon, K. P. Ko, and S. I. Yoo. Development of long-length SmBCO coated conductors using a batch-type reactive co-evaporation method. *Superconductor Science and Technology*, 21(3), 2008. (see page: 75)

[113] Vladimir Matias, E. John Rowley, Yates Coulter, B. Maiorov, Terry Holesinger, Chris Yung, Viktor Glyantsev, and Brian Moeckly. YBCO films grown by reactive co-evaporation on simplified IBAD-MgO coated conductor templates. *Superconductor Science and Technology*, 23(1):1–6, 2010. (see page: 75)

[114] Venkat Selvamanickam. Quadrupling critical current in HTS superconductor wires. Technical report, University of Houston, 2017. (see page: 76)

[115] Martin W. Rupich, Srivatsan Sathyamurthy, Steven Fleshler, Qiang Li, Vyacheslav Solovyov, Toshinori Ozaki, Ulrich Welp, Wai Kwong Kwok, Maxime Leroux, Alexei E. Koshelev, Dean J. Miller, Karen Kihlstrom, Leonardo Civale, Serena Eley, and Asghar

Kayani. Engineered Pinning Landscapes for Enhanced 2G Coil Wire. *IEEE Transactions on Applied Superconductivity*, 26(3):34–37, 2016. (see page: 76)

[116] T Kiss, T Nakamura, H Takeo, K Kuroda, Y Matsumoto, and F Irie. Flux creep characteristics in the presence of a pinning distribution for Y/sub 1/Ba/sub 2/Cu/sub 3/O/sub 7-/spl delta// superconducting thin films. *IEEE Transactions on Applied Superconductivity*, 5(2):1363–1366, jun 1995. (see page: 76)

[117] G Blatter, M V Feigel'Man, V B Geshkenbein, A I Larkin, and V M Vinokur. Vortices in high-temperature superconductors. *Reviews of Modern Physics*, 66(4):1125–1388, 1994. (see page: 76)

[118] Nicolò Riva, Francesco Grilli, and Bertrand Dutoit. A stand-alone executable app to teach about superconductors for power applications: The Superconducting Fault Current Limiter. *Under preparation*, 2020. (see page: 79)

[119] A Kudymow, C Schacherer, M Noe, and W Goldacker. Experimental Investigation of Parallel Connected YBCO Coated Conductors for Resistive Fault Current Limiters. *IEEE Transactions on Applied Superconductivity*, 19(3):1806–1809, jun 2009. (see page: 80)

[120] S Hellmann, M Abplanalp, S Elschner, A Kudymow, and M Noe. Current Limitation Experiments on a 1 MVA-Class Superconducting Current Limiting Transformer. *IEEE Transactions on Applied Superconductivity*, 29(5):1–6, aug 2019. (see page: 80)

[121] Christian Lacroix and Frederic Sirois. Concept of a current flow diverter for accelerating the normal zone propagation velocity in 2G {HTS} coated conductors. *Superconductor Science and Technology*, 27(3):35003, jan 2014. (see page: 81)

[122] Pascal Tixador. *Superconducting Fault Current Limiter*. World Scientific, 2018. (see page: 89)

[123] John Rozier Cannon. *The one-dimensional heat equation. Foreword by Felix E. Browder.*, volume 23. Cambridge University Press, Cambridge, 1984. (see page: 93)

[124] Alfio Quarteroni and Gianluigi Rozza. *Reduced Order Methods for Modeling and Computational Reduction*. Springer Publishing Company, Incorporated, 2013. (see pages: 93, 102)

[125] A Quarteroni, A Manzoni, and F Negri. *Reduced Basis Methods for Partial Differential Equations - An Introduction*. Springer, 2016. (see pages: 93, 102)

[126] Roberto Brambilla, Francesco Grilli, and Luciano Martini. Development of an edge-element model for AC loss computation of high-temperature superconductors. *Superconductor Science and Technology*, 20(1):16–24, 2007. (see page: 95)

[127] S C Fan and J C Chut. Thermal Stratification in Closed Cryogenic Containers. *Cryogenics*, 26(12):697, 1986. (see page: 99)

Nicolò **Riva**

PhD Student in Electrical Engineering and Applied Superconductivity

Rue du Maupas 16, CH 1004 Lausanne (Switzerland)

(+39) 320-6729685 | nicolo.riva@epfl.ch | Nicolò Riva | nicolorivaprina

Google Scholar | Research Gate | orcid.org/0000-0002-3359-7013

Education

PRINCIPAL EDUCATION:

École polytechnique Fédérale de Lausanne - Karlsruhe Institute for Technology   *Lausanne - Karlsruhe*
PHD STUDENT IN ELECTRONIC ENGINEERING AND APPLIED SUPERCONDUCTIVITY   *May 2017 - November 2020*
- Quench behaviour of High-Temperature Superconductor tapes for power applications: a strategy toward resilience
  Thesis director: Dr. Bertand Dutoit, EPFL - **Thesis co-director:** Priv.-Doz. Dr. Francesco Grilli

Università degli Studi di Milano   *Milano-Genova, Italy*
M.S. IN PHYSICS ACCELERATOR AND APPLIED SUPERCONDUCTIVITY - 110/110 CUM LAUDEM   *October 2014 - October 2016*
- Thesis : Study of a superconducting magnetic diverter for the Athena X-Ray space telescope (Link) (ESA)
- During my master thesis, I taught physics at the Antonio Rosmini High School (Domodossola-Italy)

Università degli Studi di Milano   *Milano, Italy*
B.S. IN PHYSICS - 104/110   *October 2010 - April 2014*
- Thesis: study of quench propagation in a superconducting magnet having non linear effects due to the saturation of the iron yoke

Experiences

Hyperloop Team EPFLoop (https://hyperloop.epfl.ch/)   *Lausanne, Switzerland*
AERODYNAMICS LEAD - PROPULSION TEAM   *October 2017 - now*
- CFD and structural FEM analysis (genetic algorithm), of a carbon fiber aeroshell (design and in-house manufacturing)
- Electromagnetic FEM analysis of a linear induction motor for the propulsion system (design and in-house manufacturing)
- Mechanical and thermal FEM analysis on main components of the POD (analysis on chassis, pressure vessels, brakes)
  Main advisor: Prof. Mario Paolone

École Polytechnique Montreal   *Montreal, Canada*
SUMMER INTERN   *July 2017 - September 2017*
- Summer Intership at PM (Polytechnique Montreal) with Prof. Frédéric Sirois:
  Quench measurements with ultra-fast pulser technique on 2G-REBCO tapes

OHB System-CGS (Compagnia generale per lo Spazio)   *Milano, Italy*
INTERN   *Oct. 2016 - May 2017*
- Study and design of an FLL for the SQUID based Cryogenic Anti-Coincidence of X-IFU for the ATHENA X-Ray space telescope(ESA)

FermiLab National Accelerator Laboratory   *Chicago, U.S.A.*
SUMMER INTERN   *July 2015 - October 2015*
- Summer Intership at Fermilab (Chicago) with Prof. Dr. Emanuela Barzi:
  Feasibility study of a surface impedance characterization (SIC) system for superconducting thin films

Antonio Rosmini High School   *Domodossola (VB), Italy*
PHYSIC'S TEACHER   *Oct. 2015 - Oct. 2016*
- Physic's teacher at Antonio Rosmini High School

Touristic organisation in Valle Antigorio (Italy)   *Baceno (VB), Italy*
SOUNDTRACK COMPOSER   *August-December 2011*
- Composition of soundtracks for local TV advertisement and trekking audio-guides

Teaching Activities

Karlsruhe Institute of Technology   *Karlsruhe, Germany*
TEACHING ASSISTANT   *April 2019 - June 2019*
- Teaching assistant at KIT for the course of *Superconducting Materials for Energy Applications*

Ecole Polytechnique Federale de Lausanne   *Lausanne, Switzerland*
TEACHING ASSISTANT   *Sept. 2017 - Sept. 2018*
- Teaching assistant at EPFL for the courses of *Classical Mechanics* and *Analysis I*

Antonio Rosmini High School   *Domodossola(VB), Italy*
Physics Teacher   *Oct. 2015 - Oct. 2016*
- Physic's teacher at Istituto Antonio Rosmini in Domodossola (Italy)

Awards

2019	**Awarded graduate study fellowship**, In recognition of academic excellence and achievement in the area of applied superconductivity (IEEE CSC Website)	*IEEE Council on Superconductivity*
2019	**Awarded IC School Special Prize**, Award in recognition of the excellent achievements in the SCI IC (Computer Science) Doctoral School	*SCI IC EPFL*
2019	**Best Poster at the COMSOL Conference 2019 Cambridge**, Fluid Damper Optimization Through CFD and Multi-Body Simulations of The Prototype Dynamic Response to Stochastic Excitation in the framework of the SpaceX Hyperloop Competition, *Jerome Harray, Lorenzo Benedetti and Nicolò Riva*	*Cambridge, COMSOL*
2019	**Team 3rd Place**, At the worlwide SpaceX Hyperloop Competition https://www.spacex.com/hyperloop	*Los Angeles, U.S.A*
2018	**Team 3rd Place**, At the worlwide SpaceX Hyperloop Competition https://www.spacex.com/hyperloop	*Los Angeles, U.S.A*

General Skills

PROFESSIONAL SKILLS:

Software skills	COMSOL, MATLAB, Blender, C/C++, ARDUINO, LabView, PSPICE, Adobe Suite, Audacity, LogicPro
Data processing	FEM (magneto/electro/thermal, superconductors, basic CFD), data regularization/processing, genetic algorithm
Experimental skills	Electronics, pulsed current measurements, cryogenic equipment, 3D printing, mechanical workshop
Languages	English (C1), French (B1), Italian (mother tongue)

EXTRACURRICULAR ACTIVITIES:

MUSIC   *Italy-Europe*
Orchestra and band performer   *Nov. 2004 - Now*
- Study of classical, jazz, and modern piano for 10 years (Roberto Olzer). Study of jazz and modern trombone for 8 years
- In 2004 I joined the **GMO orchestra** in Domodossola (VB), with which I've record different CDs and undertake tournèe and international exchange in Italy, Germany, Portugal e Switzerland from 2009 until 2019
- In 2008 I joined Blues4People recording the CD "*O Soul Mio*" and playing in tournée (in Italy between 2009-2011) with the **Original Blues Brothers Band** (the same acting in the Blues Brothers e Blues Brothers 2000 movies). I had the great opportunity to share the stage with important artists such as **Lou Marini**, **Steve Cropper**, **Alan Rubin** and more
- Since 2010 I'm part of the **White Spirit Gospel Choir**, occasionally performing in the Musical "The Lion King" in Italy
- From 2016 to 2018 I performed in brass formations such as New Tone Trombone Quartet and Accademia Big Band

C.O.S.A.   *Italy*
VOLUNTEER   *Nov. 2009 - Now*
- C.O.S.A. Africa di Milano e Amici di Gabriele Riva

Associazione SuoniAMO   *Italy*
VOLUNTEER   *Feb. 2009 - 2019*
- GMO Orchestra of SUONIAMO association: musician and sound technician

Science Communication   *Italy*
VOLUNTEER   *Feb. 2016 - Now*
- Collaboration with schools (Domodossola - Milano) presenting and helping in the organization of science dissemination events such as the annual event "*La settimana della Scienza*"

SPORT
Amateur level   *2005 - Now*
- Runner (half-marathon and marathon amateur races)
- Practice of Kung-fu Pak Hok Pai style in Domodossola (former amateur)

Research output list

Publications in peer-reviewed scientific journals

2020 **N. Riva**, F. Grilli, F. Sirois, B. Dutoit, C. Lacroix, W.B.T. de Sousa - *Resistivity of HTS tapes in overcritical current regime: impact on Superconducting Fault Current Limiter modeling*, Superconductor Science and Technology, (Link to publication)

2020 **F. Grilli**, A. Morandi, E. Pardo, V. M. R. Zermeno, R. Brambilla, T. Benkel, **N. Riva** - *Electromagnetic Modeling of Superconductors with Commercial Software: Possibilities with Two Vector Potential-Based Formulations*, IEEE Transactions on Applied Superconductivity, (Link to publication)

Peer-reviewed conference proceedings

2019 **N. Riva**, S. Richard, F. Sirois, C. Lacroix, B. Dutoit, F. Grilli - *Over-Critical Current Resistivity of YBCO Coated Conductors through Combination of Pulsed Current Measurements and Finite Element Analysis*, IEEE Transactions on Applied Superconductivity, (Link to publication)

2018 **N. Riva**, V. Calvelli, R. Musenich, S. Farinon, S. Lotti, P. Saracco - *Study of a Superconducting Magnetic Diverter for the ATHENA X-Ray Space Telescope*, IEEE Transactions on Applied Superconductivity, (Link to publication)

Conference proceedings

2019 **M. Seydoux**, **N. Riva**, S. Rametti, N. Bollier, L. Benedetti, A. Hodder, T. Dimier, M. Jufer - *Design and Manufacturing of A Linear Induction Motor for the 2019 EPFLoop Prototype in the Framework of the SpaceX Hyperloop Competition*, Cambridge COMSOL Conference 2019, (Link to publication)

2018 **Z. Sajó**, L. Benedetti, **N. Riva** - *Modeling The Hyperloop With COMSOL Multiphysics: On The Design Of The EPFLoop Pressurized Systems*, Lausanne COMSOL Conference 2018, (Link to publication)

2018 **N. Riva**, L. Benedetti, Z. Sajó - *Modeling The Hyperloop With COMSOL Multiphysics®: On The Aerodynamics Design Of The EPFLoop Capsule*, Lausanne COMSOL Conference 2018, (Link to publication)

Unpublished work (Under preparation or submitted)

2020 **N. Riva**, F. Grilli, F. Sirois, C. Lacroix, A.Akbar and B. Dutoit - *Optimization Method for Extracting Stabilizer Geometry and Properties of REBCO Tapes*, Submitted (ASC 2020 Issue)

2020 **N. Riva**, F. Grilli, B. Dutoit - *Superconductors for power applications: an executable and web application to learn about resistive fault current limiters*, Submitted - European Journal of Physics

2020 **A. Akbar**, **N. Riva**, Z. Yang, B. Dutoit - *Fast Hotspot Detection in SFCLs by Exploiting Strain Response in Optical Fiber Sensing*, Submitted (ASC 2020 Issue)

2020 **N. Riva**, F. Sirois, B. Dutoit, F. Grilli, C. Lacroix - *Improved resistivity model of REBCO tapes for numerical simulations in the overcritical current regime*, Under preparation - Draft available upon request

2020 **J. Nicholson**, **N. Riva**, F. Grilli - *Non-parametric constrained regularization method applied to the electrical resistivity data of REBCO tapes for finite element modeling*, Under preparation - Draft available upon request

Contributions to international conferences

Oral Presentations

October 2020 **N. Riva**, F. Sirois, F. Grilli, C. Lacroix, B. Dutoit *Optimization method for extracting stabilizer geometry and properties of REBCO tapes using an optimization procedure based on the finite element method and pulsed current experimental data*, Oral presentation at the Online Applied Superconductivity Conference, (Link to video presentation)

September 2020 **N. Riva**, F. Grilli, B. Dutoit - *Teaching future engineers about superconductors for power applications with an App*, Oral presentation at the Online COMSOL Conference 2020 Europe, (Link to video presentation)

September 2019 **M. Seydoux**, **N. Riva**, S. Rametti, N. Bollier, L. Benedetti, A. Hodder, T. Dimier, M. Jufer - *Design and Manufacturing of A Linear Induction Motor for the 2019 EPFLoop Prototype in the Framework of the SpaceX Hyperloop Competition*, Oral presentation at the Cambridge COMSOL Conference 2019 (UK), (Link to presentation)

September 2019 **L. Benedetti**, J. Harray, **N. Riva**, Z. Sajo, A. Gimonnet - *SpaceX Hyperloop Competition: Design and Manufacturing of A Carbon Fiber Composite Chassis for the 2019 Epfloop Prototype Using COMSOL Multiphysics® Composite Materials Module*, Oral presentation at the Cambridge COMSOL Conference 2019 (UK), (Link to presentation)

September 2019 **N. Riva**, F. Grilli, F. Sirois, B. Dutoit, C. Lacroix, W.B.T. de Sousa, *Resistivity of HTS tapes in overcritical current regime: Impact on Superconducting Fault Current Limiter*, Oral presentation at the European Conference on Applied Superconductivity, Glasgow (UK), (Link to presentation)

July 2019 **N. Riva**, F. Grilli, B. Dutoit, M. Masse, F. Sirois, C. Lacroix - *1D and 2D finite-element approaches to extract the resistivity of the superconductor material from pulsed current measurements on HTS commercial tapes*, Oral presentation at CHATS on Applied Superconductivity, Warsaw (Poland), (Link to presentation)

October 2018	**N. Riva**, S. Richard, F. Grilli, F. Sirois, B. Dutoit, C. Lacroix, *Isothermal Resistivity Curves of HTS Coated Conductors: A Synergy Between Experiment and Simulation* , Oral presentation at the Applied Superconductivity Conference, Seattle (USA), (Link to presentation)
October 2018	**L. Benedetti**, Z. Sajó and **N. Riva** - *Modeling the Hyperloop with COMSOL®: on the Mechanical Design of the EPFLoop Capsule*, Oral presentation at the Lausanne COMSOL Conference 2018, (Link to presentation)
September 2018	**N. Riva**, S. Richard, F. Grilli, F. Sirois, B. Dutoit, C. Lacroix, *Isothermal Resistivity Curves of HTS Coated Conductors: A Synergy Between Experiment and Simulation* , Oral presentation at the Material Science and Engineering congress, Darmstadt (Germany)

Invited posters

October 2020	**N. Riva**, F. Sirois, C. Lacroix, F. Grilli, B. Dutoit *Comparative investigation of the overcritical current regime on REBCO commercial tapes subjected to ultra-fast current pulses*, Invited poster at the Applied Superconductivity Conference, Online (USA)
September 2020	**N. Riva**, F. Grilli, B. Dutoit - *Teaching future engineers about superconductors for power applications with an App*, Invited poster at the COMSOL Conference 2020 Europe, Online
January 2020	**N. Riva**, F. Sirois, C. Lacroix, F. Grilli, B. Dutoit *Over-critical current resistivity characterization of REBCO commercial coated conductors: modified E-J curves*, Invited poster at the Conference on Superconductivity and Functional Oxides, S. Margherita Ligure (Italy), (Link to poster)
September 2019	**J. Harray**, L. Benedetti, **N. Riva** - *SpaceX Hyperloop Competition: Fluid Damper Optimization Through CFD and Multi-Body Simulations of The Prototype Dynamic Response to Stochastic Excitation*, Invited poster at the Cambridge COMSOL Conference 2019, (Link to poster)
September 2018	**Z. Sajó**, L. Benedetti, **N. Riva** - *Modeling The Hyperloop With COMSOL Multiphysics: On The Design Of The EPFLoop Pressurized Systems*, Invited poster at the Lausanne COMSOL Conference 2018, (Link to poster)
September 2018	**L. Benedetti**, Z. Sajó, **N. Riva** - *Modeling the Hyperloop with COMSOL®: on the Mechanical Design of the EPFLoop Capsule*, October 2018 Conference: Lausanne COMSOL Conference 2018, (Link to poster)
September 2018	**N. Riva**, L. Benedetti, Z. Sajó - *Modeling The Hyperloop With COMSOL Multiphysics®: On The Aerodynamics Design Of The EPFLoop Capsule*, October 2018 Conference: Lausanne COMSOL Conference 2018, (Link to poster)
June 2018	**N. Riva**, F. Grilli, F. Sirois, B. Dutoit *Reduced Basis Method for meso/large-scale superconducting application: A resilient strategy towards a robust design*, Invited poster at the Sixth International Workshop on Numerical Modelling of HTS in Caparica, (Portugal)
September 2017	**N. Riva**, V, Calvelli, R. Musenich, S. Farinon, S. Lotti, and P. Saracco - *Study of a Superconducting Magnetic Diverter for the ATHENA X-Ray Space Telescope*, Invited poster at the European Conference on Applied Superconductivity, Geneva (Switzerland)

OUTREACH ACTIVITIES

January 2020	**N. Riva**, *I superconduttori ed il futuro della tecnologia: Dalla fusione nucleare ad Hyperloop, il treno supersonico*, Science dissemination event at Institutes Marconi-Einaudi-Galletti for the Settimana della Scienza, Domodossola (Italy), (Link to video)
January 2020	**N. Riva**, *My Thesis in 180 Seconds*, Competition at EPFL
December 2019	**N. Riva**, F. Grilli, F. Sirois, B. Dutoit - *A better knowledge of High Temperature Superconductor for power applications: a strategy toward resilience*, Poster at Scientastic EDEE day at EPFL, Lausanne (Switzerland)
June/July 2019	**N. Riva**, *Moving fast and breaking records: On the physics and challenges of the Hyperloop concept*, Outreach activities in multiple seminars (Cambridge-Karlsruhe seminar/SupraSeminar in Karlsruhe)
September 2018	**EPFLoop Team**, M. Paolone, L. Benedetti, **N. Riva**, Z. Sajó - *Use Simulation to Design a Hyperloop Pod*, Invited Keynote COMSOL Conference Lausanne (Switzerland), (Link to video)
September 2018	**EPFLoop Team**, M. Paolone, L. Benedetti, **N. Riva**, Z. Sajó - *Inspiring Young Engineers to Design for the Future at EPFL*, Invited article on Comsol magazine, (Link to article)
March 2018	**N. Riva**, L. Benedetti, EPFLoop Team - *EPFL SpaceX Hyperloop Pod Competition: Mechanical Design Challenges*, Unveiling event of the EPFLoop 2018 Hyperloop prototype Lausanne (Switzerland), (Link to video)
April 2017	**N. Riva**, *La superconduttività: dal Klondike alla Woodstock della Fisica*, Science dissemination event at Institute Spezia, Domodossola (Italy)

OTHER ARTIFACTS WITH DOCUMENTED USE

Summer 2015	**N. Riva**, M. Graffiedi, D. Turrioni, E. Barzi *Design and project of a Surface Impedance Characterization system (SIC) for thin film of advanced superconductors*, Final report for the FermiLab Summer School - (Link to the report)
Summer 2015	**N. Riva**, M. Graffiedi, D. Turrioni, E. Barzi *Design and project of a Surface Impedance Characterization system (SIC) for thin film of advanced superconductors*, Presentation at FermiLab for the FermiLab Summer School final terms, (Link to presentation)